PROCESS CONTROL AND DEVELOPMENT FOR ULTRASONIC ADDITIVE MANUFACTURING WITH EMBEDDED FIBERS

DISSERTATION

Presented in Partial Fulfillment of the Requirements for the Degree Doctor of Philosophy in the Graduate School of The Ohio State University

By

Adam J. Hehr, B.S., M.S.

Graduate Program in Mechanical Engineering

The Ohio State University

2016

Dissertation Committee:

Professor Marcelo J. Dapino, Advisor

Professor Krishnaswamy Srinivasan

Professor Blaine Lilly

Professor Peter M. Anderson

© Copyright by
Adam J. Hehr
2016

ABSTRACT

Ultrasonic additive manufacturing (UAM) is a recent additive manufacturing technology which combines ultrasonic metal welding, CNC machining, and mechanized foil layering to create large gapless near net-shape metallic parts. The process has been attracting much attention lately due to its low formation temperature, the capability to join dissimilar metals, and the ability to create complex design features not possible with traditional subtractive processes alone. These process attributes enable light-weighting of structures and components in an unprecedented way. However, UAM is currently limited to niche areas due to the lack of quality tracking and inadequate scientific understanding of the process. As a result, this thesis work is focused on improving both component quality tracking and process understanding through the use of average electrical power input to the welder. Additionally, the understanding and application space of embedding fibers into metals using UAM is investigated, with particular focus on NiTi shape memory alloy fibers.

Recently, 9 kW UAM process variables have been empirically correlated to bond strength for Al 6061-H18 builds using a statistical design of experiments study. The process variables evaluated in the study were welder amplitude, normal force, welder travel speed, and baseplate temperature. The UAM process variables and property relationships identified in the statistical study inspired the development of an energy based model and control approach for improved UAM builds. In particular, input average electrical weld power, which has been empirically measured from the ultrasonic transducers, has been found to correlate with resultant weld microstructure and mechanical strength of builds. To understand the conversion of electrical to mechanical energy in the welder, a linear time invariant (LTI) model was developed using classic electroacoustics theory and in-situ measurements of sonotrode motion, applied transducer voltage, and average electric power. Using this model with 6061-H18 weld foil, imparted shear force on the welder during welding operations was found to be on the order of 2000 N, welder efficiency computed to be near 80%, and the influence of changing process variables on energy conversion understood. The influence of dissimilar weld foils on the required energy and power in the UAM process was also evaluated. The metallic foils of Al 6061-T6, annealed 110 Cu, and annealed 4130 steel were used due to their substantial differences in strength. Instead of weld foil strength influencing the effort of the welder, it was found that the linear elastic stiffness of the UAM component had the largest effect, including the baseplate material and welding fixture (vacuum chuck). Further, qualitative and quantitative correlations between welder power draw and system stiffness have been proposed to aid in predicting required welder amplitude for a given material or fixture configuration. Aside from using weld power to study the energy flow, component quality and defect tracking can also be accomplished because component compliance and weld defects influence electric power input. This in-situ power tracking and correlation with bond quality is needed in UAM to predict build performance, minimize defects, ensure consistent properties throughout builds, and to reliably create large compliant components.

Unique light-weight composite structures can be created using UAM. NiTi-Al composites are one example for reduced thermal expansion applications. However, scaling-up composite fabrication has proved to be challenging with undesired failure modes during construction and testing. As a result of these challenges, a fiber embedding framework has been developed to create robust interface joints between NiTi and Al. This framework includes groove design for fiber placement, selection of fiber geometry and surface finish, strength characterization of the NiTi-Al interface, microstructure analysis of Al around encapsulated fibers, and spectroscopy of the NiTi-Al interface. This framework is not unique to NiTi fibers alone. Instead, fiber optic cables, carbon fiber bundles, and other fiber types have been successfully embedded using aspects of the developed framework. This improved interface design and understanding enabled the construction of a multi-fiber composite which demonstrated an average thermal expansion near 6.5 $\mu\epsilon/^{o}C$ over multiple temperature cycles. This thermal expansion is near 28% of homogeneous aluminum and less than 50%

of the density of Invar. Furthermore, improved modeling of these NiTi-Al composites has been carried out by improving upon past phenomenological modeling efforts in addition to using a microsctructural FEA model through collaboration. These two models are required to improve understanding and design of NiTi-Al composites at various levels of detail.

To my wife, Kelly.

Acknowledgments

I would like to thank my family, friends, and work colleagues along the way. Your confidence and support in me has helped me work toward this degree. I'd like to thank the late Chris Larsen of Etegent Technologies for getting me involved with small business research in my undergrad, being extremely patient, and inspiring me to want more. I would not have done grad school without working in private sector research at Etegent Technologies (formally Sheet Dynamics). Dr. Mark Schulz had a huge impact on my graduate studies by helping me dream, encouraging me to apply for graduate fellowships, and leading by example. I'd like to thank my UAM colleagues for their patience, help, and support during my time here at Ohio State. It has been a fun ride working with you: Paul Wolcott, Xiang Chen, Justin Scheidler, Josh Pritchard, Matt Scheidt, Bryant Gingerich, Jack Schomer, Emilie Baker, Gowtham Venkatraman, Tianyang (Tyler) Han, Chris Pawlowski, and Leon Headings.

Next, I would like to thank the National Science Foundation (NSF). I am extremely thankful for their strong involvement with science in the US, either it be funding an educational program on PBS for children, funding graduate students, or funding university research. I was fortunate to benefit from all three–LeVar Burton is the man! I also would not have mustered the guts to pursue a PhD or engage with local area high schools without the NSF graduate research fellowship program.

Operating a 9 kW UAM machine the past few years has been a lot of fun, and it has also been extremely challenging at times. A special thank you to Cameron Benedict, Justin Wenning, Hilary Johnson, Brian Miracle and Mark Norfolk of Fabrisonic for helping during those challenging times. A special thanks to Karl Graff of EWI for his zeal and brilliance toward ultrasonic technologies–including UAM.

The staff at Ohio state is truly amazing. Research (including my own) and life here would be subpar without their expertise and willingness to help. Special thanks to Jason Dreyer, Chad Bivens, Kevin Wolf, Walter Green, Joe West, Nick Breckenridge, Janeen Sands, Charles (Greg) Slonaker, Caterina Runyon-Spears, Elizabeth Cumpston, Ralph Orr, Steve Bright, Ross Baldwin, Cameron Begg, and Dan Huber.

I'd also like to thank the terrific faculty on my committee: Marcelo Dapino, Blaine Lilly, Cheena Srinivasan, and Peter Anderson. Your time, effort, and criticism during my studies here has been priceless. Suresh Babu of the University of Tennessee has also provided valuable feedback and enthusiasm during my graduate work. I'd also like to thank my adviser, Marcelo Dapino, for allowing me to come directly into the group, work in the lab, mentor students, contribute toward proposals, go to conferences, submit journal papers, and work on patents. I learned a lot along the way.

Vita

June, 2012	B.S., Mechanical Engineering, Summa Cum Laude, University of Cincinnati, Cincinnati, OH
April, 2013	M.S., Mechanical Engineering, University of Cincinnati, Cincinnati, OH
2012 - 2015	NSF Graduate Research Fellow, Grant No. 1102690
2015 - 2016	Graduate Research Assistant: NSF CMMI Program, Grant No. 1538275

Publications

Journal Publications

P. Wolcott, A. Hehr, M. J. Dapino. 2014. Optimized welding parameters for Al 6061 ultrasonic additive manufactured structures. *Journal of Materials Research*, 29 (17).

A. Hehr and M. J. Dapino. 2015. Interfacial shear strength estimates of NiTiAl matrix composites fabricated via ultrasonic additive manufacturing. *Composites Part B: Engineering*, 77.

A. Hehr, P.J. Wolcott, M. J. Dapino. 2016 Effect of Weld Power and Build Compliance on Ultrasonic Consolidation. *Rapid Prototyping Journal*, 22 (2).

X. Chen, A. Hehr, M. J. Dapino, P. M. Anderson. 2015. Deformation Mechanisms in NiTi-Al Composites Fabricated by Ultrasonic Additive Manufacturing. *Shape Memory and Superelasticity*, 1(3), pp 294-309.

P.J. Wolcott, A. Hehr, C. Pawlowski, M. J. Dapino. 2016 Process Improvements and Characterization of Ultrasonic Additive Manufactured Structures. *Journal of Materials Processing Technology*, 233, pp 44-52.

A. Hehr and M. J. Dapino. Dynamics of Ultrasonic Additive Manufacturing. *Ultrasonics*, In Review.

A. Hehr, G. Venkatraman, E. Baker, L. Headings, M. J. Dapino. Effect of Dissimilar Metals on Welder Power. *Journal of Materials Processing Technology*, To be submitted.

Conference Presentations and Publications

P. Wolcott, A. Hehr, M. J. Dapino. Optimal welding parameters for very high power ultrasonic additive manufacturing of smart structures with aluminum 6061 matrix. Proc. SPIE Smart Structures and Materials + Nondestructive Evaluation and Health Monitoring, San Diego, CA, March, 2014.

A. Hehr, J. Pritchard, M. J. Dapino. Interfacial shear strength estimates of NiTi - Al matrix composites fabricated via Ultrasonic Additive Manufacturing. Proc. SPIE Smart Structures and Materials + Nondestructive Evaluation and Health Monitoring, San Diego, CA, March, 2014.

A. Hehr, J. Pritchard, M. J. Dapino. Ultrasonic additive manufacturing of NiTi - aluminum matrix composites. Proc. International Conference on Shape Memory and Superelastic Technologies (SMST), Pacific Grove, CA, May, 2014.

A. Hehr, X. Chen, J. Pritchard, M. J. Dapino, P. M. Anderson. Al-NiTi Metal Matrix Composites for Zero CTE Materials: Fabrication, Design, and Modeling. Proc. TMS, Orlando, FL, March, 2015.

A. Hehr and M. J. Dapino. Influence of Weld Power on Build Quality in Ultrasonic Additive Manufacturing Proc. TMS, Orlando, FL, March, 2015.

A. Hehr and M. J. Dapino. Power Transfer during Ultrasonic Additive Manufacturing Proc. MS&T, Columbus, OH, October, 2015.

A. Hehr and M. J. Dapino. Electroacoustics modeling of piezoelectric welders for ultrasonic additive manufacturing processes. Proc. SPIE Smart Structures and Materials + Nondestructive Evaluation and Health Monitoring, Las Vegas, NV, March, 2016.

Invention Disclosures

M. J. Dapino, D. Detwiler, M.B. Gingerich, R. Hahnlen, L. Headings, A. Hehr, M. Scheidt. Filed 7/16/2014. Hybrid joining of metals and continuous fiber materials using ultrasonic additive manufacturing.

M. J. Dapino, L. Headings, A. Hehr, P. Wolcott. Filed 10/18/2014. Process control for ultrasonic additive manufacturing.

Fields of Study

Major Field: Mechanical Engineering

Studies in:

Ultrasonic Additive Manufacturing	Prof. M.J. Dapino
Shape Memory Alloys	Profs. M.J. Dapino and P.M. Anderson

Table of Contents

Page

Abstract ii
Dedication v
Acknowledgments vi
Vita viii
List of Figures xiv
List of Tables xxv

Chapters

1 Introduction **1**
  1.1 Overview and Motivation 1
  1.2 Ultrasonic Additive Manufacturing 3
  1.3 UAM Process Variables and Property Relationships 8
  1.4 NiTi-Al Composites 12

2 Build Compliance, Power Compensation, and Microstructural Energy Storage **14**
  2.1 Introduction 14
  2.2 Build Compliance and Power Compensation 15
  2.3 Sample Construction and Testing 19
  2.4 Energy Storage 24
  2.5 Summary 27

3 Welder Operation and Linear Time Invariant Model **28**
  3.1 Introduction 28
  3.2 UAM Control Background 29
  3.3 Time-Invariant Linear Model of UAM Process 31
  3.4 Welder Characterization 36
    3.4.1 FRF Estimation of UAM Welder Components 36
    3.4.2 FRF Estimation of UAM Welder Assembly 42
    3.4.3 Welder Operation Measurements 46
  3.5 Welder Frequency Shift and Decrease in Amplitude 50
  3.6 Influence of UAM Build Dynamics 54

3.7 Summary 56

4 Welder Shear Force and Efficiency 58

4.1 Introduction 58

4.2 Welder Velocity Response during UAM 59

4.2.1 Effect of Shear Force 59

4.2.2 Effect of Build Compliance 62

4.3 Shear Force Estimates and Welder Efficiency 68

4.4 Influence of UAM Processing Conditions on Shear Force and Efficiency . . . 71

4.5 Summary 76

5 Influence of Dissimilar Materials on UAM 77

5.1 Introduction 77

5.2 Dissimilar Metal Welding Evaluation 78

5.2.1 Weld Foils 78

5.2.2 Baseplates 85

5.3 Modeling 90

5.4 Chuck Impedance and Baseplate Slip 100

5.5 Summary 106

6 Ni-Al Interface Strength and Bonding Mechanisms 107

6.1 Introduction 107

6.2 Sample Manufacture 108

6.3 Fiber Pullout Testing 111

6.4 Fiber Pullout Modeling 113

6.5 Microscopy and Microstructure Characterization 119

6.5.1 Consolidation Quality and Interface Composition 120

6.5.2 Microstructure Characterization for Pulled-Out Samples 122

6.6 Summary 127

7 Scaling-up NiTi-Al Composites 129

7.1 Introduction 129

7.2 Composite Manufacture and Testing 130

7.2.1 Material Stabilization (Training) and Characterization 130

7.2.2 Composite Design, Fabrication, and Testing 133

7.3 Composite Modeling 140

7.4 State-of-the-Art 146

7.5 Summary 150

8 Improvements to the Hahnlen Model 151

8.1 Introduction 151

8.2 Hahnlen Model Summary and Limitations 152

8.3 Improvements to the Model 154

8.4 Empirical Validation . . . 159
8.5 Summary . . . 160

9 Conclusion . . . 162
9.1 Summary of Findings . . . 162
9.2 Contribution and Significance . . . 166
9.3 Future Work . . . 170
9.3.1 Future Research within Scope of Thesis . . . 170
9.3.2 Required Research Outside of Thesis Scope . . . 176

Appendices

A Push-Pin Sample Manufacture, Testing, and Analysis . . . 180

B Identifying LTI Model Parameters . . . 185

C In-Situ Measurement Welding Procedure . . . 188

D Fiber Pullout Manufacture and Testing . . . 191

E NiTi-Al Composite Manufacture and CTE Testing . . . 201

F Improved Hahnlen Model Algorithm Flowchart . . . 206

Bibliography . . . 207

List of Figures

Figure **Page**

1.1 Potential UAM applications and capabilities. The low formation temperature of the UAM process allows joining dissimilar metals (without the formation of brittle intermetallics) and the integration of temperature sensitive components, smart materials, cooling channels, organic polymers, and electronics into metal matrices. 2
1.2 Schematic of 9 kW UAM process with key components detailed. 4
1.3 Comparison of cross sections of aluminum UAM builds: (a) first generation UAM system, 1 kW weld power, showing voids along tape interfaces; (b) current UAM technology, 9 kW weld power, creates gapless builds. Image courtesy of P.J. Wolcott [92]. 4
1.4 Symmetry of 9 kW UAM welder while actuating the welder under no load. To actuate with 1 transducer, the slave transducer was disconnected. The peak welder velocity is very similar between double and single transducer actuation, the excitation frequency is identical, and total average electric power is similar. To maintain peak welder velocity, the system increases total current, i.e., welder power. 5
1.5 Resultant interface grain structure observed from the UAM process: (a) welding Al 6061-H18 tape onto a Al 6061-T6 baseplate; (b) welding two Al 6061-H18 tapes together. These images were taken using a dual focused ion beam (FIB)/scanning electron microscope (SEM). 7
1.6 9 kW SonicLayer 4000 UAM system utilized to fabricate components in this thesis. 8
1.7 DOE Power Obversvations: (a) correlation of push-out energy from parametric study [92] and the average of the measured peak weld power during sample construction at layers 2, 8, 13, and 20.; (b) behavior of peak power with layers for various DOE samples. In (a) bond strength increases with increasing peak weld power for the same weld speed. For slower weld speeds, weld strength increases further. In (b) the peak weld power decreases with weld layers in an asymptotic manner and the peak weld power is grouped per amplitude setting. 11
1.8 Schematic representation of NiTi phase dependence on applied stress [36] and temperature with empirical data supporting trends and behaviors. . . . 12

2.1 Instantaneous power along the length of a weld for the 2nd and 20th layers in a single tape wide UAM stack. 16
2.2 Effect of build compliance on weld input power for a stack of welded Al foils: (a) measured average power over steady-state weld zone with one standard deviation error bars; (b) estimated build stiffness as a function of layer number assuming an ideal cantilever beam. 17
2.3 Power Compensation Concept: (a) schematic of UAM build during welding showing areas of elastic and plastic deformation, modified from Hehr et al [39].; (b) comparison of measured average electric power draw percent for build with (compensated) and without (uncompensated) power control [39]; (c) proposed bilinear shear force profile during welding. 19
2.4 Push-pin samples constructed with 9 kW UAM system and integrated CNC milling stage. In the image, C stands for compensated while R stands for reference, i.e., uncompensated. 20
2.5 Average electric power measurements during push-pin sample construction: (a) uncompensated build power curves; (b) compensated build power curves; (c) average of power trace at each layer for both uncompensated and compensated builds. 20
2.6 Push-Pin testing: (a) Gleeble thermal-mechanical tester utilized for push-pin testing with key test details shown in the inset; (b) push-pin sample details with key sample details shown for testing and failure. 21
2.7 Comparison between compensated and uncompensated push-pin samples: (a) photo comparing failure behavior; (b) force-displacement plots. 22
2.8 Interface microstructure at layers 5 and 15 for uncompensated and compensated samples. Samples were sectioned and polished for analysis near 15 cm of weld length to avoid transient weld regions. Arrows have been added to indicate the approximate interface region. Grain refinement can be seen at the interface regions as expected, yet poor mixing and less grain refinement are observed at the uncompensated 15th layer while the compensated 15th layer is like the uncompensated 5th layer. The difference in mixing and grain refinement originates from the uncompensated sample having received less strain energy. 25

3.1 UAM system dynamics and control when not welding, i.e., exciting welder in air without load, and welding Al 6061 foil: (a) peak sonotrode or welder velocity; (b) excitation frequency; (c) average electric power draw from one of the ultrasonic transducers. Data was collected using the welding process variables of 32.5 μm peak-peak prescribed welder vibration, a down force of 5000 N, and a rolling speed of 5 m/min (200 in/min). Data was sampled at 50 kHz and processed with a block size of 8192 points, welder vibration was measured with a non-contact laser vibrometer, welder frequency was obtained using a short time windowed FFT, and power draw was sampled directly from the ultrasonic generator. 31

3.2 UAM weld assembly analysis: (a) schematic of assembly with components, voltages, forces, and degrees of freedom detailed; (b) equivalent circuit of weld assembly with transducers and sonotrode modeled separately; (c) simplified equivalent circuit of weld assembly by lumping the transducers and sonotrode dynamics together. 33
3.3 Equivalent circuit for welder operation: (a) mobility form of system with added inductance to 'zero out' transducer capacitance; (b) simplified mobility form of system without electrical influences from transducer, i.e. motional feedback form. 34
3.4 Characterization of the 5 kW piezoelectric transducer: (a) schematic of transducer with important test conditions and variables detailed; (b) equivalent circuit of piezoelectric transducer (Mason circuit). The piezoelectric transducer case is attached at the node point with rubber o-ring washers. This node point attachment isolates the dynamics of the transducer. Foam is used as a precautionary measure. Piezoelectric transducer schematic modified from AWS Handbook [29]. 37
3.5 Comparison of experimental and analytical FRFs with corresponding phase angle. The phase difference is believed to exist from the amplifier used to to measure voltage and current. 38
3.6 Transducer evaluation: (a) excitation at various voltage levels to evaluate transducer linearity; (b) comparison of transducers at 10 V excitation level. The transducers exhibit linear response over the range of evaluated voltages and they have similar response characteristics, i.e., magnitude and frequency is similar. 40
3.7 Characterization of sonotrode: (a) sonotrode resting in welding assembly with important test conditions and variables detailed; (b) equivalent circuit of the measured mechanical impedance. 40
3.8 Admittance of the sonotrode or the inverse of impedance from 0-40 kHz. The ordinary coherence function is plotted with the admittance measurement. 41
3.9 Approach and equipment used to measure experimental FRF measurements of weld assembly. Characterization was done inside the UAM machine to emulate operating boundary conditions. 42
3.10 Conditions for assembly FRF measurements: (a) H_e and H_{em} measurements by driving one transducer and leaving the other open; (b) H_m measurement by shorting both transducers with a low resistance wire. 43
3.11 Experimental FRF measurements of weld assembly near 20 kHz: (a) comparison of H_e, H_{em}, and H_m FRFs; (b) H_m resonance dependence on shorted and open circuit conditions. The system resonance is different for short and open circuit conditions because the piezoelectric crystal stiffness is different between the two electric boundary conditions. 44
3.12 System FRF comparison between measurement and system level model. . . 45
3.13 Operation of welder operating under no load, i.e., not welding: (a) comparison of peak welder velocity and average electric power draw as a function of amplitude setting; (b) applied voltage as a function of amplitude setting. . . 47
3.14 Correlation of mechanical mobility model to average electric power. 48

3.15 Sonotrode deformation analysis from shear loading: (a) reduced model of sonotrode tool piece with assumptions; (b) deformation contour of 9.65 cm diameter tool piece with applied 2000 N distributed load. 52
3.16 Estimation of UAM build stiffness via a 75 Hz frequency shift and the investigation of UAM build stiffness on FRF magnitude. Due to stiffness not influencing FRF magnitude, FRF magnitude would be consistent when system resonance changes under load. Damping or energy leaving the system is shown to decrease system response. 55
3.17 Nyquist plots: (a) estimated motional impedance locus, H_e^*; (b) measured admittance locus, H_{em}. Resonant frequencies for each locus are marked with an asterisk while adjacent locus points are marked with circles. Loading the system without damping does not change the motional impedance locus due to the diameter remaining constant. The decrease in locus diameter occurs only when damping is introduced [44]. The resonant frequency location in the motional impedance locus occurs at 0 degrees because the electromechanical coupling coefficient is assumed to be real valued [44]. To verify this assumption, the H_{em} admittance locus is plotted. The resonant peak has a phase location < 1 degrees, which supports the real valued coupling coefficient assumption of 0 degrees. 56

4.1 Sonotrode or welder velocity character during UAM compared to actuating the welder without load, i.e. not welding: (a) time history comparison of signals; (b) frequency domain comparison of signals. Signals were sampled at 512 kHz with an amplitude level of 60% (32.5 μm setpoint). The phase delay in (a) is of no significance. The small decrease in welder amplitude during welding is discussed in Chapter 3. Frequency data was obtained by averaging the velocity signal magnitude with a block size of 81920 points and without windowing. Windowing was not used to illustrate increased frequency content more clearly. Due to windowing not being used, some leakage may be present in the figure. 60
4.2 H_{em} and H_m^* FRF estimates of the welder from 0 to 100 kHz. The nominal resonance of the welder is 19.757 kHz, and its harmonics are marked with astericks on the FRFs. The 2nd harmonic (39.514 kHz) is given as an example. The locations of the harmonic frequencies were investigated to see if they coincided with any system resonances. No harmonics showed correlation with system resonances, so amplification is not significant during welding. FRFs were estimated using the high speed data acquisition system of the laser vibrometer. 62
4.3 Power and excitation frequency shift during UAM stack construction: (a) average electric weld power vs. number of layers; (b) excitation frequency shift vs. number of layers. The compensated power trace in (b) shows an increased amount of frequency shift. 64
4.4 Frequency shift mechanisms during UAM: (a) less plastic hardening decreases the effective build stiffness; (b) more plastic deformation decreases the effective build stiffness. 65

4.5 Harmonic content during UAM stack construction for the approximate locations of 20, 40 ,and 60 kHz: (a) 1st harmonic, 20 kHz; (b) 2nd harmonic, 40 kHz; (c) 3rd harmonic, 60 kHz. The influence of power compensation increases the 1st harmonic's content, but does not influence the other harmonics. Due to the UAM build becoming more compliant with construction, the 3rd harmonic's content decreases. Harmonic content was found using FFT analysis using a Hamming processing window, a block size of 81920 (6.5 Hz resolution), and by averaging the harmonic peak value with three points below and above it, i.e., seven total points total used to estimate content around the peak. Seven points were used for averaging content because reliably and consistently estimating the peak harmonic response is difficult with the processing block resolution. 66

4.6 Proposed shear force profile during welding using evidence from welder velocity frequency response measurements and H_m^*: (a) force-displacement; (b) force-time. Due to the UAM build becoming more compliant with more layers, the behavior of the forcing function becomes less square like with more layers. 68

4.7 Estimate of welder shear force from in-situ velocity and power measurements. Welder excitation frequency is also compared to illustrate system stiffening when welding. 70

4.8 Comparison of system dynamics as a function amplitude level. Other UAM processing conditions were held constant in this study. In particular, normal load was 5000 N, linear weld speed was 5 m/min (200 in/min), and welds were made at room temperature. 72

4.9 Comparison of system dynamics as a function of normal force. Other UAM processing conditions were held constant in this study. In particular, prescribed welder amplitude was 60% (32.5μm), linear weld speed was 5 m/min (200 in/min), and welds were made at room temperature. 74

4.10 Comparison of system dynamics as a function of weld speed. Other UAM processing conditions were held constant in this study. In particular, prescribed welder amplitude was 60% (32.5μm), normal force was 5000 N, and welds were made at room temperature. 75

5.1 Weld foil stress-strain curves collected using DIC: (a) full stress-strain; (b) linear elastic region. Data courtesy of M. Scheidt and B. Losey. 79

5.2 Welded foils along with ultimate tensile strength (UTS) for reference. Two layers of each foil were welded respectively. 80

5.3 Micrograph comparison of two layers of foil onto a baseplate: (a) Al 6061-T6 onto Al 6061 T6; (b) 110 Cu onto Al 6061-T6; (c) 4130 steel onto Al 6061-T6; (d) 4130 steel onto 4130 steel. The hardness (strength) mis-match of the foils onto the baseplate influences the shear behavior of the asperities. Some voids are present in the steel-steel weld on the Al baseplate in (c). Approximate weld interface locations are marked with arrows. 81

5.4 Weld interface examination: (a) Al 6061-T6 onto Al 6061 T6; (b) 110 Cu onto Al 6061-T6; (c) 4130 steel onto Al 6061-T6; (d) 4130 steel onto 4130 steel. Approximate weld interface locations are marked with arrows. 82

5.5 Welding different weld foils onto an Al 6061-T6 baseplate. The influence of weld foil properties has little to no influence on the UAM process. 83
5.6 Qualitative surface difference between welding steel on different baseplates: (a) Al 6061-T6, 9.53 mm (0.375 in) thick; (b) Annealed 4130 St, 3.18 mm (0.125 in.) thick. The steel baseplate weld develops a brown surface finish due to enhanced slipping from improved bonding. 84
5.7 Welder behavior for welding steel on different baseplates: (a) Al 6061-T6, 9.53 mm (0.375 in) thick; (b) Annealed 4130 St, 3.18 mm (0.125 in.) thick. The steel baseplate weld required enhanced power effort to achieve the prescribed motion. 85
5.8 Welder behavior for welding Al 6061-H18 on different baseplates: (a) Annealed 4130 St, 3.18 mm (0.125 in.) thick; (b) Al 6061-T6, 9.53 mm (0.375 in) thick. The steel baseplate weld required enhanced power effort to achieve the prescribed motion. 87
5.9 Evaluation of accumulative baseplate stiffness interaction with the UAM process: (a) total average electric power draw; (b) peak welder velocity. The aluminum baseplate is 9.53 mm (0.375 in) thick while the steel is 3.18 mm (0.125 in.) thick. Both baseplates have similar masses. 88
5.10 Imaging of Al 6061-H18 stack onto baseplates: (a) Al 6061-T6; (b) Annealed 4130 steel. 89
5.11 Steel asperity deformation when joining Al 6061-H18. Large asperity deformation and cracking is observed. Large deformation is possible due to the high ductility of the steel. Cracking may occur due to work hardening during the texture and welding pass. 90
5.12 UAM stack and system dynamics: (a) schematic illustration of system with key inputs and outputs; (b) equivalent circuit of system. 91
5.13 FEM of stack and baseplate: (a) contact surface used for loads and analysis; (b) transverse displacement of stack (y-direction). 92
5.14 Mesh density of FEM. A graded mesh was utilized near the contact surface to accurately describe the deformation behavior of the stack. 93
5.15 First mode of vibration of stack in shear is near 60 kHz, which is far above the 20 kHz excitation frequency. 93
5.16 Qualitative comparison of measurement and simulation: (a) measured average electric power; (b) calculated effective stiffness assuming elastic deformation solely and 0.9 mm contact width. Both trends are similar in qualitative behavior. 95
5.17 Correlation of measured average electric power and estimated stiffness from 0.9 mm contact width. Both data sets show linear trend behavior and similar slopes. 96
5.18 UAM stack motion experiment: (a) schematic illustration of experiment; (b) experimental acceleration data for top of UAM stack and side of baseplate. 97
5.19 Simulation of UAM stack displacement in lateral or y-direction: (a) isotropic view of model; (b) surface in contact with welder; (c) surface on side of UAM stack, which is visible by laser vibrometer. 98

5.20 UAM stack motion comparison: (a) contour plot of y-displacement of side of UAM stack; (b) experimental displacement for top of UAM stack. Due to the laser measuring near the top of the stack, the peak displacement cannot be feasibly measured and will be less. As a result, the model and experiment show good correlation. 99
5.21 Modal hammer testing of baseplate and vacuum chuck anvil structure. This test is used to measure the mechanical impedance of the structure. 101
5.22 Frequency response function analysis of the mechanical admittance with corresponding coherence. All of the curves are similar near 20 kHz except the baseplate driving point measurement. 102
5.23 Mechanical impedance of baseplate/vacuum chuck anvil. The impedance is about 2 GN/m near 20 kHz. 102
5.24 Slip evaluation of baseplate on vacuum chuck. Sonotrode motion was also measured to evaluate phase relationships between the baseplate and chuck. 103
5.25 Test design for evaluating baseplate slip between sonotrode and vacuum chuck. 104
5.26 Correlation between phase angle and average electric power. 105

6.1 Sample manufacture with details. 109
6.2 Sample details: (a) schematic of sample cross section with key fabrication details; (b) physical sample ready to test post manufacture. 110
6.3 Custom fiber pullout test fixture used in study. 111
6.4 TestResources load frame used for testing with key specifications listed. The area boxed in red illustrates how the test fixture and sample are loaded into the machine. 112
6.5 Representative pullout test result for oxide sample 7: (a) photo of sample after failure illustrating adhered aluminum to surface of fiber; (b) detailed force-displacement pullout test curve. 113
6.6 Influence of NiTi geometry: (a) ribbon; (b) fiber. The ribbon geometry does not exhibit matrix failure via plastic deformation. 114
6.7 Room temperature stress-strain curves of fibers utilized in this study. Data was taken using ASTM F2516 - 07e2, Standard Test Method for Tension Testing of Nickel-Titanium Superelastic Materials. Data shows a high detwinning stress and large elongation to form Martensite. 116
6.8 Graded mesh of FEM with zoomed in region on fiber. 116
6.9 FEM of fiber pullout test showing key assumptions and details: (a) top view of sample; (b) bottom view of sample; (c) displacement view from top of sample; (d) displacement view from bottom of sample. 117
6.10 Shear stress analysis of fiber-matrix interface for 40 N load: (a) stresses were calculated on the line shown; (b) shear stress calculation along the thickness of the aluminum sample, for the three different sample thicknesses considered. Peak stresses are observed to occur at the same depth in the aluminum sample. 119
6.11 SEM images of embedded NiTi fibers utilized in study: (a) oxide surface finish; (b) mechanically roughened surface finish; (c) chemically etched surface finish; (d) mechanically polished surface finish. 121

6.12 SEM image of top of oxide surface finish fiber with corresponding EDS line scan. 122
6.13 SEM image of top of mechanically roughened surface finish fiber with corresponding EDS line scan. 123
6.14 SEM image of top of chemically etched surface finish fiber with corresponding EDS line scan. 123
6.15 SEM image of top of mechanically polished surface finish fiber with corresponding EDS line scan. 123
6.16 Optical images of etched sample at various magnifications using DIC to show grain structure around pulled out fiber: (a) overall view; (b) right top and side; (c) left top and side; (d) zoomed-in left side. 124
6.17 Focused ion beam etched surface: (a) grain structure without flow detail; (b) grain structure with flow detail. 125
6.18 Analysis of pristine roughened NiTi fiber prior to pullout. Arrows identify the approximate tape interface. 126
6.19 Influence of NiTi geometry: (a) ribbon; (b) fiber. The ribbon geometry exhibits delamination while the fiber geometry remains intact due to the interface crimping near the fiber. 127

7.1 Stabilization or training of NiTi fibers prior to embedding. 130
7.2 Isotemperature stress-strain curves of NiTi fiber at various temperatures. . 131
7.3 Differential scanning calorimeter measurements on as-received (not stabilized) and stabilized measurements. 132
7.4 Stress-temperature phase diagram for stabilized NiTi. The diagram was assembled using isotemperature stress-strain and DSC measurements. This phase diagram can be used to shed insight into composite performance. . . 133
7.5 Composite design: (a) fibers were strategically placed to eliminate shared interface boundaries and minimize possible delamination; (b) pocket design for fiber placement. 134
7.6 Manufacture of composite. The fibers are manually placed in the milled channels and constrained via the fabrication fixture. An ideal consolidation layer shows no shinny spots, i.e., voids around fibers or unwelded areas. . . 135
7.7 Composite removed from baseplate and ready for thermal expansion testing. 136
7.8 Thermal test utilized to measure composite CTE. Important test elements have been detailed. 137
7.9 Empirical strain-temperature results: (a) 13% NiTi volume fraction composite for 3 cycles; (b) comparison of Al (no NiTi), composite with 13% volume fraction and composite with 13.8% volume fraction. Fit slopes from 40 to 100°C are given. 138
7.10 Schematic illustration of axial stress state of NiTi during temperature cycling, shown on the stress-temperature phase diagram. The first temperature cycle of the material creates a state of tension due to the material not fully transforming back to the initial Martensitic volume fraction. Subsequent cycles coalesce. 138

7.11 End cross section of 13.8% NiTi composite: (a) the composite before heating, some void presence can be seen with no obvious cracking; (b) the composite after 3 heating cycles, little to no cracking formed during thermal cycling. . 139
7.12 Al 6061-H18 plasticity at 100°C: (a) stress-strain showing ductility after 200 MPa; (b) creep test showing decreasing creep with cycling. 140
7.13 NiTi FE model calibration showing the fit to experimental data: (a) uniaxial tension at 65°C and 85°C for a <110>B2-oriented NiTi fiber; (b) DSC curves. 141
7.14 Simulated mechanical and thermal loadings: the NiTi fiber is first cooled under a tensile stress of $\sigma_{\text{bias}} = 400$ MPa in the absence of Al matrix to induce oriented martenite, and then unloaded at 22°C (blue regime). This is followed by embedding the fiber in matrix at $t = 500$s. The heating-cooling cycle of the composite from 22°C to 100°C is repeated 4 times (orange regime) to study the evolution of performance. 142
7.15 The finite element model of the composite. Three mirror-plane conditions are applied two of them through the center axis of the fiber (shown in blue), while the remainder is perpendicular to the fiber. 143
7.16 Simulation results for a Al-NiTi composite with a thermo-elastic (non-plastic) matrix: (a) first cycle; (b) subsequent cycles (which overlap); (c) and (d) corresponding evolution of martensite volume fraction in the NiTi fiber. The simulation describes general trends with modest quantitative agreement. 144
7.17 Simulation results for a Al-NiTi composite with plasticity, void collapse, and a modified driving force for the NiTi: (a) first cycle; (b) subsequent cycles (which overlap); (c) and (d) corresponding evolution of martensite volume fraction in the NiTi fiber. The simulation describes general trends with close quantitative agreement. 145
7.18 Consolidation evaluation of NiTi fibers near 500 μm in diameter. A more rough surface finish enables improved consolidation quality. 146
7.19 Estimated thermal expansion response using improved Hanlen NiTi-Al composite model. A thermal expansion of 5 $\mu\epsilon/^{o}C$ was obtained using a volume fraction of 18%. 148
7.20 Thermal expansion response of state-of-the-art NiTi-Al composite. A thermal expansion reduction of 72% was obtained when compared to homogeneous Al. 149
7.21 State-of-the-art NiTi-Al composite cross section. Cracks and voids are present within the build due to inadequate channel depth. Despite non-ideal consolidation characteristics, the composite performs near expectations. . . 149

8.1 NiTi-Al composite force analysis: (a) xy plane of representative composite area element; (b) projected forces from (a) onto the matrix; (b) projected forces from (a) onto the fiber; (d) zy plane of representative composite area element; (e) projected forces from (d) onto the matrix; (f) projected forces from (d) onto the fiber. In general, the interface is in tension, which, in turn puts the matrix in compression in the z and y directions and the fiber in tension in the z and y directions. 155

8.2 Volume fraction analysis for y stress: (a) a representative composite element illustrating how the stress will be localized to the area bound by the fiber; (b) COMSOL simulation of 13% NiTi and Al illustrating validity of assumption due to the entire fiber being in tension while only areas bound by the fiber in the matrix are in compression. 158
8.3 Comparison of original (1D) and improved Hahnlen model (3D): (a) models shown against experiment for 13% v_f; (b) models with 18% v_f. The 1D model over-estimates response, and this error becomes larger at higher volume fractions. 159
8.4 Validation of model against 19.5% v_f: (a) first cycle of axial (x) strain; (b) first cycle of lateral (y) strain. Arrows are shown to illustrate heating and cooling response directions of the composite. General trends and magnitudes are described with the model. 160

9.1 In-situ laser vibrometer measurements on sonotrode, weld foil, and baseplate from D. Foster [21]. 171
9.2 Stress-strain comparison of 6061 weld foils. T6 heat treatment increases the strength and ductility of the weld foil. 173
9.3 Preliminary results for joining NiTi to Al. The weld was achieved by using a slow travel speed, i.e. imparting large amounts of strain energy into the weld interface. It can be seen that the horn left a texture on the NiTi. . . . 174
9.4 SEM images of Al-NiTi weld quality. It can be seen that the Al firmly sticks to the NiTi when welded due to high shear deformation while the welded NiTi onto the Al does not demonstrate much interface mixing due to the flat interface character. 174
9.5 Tape veer identification using average electric weld power. The gradual change in contact stiffness can be observed in the power trace. 175
9.6 Push-pin results: (a) 14 μm Ra; (b) 7 μm Ra. 14 μm Ra shows consistently higher peak force and energy under the force-displacement curve [93]. . . . 177
9.7 Cross section of UAM builds: (a) 14 μm Ra; (b) 7 μm Ra [93]. 177
9.8 Baseplate cracking observed in large UAM build construction. 178

A.1 Push-pin samples ready for EDM or band saw. 181
A.2 Finalized push-pin sample drawing. 182
A.3 Push-Pin testing: (a) Gleeble thermal-mechanical tester utilized for push-pin testing with key test details shown in the inset; (b) push-pin sample details with key sample details shown for testing and failure. 183
A.4 Push-Pin test result summary. Examples of good and bad welds with their corresponding force-displacement curves. 184

B.1 Wire schematic for finding mechanical mobility circuit model parameters for welder. 185

C.1 Wire schematic for finding mechanical mobility circuit model parameters for welder. 188

D.1 Pullout sample manufacture with details. 193

D.2 Photo of removed foil after razor blade scoring, step 8. The NiTi wires are visible. 194
D.3 3-axis milling: (a) weld side with perpendicular notch penetrating through the entire sample; (b) backside of sample with removed baseplate material and cut notches. 194
D.4 Drawing of wire EDM cutting passes and dimensions. These cutting passes were selected to minimize stress on samples. This cutting path may not be optimal for reducing stress or for reducing EDM cutting time. 195
D.5 Wire EDM cutting: (a) G-code for sample removal; (b) machine path for sample removal; (c) removed samples showing location where wire came into baseplate. 195
D.6 Pullout sample details: (a) schematic of sample cross section with key fabrication details; (b) physical sample ready to test post manufacture. 196
D.7 Pullout testing fixture drawings: (a) pullout fixture; (b) grip adapter. . . . 198
D.8 Custom fiber pullout test fixture used in study. 199
D.9 TestResources load frame used for testing with key specifications listed. The area boxed in red illustrates how the test fixture and sample are loaded into the machine. 199
D.10 Representative pullout test result for oxide sample 7: (a) photo of sample after failure illustrating adhered aluminum to surface of fiber; (b) detailed force-displacement pullout test curve. 200

E.1 Example scaled composite schematic to aid in composite manufacture. . . . 202
E.2 Composite removed from baseplate and ready for thermal expansion testing. 203
E.3 Thermal test utilized to measure composite CTE. Important test elements have been detailed. 204
E.4 LabVIEW VI used to measure strain and temperature of samples during thermal cycling. 205

F.1 Big picture algorithm flow diagram of improved Hahnlen model. Other more detailed flow diagrams of the model are given in Hahnlen's thesis [34]. . . . 206

List of Tables

Table **Page**

2.1 Power compensation approach by changing amplitude per layer. 18
2.2 UAM control variables utilized for welding samples. 20
2.3 Push-pin testing results for uncompensated and compensated samples. Peak Force (P. Force) and Push-out Energy (Energy) is reported along with the mean and first standard deviation (Std) for the sample set. 22

3.1 Lumped parameter values for Mason circuit model of piezoelectric transducer. 39
3.2 Lumped parameter model values for equivalent circuit of welding assembly dynamics. 46
3.3 Coefficients used to validate mechanical mobility representation. 49
3.4 Frequency of welder velocity as a function of amplitude level. Frequency found via windowed FFT with frequency resolution near 3 Hz. The median frequency of 19.757 kHz agrees well with FRF measurements. A Hamming processing window was utilized to minimize leakage when estimating frequency. 49
3.5 COMSOL model results for peak sonotrode deformation for a given tool diameter and distributed shear force. Results are in units of micron (μm). . 53
3.6 Key lumped parameter values to describe UAM stack dynamics. Effective build stiffness (k_{eff}) was chosen by increasing the system resonance 75 Hz. A high loss factor (η) was chosen to illustrate the influence of the large amount of plastic deformation on system response during UAM. 54

4.1 Power compensation approach by increasing prescribed peak-to-peak displacement (δ_L) of the welder. Amplitude percentage was input into the UAM machine controller to achieve the given displacement. 63
4.2 Welder efficiency comparison between the states of not welding and welding. A small efficiency is calcualted for the state of not welding due to a small residual shear force being present from the calculation of shear force (4.6). . 71
4.3 Welder efficiency comparison between different amplitude settings. 72
4.4 Welder efficiency comparison as a function of normal force. 74
4.5 Welder efficiency comparison as a function of weld speed. 75

5.1 Stress-strain property summary of foils. 79

5.2 UAM welder parameters for welding dissimilar foil. 80
5.3 UAM welder parameters for welding Al 6061-H18 foil onto aluminum and steel baseplates. 86
5.4 Influence of weld foil on effective system stiffness. Stiffer weld foils do stiffen the overall system, yet the change is small for the two contact width bounds of 0.9 ($K_{FEM,L}$) and 2.54 mm ($K_{FEM,H}$). All units in (MN/m). 94

6.1 Ultrasonic welding parameters used in study. 109
6.2 Fiber pullout summary for all surface finishes. 114
6.3 FEM material properties. 115
6.4 Fiber pullout comparison between FEM and empirical results. Average peak shear stress was computed by averaging first 5 data points near fiber edge while average shear stress averaged all data points over fiber length. 118

7.1 Phenomenological properties of NDC 380 μm diamter NiTi found via characterization. 133
7.2 Ultrasonic welding parameters used in study. 135
7.3 Phenomenological properties of 580 μm diameter FWM NiTi No. 6 found via characterization. 147

Chapter 1

INTRODUCTION

1.1 Overview and Motivation

Additive manufacturing and dissimilar metal joining are two advanced manufacturing technological areas which have been attracting much attention recently due to the need to reduce weight (light-weighting) and enhance product performance [5, 9]. One example of the need to reduce weight while simultaneously improving product performance is the 54.5 mpg fuel economy requirement for automobiles by the year 2025 in the United States [71]. Also, growth in metal based additive manufacturing technologies the past four years has been near 30% (CAGR) [9]. Ultrasonic additive manufacturing (UAM) is a recent technology which combines dissimilar metal joining and additive manufacturing. The technology also demonstrates scalability promise for production environments. As a result, commercial interest in UAM and its applications have grown quickly since its inception, like other metal based additive manufacturing technologies, while its full potential has yet to be discovered.

A distinguishing characteristic of UAM from other additive manufacturing and dissimilar metal joining technologies is its low formation temperature. This low formation temperature enables the joining and incorporation of components into metals without melting and solidifying the constituent materials. As a result, metals prone to solidification cracking, e.g., alumium alloys, can be reliably joined, dissimilar metal joints can be formed with minimal or no intermetallic compounds [47, 70, 41, 87, 80], and temperature sensitive components like sensors, polymers, and smart materials can be built into metals without degrading functionality [53, 56, 81, 16, 34]. Smart materials couple energy behaviors across different physical domains. An example of a smart material is NiTi shape memory alloy, which couples the domains of temperature (thermal) and strain (mechanical). The low temperature characteristic of UAM enables the creation of unique metal matrix composites and components not possible with traditional manufacturing methods or laser based additive manufacturing technologies. Areas of application which have been identified for UAM are schematically shown in Figure 1.1.

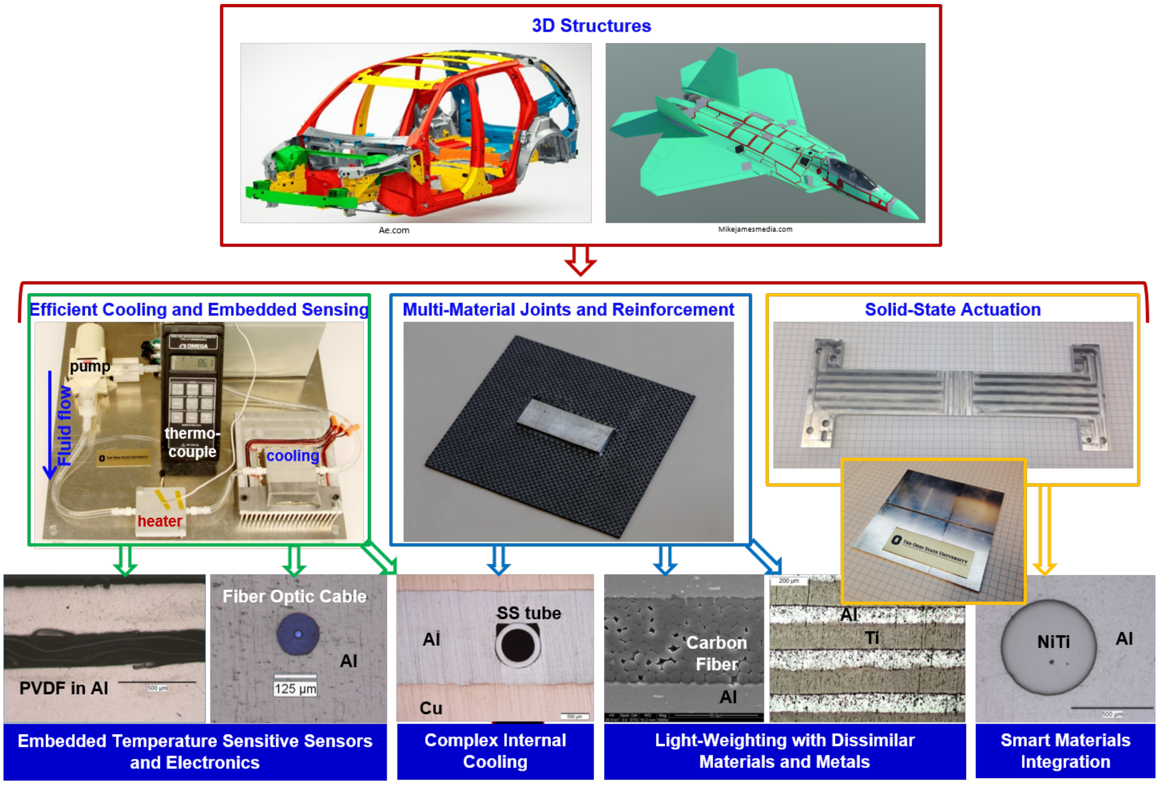
3D Structures
Ae.com
Mikejamesmedia.com
Efficient Cooling and Embedded Sensing
pump
Fluid flow
thermo-couple
cooling
heater
Multi-Material Joints and Reinforcement
Solid-State Actuation
PVDF in Al
Fiber Optic Cable
Al
125 μm
SS tube
Al
Cu
Carbon Fiber
Al
Al
Ti
NiTi
Al
Embedded Temperature Sensitive Sensors and Electronics
Complex Internal Cooling
Light-Weighting with Dissimilar Materials and Metals
Smart Materials Integration

Figure 1.1: Potential UAM applications and capabilities. The low formation temperature of the UAM process allows joining dissimilar metals (without the formation of brittle intermetallics) and the integration of temperature sensitive components, smart materials, cooling channels, organic polymers, and electronics into metal matrices.

The capability of UAM is very promising, yet key challenges exist with the technology which limit expansion in use. Like many metal based additive manufacturing technologies, (i) the relationships between build properties and processing parameters are not very clear, i.e. physics based models are lacking. (ii) Quality tracking techniques are impractical to implement in production environments due to cost, complexity, and reliability. Lastly, (iii) qualifying the component for a given application cannot be guaranteed due to inadequate standards and process control to ensure part consistency [9, 12, 72].

This research focuses on developing feasible solutions to address the key challenges above along with expanding the application space for UAM. In particular, input welder power of the UAM process is used to understand the relationship between processing parameters and part quality, to monitor part quality, and to use in feedback control for the UAM process. This thesis also aims to expand the use and understanding of embedding fiber materials into metallic structures, with particular focus on embedding NiTi shape memory alloy wires. The following sections provide background to the key thesis components of using input welder power to understand, monitor, and improve the UAM process along with describing the integration of NiTi wires into aluminum matrices.

1.2 Ultrasonic Additive Manufacturing

Ultrasonic additive manufacturing (UAM) or ultrasonic consolidation, is a recent additive manufacturing process where thin foils of similar or dissimilar metals are ultrasonically welded together near 20 kHz in a layer by layer process to form gapless, 3D metal parts [91, 28]. Along with welding, periodic machining is utilized intermittent and post welding to create complex designs and features not possible with traditional machining processes alone. A schematic of the UAM process along with its detailed components are shown in Figure 1.2. The process is made continuous due to the circular design of the weld tooling, called the sonotrode. The deposition rates of the process are also quick relative to laser based technologies [9], on the order of 5 m/min (200 in/min). Recently, the UAM process has been improved by increasing the normal force and ultrasonic power nearly an order of magnitude relative to early UAM processes [32]. These increases in normal force and weld power remedy poor interfacial properties and consolidation quality observed in early UAM processes [57, 54, 48, 42]. The advantage of current 9 kW UAM systems over previous generation UAM is illustrated in Figure 1.3.

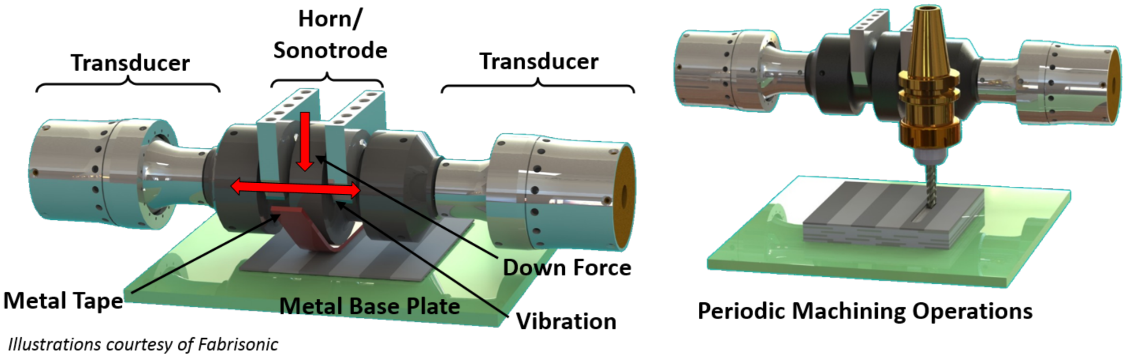
Horn/
Sonotrode
Transducer
Transducer
Metal Tape
Metal Base Plate
Down Force
Vibration
Periodic Machining Operations
Illustrations courtesy of Fabrisonic

Figure 1.2: Schematic of 9 kW UAM process with key components detailed.

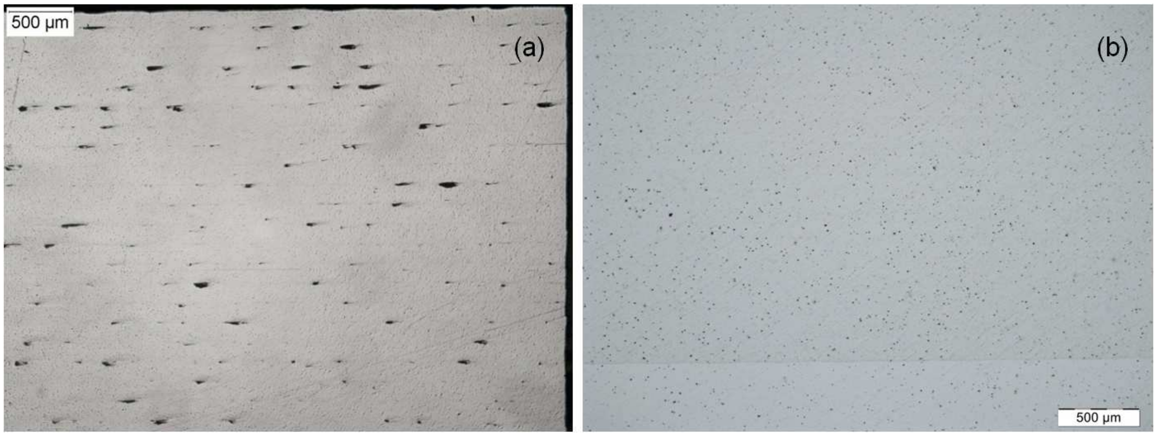
500 μm
(a)
(b)
500 μm

Figure 1.3: Comparison of cross sections of aluminum UAM builds: (a) first generation UAM system, 1 kW weld power, showing voids along tape interfaces; (b) current UAM technology, 9 kW weld power, creates gapless builds. Image courtesy of P.J. Wolcott [92].

UAM process power was increased from 1 kW to 9 kW by (i) using two transducers operating in a push-pull or master-slave configuration and by (ii) using two 4.8 kW transducers opposed to a single 1 kW transducer [32]. This push-pull configuration is shown in Figure 1.2 via two transducers on either side of the sonotrode. Because the welder is geometrically symmetric in terms of transducer type/size and sonotrode design, each transducer contributes an equal amount of energy for a given prescribed motion. The relation of welder symmetry and energy consumption for actuating one or both transducers is shown in Figure 1.4. It is shown that the welder motion (peak welder velocity) is the same for single and double actuator operation due to system symmetry. Likewise, system frequency also does not change. The difference between single and double transducer operation is shown when evaluating the welder power. In particular, power of the Master transducer doubles when the slave transducer is disconnected because the welder is able to track total motion through total response voltage. This response voltage is achieved when a particular current level, i.e., welder power, is reached. Once the slave is reconnected, the power for each transducer decreases to half the required power for a single transducer. The control framework used in the UAM process will be discussed in more detail in Chapter 3.

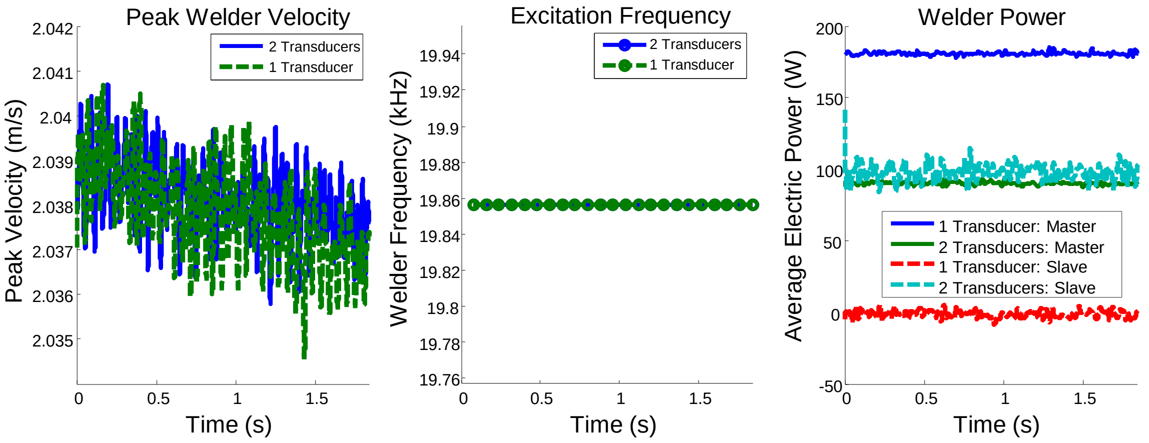

Figure 1.4: Symmetry of 9 kW UAM welder while actuating the welder under no load. To actuate with 1 transducer, the slave transducer was disconnected. The peak welder velocity is very similar between double and single transducer actuation, the excitation frequency is identical, and total average electric power is similar. To maintain peak welder velocity, the system increases total current, i.e., welder power.

Ultrasonic metal welding (UMW) is a solid-state (no melting) welding process which works by scrubbing two metals together under pressure at ultrasonic frequencies. The vibration magnitudes of the UMW process are on the order of 20 μm in magnitude while the vibration frequency for most UMW systems is near 20 kHz. The exact displacement and frequency of the UMW process is dependent on the design of the weld tooling. The key mechanisms of ultrasonic metal welding include surface oxide fracture and plastic deformation of surface asperities through shear [68, 17, 29]. The fracture and dispersal of thin surface oxides under pressure allows nascent metal surfaces to come into contact and form metallic bonds while large surface asperity deformation promotes dynamic recrystallization of the interface microstructure [49, 20, 84, 24]. The mechanistic result of scrubbing surface asperities together near 20 kHz with low vibration amplitudes is a narrow weld zone, on the order of 10-20 μm, and bulk temperatures far below metallic melting temperatures [85].

Like many other metal forming processes where ultrasonics are used, the ultrasonic vibration of the UMW process causes softening or lowering of the yield strength of the metal. Two schools of thought have been proposed to describe this softening effect since its discovery in the mid 1950's, dislocation motion due to localized heating at defects in the metal latice (acoustic softening or Blaha effect) or superposition of static and dynamic stresses, which together causes yielding. Graff gives a comprehensive history overview of the softening debate and outlines key pieces of work which describe the contributing physics of the effect [30]. In short, the exact mechanisms of this softening, the relationship(s) between the mechanisms, and the contributions of each mechanism to the effect are not well understood till this day and have been debated since its discovery. Likely, both schools of thought are influential in the net yield strength reduction since strong proof for both arguments have been presented in the ultrasonic metal forming literature.

Although the interaction between ultrasound and metal plasticity is not well understood, the weld yield strength of the weld metal decreases substantially during the UAM process. Consequently, large plastic strains are imparted onto the asperities near the weld interface with minimized effort from the welder. These large strains lead to additional dislocation formation and plastic deformation heating [85], which creates a kinetic path for dynamic recrystallization, i.e., grain refinement from simultaneous applied strain and heat.

Observed recrystallized grains from the UAM process are equiaxed and on the order of a micron in size [49, 20], which is similar to other hot working processes where dynamic recrystallization occurs, such as hot rolling and forging [43]. Resultant grain structure can be seen in Figure 1.5 for welding Al 6061-H18 tape to a Al 6061-T6 baseplate and welding two Al 6061-H18 tapes together. As seen in the photo, new grains on the baseplate layer are submicron due to the large difference in baseplate grain size and strength. The size, statistical distribution, and hardness of surface asperities influences interface deformation and likely the recrystallization behavior [87, 73, 41]. The size of surface asperities have also been found to influence interfacial bond strength [60, 93]. However, the connection between asperity properties, deformation behavior and resultant bond strength in UAM requires more thorough investigation and will be discussed in the future work section of this thesis.

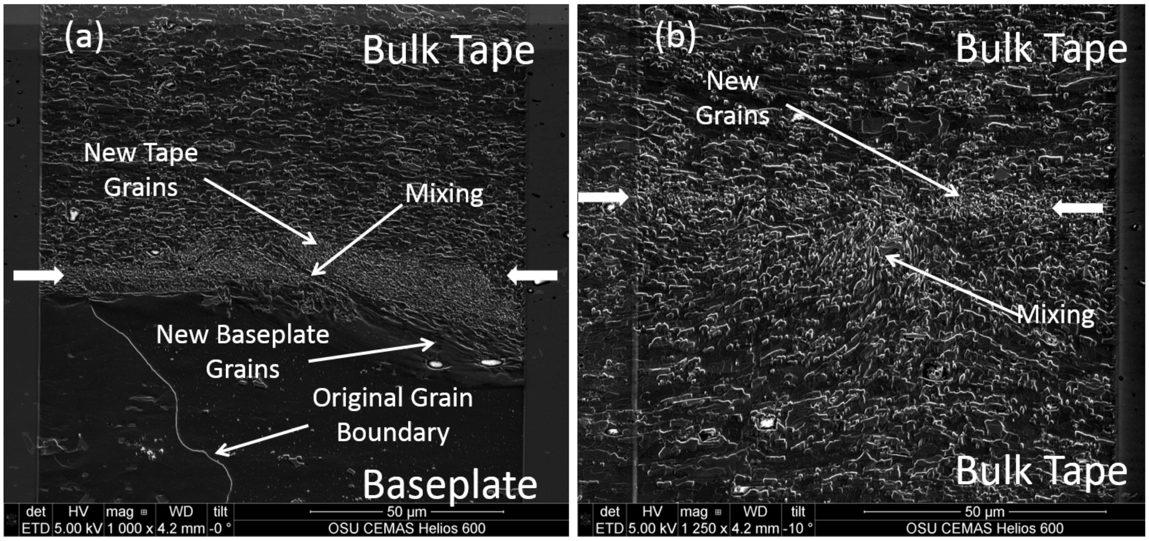
(a)
Bulk Tape
New Tape Grains
Mixing
New Baseplate Grains
Original Grain Boundary
Baseplate
det HV mag WD tilt
ETD 5.00 kV 1 000 x 4.2 mm -0 °
50 μm
OSU CEMAS Helios 600
(b)
Bulk Tape
New Grains
Mixing
Bulk Tape
det HV mag WD tilt
ETD 5.00 kV 1 250 x 4.2 mm -10 °
50 μm
OSU CEMAS Helios 600

Figure 1.5: Resultant interface grain structure observed from the UAM process: (a) welding Al 6061-H18 tape onto a Al 6061-T6 baseplate; (b) welding two Al 6061-H18 tapes together. These images were taken using a dual focused ion beam (FIB)/scanning electron microscope (SEM).

Recently, a 9 kW UAM system was installed at The Ohio State University, see Figure 1.6. This machine is built into a CNC framework, is fully automated, includes traditional and laser machining capabilities, and allows the user to record and analyze various machine variables of concern during a welding operation, like down force or ultrasonic power. This 9 kW machine was utilized to fabricate all UAM components for this thesis work.

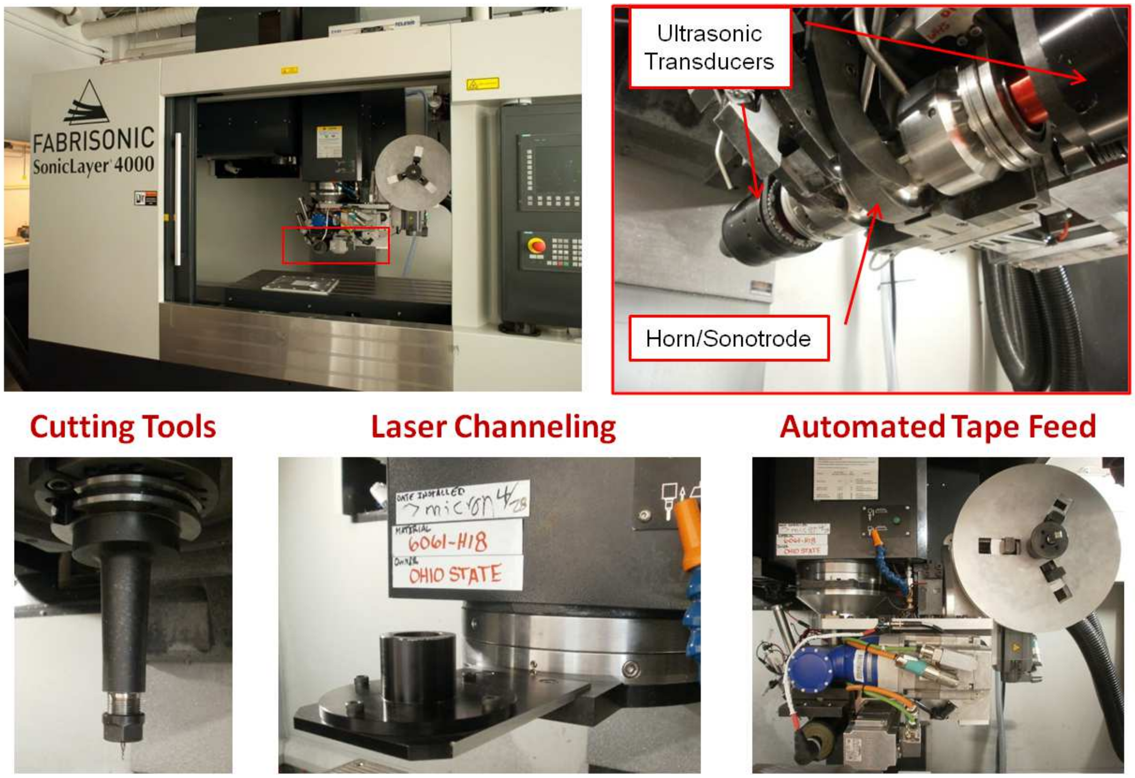
FABRISONIC
SonicLayer 4000
Ultrasonic Transducers
Horn/Sonotrode
Cutting Tools
Laser Channeling
Automated Tape Feed
DATE INSTALLED
7 micron 4/28
MATERIAL
6061-H18
OWNER
OHIO STATE

Figure 1.6: 9 kW SonicLayer 4000 UAM system utilized to fabricate components in this thesis.

1.3 UAM Process Variables and Property Relationships

The controllable processing variables of the UAM process include welder amplitude or scrubbing motion, welder down force (contact pressure), rolling speed of the welder along the baseplate surface, and baseplate temperature. Sonotrode surface roughness, weld tape geometry, and sonotrode frequency are fixed processing variables for a given sonotrode design. To improve understanding of the connection between these controllable processing variables and interlaminar bond properties, several parametric studies on aluminum alloys have been carried out since the inception of UAM.

Initial studies evaluated the the linear weld density and peel strength of welded aluminum foils bonded with similar aluminum foils in the low power UAM process [54, 57]. Researchers found that higher welder amplitudes, higher down forces (contact pressures), and slower weld speeds improved peel strength and linear weld density. Similar correlations between linear weld density and processing variables were confirmed by other researchers as well [48]. Albeit a simple test, peel testing is limited in its ability to measure weld strength for strong welds since failure was found to occur in the bulk foil near the interface instead of the interface itself. As a result, further bond strength-parameter correlations were carried out with micro hardness testing [58]. Researchers found that hardness increased with higher amplitudes, higher contact pressures, and slower weld speeds. This correlation was rationalized by the increase in dislocation density from the process, i.e., acoustic hardening. It should be noted that the hardness testing was too large to measure the interface properties directly. Instead, measurements are from the bulk foil near the interface.

Because peel testing is limited in its ability to estimate weld strength and measuring interface hardness is difficult, further research was carried out using improved mechanical testing techniques. Push-pin testing was originally presented by Zhang in low power UAM [98]. Push-pin testing uses a steel pin inserted into a blind hole to push against several layers of welded material. The test measures the delamination resistance through multiple layers, which allows the inclusion of interface and bulk tape failure modes simultaneously. Similar to earlier peel testing work, it was found that slower speeds, higher welder amplitudes, and higher down forces produced improved bonds or delamination resistance. Researchers at Ohio State utilized more standardized testing techniques to measure build properties, i.e., out-of-plane tensile and shear testing [78, 42]. Like previous work, higher welder amplitudes, higher down forces, and slower weld speeds produced improved bond properties at constant temperature.

Recently, a statistical design of experiment study with Al 6061-H18 was carried out with high power or 9 kW UAM using push-pin testing [92]. As mentioned earlier, 9 kW UAM samples are gap-less due to higher loads and amplitudes. Consequently, earlier work which correlated bond strength to linear weld density becomes limited in use and inadequate to describe bond quality. Hence, a re-evaluation of processing conditions and bond strength relationships were required for 9 kW UAM. Push-pin testing was used in the study since the fabrication of tensile and shear samples is costly in both time and resources. Like the previous low power UAM studies, researchers found that increased welder amplitude and slower weld speeds improved bond quality. On the other hand, normal force and temperature were found to not improve or degrade the bond quality. It should be noted that this high power UAM parametric study utilized much higher amplitudes and down forces when compared against earlier low power studies. The studied temperatures were also substantially lower than in earlier UAM work. It is suspected that the down force did not influence the bond properties in this study because the asperities were fully collapsed. In earlier UAM work, gap-less consolidation was never fully achieved, and down force likely played a more influential role. It is believed that temperature was not influential due to substantial softening of the aluminum not occurring at the tested temperature. Despite the differences in processing condition magnitudes, this study supports the fact that the governing physics behind the UAM process are similar between the low and high power systems. This study also supports the fact that bond quality is largely influenced by mechanical energy input into the weld [96, 39],

$$E_{weld} = \int P_{mech} \cdot dt = \frac{1}{V_m} \cdot \int F_s \cdot \delta \cdot \omega \cdot dx, \tag{1.1}$$

where P_{mech} is the mechanical power, V_t is the linear travel speed of the welder, F_s is the shear force of the sonotrode onto the weld foil, δ is the welder displacement, ω is the welder frequency, and dx is the spatial coordinate which the welder rolls.

Yang used a form of 1.1 to correlate earlier observations of linear weld density and peel strength to energy input. It was found that the calculated energy input was directly related to linear weld density and peel strength. More recently, the author found that measured peak electrical power was related to bond strength shortly after completing the high power UAM parametric study, see Figure 1.7(a). Peak electrical power is reported by the controller of the SonicLayer for each weld, and if one assumes constant power conversion and transfer from the piezoelectric transducers to the sonotrode, the mechanical power can be estimated. The figure illustrates that higher push-out energies were achieved when higher electric power (mechanical power) was utilized to achieve the prescribed welding conditions during the construction of the sample. Further, bond strength for a given power level was related to the welder speed. In particular, a slower weld speed or higher energy input increased the push-out energy. Hence, bond strength is related to the electric power and welder rolling speed used during manufacture. It is shown in Figure 1.7(b) that the peak power draw is a function of the number of layers of the UAM build. The average power draw to build each sample is also grouped by the amplitude setting. These two observations imply that the power consumption of the piezoelectric transducers is related to the stiffness of the UAM build, and that amplitude has a large impact on the electric power magnitude of the process. Consequently, build stiffness can influence the overall part quality and amplitude can be used to adjust the consumed electric power of the process. The observations and correlations in Figure 1.7 motivated the work in Chapters 2-4 of this thesis.

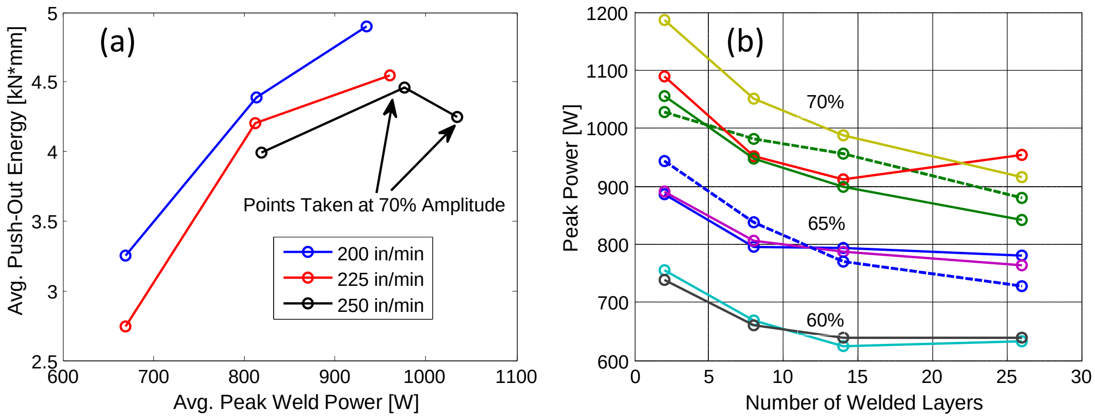

Figure 1.7: DOE Power Obversvations: (a) correlation of push-out energy from parametric study [92] and the average of the measured peak weld power during sample construction at layers 2, 8, 13, and 20.; (b) behavior of peak power with layers for various DOE samples. In (a) bond strength increases with increasing peak weld power for the same weld speed. For slower weld speeds, weld strength increases further. In (b) the peak weld power decreases with weld layers in an asymptotic manner and the peak weld power is grouped per amplitude setting.

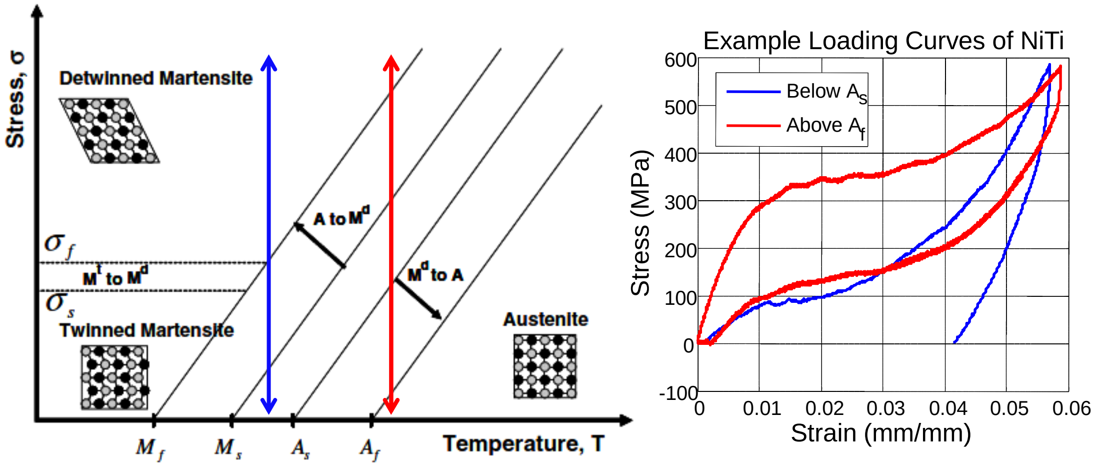

Figure 1.8: Schematic representation of NiTi phase dependence on applied stress [36] and temperature with empirical data supporting trends and behaviors.

1.4 NiTi-Al Composites

Nitinol (NiTi) shape memory alloy (SMA) has been built into Al matrices recently for thermal expansion and stiffness control applications [34]. NiTi is a promising SMA for UAM applications because it has been commercialized by many companies for the medical field and is readily available, exhibits large recoverable strain (4-8%), exhibits large actuation forces, and is metallic in origin. Consequently, NiTi can be utilized to fabricate self-actuating metallic structures and composites that exhibit no moving parts. Examples include hinges and latch mechanisms. However, before these concepts can be fully realized, reliable and robust integration of NiTi into metal matrices at a large scale needs to be achieved.

The large recoverable strain observed in SMAs originate in a solid-state phase transformation, which is driven by both temperature and stress. The low temperature monoclinic phase in NiTi is called Martensite while the high temperature cubic phase is called Austenite [59]. The relationship between these two phases, temperature, and applied stress is illustrated in Figure 1.8. For example, if NiTi is below the Austenite start temperature (A_s) and is loaded past the Martensite finish temperature (M_f), the material will have recoverable strain when unloaded. On the other hand, if the material is above the Austenite finish temperature (A_f) and is loaded above M_f, the material will transform back to Austenite when unloaded since the material passes through the A_s and A_f temperatures.

Using the the phase transformation behavior of the SMA and light-weight aspect of aluminum alloys, NiTi-Al composites are a new attractive material for thermal expansion applications with weight concerns [34]. The composite works because the NiTi fibers reduce the expansion of the aluminum. Specifically, when the composite is heated, the strain recovery of the NiTi fibers counteracts the expansion of the aluminum matrix. UAM comes into play with the fabrication of these composites due to the low formation temperature of the process, which allows integration of NiTi in the detwinned Martensitic phase without the material actuating. Recent effort has shown a 60% reduction in the average coefficient of thermal expansion for Al 3003 up to 100 C. Yet, metallic bonding between the aluminum matrix and NiTi fibers is not always observed. Instead, the interface is believed to be predominately supported by mechanical coupling in the form of a friction fit [33]. Although metallic bonding is ideal at the interface, mechanical coupling may be sufficient if the interface strength exceeds thermal blocking stresses generated throughout temperature cycling. Previous efforts have shown evidence of interface failure when significant blocking stresses arise. Consequently, it is of interest to better understand the strength of the interface and to optimize this strength so robust composites can be constructed.

Due to the scalability of UAM, large engineering structures with embedded NiTi can potentially be fabricated if optimized build procedures are developed. Prior to fabricating large scale NiTi-Al composites, UAM requires development itself to ensure large metallic structures with robust joints, consistent properties, and low void presence [93]. In order to achieve these build property traits, improved build procedures are required along with reliable process models. Consequently, Chapters 2-5 of this thesis discusses understanding, modeling, and improving the UAM process with the use of energy transfer and storage while Chapters 6-8 focuses on scaling up the fabrication of NiTi-Al composites for commercial use.

Chapter 2

BUILD COMPLIANCE, POWER COMPENSATION, AND MICROSTRUCTURAL ENERGY STORAGE

2.1 Introduction

The aim of this Chapter is to more rigorously explore the average electric power draw observations seen in Figure 1.7. In particular, (i) it is unclear why increased average electric power draw leads to improved properties, (ii) the decreasing average electric power with build height requires improved understanding, and (iii) it is of interest to investigate if changing the welder amplitude can be utilized to control average electric power consumption, which in turn would allow control over bond quality. These questions were addressed and answered by recording the average electric power draw during the construction of samples, by using mechanical push-pin testing to measure average bond strength, and using focused ion beam etching and scanning electron microscopy to expose the interface grain structure for imaging, respectively.

The increased average electric power draw during the process was found to enhance the recrystallized grain volume at the weld interface due to enhanced strain energy input. As a result, a Conservation of Energy expression has been proposed to describe this relationship between average electric power draw and recrystallized grain volume. The decreasing average electric power draw with build height was found to be closely related to the elastic compliance behavior of a cantilever beam. When the welder amplitude is increased, the average electric power draw was found to correspondingly increase due to enhanced strain energy input into the weld. Hence, welder amplitude can be used to control the average electric weld power and resultant component quality. This chapter was submitted and accepted to the *Rapid Prototyping Journal* [39].

2.2 Build Compliance and Power Compensation

To more carefully evaluate the decrease in average electric power with build height seen in Figure 1.7(b), a 8.9 cm (3.5 in) long single tape wide UAM stack was built while measuring the instantaneous average electric power along the weld at each weld layer. The stack width was 2.4 cm (15/16 in). The instantaneous power, time, and displacement (welder rolling motion) were measured using the built-in trace option in the control panel of the SonicLayer UAM system. Data was then exported to Microsoft Excel and Matlab for subsequent data analysis. The recorded average electric power is from the master ultrasonic generator. Thus, the total power of the system is near double the original measurement as described earlier in Chapter 1.

Power traces for the 2nd and 20th layer of the stack are shown in Figure 2.1. As the stack increases from the 2nd to the 20th layer, the power decreases. The welder also exhibits transient regions during the initial 2.54 cm (1 in) of the weld (called the spot transient) and during the last centimeter of the weld (called the end transient). The spot transient occurs due to the welder not getting up to full oscillatory motion prior to rolling, which in turn requires less power from the welder. The end transient occurs due to the welder still vibrating after rolling has ceased. As a result, the welder can stir and plasticize the weld foil at the end of the weld, which can then create a condition for sticking and a rise in corresponding power.

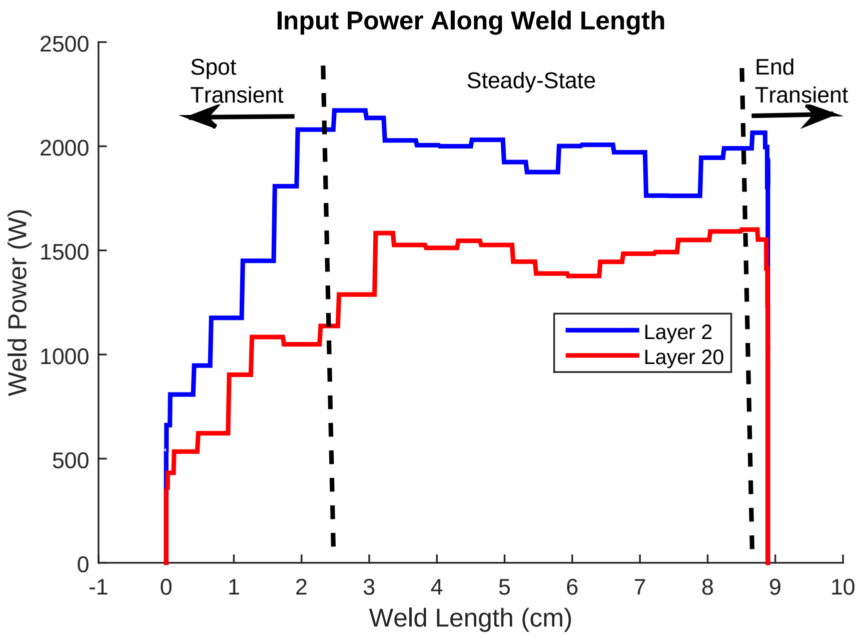

Figure 2.1: Instantaneous power along the length of a weld for the 2nd and 20th layers in a single tape wide UAM stack.

The average electric power as a function of build height is analyzed further by evaluating the average power consumption during the steady-state zone of the weld in Figure 2.1. The steady-state magnitude of welder power with first standard deviation error bars is shown in Figure 2.2(a) against layers in the stack. As the stack increases in height, the average electric power decreases in an asymptotic manner. This asymptotic behavior is similar to the changing stiffness of an eleastic cantilever beam (2.1),

$$k = \frac{3EI}{(Nt)^3}, \tag{2.1}$$

where E is the modulus of elasticity, I is the second moment of inertia, N denotes the number of layers, and t represents the foil thickness. This expression is plotted in Figure 2.2(b) with elastic parameters for the UAM stack. It becomes clear that power decreases exponentially in practice once this stiffness expression is substitued into the expresion for mechanical energy (1.1),

$$E_{weld} = \frac{1}{V_m} \cdot \int k \cdot \delta^2 \cdot \omega \cdot dx. \tag{2.2}$$

Because build stiffness and amplitude influence the integral in the expression, i.e., power component, welder power is influenced by both variables.

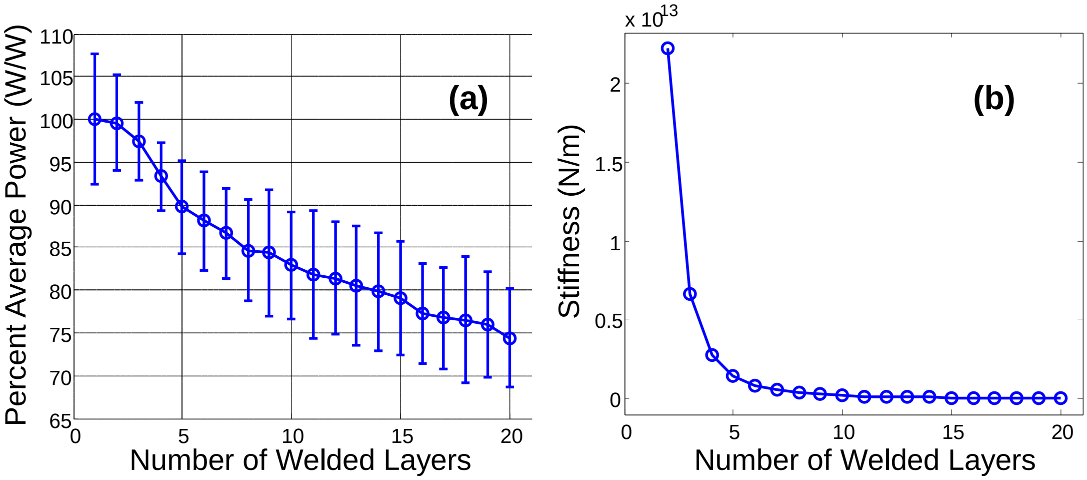

Figure 2.2: Effect of build compliance on weld input power for a stack of welded Al foils: (a) measured average power over steady-state weld zone with one standard deviation error bars; (b) estimated build stiffness as a function of layer number assuming an ideal cantilever beam.

Welder amplitude in the UAM process is held constant during welding operations because welder amplitude is a legacy control variable from the ultrasonic spot welding process. Part compliance does not change in the ultrasonic spot welding process, so the interaction of the welder with the stiffness of the component has not been considered. However, in UAM, part compliance changes through construction. This changing compliance influences the effort of the welder or the required electric power to reach a prescribed amplitude. Consequently, the power or net energy used to construct the UAM build will change correspondingly with compliance. Further, this change in input energy can directly influence build properties.

To maintain welder energy input into the build and ultimately part quality, the welder amplitude can be appropriately adjusted to influence welder power (see 1.1). This concept of adjusting the welder amplitude to control average electric power is called 'power compensation'. This amplitude adjustment is done manually due to UAM equipment not exhibiting this feature. The power compensation concept is illustrated in Figure 2.3 with schematics and empirical data.

Table 2.1: Power compensation approach by changing amplitude per layer.

Layer	1-2	3	4	5-6	7-8	9-12	13-15	16-20
Amplitude (%)	70	72	74	76	77	78	79	80
Amplitude (μm)	32.7	33.6	34.6	35.5	36	36.4	36.9	37.4

Figure 2.3(a) illustrates that the elastic compliance of the stack influences the plastic deformation region of the stack as compliance changes. Because plastic deformation is a leading mechanism for bond formation, a difference in plastic deformation can lead to a difference in bond quality. To compensate for changes in plastic deformation magnitudes, the amplitude of the welder can be correspondingly adjusted to maintain this plastic deformation magnitude, see Table 2.1. This change in welder magnitude then influences the welder effort or power consumption, see Figure 2.3(b). Schematically, this change in welder amplitude and energy consumption is shown in Figure 2.3(c) by analyzing the elastic and plastic deformation behavior of the system. A bi-linear shear force profile is used to represent the elastic and plastic deformation regions. It is suspected that plastic deformation hardening occurs during welding because larger welder amplitudes lead to an increase in average electric power. These two regions of elastic ($E_{weld,e}$) and plastic deformation ($E_{weld,p}$) energy can be described as the summation of the total imparted strain energy for a given spatial dimension (1.1),

$$E_{weld} = \frac{1}{V_m} \cdot \int_0^x \left[\int_0^{\delta_E} F_s \cdot d\delta + \int_{\delta_E}^{\delta_L} F_s \cdot d\delta \right] \cdot \omega \cdot dx = E_{weld,e} + E_{weld,p}. \tag{2.3}$$

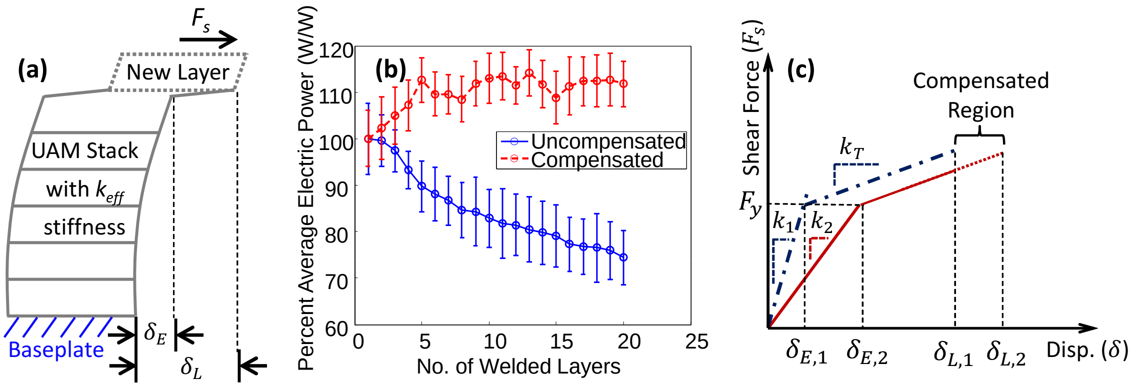

Figure 2.3: Power Compensation Concept: (a) schematic of UAM build during welding showing areas of elastic and plastic deformation, modified from Hehr et al [39].; (b) comparison of measured average electric power draw percent for build with (compensated) and without (uncompensated) power control [39]; (c) proposed bilinear shear force profile during welding.

2.3 Sample Construction and Testing

Power compensation provides a feasible solution for changing part compliance in UAM without adding additional hardware to the system. For validation purposes of the concept, push-pin samples were constructed and tested with and without the use of power compensation. After mechanical testing, sample microstructure was studied near various weld interfaces using focused ion beam and scanning electron microscopy. Samples are shown in Figure 2.4 while power traces are shown in Figure 2.5. The welding variables utilized for sample contruction are given in Table 2.2. Al 6061-H18 [1] foil was utilized in this study because of its compatibility with UAM and its use in industry. Because power compensation is implemented manually, the average electric power is not held perfectly constant during sample manufacture.

[1] Al 6061-H18 foil was fabricated by work hardening annealed Al 6061 through a H18 process.

Table 2.2: UAM control variables utilized for welding samples.

Temperature	22C (72F)
Weld Force	5,000 N
Amplitude	32.76-37.4 μm (70-80%)
Weld Speed	84.6 mm/sec (200 in/min)

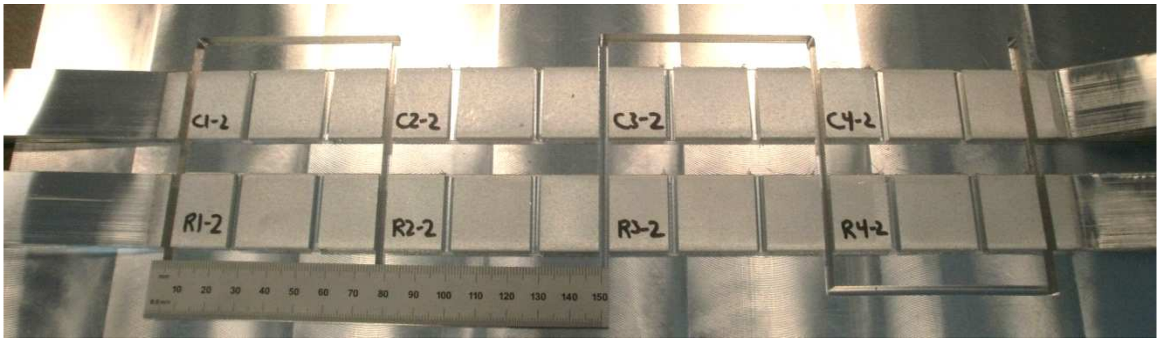

Figure 2.4: Push-pin samples constructed with 9 kW UAM system and integrated CNC milling stage. In the image, C stands for compensated while R stands for reference, i.e., uncompensated.

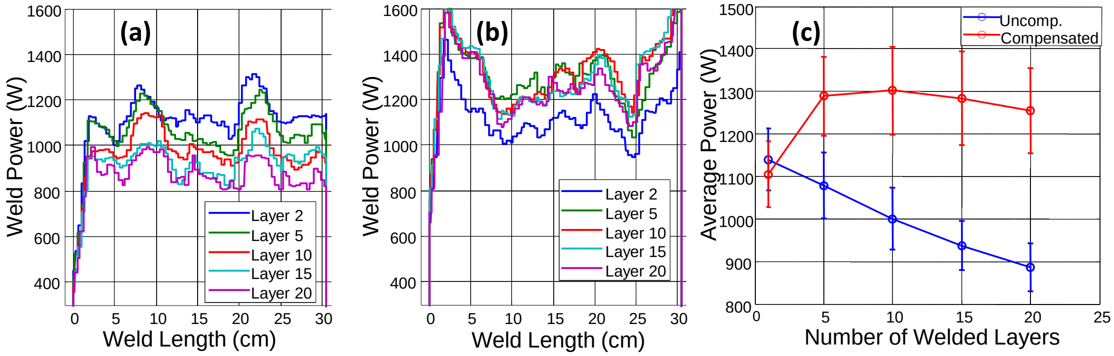

Figure 2.5: Average electric power measurements during push-pin sample construction: (a) uncompensated build power curves; (b) compensated build power curves; (c) average of power trace at each layer for both uncompensated and compensated builds.

Push-pin testing has successfully been utilized by the author to evaluate UAM sample bond quality. Details for the test and sample are shown in Figure 2.6 and described in earlier work [92]. Additional detail for the test can be found in Appendix A. In short, the test measures the crack propagation resistance through multiple layers in the UAM build. As a result, improved bonding between layers will cause the crack to propagate through the bulk metal foil instead of along the interface. This increased resistance to crack propagation can correspondingly be measured by evaluating the force-displacement curve of the test. Additionally, the surface of the failed sample can be analyzed to infer the quality of the bond. Representative results for testing are shown in Figure 2.7. A total of 4 samples were tested for each build condition and their respective results are given in Table 2.3.

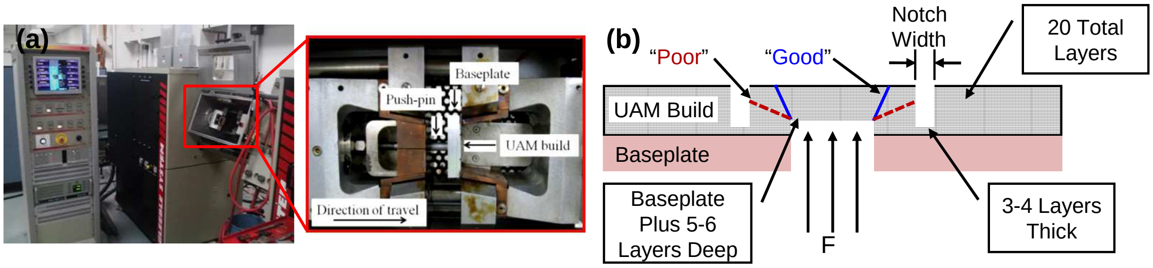
(a)
Baseplate
Push-pin
UAM build
Direction of travel
(b)
"Poor"
"Good"
Notch Width
20 Total Layers
UAM Build
Baseplate
Baseplate Plus 5-6 Layers Deep
F
3-4 Layers Thick

Figure 2.6: Push-Pin testing: (a) Gleeble thermal-mechanical tester utilized for push-pin testing with key test details shown in the inset; (b) push-pin sample details with key sample details shown for testing and failure.

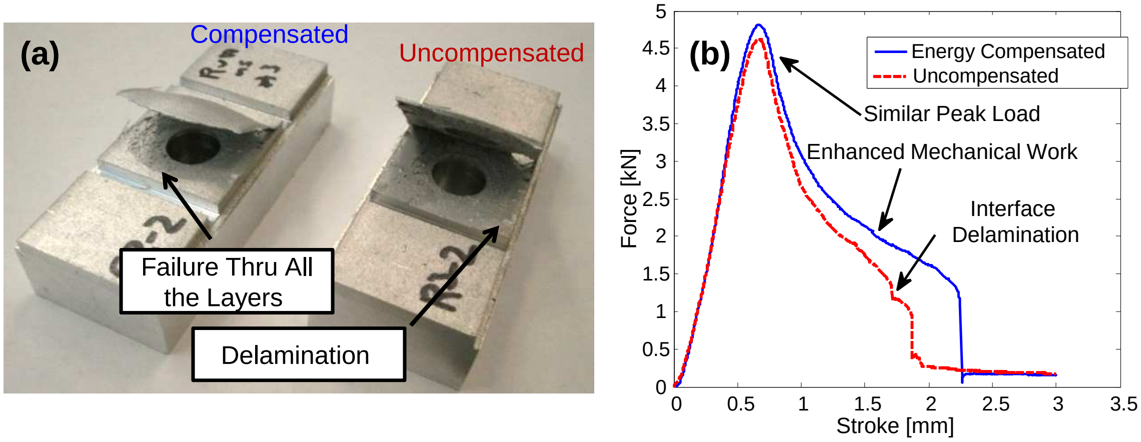

Figure 2.7: Comparison between compensated and uncompensated push-pin samples: (a) photo comparing failure behavior; (b) force-displacement plots.

Table 2.3: Push-pin testing results for uncompensated and compensated samples. Peak Force (P. Force) and Push-out Energy (Energy) is reported along with the mean and first standard deviation (Std) for the sample set.

	Uncompensated		Compensated	
No.	P. Force (kN)	Energy (kN*mm)	P. Force (kN)	Energy (kN*mm)
1	4.72	3.64	5.02	5.4
2	4.67	4.78	4.83	5.53
3	4.66	4.63	5.2	6.19
4	4.25	4.81	4.5	4.75
Mean	4.58	4.47	4.89	5.47
Std	0.19	0.48	0.26	0.51

The sample failure behavior and force-displacement curves in Figure 2.7 support the hypothesis that power compensation leads to improved bond quality throughout the sample. As the failure crack progresses through the sample, the crack propagation resistance at each layer remains similar for the compensated sample. As a result, the crack propagates through all the welded layers. On the other hand, the crack propagation resistance declines at each weld layer for the uncompensated sample, which enables delamination or failure along the interface once the resistance becomes low, see Figure 2.7(a). The result is that the compensated samples show nearly 22% more push-out energy over the uncompensated samples. The peak force levels are not very different in Figure 2.7(b) due to similar weld energy levels being used to fabricate the layers near crack initiation. However, differences in the force-displacement curves arise as the crack moves through the upper layers of the sample–layers where power compensation was utilized.

Interface grain structure was analyzed in the samples post testing to improve the mechanistic understanding of why increased welder energy leads to improved bond character. Cross sections were cut near 15 cm of weld length to avoid transient regions and to use a region representative of the average weld power, see Figure 2.5. To avoid damaging sensitive interface microstructure with chemical etch solutions, focused ion beam (FIB) microscopy was utilized at an oblique angle to expose the grain structure. Subsequently, imaging of the exposed microstructure was done with the use of a scanning electron beam or microscope (SEM). This particular microscope is called a dual-beam FIB/SEM[2]. Prior to etching/imaging, samples were prepared using standard Al alloy polishing procedures followed by vibro-polishing with colloidal silica solution. Polished samples were then thoroughly cleaned with soap, alcohol, and a low temperature vacuum furnace to drive-off contaminates.

Representative microstructure analysis for the 5th and 15th tape interfaces for the uncompensated and compensated power samples is shown in Figure 2.8. Interface 5 and 15 were chosen for comparison because push-pin testing occurs near layer 5 and above. The compensated power samples had nearly identical power inputs at these interfaces, and uncompensated power samples were subjected to a significantly different power input, see Figure 2.5. Fine grains at all the interfaces are shown in Figure 2.8. However, for the 15th uncompensated power weld interface, the recrystallized region is narrow, showing little to no mixing in some areas. On the other hand, the 15th compensated power interface shows strong mixing character and dimensions similar to the 5th power compensated interface.

---

[2] Microscopy was done at OSU's Center for Electron Microscopy and Analysis (CEMAS) using a FEI Helios NanoLab 600 DualBeam FIB/SEM. The dual beam feature of this microscope allows the user to toggle back and forth seamlessly between the ion and electron beam columns.

This difference in recrystallization behavior originates in the difference in imparted strain energy (welder power) at the interface during welding.

2.4 Energy Storage

The improved mechanical testing results of the compensated samples over the uncompensated samples show that imparted build energy was stored within the build after manufacture. This stored energy then leads to improved mechanical properties. Further, the compensated samples exhibited enhanced recrystallization behavior or a higher density of new small grains at upper weld interfaces in the UAM stack when compared to the uncompensated samples. These new small grains are a measure of the microstructural energy storage in the sample.

New small grains are a measure of stored energy because grain boundary area has an associated energy [6]. Consequently, the presence of many small grains implies increased energy storage due to an increase in net grain boundary area. According to the Hall-Petch relationship, high volumes of small grains lead to improved mechanical properties [6], which in turn supports why improved mechanical properties are observed with power compensated builds over uncompensated power builds. This energy conversion from weld input to microstructure storage can be expressed with the proposed energy balance,

$$E_{weld,p} + E_{surf} = E_{bulk} + E_{recryst} + E_{thermal}, \tag{2.4}$$

where E_{weld_p} is the imparted plastic mechanical energy onto the two surfaces by the welder, a function of processing variables as described earlier (2.3). This variable is directly correlated to the measured power of the welder. E_{surf} is the combined surface energy of the surface to weld onto and the surface of the tape which will soon be welded. This is a constant empirical parameter because surfaces are not altered prior to welding and assumed to be constant. E_{bulk} is the energy corresponding to the joined surfaces, solely. This energy is a function of oxide dispersal and bond quality, which is influenced by $E_{weld,p}$. $E_{recryst}$ is the energy corresponding to the volume of material near the interface which undergoes

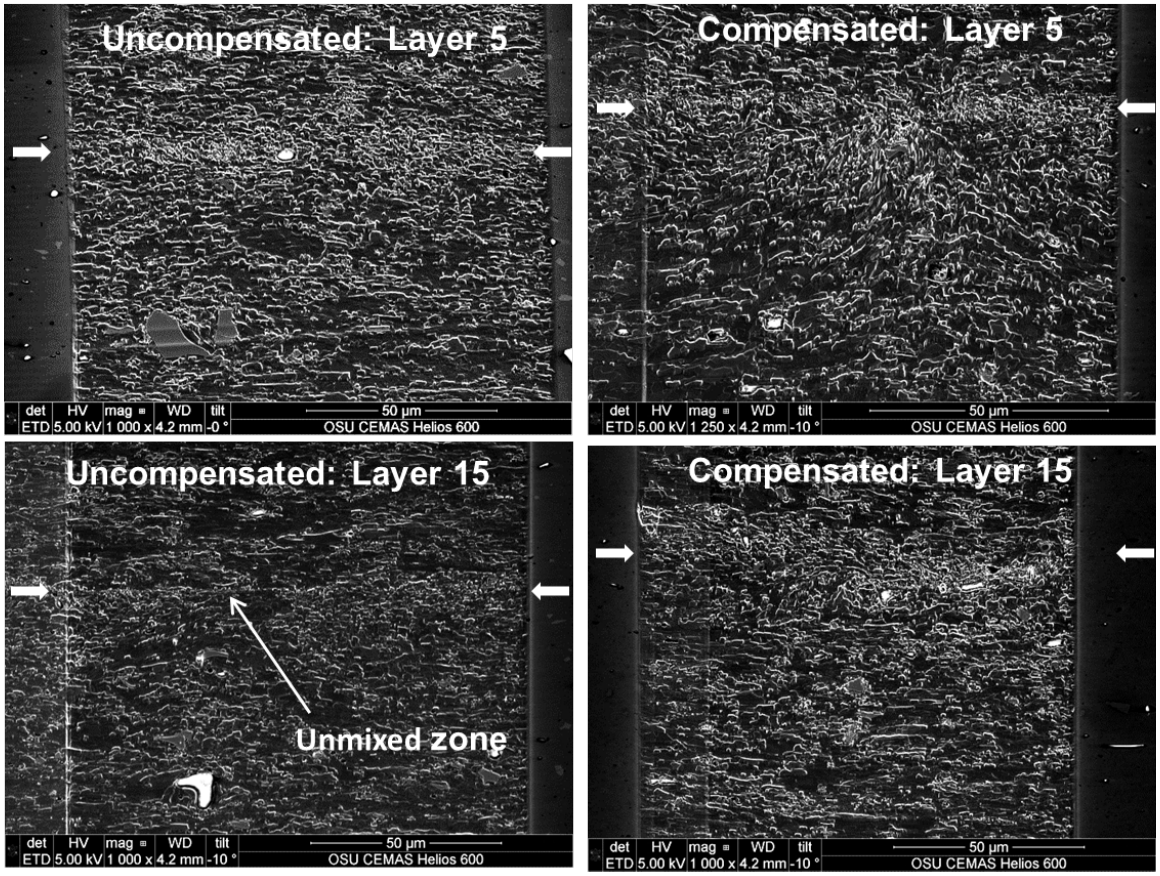
Uncompensated: Layer 5
Compensated: Layer 5
Uncompensated: Layer 15
Compensated: Layer 15
Unmixed zone
det HV mag WD tilt 50 µm
ETD 5.00 kV 1 000 x 4.2 mm -0 ° OSU CEMAS Helios 600
ETD 5.00 kV 1 250 x 4.2 mm -10 ° OSU CEMAS Helios 600
ETD 5.00 kV 1 000 x 4.2 mm -10 ° OSU CEMAS Helios 600
ETD 5.00 kV 1 000 x 4.2 mm -10 ° OSU CEMAS Helios 600

Figure 2.8: Interface microstructure at layers 5 and 15 for uncompensated and compensated samples. Samples were sectioned and polished for analysis near 15 cm of weld length to avoid transient weld regions. Arrows have been added to indicate the approximate interface region. Grain refinement can be seen at the interface regions as expected, yet poor mixing and less grain refinement are observed at the uncompensated 15th layer while the compensated 15th layer is like the uncompensated 5th layer. The difference in mixing and grain refinement originates from the uncompensated sample having received less strain energy.

recrystallization, i.e., nucleation of new grains. It can be quantified by measuring the volume of material which has new grains (total new grain surface area). $E_{thermal}$ is the thermal energy which does not contribute to dynamic recrystallization and is waste. $E_{recryst}$ can be qualitatively described by using the definition of grain boundary area energy and the Arrhenius equation to model recrystallized grain formation [6],

$$E_{recryst} = \gamma_G \cdot Ce^{\frac{-Q_r}{RT}} \cdot \Delta t, \tag{2.5}$$

where γ_G is the grain surface energy density for a particular metal grain, C is a material dependent constant in the Arrhenius equation, Q_r is the activation energy for recrystallization, R is the international gas constant, T is the temperature, and t is the total time allotted for recrystallization. Because each sample was generated with the same weld speed, the time for recrystallization is equal for both the compensated and uncompensated samples. The activation energy (Q_r) for recrystallization is dependent on the metal type, cold work history, strain magnitude, and strain rate [6, 43]. Increased strain magnitude and rate have been found to lower the activation energy for recrystallization. Further, increased temperature leads to faster recrystallization. Because interface heat generation or temperature in UAM is correlated to plastic deformation [84], an increase in strain magnitude and rate also increases temperature for recrystallization.

Other researchers have also utilized energy principles to model the UAM process [58, 96, 51]. However, their formulations do not utilize empirical weld power to validate their method and do not consider microstructure effects. Instead, they fit physics-based models to peel strength and linear weld density correlations. Others have modeled the UAM process with sophisticated FEM techniques which theorize frictional heating [19, 97, 79], vacancy motion [95], acoustic softening [50], and dislocation accumulation [73] as the primary bonding mechanism. However, these models are complex, have many fitting parameters, and dont have strong empirical evidence to support in-situ estimation of bond quality. In-situ bond tracking has been carried out using a photonic Doppler velocimeter [21], yet significant development is required to correlate velocity behavior with bond quality, expensive equipment is required for the technique, and focusing on components of concern is difficult due to small tape thickness.

The proposed energy conversion (2.4) from the mechanical to the metallurgical domain is the first of its kind for UAM. The model describe microstructural observations in a qualitative manner, yet has limitations in (i) quantitatively estimating the energy terms and (ii) the model does not account for bulk tape deformation effects [24, 83]. Further proposed improvements to this energy balance are explained in Chapter 9.

2.5 Summary

The hypothesis of structural compliance influencing ultrasonic weld power and corresponding mechanical strength and microstructure was tested in this study and found to be significant. It was shown that both mechanical testing and microstructure analysis correlate with variations in weld power input due to poor properties being observed when power was not held constant throughout the UAM process. The source for the differences in weld quality originates in the microstruture energy storage within the UAM build via new recrystallized grains. This is the first time in UAM where processing conditions have been linked to interface microstructure using physics-based principles.

Evidence presented in this chapter supports energy storage within the microstructure considering the comparative nature of the push-pin test and small fraction of investigated microstructure. Consequently, a more rigorous investigation of out-of-plane tensile testing and microstructure examination is required for full hypothesis and presented model validation. Future microstructure examination will require additional samples and the potential use of electron backscatter diffraction (EBSD) to more fully understand energy transfer to interface microstructure.

Chapter 3

WELDER OPERATION AND LINEAR TIME INVARIANT MODEL

3.1 Introduction

The aim of this chapter is to describe UAM system dynamics with a linear time-invariant (LTI) model of the welder. The model utilizes classic electroacoustics theory for piezoelectric materials to describe welder system dynamics and requires no fudge factors. The model describes the conversion and transfer of electrical to mechanical power within the welder using linear system theory because (i) the piezoelectric transducers used in UAM are designed to be linear within the range of operation, (ii) the sonotrode is a linear device, and (iii) the proposed linear model was found to describe the system dynamics accurately. The model does not directly describe energy transfer to the weld, although it can be used as part of a broader modeling framework to quantify the complete flow of energy through the welder into the workpiece (discussed in Chapter 4). It should be noted that any non-linear attributes of the system inputs (shear force or electric current) will be transferred through the system and converted to the system outputs in a linear manner due to the modeling assumptions used herein.

Understanding the energy flow in UAM is important because imparted welder energy is correlated to weld strength or quality (see Chapters 1-2). The proposed LTI model explicitly specifies welder shear force and electric current as system inputs. The outputs of the model are welder velocity and electric voltage. Conventional LTI models for ultrasonic systems lump the influence of shear force or load into the motional feedback of the entire system for control purposes [88], i.e., Van Dyke system representation [76]. Because the focus of the chapter is to describe the energy conversion within the welder, it is required to explicitly express shear force as a system input so mechanical power can be estimated.

For benchmarking purposes, the chapter begins with describing how the process is controlled currently and how this control relates to UAM welder performance. The system is then described in terms of impedance relations in order to convey the proposed LTI model. Experimental frequency response functions (FRFs) of the welding assembly and its components are then characterized using these impedance relations and compared to theory. Close agreement was found between theory and the experimental FRFs. In-situ measurements of the welder operating under no load were then taken to evaluate welder performance as a function of amplitude level. These in-situ measurements were then used to verify and find the modeling parameters for the proposed LTI model. Aspects of this chapter were submitted to the journal *Ultrasonics* [38].

3.2 UAM Control Background

UAM has been utilized for over a decade, yet no system level model of the process exists. Instead, the process utilizes legacy ultrasonic metal welding control strategies developed several decades ago. These control strategies work well when joining two pieces of metal together because joint geometry is constant. On the other hand, many joints are made throughout the UAM process, which in turn causes the build geometry to continually change throughout component construction. Because UAM build geometry changes during fabrication and vibration is used for welding, structural dynamics can influence process performance and weld quality [77, 26, 27, 39]. As a result of this structural dynamic interaction with the process, a control strategy unique to UAM is needed to avoid or minimize undesired structural dynamics and to maintain weld quality throughout the component. Such a control strategy can be developed with a reliable system level model of the UAM process.

Control dynamics of the UAM process change when welding vs. actuating the sonotrode without load (no welding), see Figure 3.1. In particular, the peak velocity of the scrubbing motion decreases 10% (Figure 3.1(a)), the frequency of the welder increases 75 Hz (Figure 3.1(b)), and the electric power draw of the piezoelectric transducers increases an order of magnitude, see Figure 3.1(c). A customized ultrasonic generator for the UAM process is responsible for the control dynamics observed in Figure 3.1. The generator uses two closed loop controllers which work simultaneously. The first controller uses a phase lock loop (PLL) algorithm to track system resonance during welding by minimizing the phase angle between the applied voltage and current [25, 31]. System resonance can change when welding due to added mass, stiffness, and heat generation from the load [31, 69, 67]. This PLL algorithm is the reason for the frequency shift seen in (Figure 3.1(b)).

The second controller works to maintain welder amplitude motion under load, i.e., welding. Welder amplitude in UAM is maintained by controlling voltage to be constant. Voltage is controlled by varying the current to maintain a set-point value for a given amplitude setting [4]. More detail on voltage control will be given later in the paper. Ultrasonic systems can also be controlled using electric current in a similar manner [88, 31].

In order to accurately track the resonance of the system for both the PLL algorithm and amplitude control, the mechanical motion of the welder needs to be measured. The most common way of measuring mechanical motion is with the use of motional feedback methods. Motional feedback works by adding a reactive element in series or in parallel with the transducer to balance-out its electrical impedance or admittance [88, 31, 69, 67]. For piezoelectric systems, this reactive element is an inductor. By removing the electrical impedance of the transducer, the motional impedance or motion of the transducer can be indirectly measured with applied current and voltage to the transducer. There are many different circuits utilized to implement motional feedback control techniques [88, 67]. The ultrasonic generator used on UAM systems utilizes such a motional feedback method for resonance tracking and amplitude control. Because amplitude is not measured directly in UAM, a decrease in vibration can occur if the reactive inductance element does not sufficiently isolate the motional impedance of the transducer or if significant compliance exists in the sonotrode, see Figure 3.1(a). This decrease in welder velocity and its relation to motional feedback and sonotrode compliance will be discussed in more detail later. Lastly, because voltage is controlled to be constant by increasing electric current during welding, the average electric power draw increases substantially to maintain welder motion, see Figure 3.1(c).

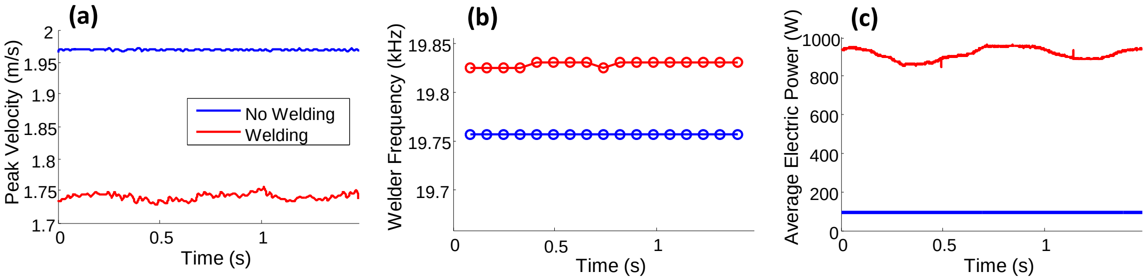

Figure 3.1: UAM system dynamics and control when not welding, i.e., exciting welder in air without load, and welding Al 6061 foil: (a) peak sonotrode or welder velocity; (b) excitation frequency; (c) average electric power draw from one of the ultrasonic transducers. Data was collected using the welding process variables of 32.5 μm peak-peak prescribed welder vibration, a down force of 5000 N, and a rolling speed of 5 m/min (200 in/min). Data was sampled at 50 kHz and processed with a block size of 8192 points, welder vibration was measured with a non-contact laser vibrometer, welder frequency was obtained using a short time windowed FFT, and power draw was sampled directly from the ultrasonic generator.

3.3 Time-Invariant Linear Model of UAM Process

To describe the system dynamics of the welder for all frequencies (ω), the following LTI system model with voltage-force as across variables and velocity-current as flow variables for the system can be written,

$$\begin{pmatrix} i(j\omega) \\ \dot{\delta}(j\omega) \end{pmatrix} = \begin{bmatrix} H_e(j\omega) & H_{me}(j\omega) \\ H_{em}(j\omega) & H_m(j\omega) \end{bmatrix} \begin{pmatrix} V(j\omega) \\ F_s(j\omega) \end{pmatrix}, \tag{3.1}$$

where H_e is the FRF between applied voltage (V) and electric current (i), H_{me} is the FRF between opposing shear force during welding (F_s) and current, H_{em} is the FRF between applied voltage and velocity of the sonotrode ($\dot{\delta}$), and H_m is the FRF between shear force and velocity. Due to the system being piezoelectric, the system is symmetric in behavior [76, 44]. In other words, piezoelectric systems follow the law of reciprocity. As a result, H_{me} and H_{em} are equal in magnitude and phase. This LTI model with force as the across variable and velocity as the flow variable is proposed initially due to piezoelectric systems conventionally using this form [88, 76, 44], and because the system is feasible to characterize in this form. An equivalent LTI model of the system using velocity as the across variable and force as the flow variable will be presented at the end of this section because the motional feedback controller of the welder utilizes this relationship. The equivalent form is derived using the principle of duality [44]. Both LTI models can be used to describe the system behavior because the system behaves in a steady manner during welding operations, see the stable welding traces in Figure 3.1. The system exhibits a small amount of variation when welding because the PLL algorithm moves the voltage excitation frequency. This small frequency shift in the PLL controller may originate from variations in the UAM build compliance and shear force character during welding. The influence of UAM build stiffness on frequency and FRF magnitude will be discussed in more detail later.

To understand the relation between system physics and the FRF terms, equivalent circuit analysis can be used to derive closed form FRF expressions near resonance. To model the electro-mechanical coupling of the piezoelectric transducers, an ideal transformer can be utilized [76, 66]. A schematic of the welding assembly along with its corresponding equivalent circuits are shown in Figure 3.2. The presented equivalent circuit analysis assumes that the welding assembly is geometrically symmetric in shape and properties and that the two transducers operate out of phase, i.e., push-pull configuration. The system can be assumed to be geometrically symmetric because the sonotrode is precision machined, and the two transducers used to drive the sonotrode are of the same model and exhibit near identical response. The transducer response will be compared in the next section. Because the system is geometrically symmetric and the transducers are operated out of phase, the transducers can be lumped together as a single transducer driving the sonotrode. The out of phase actuation of the welder is shown in Figure 3.2(a) with opposing voltage directions.

The sonotrode in Figure 3.2(b) is modeled as a black box 2-port electrical network because (i) the transducers actuate the sonotrode at a different location than the shear force, and (ii) the sonotrode design influence on system performance is not considered in this paper. Because sonotrode design is not an aspect of this paper, Figure 3.2(b) can be simplified by lumping the transducer and sonotrode dynamics together, see Figure 3.2(c). These two devices can be lumped together because both the transducers and sonotrode are designed to resonate at the driving frequency of 20 kHz. The equivalent circuit seen in Figure 3.2(c) is commonly called the Mason circuit representation for piezoelectric devices [76].

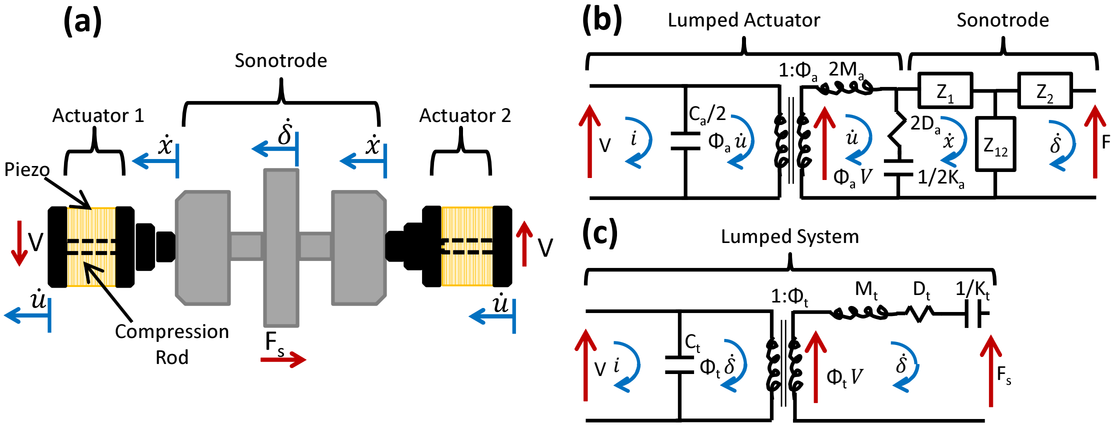
(a)
Sonotrode
Actuator 1
Actuator 2
Piezo
Compression Rod
V
V
$\dot{x}$
$\dot{\delta}$
$\dot{x}$
$\dot{u}$
$\dot{u}$
F_s
(b)
Lumped Actuator
Sonotrode
1:Φ_a
$2M_a$
$C_a/2$
Z_1
Z_2
Z_{12}
$2D_a$
$1/2K_a$
V
i
$\Phi_a \dot{u}$
$\dot{u}$
$\Phi_a V$
$\dot{x}$
$\dot{\delta}$
F_s
(c)
Lumped System
1:Φ_t
M_t
D_t
$1/K_t$
C_t
V
i
$\Phi_t \dot{\delta}$
$\Phi_t V$
$\dot{\delta}$
F_s

Figure 3.2: UAM weld assembly analysis: (a) schematic of assembly with components, voltages, forces, and degrees of freedom detailed; (b) equivalent circuit of weld assembly with transducers and sonotrode modeled separately; (c) simplified equivalent circuit of weld assembly by lumping the transducers and sonotrode dynamics together.

System FRFs can be derived from the equivalent circuit shown in Figure 3.2(c) by shorting out one input at a time and relating system outputs [76],

$$H_e = \frac{i}{V} = j\omega C_t + \frac{\Phi_t^2}{j\omega M_t + D_t + \frac{K_t}{j\omega}}, \tag{3.2}$$

$$H_{em} = \frac{\dot{\delta}}{V} = \frac{\Phi_t}{j\omega M_t + D_t + \frac{K_t}{j\omega}}, \tag{3.3}$$

$$H_m = \frac{\dot{\delta}}{F_s} = \frac{1}{j\omega M_t + D_t + \frac{K_t}{j\omega}}, \tag{3.4}$$

where C_t is the capacitance of the transducers, Φ_t is the electro-mechanical transformer coefficient or turns ratio of the system, M_t is the effective mass of the system, K_t is the effective stiffness of the system, and D_t is the effective damping of the system.

Using the principle of duality, the equivalent circuit in Figure 3.2(c) can be redrawn using velocity as the across variable and shear force as the flow variable, see Figure 3.3. This system form is called the mechanical mobility equivalent circuit of the system [44], and the welder utilizes it for control purposes. As mentioned earlier, motional feedback or purely electric signal feedback is utilized by the ultrasonic generator to maintain welder amplitude or velocity during welding. Motional feedback works by inserting an external inductor in series with the capacitive element of the transducer, see Figure 3.3(a). If the impedance of the inductor is chosen to be equal to the impedance of the capacitor at resonance, the electrical impedance of the transducer is balanced-out or removed from the circuit, see Figure 3.3(b). By removing the capacitance of the transducer near resonance, the motional impedance of the transducer can be isolated for control purposes, hence the name motional feedback. Welder velocity is directly related to applied voltage too with this circuit and can be used for amplitude control purposes.

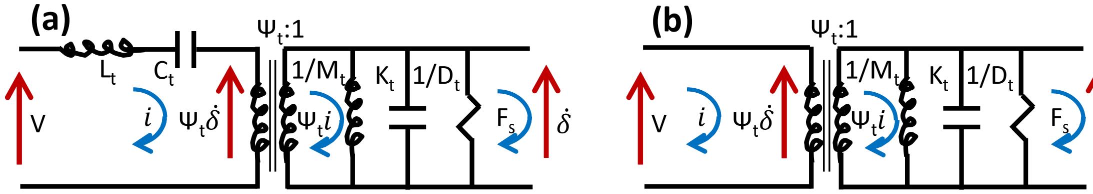

Figure 3.3: Equivalent circuit for welder operation: (a) mobility form of system with added inductance to 'zero out' transducer capacitance; (b) simplified mobility form of system without electrical influences from transducer, i.e. motional feedback form.

An equivalent LTI model using current and shear force as inputs and velocity and voltage as outputs can then be written,

$$\begin{pmatrix} V(j\omega) \\ \dot{\delta}(j\omega) \end{pmatrix} = \begin{bmatrix} H_e^*(j\omega) & H_{me}^*(j\omega) \\ H_{em}^*(j\omega) & H_m^*(j\omega) \end{bmatrix} \begin{pmatrix} i(j\omega) \\ F_s(j\omega) \end{pmatrix}, \tag{3.5}$$

where H_e^* is the FRF between electric current and voltage (V), H_{me}^* is the FRF between shear force and voltage, H_{em}^* is the FRF between electric current and welder velocity, and H_m^* is the FRF between shear force and velocity. H_{me}^* and H_{em}^* are equal in magnitude and phase like the other LTI model of the welder. These FRFs can written in terms of lumped system parameters and assuming that the electrical impedance of the transducers is suppressed,

$$H_e^* = \frac{V}{i} = \frac{\Psi_t^2}{j\omega M_t + D_t + \frac{K_t}{j\omega}}, \tag{3.6}$$

$$H_{em}^* = \frac{\dot{\delta}}{i} = \frac{\Psi_t}{j\omega M_t + D_t + \frac{K_t}{j\omega}}, \tag{3.7}$$

$$H_m^* = \frac{\dot{\delta}}{F_s} = \frac{1}{j\omega M_t + D_t + \frac{K_t}{j\omega}}, \tag{3.8}$$

where Ψ_t is the electro-mechanical transformer coefficient of this equivalent form. The other lumped paramters are assumed to not be dependent on the particular equivalent circuit form because they influence the system resonance and system resonance is nearly identical between the two forms. The shear force and applied electrical current in (3.5) are out of phase at the 20 kHz driving frequency (ω_o) because shear force opposes welder vibration directly. This out of phase shear force can be expressed with a minus sign,

$$\dot{\delta}(j\omega_o) = H_{em}(j\omega_o)i(j\omega_o) - H_m(j\omega_o)F_s(j\omega_o). \tag{3.9}$$

Similarly for voltage,

$$V(j\omega_o) = H_e(j\omega_o)i(j\omega_o) - H_{me}(j\omega_o)F_s(j\omega_o). \tag{3.10}$$

Relations (3.9) and (3.10) assume harmonic excitation and that system dynamics at resonance can be described with harmonic excitation. These relations will be used later in Chapter 4 to back calculate welder shear force. Evidence supporting these relations will be presented later in Chapter 4 as well. Prior to using the model to estimate shear force and welder efficiency, it is of interest to show that the presented lumped system models are valid and can be used to describe UAM dynamics. Verification of the model along with identifying the lumped parameters is done in the next section utilizing experimental FRF measurements and characterization techniques, respectively.

3.4 Welder Characterization

3.4.1 FRF Estimation of UAM Welder Components

Two 5 kW piezoelectric transducers are used to actuate the sonotrode near 20 kHz in a push-pull configuration during the UAM process. These transducers are designed to operate in resonance to actuate ultrasonic metal welding sonotrodes. They are not intended for broadband excitation applications. To characterize transducer performance as a function of frequency, a controlled voltage can be applied while current and transducer velocity are measured [76]. Like the welding assembly, H_e, H_{em}, and H_m FRFs can be measured for a piezoelectric transducer. For clarity, these are called H_e^a, H_{em}^a, and H_m^a in this section. Transducer H_m^a was not measured because electro-mechanical symmetry was assumed, i.e., H_{em}^a is equal to H_{me}^a, which, in turn does not require H_m^a for transducer characterization. Using these FRF measurements, the lumped parameters of the piezoelectric transducer as described in (3.2)-(3.4) can be estimated [76].

To apply a controlled voltage and measure current, an AE Techron LVC 5050 was utilized. A Polytec PSV-400 Doppler laser vibrometer was used to measure transducer velocity at the driving face in a non-contact manner. The ability to measure welder vibration in a non-contact way is important because any added mass and geometry (like an accelerometer) will adversely influence the tuned resonance behavior of the transducer. Because the transducer operates at resonance, a Mason circuit can be used to model the transducer dynamics, like the welding assembly [76, 66]. A schematic of the transducer is shown in Figure 3.4(a) with measured inputs and outputs, and the corresponding free-free boundary condition equivalent circuit for the transducer is shown in Figure 3.4(b). The transducer is designed in such a way to operate in free-free condition when not bolted onto the sonotrode because the case is mounted at the node point of the transducer. Nonetheless, to ensure a free-free boundary condition the transducer was placed on foam during characterization.

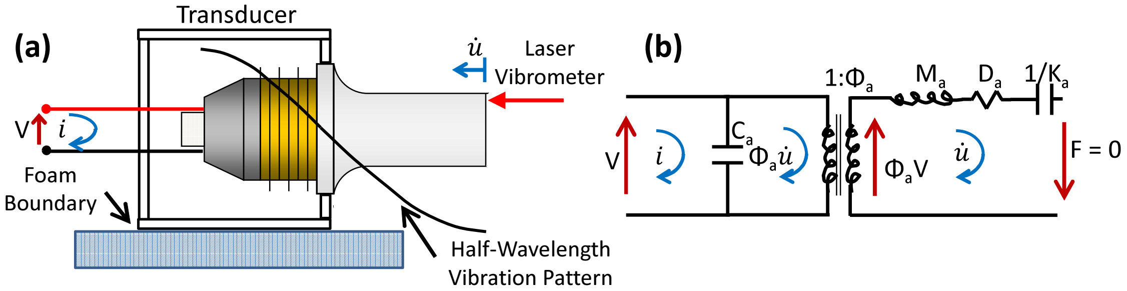

Figure 3.4: Characterization of the 5 kW piezoelectric transducer: (a) schematic of transducer with important test conditions and variables detailed; (b) equivalent circuit of piezoelectric transducer (Mason circuit). The piezoelectric transducer case is attached at the node point with rubber o-ring washers. This node point attachment isolates the dynamics of the transducer. Foam is used as a precautionary measure. Piezoelectric transducer schematic modified from AWS Handbook [29].

FRF measurements of the transducer were made with a Data Physics QUATTRO Dynamic Signal Analyzer utilizing a H_1 FRF algorithm. This H_1 FRF algorithm was used because little to no measurement noise was expected in the excitation signal. To expedite characterization, a periodic chirp excitation was utilized from 0-40 kHz. The processing block size was 8192 points (frequency resolution of 4.88 Hz) and 100 complex linear averages were used for the final FRF estimate. Due to the periodicity of the input with the processing block, no processing window was required [8]. FRF measurements for one of the transducers is shown in Figure 3.5 along with the Mason circuit model presented in Figure 3.4. Model parameters were found using the measured FRF forms discussed earlier and with procedures given for an ideal Mason circuit [76]. The H_e^a FRF was used to estimate the capacitance, mass, stiffness, and damping of the transducer. The electro-mechanical transformer coefficient is found via the ratio of the mobility loop diameters of H_{em}^a and H_e^a. As seen in the Figure, the model shows good correlation in magnitude with some error in phase. Phase error is believed to originate in the linear amplifier used to make the voltage and current measurements because 20 kHz is near the operating limit of the device. Consequently, phase error on the order of 15 degrees is possible [7]. The lumped parameters for the transducer found using the described procedure are listed in Table 3.1.

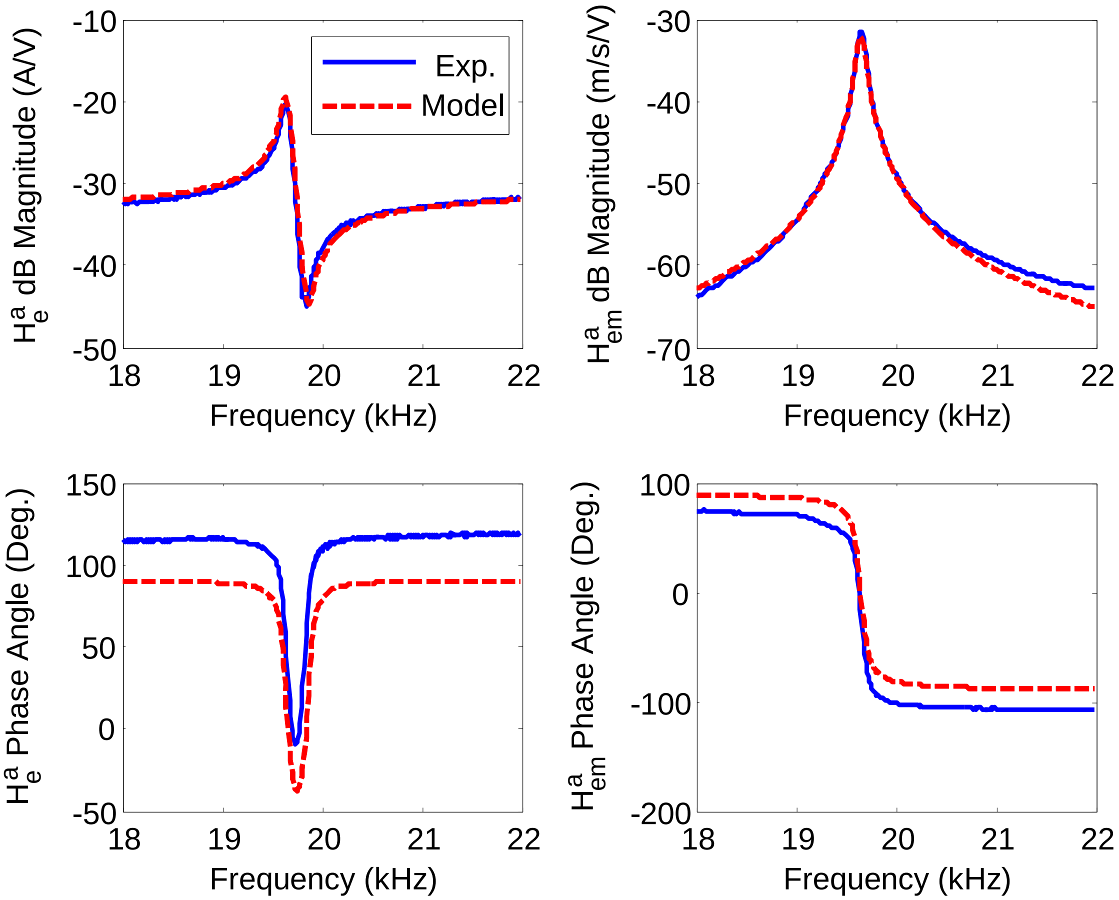

Figure 3.5: Comparison of experimental and analytical FRFs with corresponding phase angle. The phase difference is believed to exist from the amplifier used to to measure voltage and current.

Model Variable	**Value**
C_p (nF)	197.60
M_a (kg)	0.26
K_a (GN/m)	3.98
D_a (Ns/m)	166.88
Φ_a (N/V)	4.07

Table 3.1: Lumped parameter values for Mason circuit model of piezoelectric transducer.

In addition to measuring transducer FRFs, the assumption of linearity was tested by exciting the transducer at different voltage levels, see Figure 3.6(a). The FRF magnitude remains constant for H_{em}^a as a function of voltage level, which implies the transducer is linear. H_e^a was also found to be constant as a function of voltage level, but is not shown for brevity. The response of two separate transducers is compared in Figure 3.6(b). Some difference in response magnitude can be seen near the resonant peak, but overall response is very similar.

The frequency response or impedance of the sonotrode can also be measured with experimental techniques. Like the transducer, the laser vibrometer was used to measure sonotrode velocity to avoid perturbing system dynamics by mass loading the structure. A high frequency modal hammer (PCB 086C30) was used to input a known force impulse into the sonotrode. A modal hammer was utilized because mass loading on the structure would be minimized compared to piezo reaction mass excitation. To emulate welding boundary conditions for the sonotrode, it was placed on the low friction bushings used in the welding assembly while all other components were removed. The test design used to measure sonotrode response is shown in Figure 3.7(a) while the equivalent circuit for the test is shown in Figure 3.7(b). Z_{sono} is used to represent the measured mechanical impedance,

$$Z_{sono} = \frac{F}{\dot{\delta}}. \tag{3.11}$$

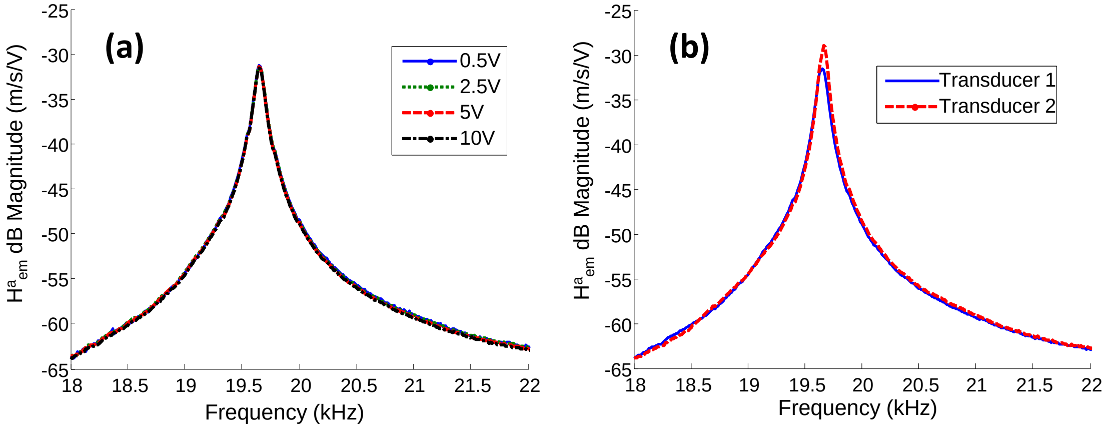

Figure 3.6: Transducer evaluation: (a) excitation at various voltage levels to evaluate transducer linearity; (b) comparison of transducers at 10 V excitation level. The transducers exhibit linear response over the range of evaluated voltages and they have similar response characteristics, i.e., magnitude and frequency is similar.

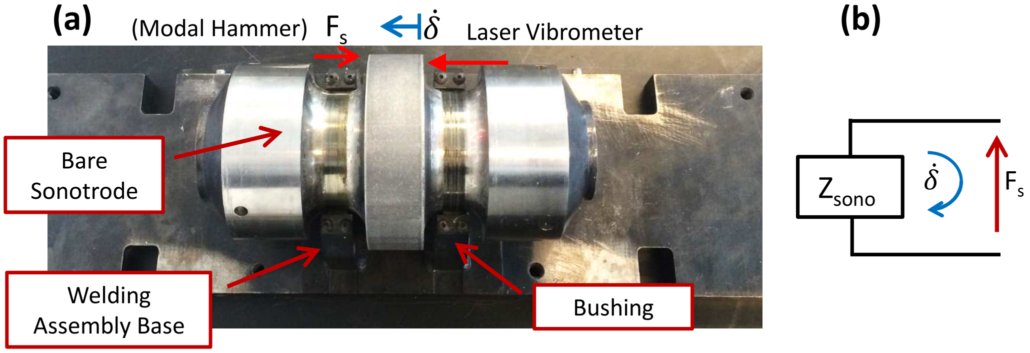
(a)
(Modal Hammer) F_s
$\dot{\delta}$
Laser Vibrometer
Bare Sonotrode
Welding Assembly Base
Bushing
(b)
Z_{sono}
$\dot{\delta}$
F_s

Figure 3.7: Characterization of sonotrode: (a) sonotrode resting in welding assembly with important test conditions and variables detailed; (b) equivalent circuit of the measured mechanical impedance.

Like the transducers, H_1 FRF estimation was done using the QUATTRO. Ten exponentially windowed complex averages were used to estimate the frequency response of the sonotrode. Impulse quality for each impact was inspected prior to using it in the total average. In addition to averaging, the ordinary coherence function was used to ensure the force input correlated with velocity response output near frequencies of concern, i.e., system resonances [8]. The admittance or impedance inverse is shown in Figure 3.8 from 0-40 kHz to identify system resonances around the 20 kHz excitation frequency. It can be seen that the sonotrode is lightly damped due to the sharp resonance behavior and that it has many resonances. Despite the sonotrode having many resonances, the 20 kHz resonant peak is at least 2 kHz away from the nearest resonance. During welding operations, the PLL algorithm moves the excitation no more than 100 Hz from the initial 20 kHz excitation. Consequently, these neighboring structural modes would have little to no impact on welder performance.

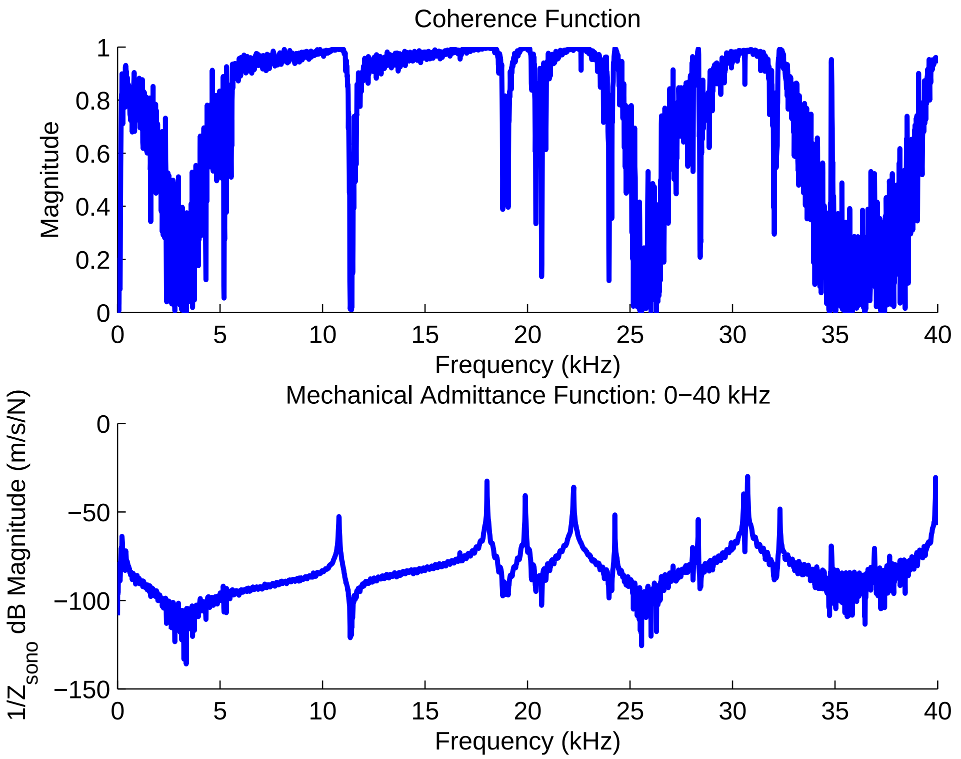

Figure 3.8: Admittance of the sonotrode or the inverse of impedance from 0-40 kHz. The ordinary coherence function is plotted with the admittance measurement.

3.4.2 FRF Estimation of UAM Welder Assembly

After the welding assembly components were characterized individually, the welding assembly itself was characterized. To accurately represent the boundary condition of the assembly, it was characterized inside the UAM machine, see Figure 3.9. Like the individual components, the laser vibrometer was used to measure welder velocity, the linear amplifier was used to apply a controlled voltage input and measure current, the high frequency modal hammer was used to apply a controlled force input, and the QUATTRO was used to estimate H_1 FRFs. The equipment used to characterize the welder is shown in Figure 3.9 while a characterization schematic is shown in Figure 3.10.

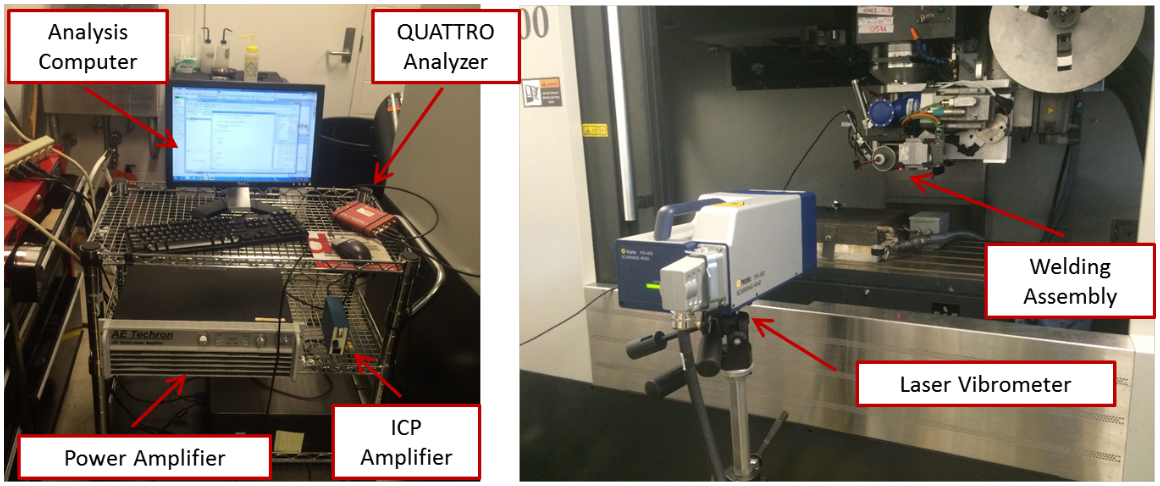
Analysis Computer
QUATTRO Analyzer
Power Amplifier
ICP Amplifier
Welding Assembly
Laser Vibrometer

Figure 3.9: Approach and equipment used to measure experimental FRF measurements of weld assembly. Characterization was done inside the UAM machine to emulate operating boundary conditions.

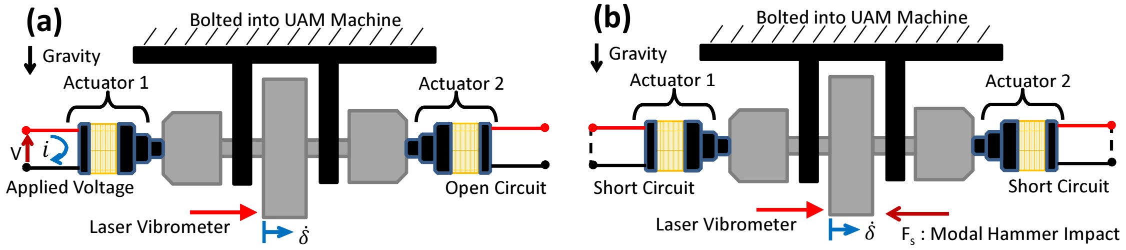
(a)
Bolted into UAM Machine
Gravity
Actuator 1
Actuator 2
V
i
Applied Voltage
Open Circuit
Laser Vibrometer
$\dot{\delta}$
(b)
Bolted into UAM Machine
Gravity
Actuator 1
Actuator 2
Short Circuit
Short Circuit
Laser Vibrometer
$\dot{\delta}$
F_s : Modal Hammer Impact

Figure 3.10: Conditions for assembly FRF measurements: (a) H_e and H_{em} measurements by driving one transducer and leaving the other open; (b) H_m measurement by shorting both transducers with a low resistance wire.

To measure H_e and H_{em}, one transducer was used to excite the system while the other was put into an open circuit condition. This characterization approach is valid because the system is symmetric, which makes the test conditions equivalent to driving the system with two transducers. Also, the open circuit condition is required to allow energy storage over the capacitor and to prohibit current flow out of the passive transducer. Because the resonance of the welder is lightly damped, swept sine excitation was utilized around the 20 kHz system resonance. Frequency spacing during the sweep was 0.5 Hz and measurements were taken until a minimum coherence value of 0.99 was reached for the frequencies of concern. To measure H_m, both transducers were short circuited with low resistance stranded wire while the modal hammer was used to excite the sonotrode. The transducers were short circuited so that energy would not be stored within the capacitive element of the transducers. Like the sonotrode, FRF estimation utilized 10 hammer impacts for averaging and an exponential processing window to minimize leakage. Frequency resolution during H_m estimation was near 2.4 Hz, so measuring the peak FRF value was difficult.

Empirical FRFs are compared in Figure 3.11(a) while the measurement of H_m for both transducers shorted, one transducer shorted, and no transducers shorted (open) is shown in Figure 3.11(b). The FRF with the largest magnitude in Figure 3.11(a) is H_e, followed by H_{em}, and then H_m. The magnitude of H_m in Figure 3.11(b) is similar for each electrical boundary condition, but the resonant frequency changes. This resonant frequency dependence on the electrical boundary condition is typical for piezoelectric devices because the piezoelectric crystal stiffness is different for an open and short circuit condition [45]. Consequently, the resonant frequency of H_m does not coincide with H_{em} directly during testing. When the capacitive element is shorted, it is analogous to making the system less stiff, which causes a downward frequency shift. On the other hand, if the capacitive element is put into an open circuit state, the capacitance stiffens the system and causes an upward frequency shift. During welder operation, the electrical boundary conditions for the transducer are not shorted nor left open. Instead, it is a mixture of the two boundary conditions, which coincides with the H_{em} resonance. Consequently, for comparison purposes in Figure 3.11(a), H_m is manually moved to coincide with H_{em}.

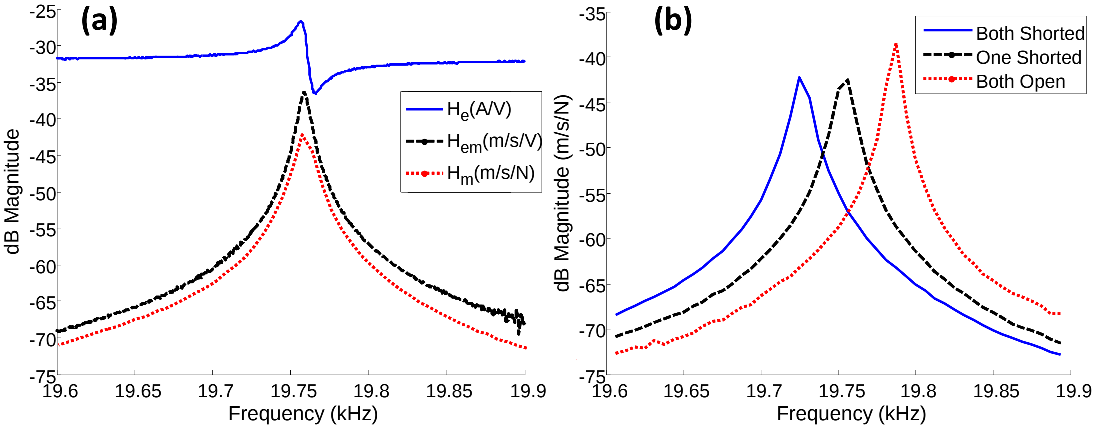

Figure 3.11: Experimental FRF measurements of weld assembly near 20 kHz: (a) comparison of H_e, H_{em}, and H_m FRFs; (b) H_m resonance dependence on shorted and open circuit conditions. The system resonance is different for short and open circuit conditions because the piezoelectric crystal stiffness is different between the two electric boundary conditions.

Because a single resonance peak occurs for the system, lumped parameter modeling can be used as explained earlier. The Mason circuit model for the welding assembly is compared against the empirical FRFs in Figure 3.12, and good agreement is achieved. The parameters for this model were found using the same procedures as done for the transducer. Lumped model parameters are listed in Table 3.2. Due to the system being lumped together, the system mass and stiffness is much larger than for a single transducer (see Table 3.1 for comparison). Also, the system damping is much lower than a single transducer because the damping of the sonotrode is very low.

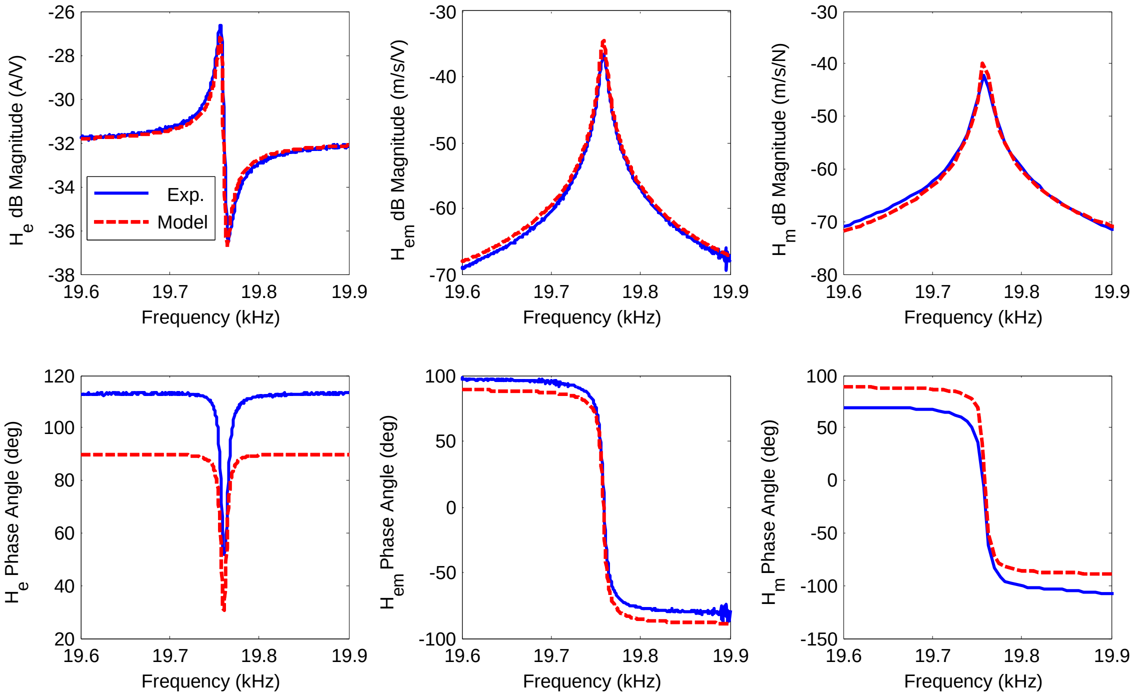

Figure 3.12: System FRF comparison between measurement and system level model.

Model Variable	**Value**
C_t (nF)	203.21
M_t (kg)	1.98
K_t (GN/m)	30.49
D_t (Ns/m)	82.05
Φ_t (N/V)	1.54

Table 3.2: Lumped parameter model values for equivalent circuit of welding assembly dynamics.

3.4.3 Welder Operation Measurements

To characterize this mechanical mobility representation of the welder (Figure 3.3), velocity, voltage, and average electric power measurements were made on the welder while it was operating without load. These three variables were evaluated at different amplitude settings of the ultrasonic generator. To measure welder velocity, the noncontact laser vibrometer was utilized. A Tektronix P6015A voltage probe was used with an Agilent 54622A oscilloscope to measure RMS voltage and P-P voltage of the welder. Power was measured by using the analog output channel on the ultrasonic generator.

To obtain accurate estimates for system voltage and power, the welder was driven with one transducer while the other was left in the open circuit condition. By driving the system with one transducer, the ultrasonic generator doubles the applied current to achieve the same voltage and welder velocity outputs, see Chapter 1. Because current doubles and the voltage is constant, the power also doubles. Peak welder velocity and average electric power draw for the amplitude levels of 40, 50, 60, 70, and 80% are shown in Figure 3.13(a) while peak voltage is shown in Figure 3.13(b). It was found that the measured applied voltage was very similar to a sine wave, so the voltage in Figure 3.13(b) was scaled by the RMS coefficient ($\frac{1}{\sqrt{2}}$) for a sine wave. As seen in Figure 3.13(a), peak welder velocity changes linearly with amplitude setting while average weld power changes in a quadratic manner.

Peak welder velocity is expected to change in a linear manner with applied voltage when no shear force is present, see (3.5). Likewise, voltage also changes linearly with the amplitude setting when there is no shear force present. Power, on the other hand is expected to change quadratically because it is a function of current squared when shear force is not present.

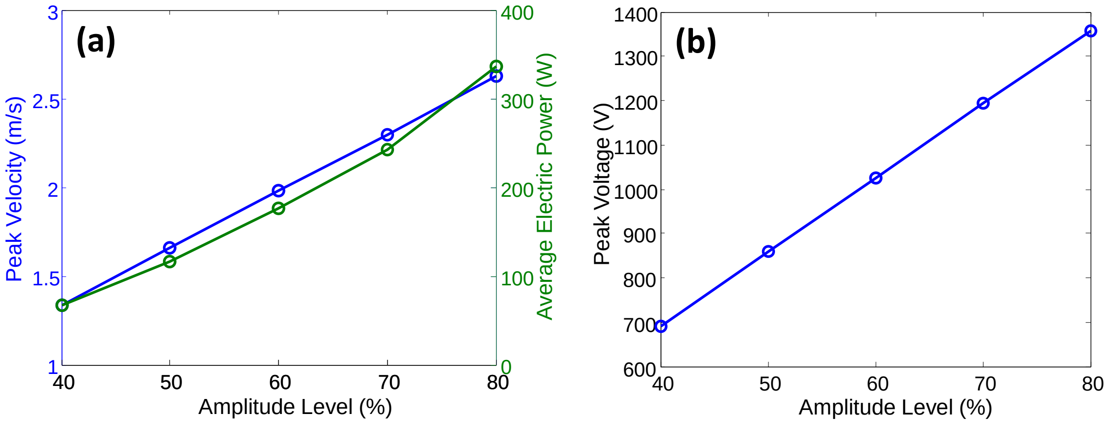

Figure 3.13: Operation of welder operating under no load, i.e., not welding: (a) comparison of peak welder velocity and average electric power draw as a function of amplitude setting; (b) applied voltage as a function of amplitude setting.

Because voltage and velocity change linearly together, the coupling constant for the mechanical mobility representation of the welder (Ψ_t) can be found by fitting a line between the two variables. As seen in (3.6)-(3.8), Ψ_t is scaled by the mechanical admittance (H_m^*) to estimate H_{em}^*. As a result, applied peak current can be estimated by using Ψ_t, H_m^*, and measured peak welder velocity. Estimated peak current can then be used with measured RMS voltage to calculate average electric power, $P_{e,avg}$. Average electric power is defined as the multiplication of RMS voltage, RMS current, and the cosine of the phase angle (θ) between voltage and current,

$$P_{e,avg} = V_{RMS} i_{RMS} \cos\theta. \tag{3.12}$$

The H_e^* FRF theoretically does not have a resonance and an anti-resonance since motional feedback is utilized in UAM. Instead, the function will behave more like a single degree of freedom model and have a phase angle of zero at resonance, see (3.6). Thus, the phase angle between applied current and voltage can be assumed to be zero in (3.12). Using this phase angle simplification, the average electric power can be estimated and compared to the measurement, see Figure 3.14. In the figure, the estimated power is higher than the measurement. To remedy this mismatch, the peak value of H_m^* was adjusted by increasing it 12%. Because the peak value of the FRF was difficult to accurately measure during characterization, increasing its value is likely more accurate as well. With this adjustment to H_m^*, the power estimate becomes closer in agreement with the measured value. The calculated constants utilized for this power calibration are listed in Table 3.3. Appendix B describes this calibration process in more detail.

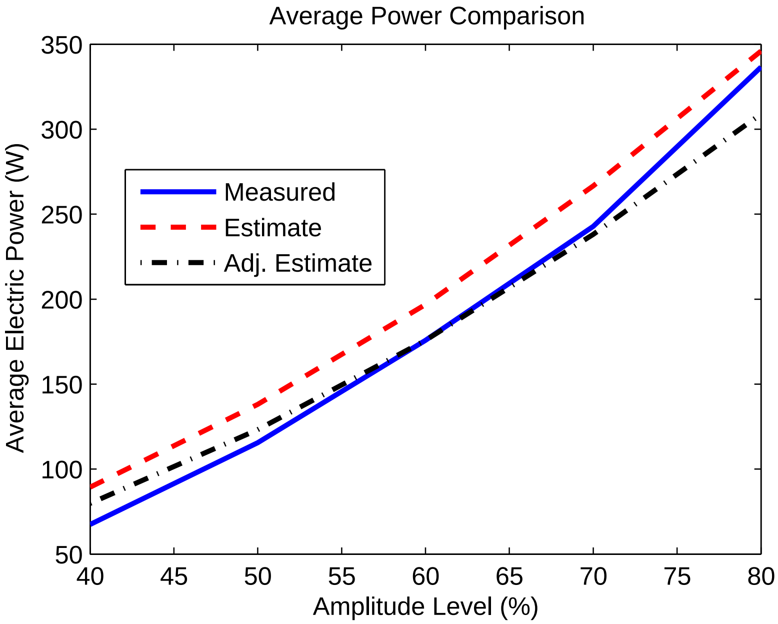

Figure 3.14: Correlation of mechanical mobility model to average electric power.

Model Variable	**Value**
Ψ_t (V*s/m)	515.3
Peak H_m^* (m/s/N)	0.010
Adjusted Peak H_m^* (m/s/N)	0.0112

Table 3.3: Coefficients used to validate mechanical mobility representation.

In addition to estimating power, the excitation frequency of the welder was compared to FRF measurements. This excitation frequency was found using the measured welder velocity signal and FFT algorithm within Matlab. The excitation frequency as a function of amplitude setting is shown in Table 3.4. It was found that the excitation frequency of the system was identical or very near the resonance of the system during FRF characterization. The small variation in excitation frequency is believed to originate in the frequency resolution of the processing block size to calculate the frequency.

Amplitude Setting %	**Frequency (kHz)**
40	19.760
50	19.757
60	19.757
70	19.754
80	19.754

Table 3.4: Frequency of welder velocity as a function of amplitude level. Frequency found via windowed FFT with frequency resolution near 3 Hz. The median frequency of 19.757 kHz agrees well with FRF measurements. A Hamming processing window was utilized to minimize leakage when estimating frequency.

3.5 Welder Frequency Shift and Decrease in Amplitude

UAM system dynamics change during welding because the weld assembly dynamics couple with the dynamics of the UAM build. The UAM build generates an opposing shear force which acts on the sonotrode, and the build stiffens the system due to the resonant frequency shifting upward. System stiffening can only occur if the sonotrode and the weld foil are not slipping on preceeding layers when welding. Instead of slipping, it is believed that a psuedo-steady stick condition occurs because a stable upward frequency shift is seen when welding, see Figure 3.1(c). If the sonotrode and weld tape did not stick to the previous layer, i.e. frictional slip, the shear force would be fully decoupled from the build and no upward system resonance shift would occur. It is believed that when the welder sticks to the UAM build, the interface of the weld tape undergoes large amounts of plastic deformation through shear, which then promotes bonding. Others have also noted low amounts of frictional slip in 9 kW UAM when welding at higher loads (4-6 kN). Specifically, heat generation within the weld was found to correlate well with plastic deformation heating and not frictional slip [84]. Also, normal force was found to not be statistically significant on UAM weld strength [92]. This concept of stick producing good bonds through shear deformation is contrary to the work of others [27]. However, this prior work did not include plastic deformation of the weld tape as a bonding mechanism. Instead, the stick condition was assumed to purely limit interfacial sliding. More analysis of the influence of down force on welder dynamics and shear force will be discussed in Chapter 4.

The 10% decrease in velocity during welding (see Figure 3.1(a)) occurs because (i) the motional feedback method employed by the ultrasonic generator may exhibit error when tracking the amplitude and (ii) the sonotrode deforms slightly during welding operations. To explore the motional feeback error, the presented LTI model can be used by evaluating the difference in welder velocity between two different welding states, i.e., welding and not welding. Because voltage is held constant between these two welding states, the voltage difference between the two states is zero. Consequently, with the use of (3.5) it can then be found that the difference in electric current is proportional to the difference in shear force,

$$H_e^* \Delta i = H_{em}^* \Delta F_s. \tag{3.13}$$

Equation (3.13) assumes that FRF magnitude is the same when welding or not welding and that system energy is predominately concentrated at the excitation frequency (ω_o). FRF magnitude dependence on welding will be discussed in the next section. Equation (3.13) can then be used to explain the difference in welder velocity by relating it to the difference in shear force,

$$\Delta \dot{\delta} = (\frac{H_{em}^{*2}}{H_e^*} - H_m^*) \Delta F_s. \tag{3.14}$$

Equation (3.14) explains that shear force can influence welder velocity if the FRF term is not zero. Ideally, this FRF term equates to zero if motional feedback completely removes the electrical impedance influence of the transducer, see (3.6). However, if the electrical impedance of the transducer is not completely removed, the FRF term will not equate to zero and welder velocity will not be held constant when welding. The electrical impedance of the transducer may not be adequately removed during welding because the inductor (L_t) used to balance out the capacitance is dependent on the inverse of frequency squared [88],

$$L_t = \frac{1}{\omega^2 C_t}. \tag{3.15}$$

As a result, if L_t is not adequately adjusted when the excitation frequency changes during welding, amplitude cannot be reliable controlled. In the case of an increasing excitation frequency, L_t would be too low, H_e^* would have a positive electrical admittance, and the FRF term in (3.14) would become negative, which correlates with a decreasing welder amplitude. Because welder amplitude decreases during welding, it is possible that L_t is not adequately adjusted.

To investigate the influence of sonotrode deformation on welder amplitude, a reduced fidelity linear elastic solid model of the sonotrode tool piece was analyzed in COMSOL Multiphysics. The goal of this simulation is not to fully describe the deformation behavior

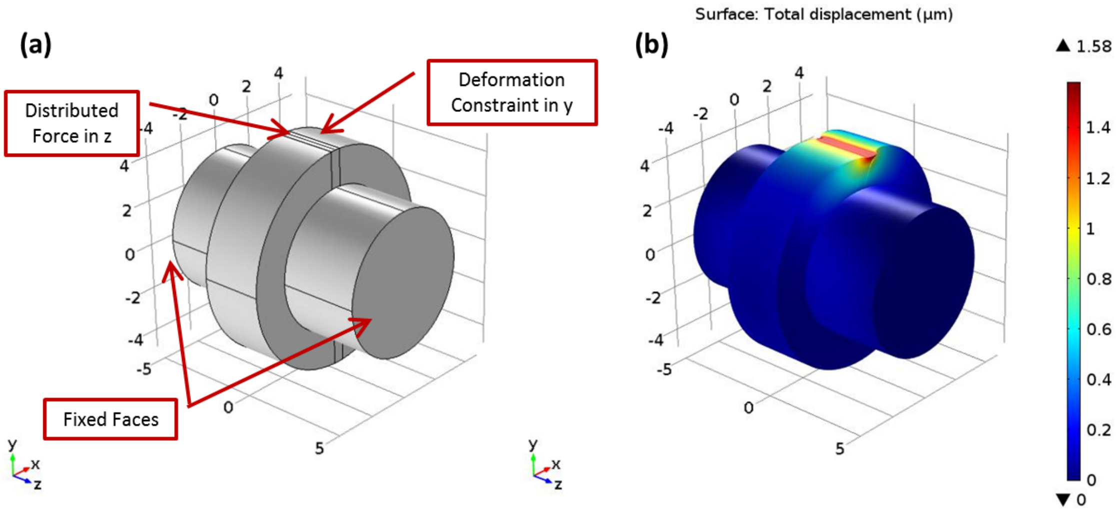

Figure 3.15: Sonotrode deformation analysis from shear loading: (a) reduced model of sonotrode tool piece with assumptions; (b) deformation contour of 9.65 cm diameter tool piece with applied 2000 N distributed load.

of the sonotrode, but to gain insight into the magnitude and behavior of the deformation. The built in High-Strength Alloy Steel material within COMSOL was used as the sonotrode material while the contact width for the force was chosen to be 0.5 cm from experimental observations. The mesh was generated using the physics controlled fine option in COMSOL. The reduced fidelity model along with boundary conditions for the simulation are shown in Figure 3.15(a). Because the sonotrode is constrained against the weld surface of the build with a prescribed normal force, a deformation constraint was placed on the tool piece. The simulation output for a 9.65 cm diameter tool piece with an applied 2000 N distributed load is shown in Figure 3.15(b). 2000 N was used because the peak force magnitude during welding of Al 6061 in Chapter 4 was found to be near this value. Because the sonotrode is designed to operate in the logitudinal mode of vibration near 20 kHz, this static assumption is valid due to the self-exciting deformation modes of the sonotrode being sufficiently far away.

It is shown in Figure 3.15(b) that the maximum deformation of the tool piece is near 1.5 μm. This deformation magnitude is similar to the velocity decrease of 0.25 m/s in

Figure 3.1(a). This velocity decrease correlates to an amplitude magnitude estimate of near 2 μm. This estimate was found by dividing the velocity decrease by frequency in rad/s. In practice, obtaining the maximum deformation of the tool piece is not feasible because the laser vibrometer cannot reliably focus on the very tip of the tool piece. Nonetheless, this analysis demonstrates that sonotrode deformation is likely a contributing factor to the decreased amplitude during welding.

To further explore the influence of tool piece diameter and shear force on tool piece deformation, the COMSOL model was used to iterate through different tool piece diameter and shear force magnitude combinations. Model results are listed in Table 3.5. The variable shear force correlates with different weld metals while the tool piece diameters correlate with the life of a sonotrode. The diameter of the sonotrode changes over its life because the tool piece gets re-texured once the electical discharge machining surface wears down after so many welds. It is shown in Table 3.5 that the tool piece diameter influences the peak deformation a small amount. On the other hand, shear force has a larger influence on the deformation. The influence of larger shear force decreasing welder amplitude more than 2 μm has been observed in practice when welding steel foil onto a steel baseplate. However, increasing loss with amplitude level has not been rigorously studied to evaluate the trends in Table 3.5.

		Tool Piece Diameter (cm)				
		9.27	**9.40**	**9.53**	**9.65**	**9.78**
Force (N)	**1000**	0.76	0.77	0.78	0.79	0.80
	2000	1.52	1.54	1.56	1.58	1.60
	3000	2.28	2.31	2.34	2.37	2.40
	4000	3.04	3.08	3.12	3.16	3.20
	5000	3.80	3.85	3.90	3.95	4.00

Table 3.5: COMSOL model results for peak sonotrode deformation for a given tool diameter and distributed shear force. Results are in units of micron (μm).

3.6 Influence of UAM Build Dynamics

The influence of UAM build dynamics on system dynamics can be studied by replacing welder shear force in Figure 3.3(b) with a prescribed forcing function or a load impedance function (Z_{LD}) to describe energy transfer into the weld for UAM components. To describe UAM build dynamics in a general way for an Al 6061 stack, a complex stiffness [18] load impedance can be used,

$$Z_{LD} = \frac{k_{eff}}{j\omega}(1 + j\eta), \tag{3.16}$$

where k_{eff} is the effective stiffness of the UAM build and η is the loss factor or energy transfer efficiency of the process. This complex stiffness expression describes UAM build stiffness and damping, independent of frequency. In other words, a hysteretic damping model was chosen to model system losses because plastic deformation character would show little change near the excitation frequency when the PLL controller moves the excitation frequency. Damping from plastic deformation is typically described with a Coulomb-friction model [18], like bilinear hysteresis [13, 46]. The purpose of the presented impedance function is not to describe the elasto-plastic interaction during UAM but to describe the UAM build dynamics in a general way.

Model Variable	**Value**
K_t (GN/m)	30.49
k_{eff} (GN/m)	0.02
η	0.25

Table 3.6: Key lumped parameter values to describe UAM stack dynamics. Effective build stiffness (k_{eff}) was chosen by increasing the system resonance 75 Hz. A high loss factor (η) was chosen to illustrate the influence of the large amount of plastic deformation on system response during UAM.

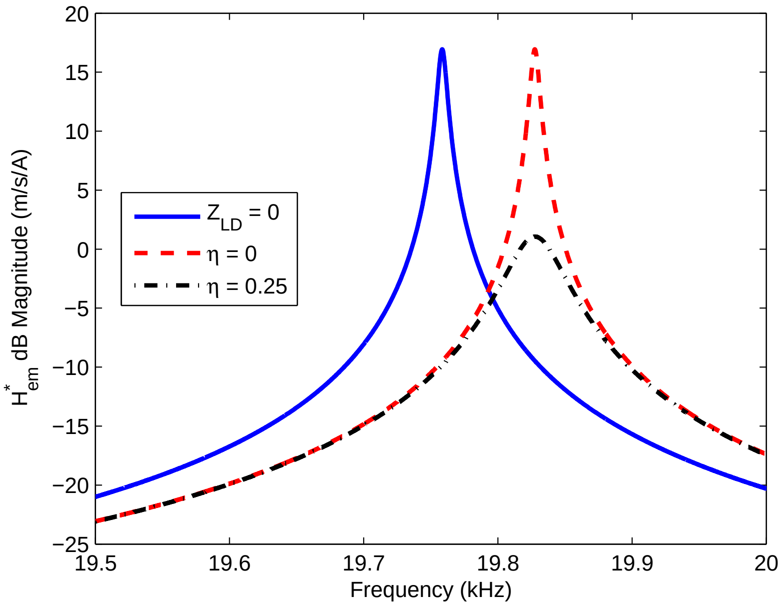

Figure 3.16: Estimation of UAM build stiffness via a 75 Hz frequency shift and the investigation of UAM build stiffness on FRF magnitude. Due to stiffness not influencing FRF magnitude, FRF magnitude would be consistent when system resonance changes under load. Damping or energy leaving the system is shown to decrease system response.

To describe the influence of the UAM build onto the system, the load impedance was implemented by introducing effective build stiffness without damping initially ($\eta = 0$) and then introducing a loss factor ($\eta = 0.25$). To estimate the effective build stiffness, system stiffness was increased until a 75 Hz frequency shift was accomplished, see $\eta = 0$ traces in Figures 3.16-3.17. This 75 Hz frequency shift was chosen because it was observed when welding an Al 6061 stack, see Figure 3.1(b). The required build stiffness to cause this frequency shift is less than 1% of the assembly stiffness. Also, because energy is being stored in the system, no change in system response magnitude occurs. Because the welder is capable of moving the excitation frequency during welding, it can be inferred that FRF response will not change due to this added stiffness. A loss factor of 0.25 or a damping capacity of 25% was chosen to illustrate system losses during UAM due to large amounts of plastic deformation occurring. Chapter 4 will discuss UAM energy transfer more thoroughly.

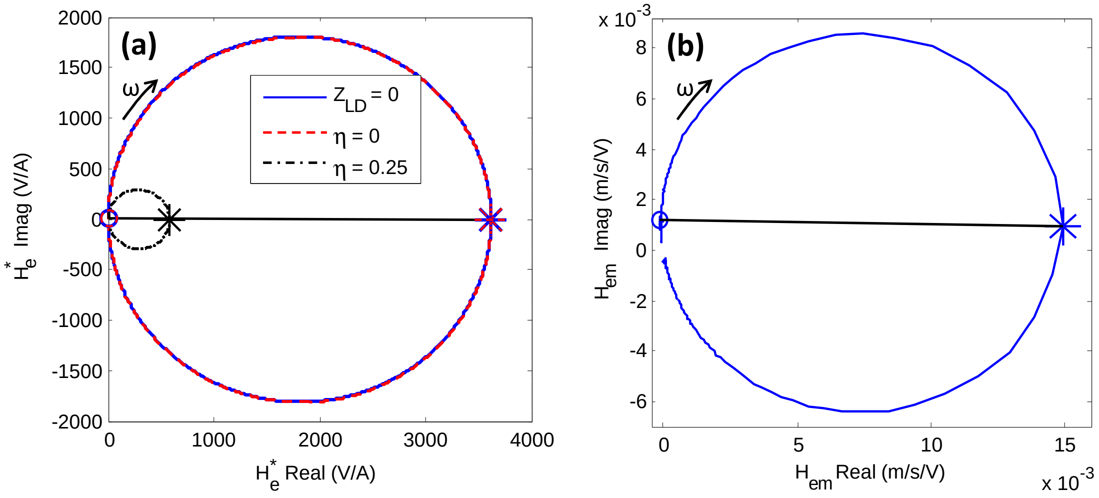

Figure 3.17: Nyquist plots: (a) estimated motional impedance locus, H_e^*; (b) measured admittance locus, H_{em}. Resonant frequencies for each locus are marked with an asterisk while adjacent locus points are marked with circles. Loading the system without damping does not change the motional impedance locus due to the diameter remaining constant. The decrease in locus diameter occurs only when damping is introduced [44]. The resonant frequency location in the motional impedance locus occurs at 0 degrees because the electro-mechanical coupling coefficient is assumed to be real valued [44]. To verify this assumption, the H_{em} admittance locus is plotted. The resonant peak has a phase location < 1 degrees, which supports the real valued coupling coefficient assumption of 0 degrees.

The $\eta = 0.25$ curves in Figures 3.16-3.17 illustrate that the system response decreases due to energy no longer being stored within the welding assembly. A summary of key lumped parameter estimates for this analysis are shown in Table 3.6.

3.7 Summary

A new linear time invariant model for the UAM process has been developed to more fully understand welder operation and energy transfer from the sonotrode and into the part. It is of interest to understand energy flow because welder energy is correlated to bond quality. This model utilizes a Mason equivalent circuit in the mechanical mobility form to incorporate welder shear force and to describe why power draw increases during welding. Imparted shear force has not been considered prior in UAM. This equivalent circuit also describes the constant amplitude control scheme that the welder uses. Experimental frequency response functions and operation measurements of the welder were investigated to confirm that a Mason circuit can be used to accurately describe system dynamics.

This model can be used to back calculate welder shear force and to evaluate welder efficiency. Welder shear force has not been estimated or measured prior in UAM. Welder efficiency also has not been estimated or measured. The next chapter estimates these quantities and exemplifies the use of this model.

Chapter 4

WELDER SHEAR FORCE AND EFFICIENCY

4.1 Introduction

The aim of this chapter is to utilize the presented model in Chapter 3 to improve understanding and quantify welder shear force magnitude during UAM. The LTI model is used in conjunction with in-situ measurements to study shear force magnitude and frequency character. Welder efficiency and the influence of processing conditions, i.e., welder amplitude, normal force, and weld speed, are also investigated.

The chapter begins by evaluating the coupling of the work piece or UAM build with the dynamics of the welder by analyzing in-situ welder velocity frequency response and resonance shifts. It is found that the welder velocity exhibits high frequency harmonic content of the driving frequency, and this harmonic content is largest at the odd harmonics. The welder excitation frequency was then found to give insight into the changing build stiffness during UAM, and the coupling of the UAM build with the welder. The LTI system level model is then utilized to estimate the magnitude of the shear force and welder efficiency during UAM by measuring in-situ welder velocity and average electric power. The shear force magnitude was found to be near 2000 N while welder efficiency was near 80% for standard Al 6061 foil welding procedures. The influence of changing processing conditions, i.e., welder amplitude, weld speed, and normal force, on shear force magnitude and efficiency is then studied. Welder velocity was found to strongly influence the shear force magnitude and efficiency while normal force and weld speed showed little to no influence. Aspects of this chapter were submitted to the journal *Ultrasonics* [38].

4.2 Welder Velocity Response during UAM

The following sections discuss the influence of shear force and build compliance on welder velocity response during UAM. The first section discusses why welder shear force influences harmonic content in the velocity spectrum of the welder. The second section examines the effect of UAM build compliance on the nominal excitation frequency and the harmonic content magnitude.

4.2.1 Effect of Shear Force

As discussed in Chapter 3, the ultrasonic generator utilizes a phase lock loop algorithm combined with motional feedback to maintain a prescribed welder vibration magnitude and to track system resonance shifts during UAM. The relationship between build stiffness and excitation frequency shifts were discussed in detail while the control framework for constant amplitude control at the nominal excitation frequency was explained. However, it was not explained that additional frequency content exists in the velocity signal response during welding, see Figure 4.1. Specifically, the lateral scrubbing velocity response increases at all frequencies and exhibits content at harmonic locations of the excitation frequency. These high frequency measurements were carried out using a Polytec PSV-400 Doppler laser vibrometer with a sampling rate of 512 kHz. High frequency harmonic content in the velocity signal during UAM has been observed prior by J. Gibert [25] when evaluating stick-slip behavior, yet no conclusive claims were made.

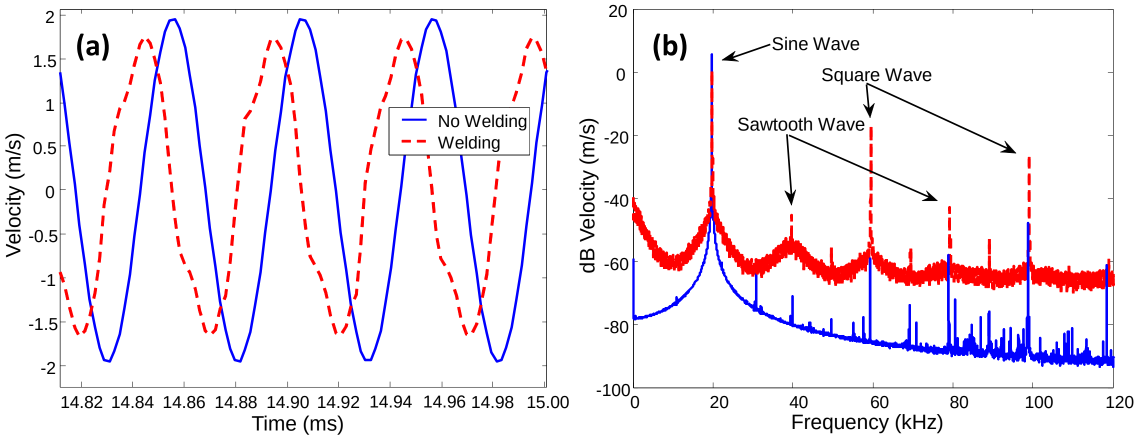

Figure 4.1: Sonotrode or welder velocity character during UAM compared to actuating the welder without load, i.e. not welding: (a) time history comparison of signals; (b) frequency domain comparison of signals. Signals were sampled at 512 kHz with an amplitude level of 60% (32.5 μm setpoint). The phase delay in (a) is of no significance. The small decrease in welder amplitude during welding is discussed in Chapter 3. Frequency data was obtained by averaging the velocity signal magnitude with a block size of 81920 points and without windowing. Windowing was not used to illustrate increased frequency content more clearly. Due to windowing not being used, some leakage may be present in the figure.

The frequency response of the welder velocity is different during welding vs. not welding because the shear force input function contains energy at all other frequencies in addition to the nominal excitation signal. The exact excitation frequency of the welder depends on the effective resonance of the sonotrode and transducers when they are bolted together (see Chapter 3. To explain why additional frequency content exists in the welder velocity signal, the proposed LTI model from Chapter 3 can be used,

$$\begin{pmatrix} V(j\omega) \\ \dot{\delta}(j\omega) \end{pmatrix} = \begin{bmatrix} H_e^*(j\omega) & H_{me}^*(j\omega) \\ H_{em}^*(j\omega) & H_m^*(j\omega) \end{bmatrix} \begin{pmatrix} i(j\omega) \\ F_s(j\omega) \end{pmatrix}, \tag{4.1}$$

where H_e^* is the FRF between applied electric current (i) and voltage (V), H_{me}^* is the FRF between opposing shear force during welding (F_s) and voltage, H_{em}^* is the FRF between electric current and velocity of the sonotrode ($\dot{\delta}$), and H_m^* is the FRF between shear force and velocity. Piezoelectric systems follow the law of reciprocity, so H_{me}^* and H_{em}^* are equal in sign and magnitude [44, 76]. To describe the relationship for welder velocity, the following expression can be found from (4.1),

$$\dot{\delta}(j\omega) = H_{em}^{*}i + H_{m}^{*}F_{s}. \tag{4.2}$$

Equation (4.2) explains that welder velocity is a linear combination of the applied electric current and resultant shear force for all frequencies. It was established in Chapter 3 that the electric current used to actuate the welder could be approximated as a sine wave because the output voltage of the welder was found to be nearly sinusoidal. This single tone excitation is corroborated when analyzing the velocity response of the welder when operating under no load because its response is also sinusoidal, Figure 4.1(b). Because the excitation signal is concentrated near resonance (ω_o), content at other frequencies must come from the shear force input function. Additionally, the observed content in the velocity spectrum is originally passed through the transfer path or frequency response function (FRF) for a given system input. These FRFs act as filters on the system, and they influence frequency content in the velocity spectrum of the welder. To understand FRF influence on velocity and system response, these functions can be measured.

Obtaining FRF measurements at frequencies above 20 kHz is difficult. For measuring H_m^*, state-of-the-art high frequency modal hammers do not demonstrate the necessary frequency response input character to reliably characterize the system upward of 20 kHz. For measuring H_{em}^*, response above resonance is low and narrow band excitation techniques are required. Despite these measurement difficulties, the general character of these FRFs can be investigated, see Figure 4.2. The FRFs in the figure were obtained using the procedures outlined in Chapter 3 and using the built-in high speed data acquisition system of the laser vibrometer. It should be noted that H_{em} in Figure 4.2 is for the velcocity-voltage FRF (H_{em}) and not the velocity-electric current FRF (H_{em}^*). However, the two FRFs have similar behavior and can be used for comparison purposes.

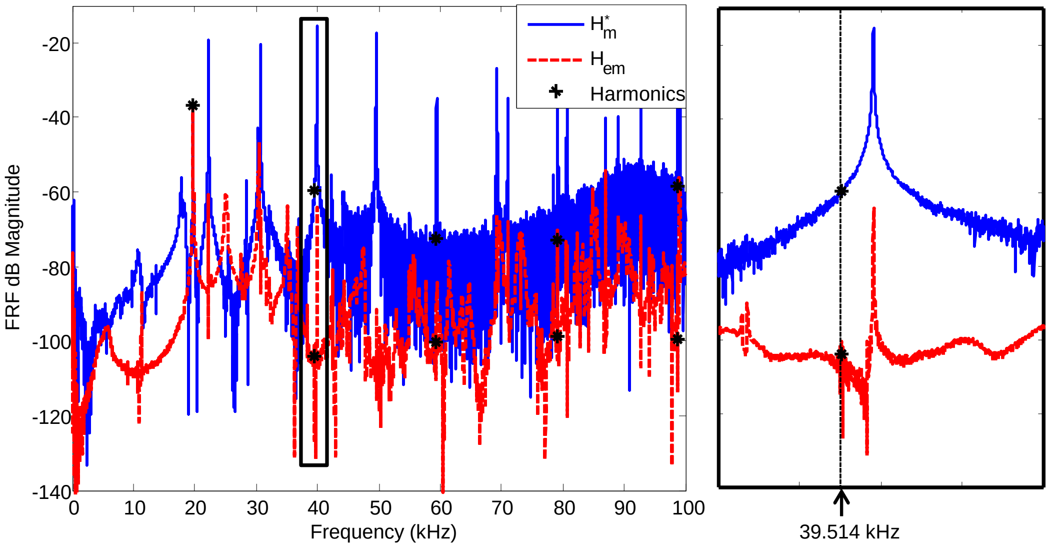

Figure 4.2: H_{em} and H_m^* FRF estimates of the welder from 0 to 100 kHz. The nominal resonance of the welder is 19.757 kHz, and its harmonics are marked with astericks on the FRFs. The 2nd harmonic (39.514 kHz) is given as an example. The locations of the harmonic frequencies were investigated to see if they coincided with any system resonances. No harmonics showed correlation with system resonances, so amplification is not significant during welding. FRFs were estimated using the high speed data acquisition system of the laser vibrometer.

The harmonic locations of the nominal resonance of 19.757 kHz are marked in Figure 4.2 with asterisks. Aside from the excitation harmonic (1st), the harmonics of the excitation signal do not coincide with any other system resonances. Consequently, significant amplification of harmonic content is not suspected during welding, and the content seen in Figure 4.1(b) must be transmitted at low response regions of the H_m^* FRF. Because harmonic content is transmitted at low response regions, the origin of the content must come from the shear force excitation function.

4.2.2 Effect of Build Compliance

To investigate the influence of build compliance on harmonic content in the velocity spectrum, in-situ welder velocity measurements were made as a function of build height. The influence of power compensation on harmonic content was also evaluated. Compensated power implies that the prescribed displacement of the welder was increased manually to maintain a constant electric power input into the UAM build, as explained in Chapter 2. Uncompensated means that the prescribed amplitude was not adjusted during construction, i.e., the default constant amplitude control was used. The power compensation approach used is listed in Table 4.1 and is similar to the approach used in Chapter 2 and previous work [39]. To measure average electric power draw as a function of weld height, the analog output signal for weld power on the ultrasonic generator was synchronized with welder velocity. Average electric power as a function of build height is shown in Figure 4.3(a) with first standard deviation error bars about a mean value for a given layer. Because welder velocity is measured, welder frequency as a function of build height can be estimated using Fourier analysis, see Figure 4.3(b). Welder frequency was found by using the FFT function in Matlab, a Hamming processing window to minimize leakage error, a 50% overlap, and a block size of 81920 (6.5 Hz resolution). Because the ultrasonic generator changes the frequency slightly during welding (see Chapter 3), first standard deviation error bars are used to show frequency variation about a mean value for each weld layer.

Layer	**1-2**	**3-4**	**5-6**	**7-8**	**9-10**	**11-15**	**16-20**
Amp. (%)	60	61	62	63	64	65	66
P-P δ_L (μm)	32.5	33	33.6	34.1	34.7	35.2	35.8

Table 4.1: Power compensation approach by increasing prescribed peak-to-peak displacement (δ_L) of the welder. Amplitude percentage was input into the UAM machine controller to achieve the given displacement.

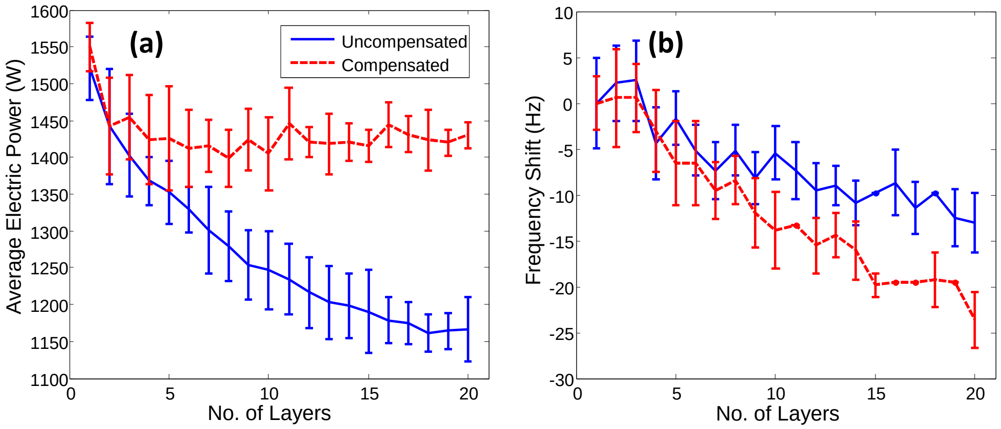

Figure 4.3: Power and excitation frequency shift during UAM stack construction: (a) average electric weld power vs. number of layers; (b) excitation frequency shift vs. number of layers. The compensated power trace in (b) shows an increased amount of frequency shift.

It is shown in Figure 4.3(b) that welder excitation frequency shifts downward with more layers and with more displacement (compensated trace). The downward frequency shift for amplitude control (uncompensated trace) corresponds to the UAM build becoming less stiff with more layers. Because the build becomes less stiff with more layers, the amount of plastic deformation hardening decreases and leads to a decrease in the effective build stiffness. On the other hand, the increased displacement for power compensatation increases this downward frequency shift. This increased frequency shift occurs because the effective build stiffness decreases with more plastic deformation. Additional evidence of this downward shift due to a larger amount of plastic deformation will be shown later when analyzing the influence of welder amplitude on welder response and performance. These two frequency shift mechanisms are schematically detailed in Figure 4.4.

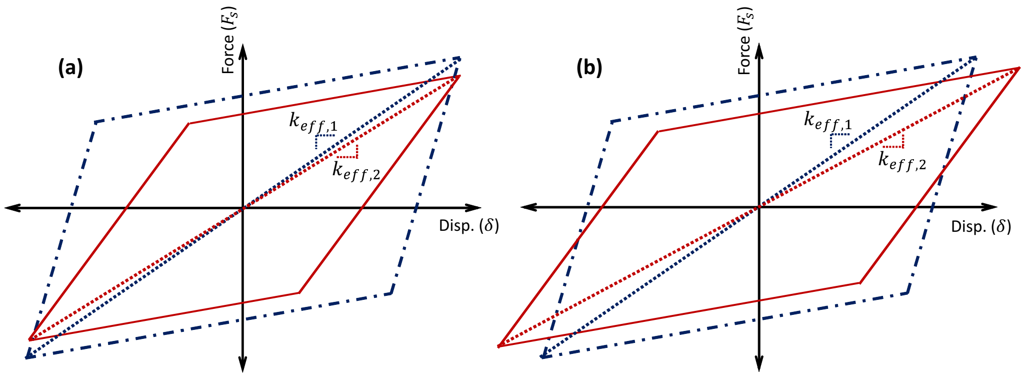

Figure 4.4: Frequency shift mechanisms during UAM: (a) less plastic hardening decreases the effective build stiffness; (b) more plastic deformation decreases the effective build stiffness.

In addition to analyzing excitation signal frequency shift as a function of build height, harmonic frequency content was examined. The dependence of this harmonic content on prescribed displacement and build stiffness can give insight into shear force and plasticity behavior of the weld foil during build construction. Averaged frequency content for the first three harmonics are shown in Figure 4.5 for the compensated and uncompensated power conditions. This data was obtained by utilizing a Hamming processing window to simultaneously minimize leakage error and obtain accurate amplitude estimates. A 50% processing block overlap was also used. The processing block size was 81920 points (6.5 Hz resolution), and this block size provided an adequate number of averages to statistically separate the trends shown in the figure. Because the processing frequency resolution was not extremely fine and the frequency is non-stable during UAM, points at and around the harmonic locations were used to estimate content by averaging them together for a given processing block. Three points were taken above and below the harmonic peak for averaging. Thus, seven total points were averaged together to produce the data shown in Figure 4.5 with the first standard deviation as error bars.

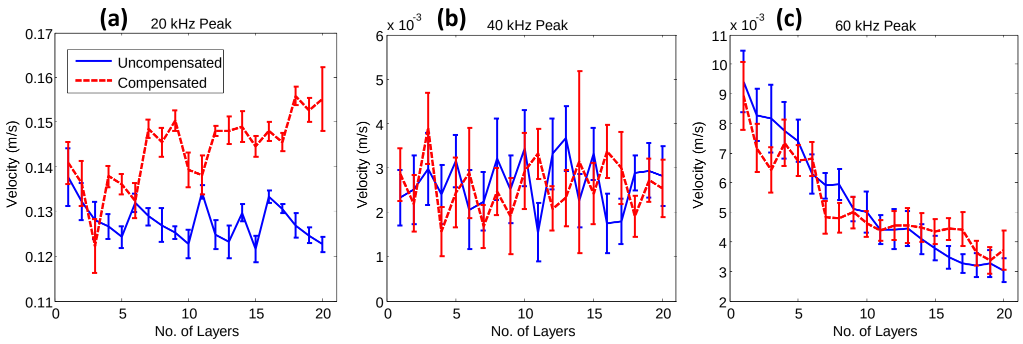

Figure 4.5: Harmonic content during UAM stack construction for the approximate locations of 20, 40 ,and 60 kHz: (a) 1st harmonic, 20 kHz; (b) 2nd harmonic, 40 kHz; (c) 3rd harmonic, 60 kHz. The influence of power compensation increases the 1st harmonic's content, but does not influence the other harmonics. Due to the UAM build becoming more compliant with construction, the 3rd harmonic's content decreases. Harmonic content was found using FFT analysis using a Hamming processing window, a block size of 81920 (6.5 Hz resolution), and by averaging the harmonic peak value with three points below and above it, i.e., seven total points total used to estimate content around the peak. Seven points were used for averaging content because reliably and consistently estimating the peak harmonic response is difficult with the processing block resolution.

In Figure 4.5(a), the nominal excitation frequency content (20 kHz) is very steady for the uncompensated trace. This steadiness is expected due to the ultrasonic generator attempting to keep amplitude constant during build construction. The cyclic variation shown in the uncompensated trace originates from periodically moving the measurement point of the laser vibrometer every 5 layers to remain on the sonotrode combined with the deformation behavior of the sonotrode discussed in Chapter 3. The increasing content in the compensated trace is expected due to the velocity or amplitude increasing during build construction. In Figure 4.5(b), the 2nd harmonic content (40 kHz) is constant as a function of build height for both the compensated and uncompensated traces. This constant content implies that the hardening behavior (sawtooth component) of the weld metal does not change significantly with build height. On the other hand, the 3rd harmonic's content (60 kHz) exhibits a large amount of change with the number of weld layers, see Figure 4.5(c). Like the excitation frequency shift in Figure 4.3(b), the compensated and uncompensated traces show decay as a function of build height. The decay in the content is expected because it is the first square wave harmonic and is the most sensitive to square wave changes, i.e., non-constant build compliance. Consequently, the increasing build compliance of the UAM stack with height influences the shear force profile.

The decreasing magnitude of the 3rd harmonic or square wave harmonic combined with the prevalent high order odd harmonics in Figure 4.1(b) and transfer path character of H_m^* (see Figure 4.2) can be used to hypothesize the shear waveform behavior during welding, see Figure 4.6. The proposed forcing function exhibits predominant square waveform behavior because the dominant high frequency harmonics in Figure 4.1(b) coincide with odd harmonic frequency content (60 and 100 kHz peaks). It is suspected that some plastic deformation hardening does exist in UAM as originally depicted in Figure 3.1(c) because the sawtooth wave or even harmonic locations in Figure 4.1(b) have content, but this content is much less than the square wave content and shows no change with build height. The content of the square wave changes with build height because the elastic stiffness of the build decreases and influences the shear force input function. In particular, the forcing function becomes less square wave like due to the build becoming more compliant with each added layer, which in turn reduces the magnitude of the 3rd harmonic with each layer. Figure 4.6 illustrates the proposed force waveform behavior with k_1 representing a stiff UAM build while k_2 represents a less stiff build. The k_1 profile is more square like than k_2.

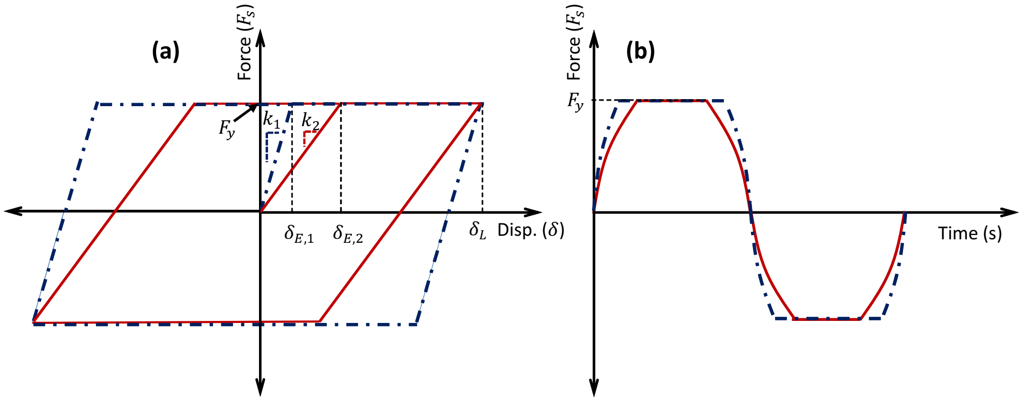

Figure 4.6: Proposed shear force profile during welding using evidence from welder velocity frequency response measurements and H_m^*: (a) force-displacement; (b) force-time. Due to the UAM build becoming more compliant with more layers, the behavior of the forcing function becomes less square like with more layers.

4.3 Shear Force Estimates and Welder Efficiency

In Chapter 3, it was discussed that average electric power could be expressed as the following when motional feedback is used,

$$P_{e,avg} = V_{RMS} i_{RMS}. \tag{4.3}$$

If one assumes that content is primarily located at the excitation frequency (ω_o) or if the content is primarily a single frequency, (4.3) can be simplified to the following,

$$P_{e,avg} = \frac{1}{2} V i. \tag{4.4}$$

Equation 4.4 is a reasonable simplification for average electric power draw considering that the weld velcocity's 1^{st}harmonic is an order of magnitude greater than all other higher order harmonics (see Figure 4.5). Because applied voltage to the piezoelectric transducers is controlled to be constant for a given amplitude set-point value, the ratio of average electric power between two welding layers or states can be equated to the ratio of weld currents,

$$\frac{P_2}{P_1} = \frac{i_2}{i_1}, \tag{4.5}$$

where P_2 and P_1 are the average electric power for welding states 2 and 1, respectively. Likewise, i_2 and i_1 are the applied peak electric current values for welding states 2 and 1. In Chapter 3, it was shown that electric current was estimated from measured welder velocity when not welding and then correlated with measured average electric power draw. Using this calibrated current and measured average electric power for not welding (state 1), applied current during welding can be estimated if average electric power draw is measured (state 2). With this estimate for applied current at the excitation frequency, welder shear force at can then be estimated using the LTI model in Chapter 3 assuming operation at resonance (calibrated peak FRF values), and using measured peak welder velocity,

$$F_s = \frac{H_{em}^{*} i - \dot{\delta}}{H_m^{*}}. \tag{4.6}$$

To illustrate the use of (4.6), the states of not welding and welding can be compared, see Figure 4.7. Along with estimated shear force between the two states, the measured average electric power, measured peak welder velocity, and calculated excitation frequency are also shown in the figure. In-situ measurements were sampled at 50 kHz (25 kHz Nyquist) with a National Instruments DAQ module. Consequently, content in Figure 4.7 is from the excitation signal (near 20 kHz) and contains no higher order harmonic content. Appendix C describes sampling synchronized welder power and welder velocity to estimate shear force in more detail. The average electric weld power increases an order of magnitude, the welder excitation frequency increases 75 Hz, the peak welder velocity decreases 10%, and shear force is near 1750 N during welding. Shear force during ultrasonic spot welding has been measured previously [19], and found to be near 1800 N for the same aluminum alloy with a similar sonotrode contact area.

The shear force of the welder exhibits similar behavior to the average electric power since (4.5) is used to estimate applied current to the welder. The reported average electric power in Figure 4.7 was measured from a single piezoelectric transducer and doubled in value because power draw is near symmetric between the two transducers on the sonotrode, see Chapter 1.

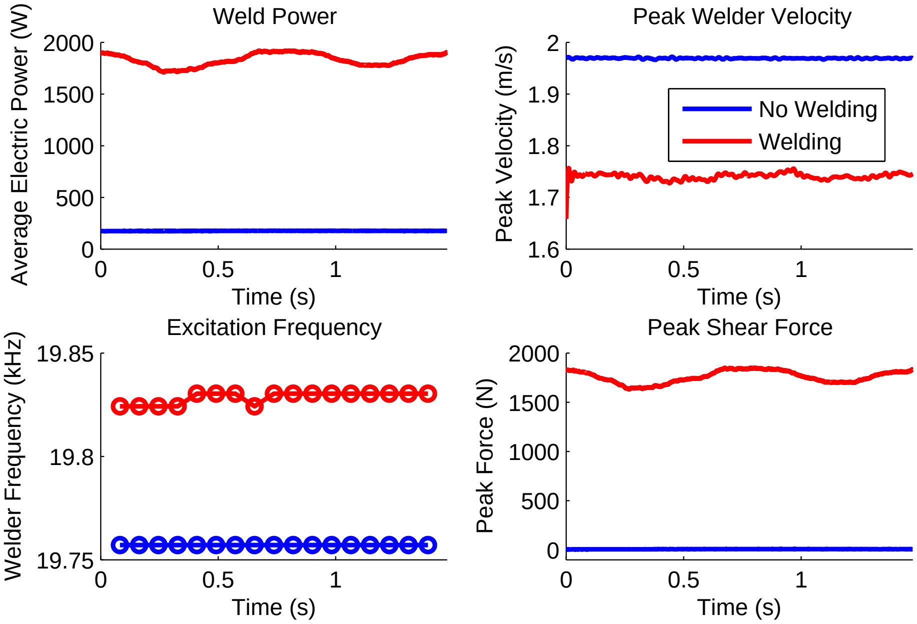

Figure 4.7: Estimate of welder shear force from in-situ velocity and power measurements. Welder excitation frequency is also compared to illustrate system stiffening when welding.

With the use of estimated peak shear force, measured peak welder velocity, and measured average electric power draw, welder efficiency (e) can then be calculated,

$$e = \frac{P_{m,avg}}{P_{e,avg}} = \frac{\frac{1}{2}\dot{\delta} F_s}{P_{e,avg}}. \tag{4.7}$$

Welder efficiency is calculated using the ratio of average mechanical power ($P_{m,avg}$) and average electric power ($P_{e,avg}$). This efficiency calculation assumes that the majority of the applied electrical energy is concentrated near the excitation frequency as well. Efficiency comparisons between the states of not welding and welding are shown in Table 4.2. The efficiency is not exactly zero when not welding because there is a small residual shear force from the calculation (4.6). Nontheless, the estimated welding efficiency is near estimates for ultrasonic metal welding systems [29] and below that of UAM piezoelectric transducers [23], which is greater than 90%. This estimate is sensible considering efficiency cannot be greater than the ultrasonic transducers themselves. Losses in the system which decrease efficiency are bushings, bolted joints, material damping within the waveguide, and friction in the spring diaphragm ball bearing. The assumption of not including higher order harmonics may also lead to an error in this efficiency calculation.

	No Welding	**Welding**
Mean	4.31	83.66
Std. Dev.	0.50	0.44

Table 4.2: Welder efficiency comparison between the states of not welding and welding. A small efficiency is calcualted for the state of not welding due to a small residual shear force being present from the calculation of shear force (4.6).

4.4 Influence of UAM Processing Conditions on Shear Force and Efficiency

In addition to comparing the shear force and efficiency estimates between the states of not welding and welding, the influence of UAM processing conditions on these estimates can be evaluated. The influence of welder amplitude or velocity on system dynamics is shown in Figure 4.8 while the efficiency for the amplitude levels of 40, 50, and 60% are listed in Table 4.3. As seen in the figure, the the average electric power draw increases with amplitude level, the peak welder velocity increases monotonically with amplitude setting, the excitation frequency decreases with higher amplitude levels, and shear force increases with higher amplitude levels. Lastly, efficiency decreases with larger amounts of deformation because larger shear forces require more electric power draw. The relationship between efficiency, shear force, and electric power draw will be discussed in more detail later to make this observation more clear.

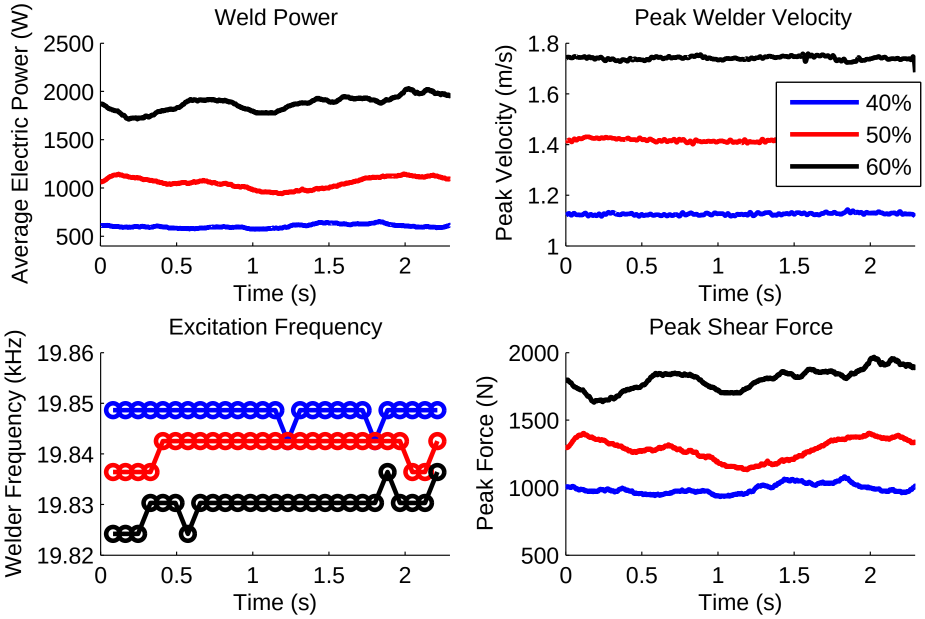

Figure 4.8: Comparison of system dynamics as a function amplitude level. Other UAM processing conditions were held constant in this study. In particular, normal load was 5000 N, linear weld speed was 5 m/min (200 in/min), and welds were made at room temperature.

	40%	**50%**	**60%**
Mean	92.4	86.2	83.7
Std. Dev.	0.53	0.43	0.47

Table 4.3: Welder efficiency comparison between different amplitude settings.

As shown in the figure, the the average electric power draw increases with amplitude level, the peak welder velocity increases monotonically with amplitude setting, the excitation frequency decreases with higher amplitude levels, and shear force increases with higher amplitude levels. Power draw and shear force increase with amplitude level because enhanced motion increases both elastic and plastic deformation of the system. This increase in deformation leads to a corresponding increase in effort from the welder. The efficiency decreases with larger welder amplitude levels because plastic deformation and some slip is present during UAM. The relationship is made more clear by evaluating the closed form relation of efficiency in terms of welder motion and shear force,

$$e = 1 - \frac{\dot{\delta}}{\dot{\delta} + H_m^* F_s}. \tag{4.8}$$

The relation explains that if the shear force and welder motion are not linearly related, the efficiency can show some variation. Since metal plasticity and some slip is present in UAM, it is suspected that their non-linearity is the reason for this efficiency variation in Table 4.3.

The next UAM processing variable to be evaluated is the normal or down force. Results for the normal force levels of 4000, 5000, and 6000 N are shown in Figure 4.9 and Table 4.4. These different normal force levels do not strongly influence UAM system dynamics from one level to the next because it has been shown that frictional slip does not strongly influence UAM at these force levels [84, 92]. Negligible magnitude difference is seen in average electric power draw and peak shear force between the different force levels. Peak welder velocity decreases near 1.5% between each force level and excitation frequency decreases in an exponential manner with normal force level. An explanation of this observed trend can be described by evaluating the inductor impedance (L_t) used in the motional impedance control strategy [88],

$$L_t = \frac{1}{\omega^2 C_t}. \tag{4.9}$$

If the inductance used to cancel out the electrical impedance of the transducer is fixed during welding, velocity will not be held constant because excitation frequency changes. Down force may influence the coupling of the welder to the build, which then ultimately influences the excitation frequency of the welder. This welder amplitude influence would then make the system less efficient since energy is being stored in the capacitor. This reasoning is supported by the decrease in efficiency in Table 4.4.

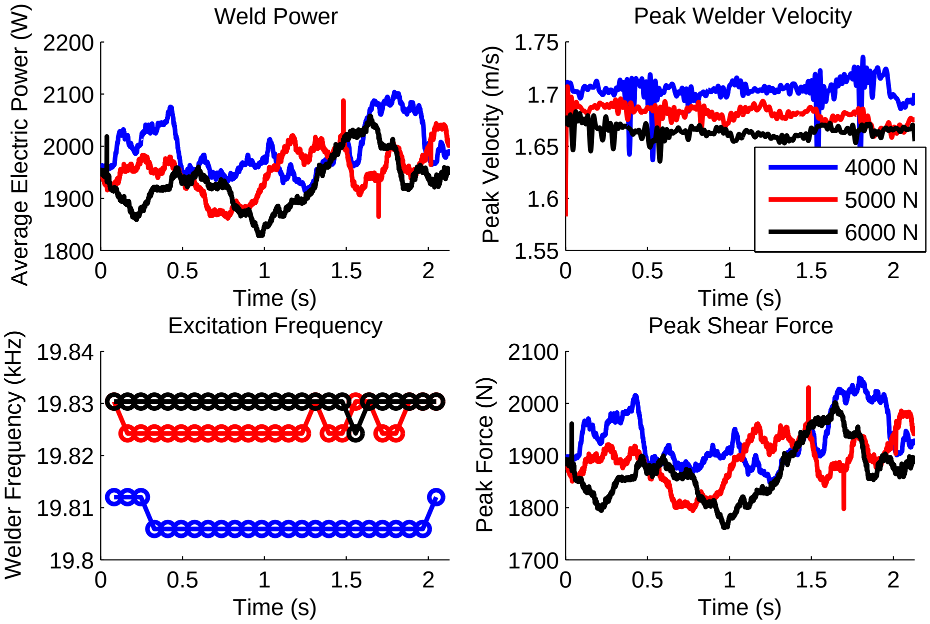

Figure 4.9: Comparison of system dynamics as a function of normal force. Other UAM processing conditions were held constant in this study. In particular, prescribed welder amplitude was 60% (32.5μm), linear weld speed was 5 m/min (200 in/min), and welds were made at room temperature.

	4000 N	**5000 N**	**6000 N**
Mean	82.48	81.34	80.56
Std. Dev.	0.60	0.36	0.36

Table 4.4: Welder efficiency comparison as a function of normal force.

The last UAM processing variable to evaluate is linear weld speed or how quickly the sonotrode rolls along the surface of the UAM build during construction. Results for the speed levels of 3.75 (150), 5.00 (200), and 6.25 m/min (250 in/min) are shown in Figure 4.10 and Table 4.5. These weld speed levels have little to no influence on welder performance or efficiency. This observation corroborates other 9 kW UAM experimentation [92] and energy transfer models [39] because slower weld speeds were found to linearly improve bond quality. In other words, the imparted energy to the weld interface, and ultimately bond quality, is linear with speed because imparted mechanical power is not a function of welder speed within the investigated speed range.

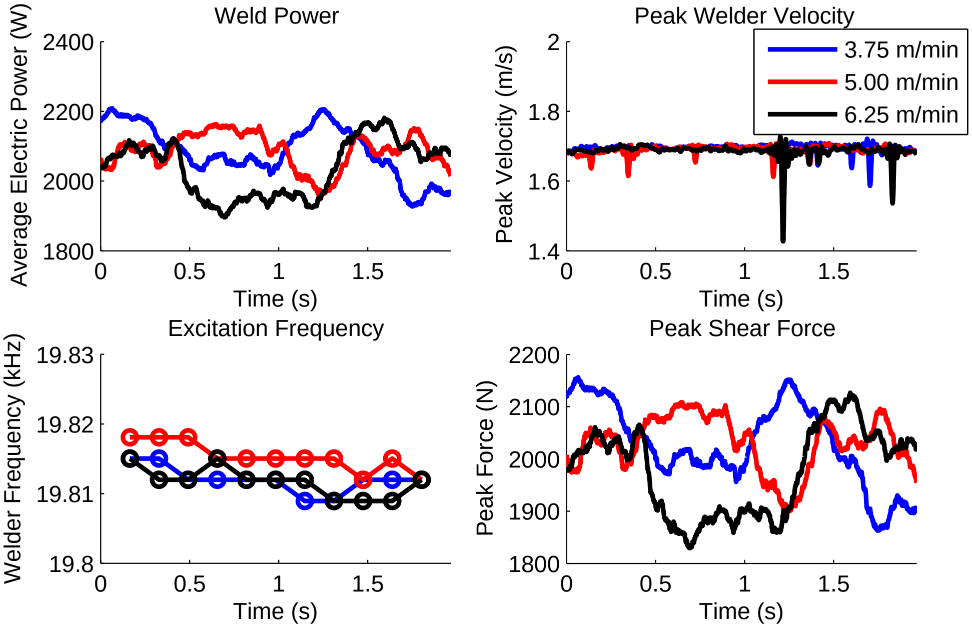

Figure 4.10: Comparison of system dynamics as a function of weld speed. Other UAM processing conditions were held constant in this study. In particular, prescribed welder amplitude was 60% (32.5μm), normal force was 5000 N, and welds were made at room temperature.

	3.5 m/min	**5 m/min**	**6.5 m/min**
Mean	82.40	82.14	81.81
Std. Dev.	0.61	0.62	1.10

Table 4.5: Welder efficiency comparison as a function of weld speed.

4.5 Summary

This chapter utilizes the new linear time invariant model presented in Chapter 3 to estimate welder shear force and welder efficiency. Due to the model construct, shear force magnitude at the 20 kHz resonance can be estimated. This magnitude is near 2000 N for welding Al 6061-H18 foil onto an aluminum baseplate with optimized welding parameters. Welder efficiency was found to be near 80%. Welder efficiency was also found to be reasonably consistent with the use of different weld parameters. This efficiency result implies that the UAM user can estimate welder shear force from average electric power if the welder amplitude is known. Further, if the user has an estimate for shear force, this shear force magnitude can be used for design purposes, i.e., sonotrode, weld fixtures, etc., and for advanced modeling, i.e., FEM analysis, weld evolution, etc.

This model was also used to evaluate high frequency harmonics in the velocity spectrum of the welder. It was determined that these high frequency harmonics originate in the shear force signal, and the shear force signal has square wave character. To fully understand the shear force profile on the welder, in-situ welder current and voltage signals are required. By measuring time dependent system inputs and outputs and with knowledge of the transfer path behavior of the system, the shear force profile can be deconvolved. The full shear force profile can be used to evaluate foil deformation and sonotrode slip in UAM.

Chapter 5

INFLUENCE OF DISSIMILAR MATERIALS ON UAM

5.1 Introduction

This chapter evaluates the influence of dissimilar metal foils and baseplate materials on the UAM process. In particular, it is of interest to understand the connection between material properties and the resultant impact on welder performance, i.e., welder power consumption and amplitude. This work aids in the understanding and development of relationships for new material combinations and weld metals. These relationships are required because dissimilar material welding in UAM is not well understood. Consequently, weld procedures for different weld metals and their respective combinations have been based solely on costly time and material weld pilot studies.

Three different weld foils with significantly different strengths were welded together in this study. These foils were annealed 4130 steel, Al 6061-T6, and annealed 110 Cu. Instead of the weld foil strength impacting the process, it was found that the elastic compliance had the largest effect. Further, it was found that the baseplate and vacuum chuck compliance also influence the welder in addition to the UAM build iteslf when all other processing variables were held constant. An equivalent circuit is given to describe the connection between component compliances and observed trends. Finite element modeling in COMSOL was carried out to qualitatively and quantitatively confirm observed trends by linearly correlating estimated system elastic stiffness with measured power draw. This chapter is planned to be submitted to the *Journal of Materials Processing Technology.*

5.2 Dissimilar Metal Welding Evaluation

5.2.1 Weld Foils

The influence of weld foil properties on UAM were studied by welding annealed 4130 steel, annealed 110 copper, and aluminum 6061-T6 weld foils onto an aluminum baseplate with the same prescribed welder amplitude and normal force. These foils were chosen because they have substantial differences in their mechanical strength and they demonstrate compatibility with the UAM process. Mechanical properties of the foils were measured using a load frame with a digital image correlation (DIC) system. Stress-strain curves for these weld foils along with Al 6061-H18 are shown in Figure 5.1. Table 5.1 summarizes the strength, stiffness, and elongation of each foil. These foils are 2.54 cm (1.00 in) wide and 152 μm (0.006 in) thick.

Al 6061-H18 and annealed 110 Cu are commonly utilized weld foils in UAM whereas Al 6061-T6 requires additional processing. To obtain Al 6061-T6, a roll of Al 6061-H18 was heat treated to the T6 condition through homogenization, water quench, and then precipitate growth [2]. This material was heat treated with the help of Fabrisonic LLC and Thermo-Fusion, an external aluminum heat treatment vendor. Manual abrassive sanding was used to remove the oxide scale from the foil after heat treatment. Annealed 4130 steel foil was obtained by P. Wolcott [94] through custom ordering and subsequent annealing heat treatment.

Table 5.1: Stress-strain property summary of foils.

	Al 6061 H18	Annealed 4130 St	110 Cu	Al 6061 T6
Elastic Modulus (GPa)	71.2	206	106	67.3
Yield Strength (MPa)	237	375.1	107.2	287.8
Ultimate Strength (MPa)	245.7	566.9	227.9	333
Elongation (%)	2.8	37.3	25.2	6.9

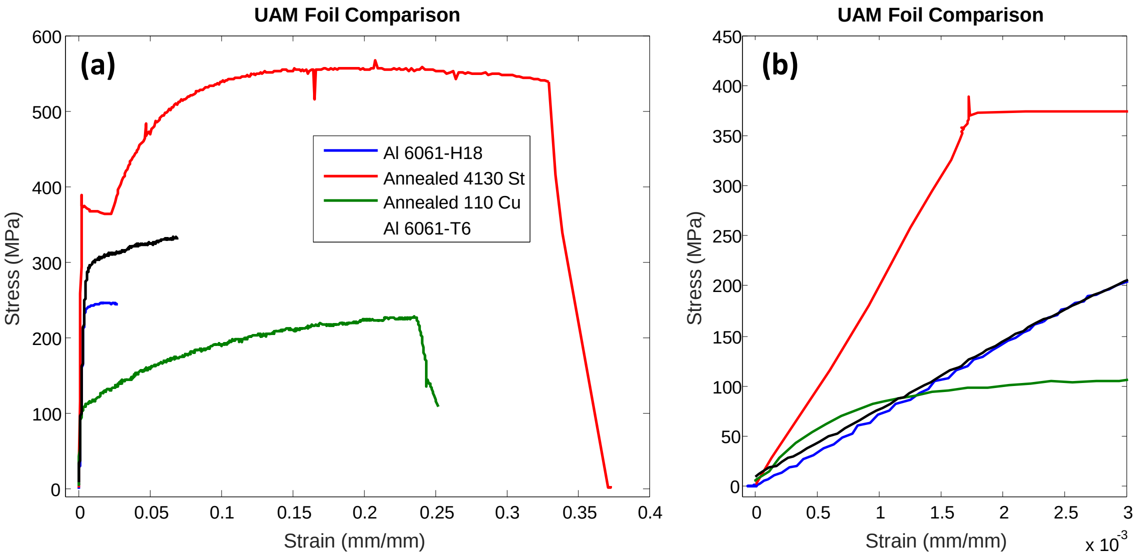

Figure 5.1: Weld foil stress-strain curves collected using DIC: (a) full stress-strain; (b) linear elastic region. Data courtesy of M. Scheidt and B. Losey.

Welder parameters for the foils are shown in Table 5.2. Parameters which are held constant for all foils are the normal force and welder amplitude due to these parameters influencing the welder shear force, see Chapter 4. Welder speed and baseplate temperature were changed for the steel foil due to enhanced energy input requirements for bonding [94]. Prior to welding foils, the baseplate was textured with 22μm of prescribed motion. Welded foils are shown in Figure 5.2. Two foils of each type were welded together onto an Al 6061-T6 baseplate. Cross sections of these welds are shown in Figure 5.3-5.4. It is shown that little to no void presence is observed in the micrographs. Foils also exhibited good qualitative bond characteristics because welds resisted delamination when hand tugging the foil ends.

Table 5.2: UAM welder parameters for welding dissimilar foil.

	Al 6061 T6	110 Cu	Annealed 4130 St
P-P Welder Amplitude (m)	37.5	37.5	37.5
Down Force (N)	6000	6000	6000
Welder Travel Speed (m/min)	2.54	2.54	1.27
Baseplate Temperature (^oC)	93.3	93.3	148.9

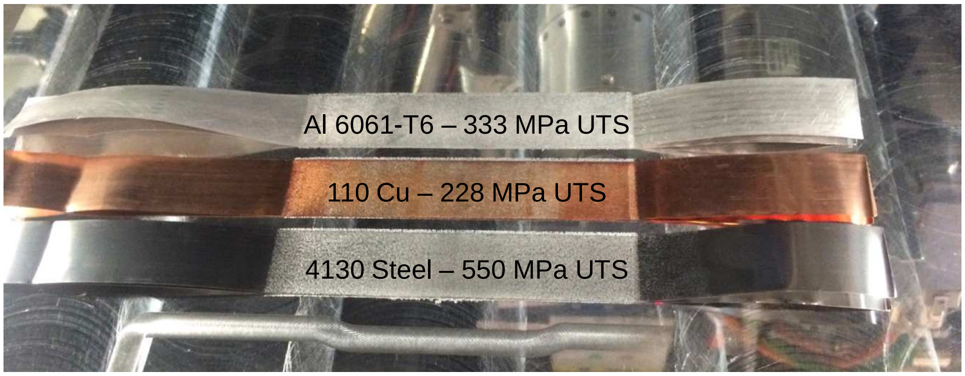

Figure 5.2: Welded foils along with ultimate tensile strength (UTS) for reference. Two layers of each foil were welded respectively.

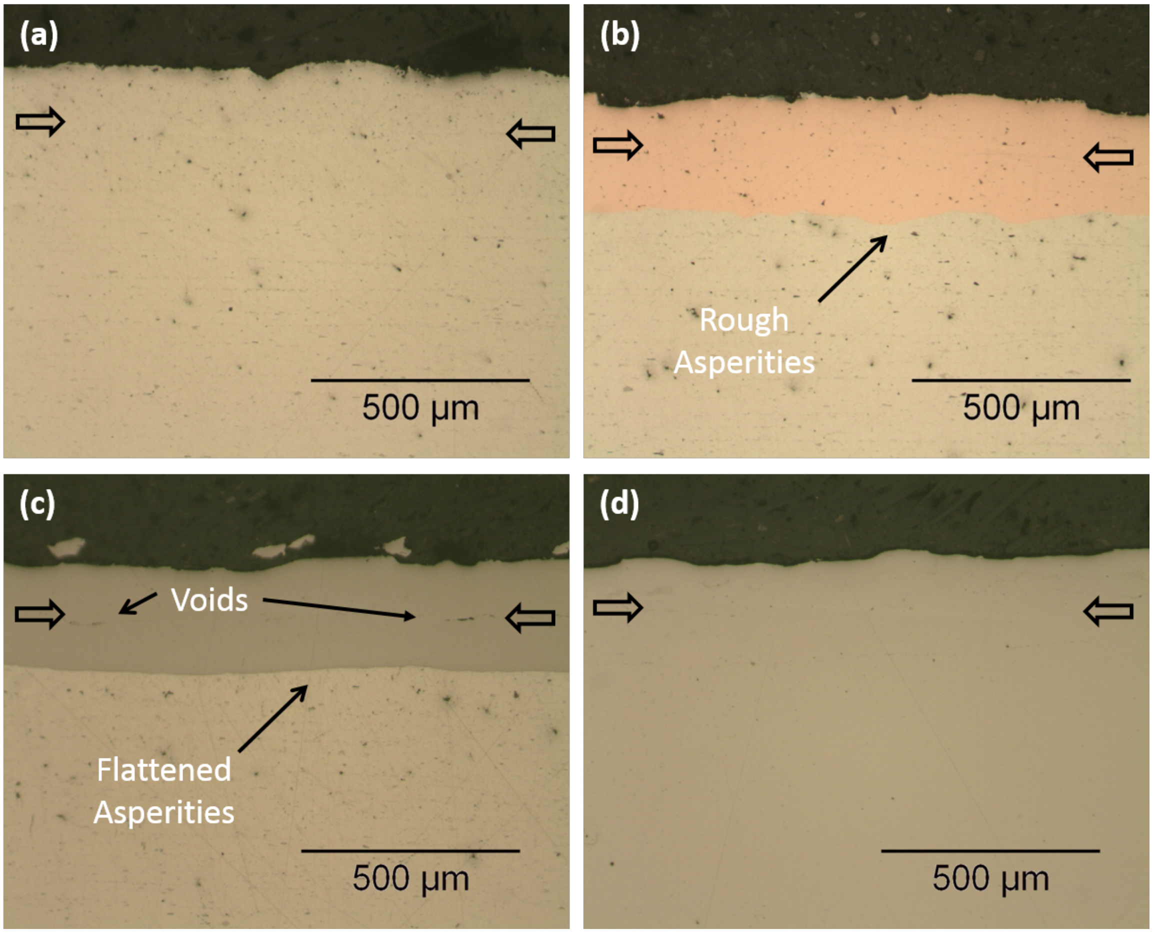
(a)
500 µm
(b)
Rough Asperities
500 µm
(c)
Voids
Flattened Asperities
500 µm
(d)
500 µm

Figure 5.3: Micrograph comparison of two layers of foil onto a baseplate: (a) Al 6061-T6 onto Al 6061 T6; (b) 110 Cu onto Al 6061-T6; (c) 4130 steel onto Al 6061-T6; (d) 4130 steel onto 4130 steel. The hardness (strength) mis-match of the foils onto the baseplate influences the shear behavior of the asperities. Some voids are present in the steel-steel weld on the Al baseplate in (c). Approximate weld interface locations are marked with arrows.

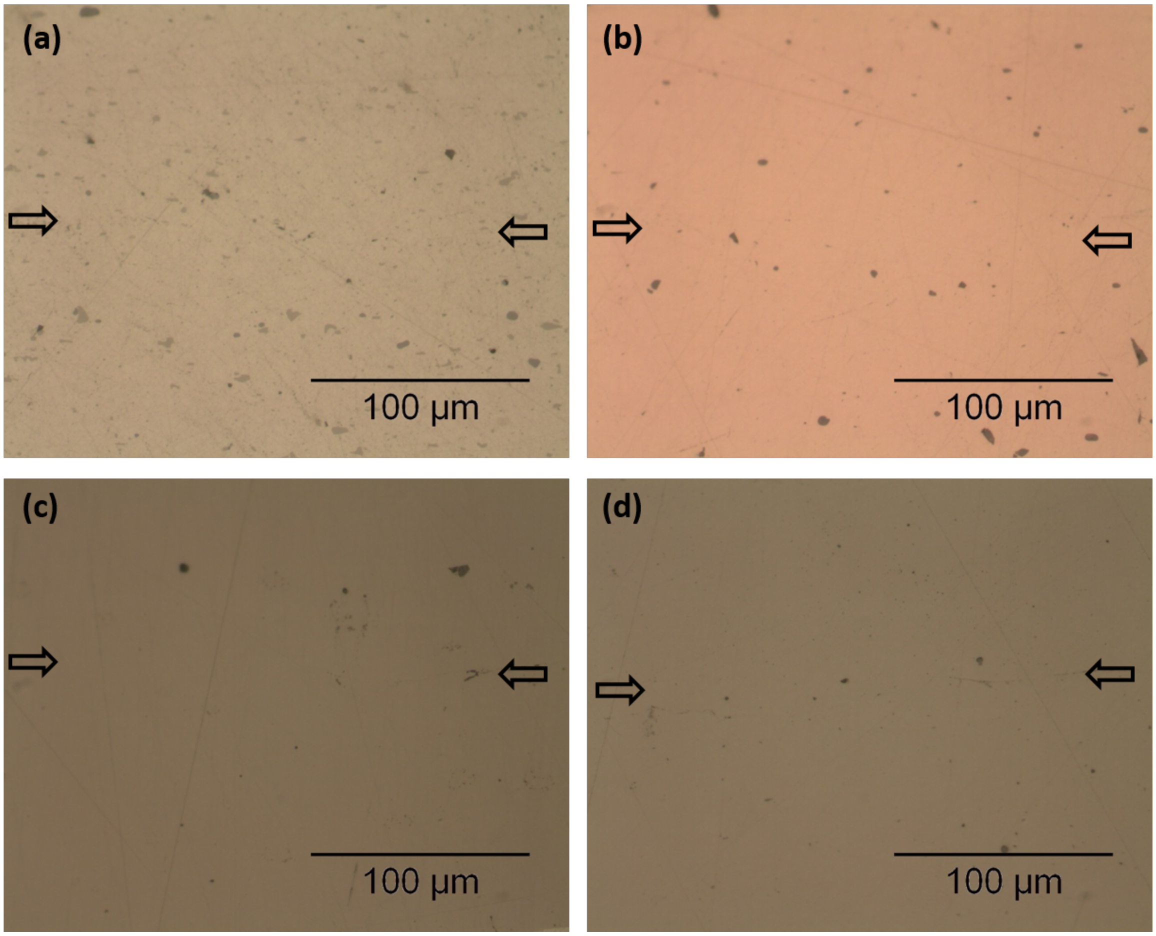

Figure 5.4: Weld interface examination: (a) Al 6061-T6 onto Al 6061 T6; (b) 110 Cu onto Al 6061-T6; (c) 4130 steel onto Al 6061-T6; (d) 4130 steel onto 4130 steel. Approximate weld interface locations are marked with arrows.

To understand the impact of the weld foil type on the UAM process, in-situ welder velocity and average electric power measurements were made during welding. Prior to welding, the welder was calibrated to the LTI model presented in Chapter 4. This calibration was done so welder shear force could be calculated directly from the model. Results are shown in Figure 5.5 for the average electric weld power, welder velocity, calculated welder frequency, and calculated shear force. Foil results are compared against the welder operating under no load in air, i.e., no welding. Welder frequency was calculated using a windowed short time Fourier transform (see Chapter 4).

For the foil data in Figure 5.5, the average electric power draw, welder velocity, welder frequency, and welder shear force are indistinguishable from one another. There is a difference when compared to actuating the welder under no load, yet this is consistent with earlier work (see Chapter 4). The result similarity in Figure 5.5 is somewhat unexpected due to the large mis-match in foil strength. The welder power is also uncharacteristically low when compared to welding 4130 foil tape onto a 4130 baseplate [94]. As a result, 4130 foil was welded onto a 4130 baseplate for comparison using the same weld parameters listed in Table 5.2 for steel. Surface finsh and weld performance data between the two baseplates are compared in Figure 5.6 and Figure 5.7, respectively.

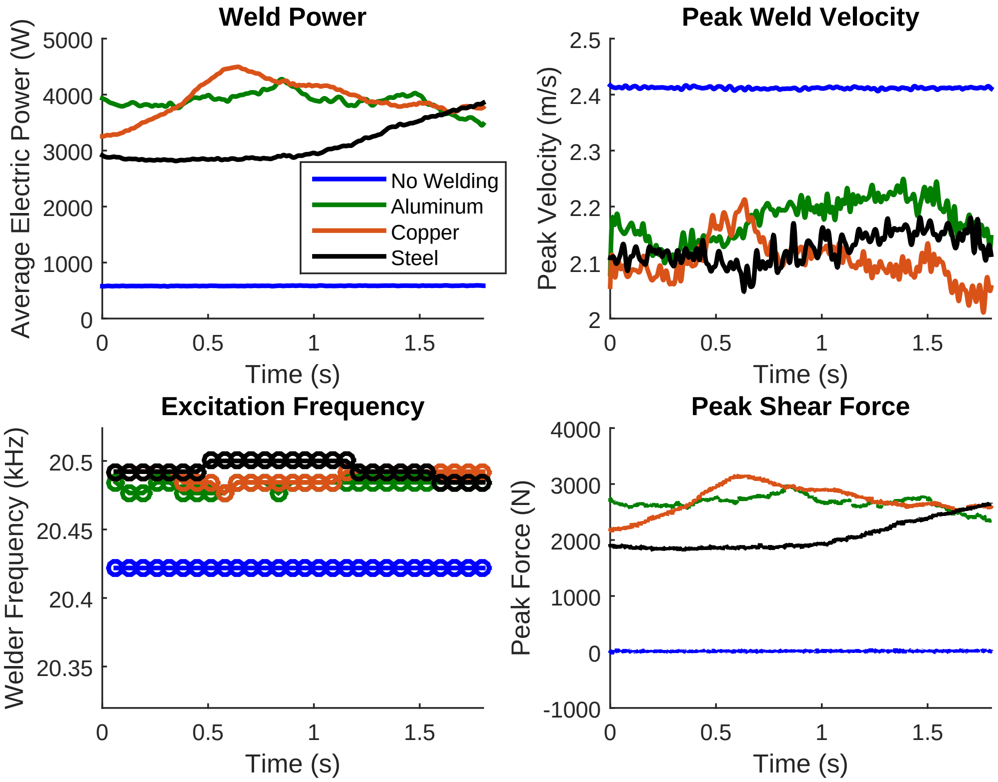

Figure 5.5: Welding different weld foils onto an Al 6061-T6 baseplate. The influence of weld foil properties has little to no influence on the UAM process.

The surface finishes of the two steel foils are qualitatively different in Figure 5.6. For the steel baseplate, a brown color appears after welding. On the other hand, no noticeable surface finish color change occurs for the aluminum baseplate welds. The surface finish color change in steel welding has been observed previously [94], and it has been linked to localized heat generation from sonotrode slip in UAM. Further, surface finish color change for steel welding is linked to improved bonds due to tape stick occurring more quickly and not moving with the sonotrode. Consequently, it can be inferred that the welds on the steel baseplate are stronger than the welds on the aluminum baseplate.

This strength improvement in the steel bond when welded onto a steel baseplate is supported by the microscope images in Figure 5.3(c)-(d). In particular, voids are observed for the aluminum baseplate and not observed for the steel baseplate. In addition to qualitative evidence, the effort or power consumption of the welder increases substantially for the steel baseplate case, see Figure 5.7. This rise in power consumption implies a higher shear force, which leads to enhanced strain energy input into the weld. The power profile is also more consistent for the steel baseplate case, which is linked to more uniform and consistent bonding during welding.

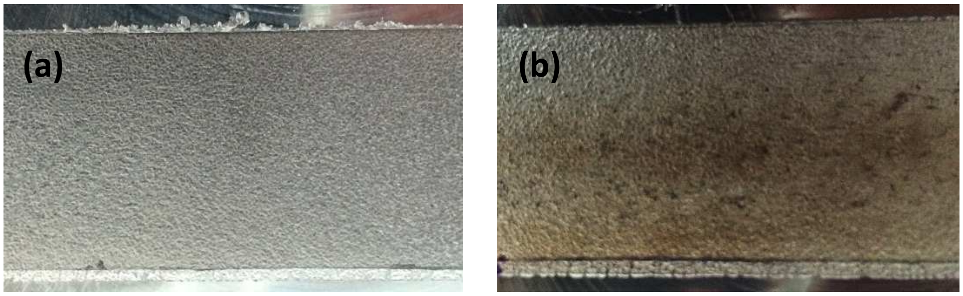

Figure 5.6: Qualitative surface difference between welding steel on different baseplates: (a) Al 6061-T6, 9.53 mm (0.375 in) thick; (b) Annealed 4130 St, 3.18 mm (0.125 in.) thick. The steel baseplate weld develops a brown surface finish due to enhanced slipping from improved bonding.

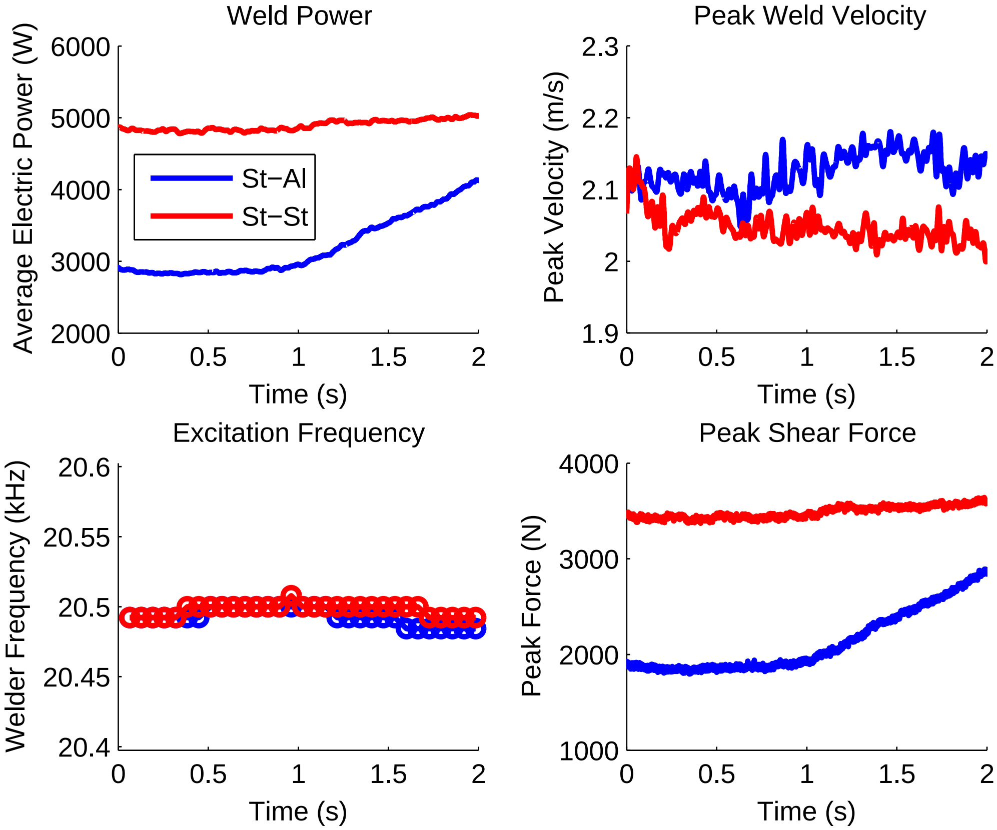

Figure 5.7: Welder behavior for welding steel on different baseplates: (a) Al 6061-T6, 9.53 mm (0.375 in) thick; (b) Annealed 4130 St, 3.18 mm (0.125 in.) thick. The steel baseplate weld required enhanced power effort to achieve the prescribed motion.

5.2.2 Baseplates

The baseplate material in the previous section was found to influence steel foil welding onto a previously laid steel foil. In particular, the baseplate material influenced the weld quality and the effort or power draw required by the welder to achieve the prescribed welder motion. To more rigorously evaluate this observation, Al 6061-H18 weld foil was welded onto a 9.53 mm (0.375 in) thick Al 6061-T6 baseplate and onto a 3.18 mm (0.125 in.) thick 4130 steel baseplate in the annealed condition. These baseplate thicknesses were chosen because they have the same mass. The importance of using the same baseplate mass will be explained in

Table 5.3: UAM welder parameters for welding Al 6061-H18 foil onto aluminum and steel baseplates.

P-P Welder Amplitude (m)	22.0
Down Force (N)	6000
Welder Travel Speed (m/min)	2.54
Baseplate Temperature (^oC)	93.3

more detail later. Al 6061-H18 weld foil was used for evaluation of baseplate effects because multiple weld layers can be achieved without weld nuggets or tape stick to the sonotrode. The welder parameters used for welding are listed in Table 5.3. These parameters were inspired by previous Al 6061-H18 welding onto steel work by Wolcott [94]. Note that the welder amplitude is about 10 μm lower when compared to typical welding of Al 6061-H18 foil. Prior to welding, the baseplates were textured with the same parameters as listed in Table 5.3.

Figure 5.8 compares data when welding aluminum foil onto an aluminum baseplate and onto a steel baseplate. Both data sets are from the second weld layer. It is shown that the welder frequency and velocity or amplitude is near identical for both baseplates. On the other hand, the electric power draw magnitude differs near a factor of two. This power magnitude difference implies a similar magnitude difference in the shear force.

Figure 5.9 illustrates how welder velocity and power consumption change with additional weld layers. Welder velocity continues to remain constant in Figure 5.9(b) similar to Figure 5.8, yet the welder power for each baseplate follows a different trend with increasing weld layers. It is shown in Figure 5.9(a) that the average electric power decreases more quickly for the steel baseplate than the aluminum baseplate.

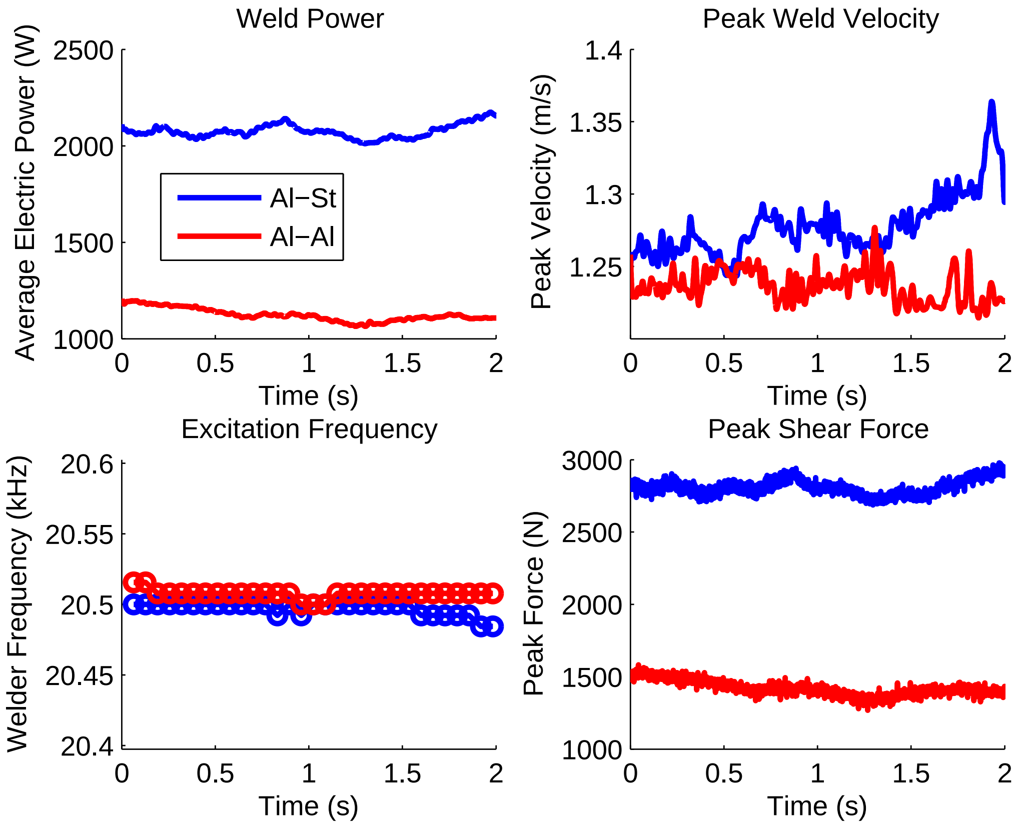

Figure 5.8: Welder behavior for welding Al 6061-H18 on different baseplates: (a) Annealed 4130 St, 3.18 mm (0.125 in.) thick; (b) Al 6061-T6, 9.53 mm (0.375 in) thick. The steel baseplate weld required enhanced power effort to achieve the prescribed motion.

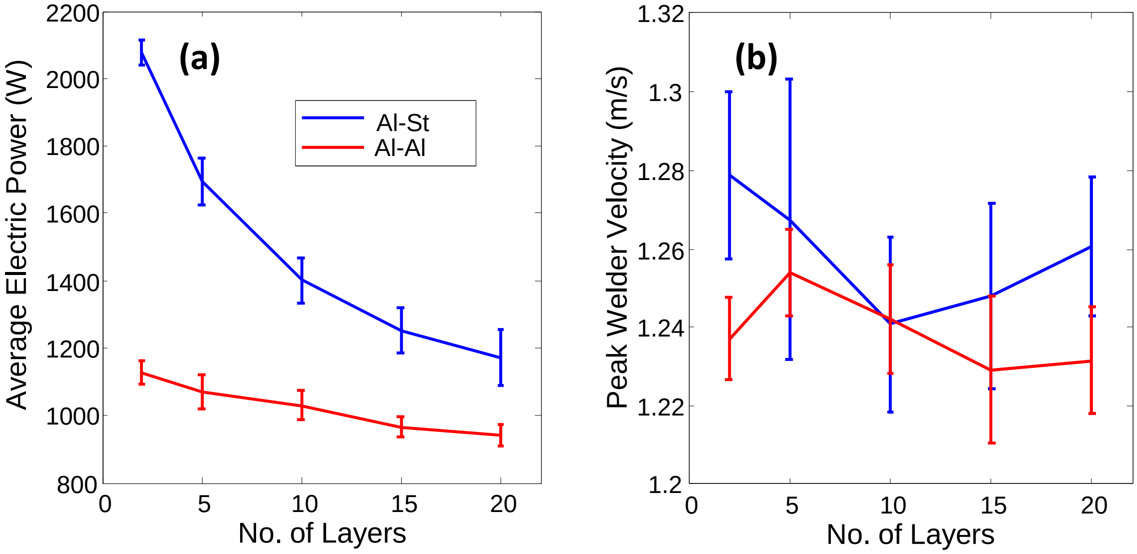

Figure 5.9: Evaluation of accumulative baseplate stiffness interaction with the UAM process: (a) total average electric power draw; (b) peak welder velocity. The aluminum baseplate is 9.53 mm (0.375 in) thick while the steel is 3.18 mm (0.125 in.) thick. Both baseplates have similar masses.

Like the steel welds, cross sectioning was carried out to compare the consolidation quality for the aluminum welds on the two baseplates, see Figure 5.10. The aluminum baseplate welds have a higher density of voids than the steel baseplate. Like the steel foil comparison earlier in Figure 5.3, higher void density occurs due to the difference in welder shear force. This enhanced shear force not only improves consolidation quality but also improves bond quality. Woloctt [94] found that Al 6061-H18 welded onto annlead 4130 steel produced very strong welds with similar weld parameters used in this study. Another difference between the two microscope images in Figure 5.10 is the baseplate asperity collapse. The steel asperities do not collapse and flatten as much as the Al 6061-T6 asperities because the steel is significantly stronger than the aluminum foil, see Table 5.1.

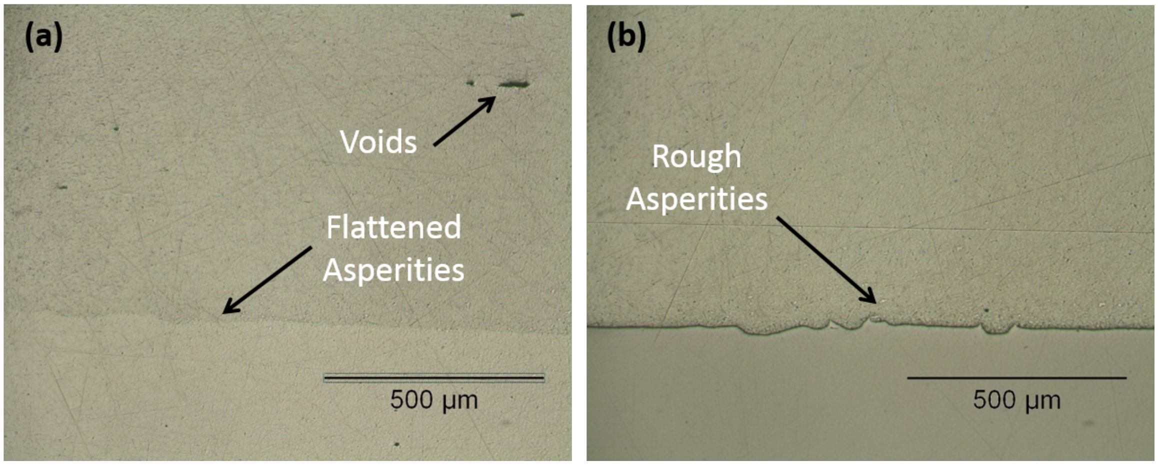

Figure 5.10: Imaging of Al 6061-H18 stack onto baseplates: (a) Al 6061-T6; (b) Annealed 4130 steel.

Figure 5.11 is a magnified microscope image of the steel asperity collapse. Large deformation and mixing is observed in one asperity while cracking is seen in another. Large deformation of the asperity is expected due to annealed 4130 steel elongating near 40% before breaking. Ultrasonic softening effects would also enhance ductility (see Chapter 2). Cracking is also expected due to interface deformations being on the order of 100% strain combined with work hardening from both the texture and welding passes.

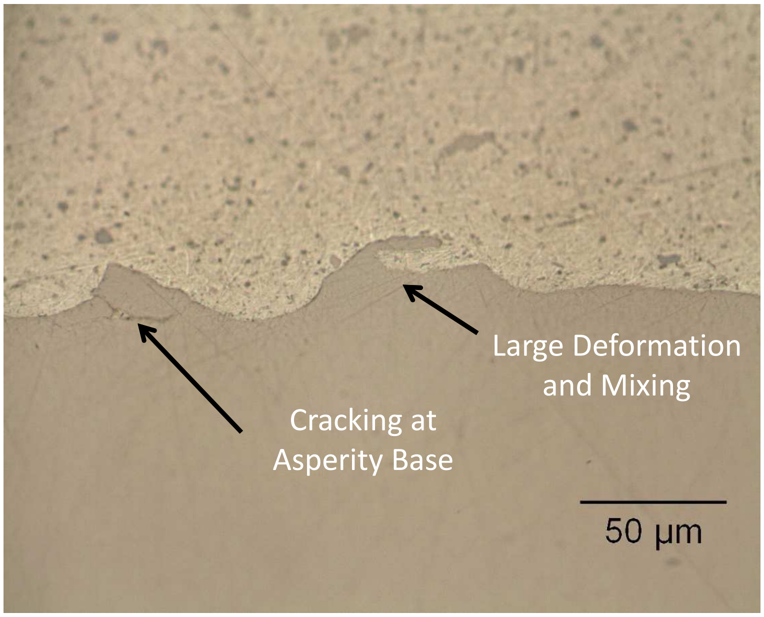

Figure 5.11: Steel asperity deformation when joining Al 6061-H18. Large asperity deformation and cracking is observed. Large deformation is possible due to the high ductility of the steel. Cracking may occur due to work hardening during the texture and welding pass.

5.3 Modeling

The foil and baseplate materials used in UAM differ in how they influence the process, i.e., welder power consumption. To understand these differences, the effective system stiffness must be considered. Figure 5.12(a) illustrates why system stiffness impacts the UAM process and what components contribute to the total system stiffness. It is shown that the UAM stack, the baseplate near the stack, and the vacuum chuck contribute to the system in addition to the UAM tape. The influence of stack stiffness on UAM has been considered prior, see Chapter 2. Figure 5.12(b) is an equivalent circuit of these components. Mass terms for the stack and baseplate are not given because the first mode of vibration for the stack in shear is assumed to be far above the 20 kHz excitation frequency. The vacuum chuck is modeled as a constant impedance term (Z_{chuck}) equal to 2 GN/m near 20 kHz. The measurement and estimation of this term will be described in the next section using modal hammer testing.

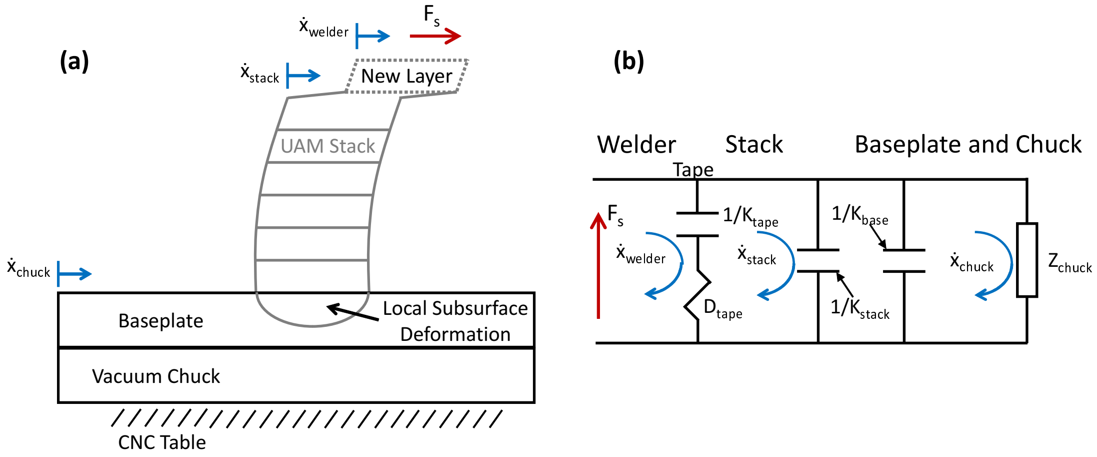
(a)
ẋwelder
Fs
ẋstack
New Layer
UAM Stack
ẋchuck
Baseplate
Local Subsurface Deformation
Vacuum Chuck
CNC Table
(b)
Welder
Stack
Baseplate and Chuck
Tape
Fs
1/Ktape
1/Kbase
ẋwelder
ẋstack
ẋchuck
Zchuck
Dtape
1/Kstack

Figure 5.12: UAM stack and system dynamics: (a) schematic illustration of system with key inputs and outputs; (b) equivalent circuit of system.

The equivalent circuit in Figure 5.12 describes the system as a summation of springs in series,

$$\frac{1}{K_{system}} = \frac{1}{K_{stack}} + \frac{1}{K_{base}} + \frac{1}{Z_{chuck}}, \tag{5.1}$$

where K_{system} is the effective system stiffness. To estimate the stiffness of the stack and baseplate together, finite element modeling (FEM) in COMSOL Multiphysics was done,

$$\frac{1}{K_{system}} = \frac{1}{K_{FEM}} + \frac{1}{Z_{chuck}}, \tag{5.2}$$

where K_{FEM} is the stiffness estimate for the stack and baseplate. The FEM for the stack and baseplate is shown in Figure 5.13. Figure 5.13 describes the contact surface and components of the model. The contact surface is where the loads of the process are applied and transverse deformation measured. Stiffness is estimated by dividing the transverse applied load (2000 N) by the average transverse deformation of the contact surface. Figure 5.13 is the transverse deformation or deformation in the y-direction from the applied loads. This transverse deformation is exported from the top of the surface and used for estimating stiffness.

The contact surface width was estimated to be between 0.90-2.54 mm (0.035-0.1 in) using elastic Hertzian contact theory [10] and empirical evidence from the end of the weld, respectively. The true contact area lies between these two extremes. The baseplate and stack components in this FEM can be modeled with different thicknesses and materials. The built-in materials within COMSOL of Copper, Al 6063-T83, and 4340 steel were used for simulation purposes. Although the alloying elements of these virtual materials differ from experiment, the linear elastic properties are identical. Because mass is not considered, the system is assumed to be static for modeling purposes.

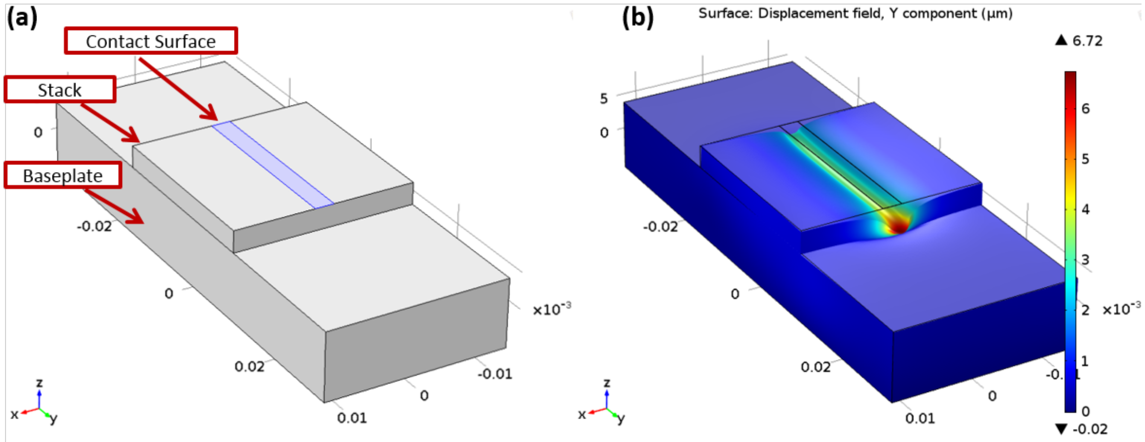
(a)
Contact Surface
Stack
Baseplate
0
-0.02
0
0.02
0.01
0
-0.01
×10⁻³
z
x
y
(b)
Surface: Displacement field, Y component (µm)
▲ 6.72
6
5
4
3
2
1
0
▼ -0.02
×10⁻³
5
0
-0.02
0
0.02
0.01
0
z
x
y

Figure 5.13: FEM of stack and baseplate: (a) contact surface used for loads and analysis; (b) transverse displacement of stack (y-direction).

A representative photo of the graded mesh density of the FEM is shown in Figure 5.14. The inset illustrates how the mesh becomes more fine around the contact surface. The first shear mode of vibration is shown in Figure 5.15. This result was found using the Eigenfrequency solver within COMSOL. The Eigenfrequency or resonant frequency is near 60 kHz and far above the excitation frequency of 20 kHz, similar to the result of Gibert [26]. As a result, the assumption of not incorporating mass in the modeling is valid because the dynamics of the stack are primarily influenced by the static stiffness at 20 kHz.

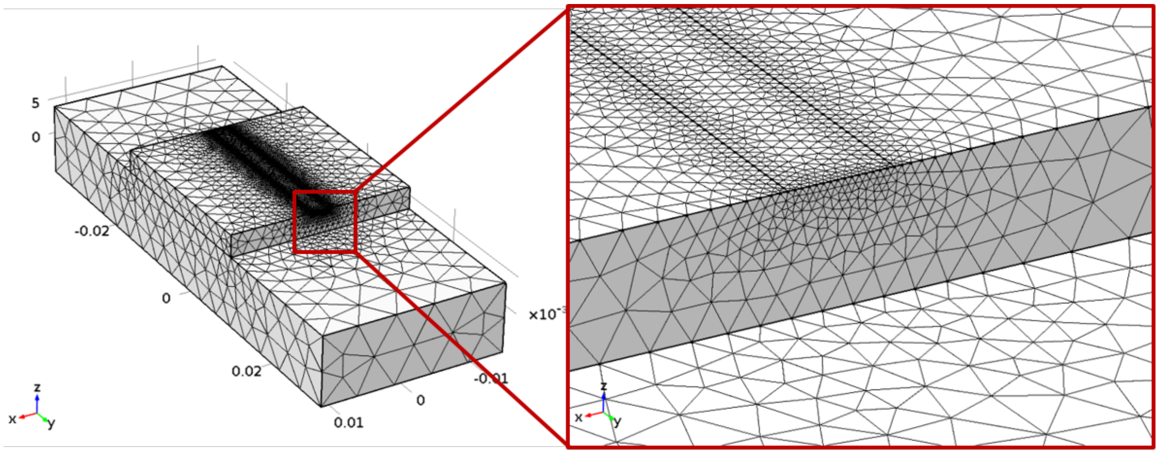

Figure 5.14: Mesh density of FEM. A graded mesh was utilized near the contact surface to accurately describe the deformation behavior of the stack.

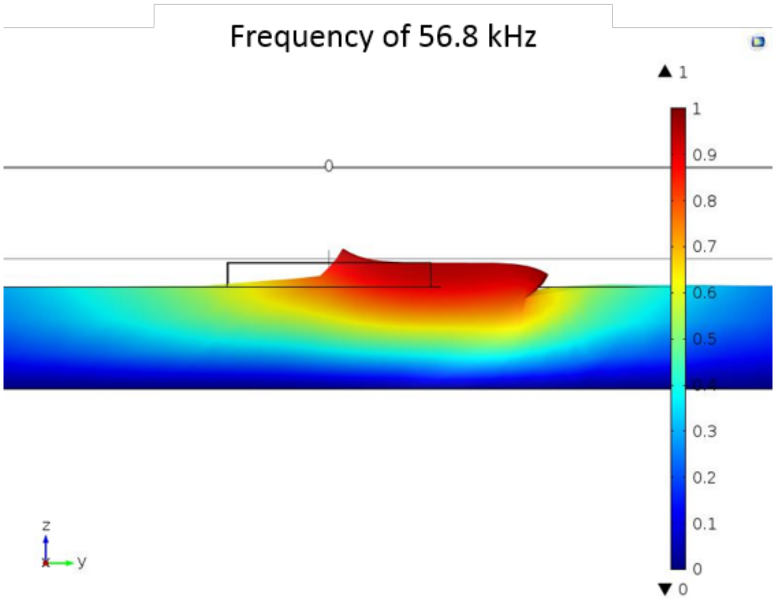

Figure 5.15: First mode of vibration of stack in shear is near 60 kHz, which is far above the 20 kHz excitation frequency.

The system stiffness for two layers of aluminum, copper, and steel weld foils on a 9.53

mm (0.375 in) thick aluminum baseplate are summarized in Table 5.4. Values for the contact widths of 0.9 and 2.54 mm are both given for a low and high stiffness estimate, respectively. System stiffness was calculated assuming the FEM and vacuum chuck are springs in series (5.2). The values in the table support the power draw results in Figure 5.5 because the stiffness values show small difference between the aluminum and steel foils (near 24% max). This small difference in stiffness causes the welder to use similar shear force magnitudes or average electric power to achieve the prescribed welder motion.

Table 5.4: Influence of weld foil on effective system stiffness. Stiffer weld foils do stiffen the overall system, yet the change is small for the two contact width bounds of 0.9 ($K_{FEM,L}$) and 2.54 mm ($K_{FEM,H}$). All units in (MN/m).

Material	K_{chuck}	$K_{FEM,L}$	$K_{system,L}$	$K_{FEM,H}$	$K_{system,H}$
Aluminum	2000	577	448	860	601
Copper	2000	657	495	927	633
Steel	2000	790	566	1035	682

Using the same modeling framework, simulations were done with an aluminum stack on an aluminum and steel baseplate. These simulations were done to evaluate the observed power decay trends with build height shown originally in Figure 5.9. These trends are shown again for completeness in Figure 5.16(a). Simulation results for a 0.9 mm (0.035 in) contact width are shown in Figure 5.16(b). Strong qualitative correlation exists between the two plots. Similar correlation occurs with the 2.54 mm (0.1 in) contact width too. These results are not shown for brevity.

The results in Figure 5.16 are plotted against each other in Figure 5.17 to evaluate their quantitative correlation. Both baseplates exhibit a strong linear trend between measured power draw and estimated transverse elastic stiffness. Further, both trend lines have near identical slopes of 2.70 and 2.78 W-m/MN for the aluminum and steel baseplates, respectively. If the 2.54 mm (0.1 in) contact width is used, the slopes become 1.56 and 1.92

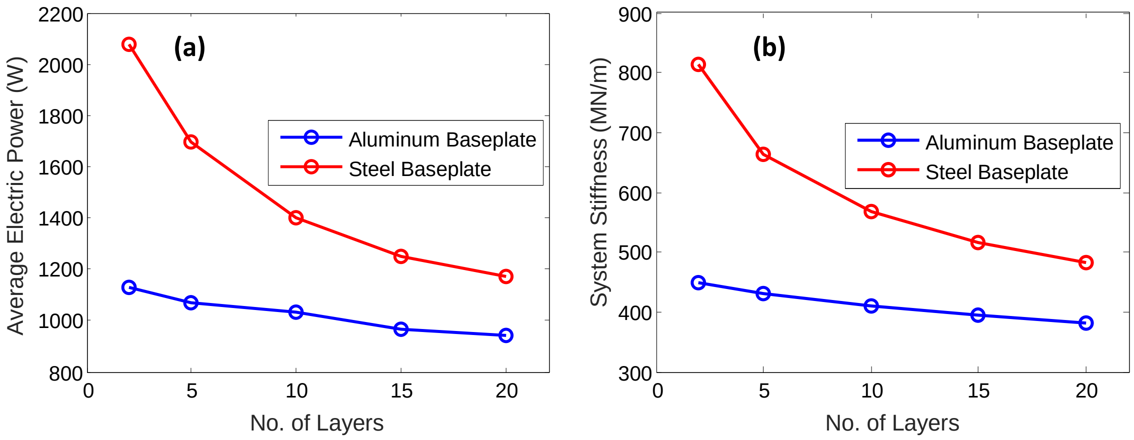

Figure 5.16: Qualitative comparison of measurement and simulation: (a) measured average electric power; (b) calculated effective stiffness assuming elastic deformation solely and 0.9 mm contact width. Both trends are similar in qualitative behavior.

W-m/MN. The slope decreases for the wider contact width due to enhanced stiffness.

The linear trend correlation between measured power and estimated elastic stiffness is expected due to welder effort or power being related to the system stiffness. This trend can be quantitatively evaluated with a power balance between the electrical power input of the welder and mechanical power output,

$$P_{e,avg} = \frac{1}{\eta} P_{m,avg}, \tag{5.3}$$

where η is the efficiency between output mechanical power ($P_{m,avg}$) and input electrical power ($P_{e,avg}$). Efficiency is near 80% in UAM, see Chapter 4. If one assumes sinusodial behavior of the system at 20 kHz, mechanical power can be put in terms of welder velocity ($\dot{x}_{welder}$) and shear force (F_s),

$$P_{e,avg} = \frac{1}{\eta}\frac{1}{2} F_s \dot{x}_{welder}. \tag{5.4}$$

The 1/2 term in the expression (5.4) originates from the definition of average power for sinusoidal functions. Further, the shear force can be replaced with the elastic stiffness

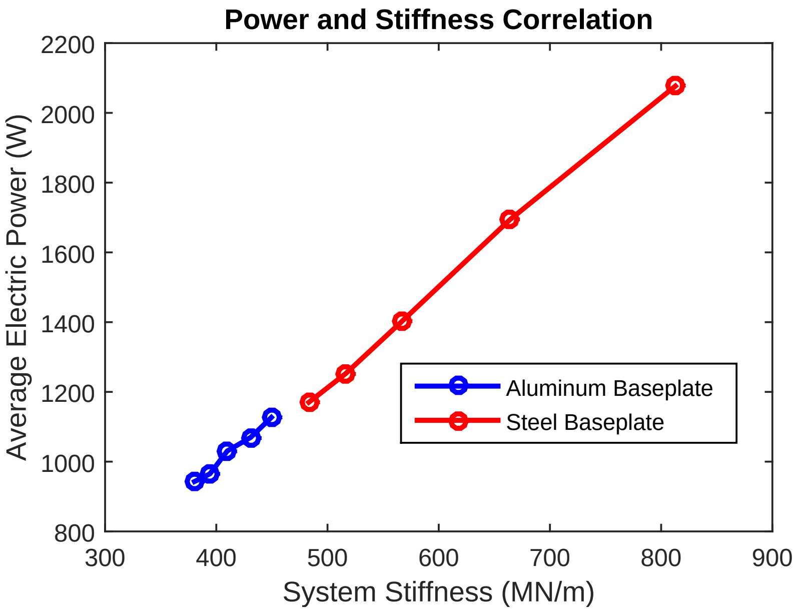

Figure 5.17: Correlation of measured average electric power and estimated stiffness from 0.9 mm contact width. Both data sets show linear trend behavior and similar slopes.

(K_{system}) and deformation (x_{system}) of the system,

$$P_{e,avg} = \frac{1}{\eta}\frac{1}{2}K_{system}x_{system}\dot{x}_{welder}. \tag{5.5}$$

Lastly, the welder velocity can be written in terms of frequency and welder amplitude,

$$P_{e,avg} = \frac{1}{\eta}\frac{1}{2}K_{system}x_{system}x_{welder}\omega. \tag{5.6}$$

This expression (5.6) relates the power draw to the system stiffness. If the welder amplitude is held constant, all the other terms in the expression other than system stiffness become constant. The magnitude of this constant is the linear slope between average electric power draw and system stiffness. System deformation (x_{system}) can be considered a constant because (i) the system is amplitude control based and (ii) slip is not strongly evident in UAM (see Chapter 3). Consequently, it can be assumed that the welder amplitude and system deformation track each other in a linear manner.

To evaluate the proposed correlation (5.6), in-situ vibration measurements were carried out on a UAM stack and baseplate, see Figure 5.18(a). These two coordinates were measured simultaneously to calculate the motion of the stack solely. A Polytec PSV-400 laser vibrometer was utilized to measure the top motion of a 20 layer stack. The side of the stack was trimmed smooth with an end-mill prior to welding to enhance signal quality of the laser and to ensure a 25.4 mm (1 in) stack width. To measure motion of the baseplate and vacuum chuck structure, a high frequency shock accelerometer was used (PCB 350B02). Acceleration was used as the common unit to compare motion, see Figure 5.18(b). Stack acceleration was calculated from the velocity measurement via numerical differentiation. Lowpass filtering was carried out before numerical differentiation to minimize high frequency noise of the measurement. In Figure 5.18(b), the baseplate and vacuum chuck structure moves near 1% of the stack. As a result, it can be assumed that the measured stack motion is equivalent to the true stack motion because the vacuum chuck moves no little in comparison to the stack.

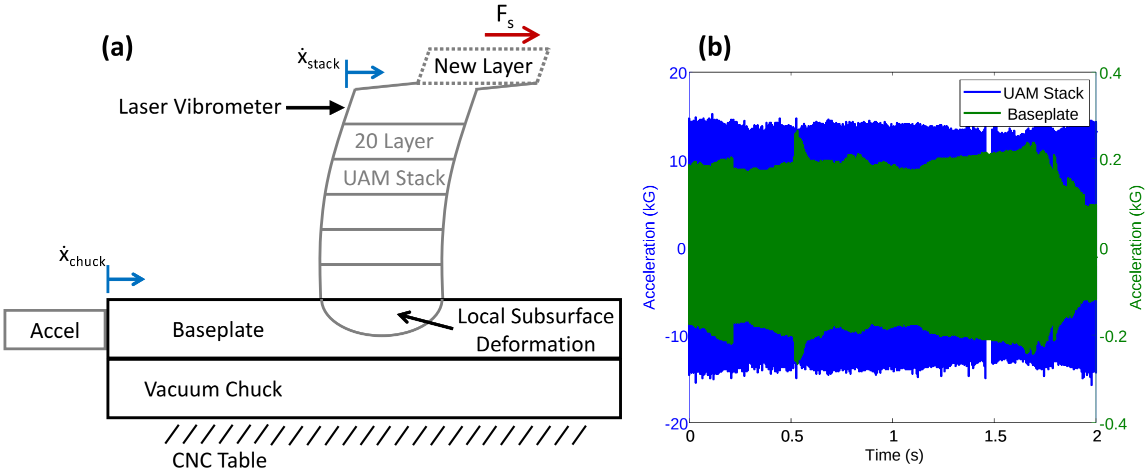

Figure 5.18: UAM stack motion experiment: (a) schematic illustration of experiment; (b) experimental acceleration data for top of UAM stack and side of baseplate.

Using a similar FEM model, lateral displacement or displacement in the y-direction was calculated using a 0.9 mm (0.035 in) contact width. The baseplate here was modeled to be

12.7 mm (0.5 in) thick while the stack was modeled to be 20 layers tall or 3.05 mm (0.12 in). The stack width of 25.4 mm (1.0 in) was also used. Forces were 2000 N in the y-direction and 5000 N in the z-direction. Load magnitudes originate from the LTI model and processing conditions, respectively. Displacement in the y direction for the model and specific surfaces of the model are shown in Figure 5.19. A maximum displacement on the side of the stack is near 9.3 μm while the mean displacement of the stack is about 4.6 μm. This mean displacement is 29% of the prescribed motion of 16 μm peak or 32 μm peak-peak. The mismatch in deformation originates in weld foil shear (see Figure 5.12(b)) and sonotrode slip. To check the accuracy of the model, the stack displacement was calculated using numerical integration. High and low pass filtering were used before integration to minimize low and high frequency noise. The stack motion from the FEM model and experiment are compared in Figure 5.20.

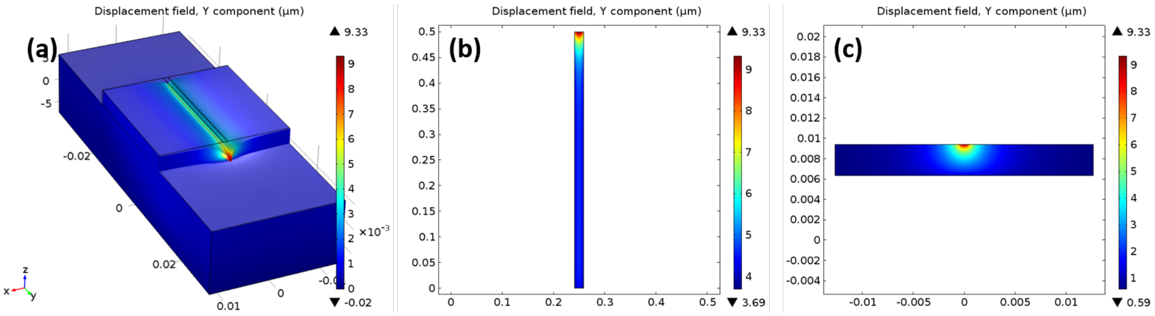

(a)
Displacement field, Y component (µm)
▲ 9.33
▼ -0.02
×10⁻³
(b)
Displacement field, Y component (µm)
▲ 9.33
▼ 3.69
(c)
Displacement field, Y component (µm)
▲ 9.33
▼ 0.59

Figure 5.19: Simulation of UAM stack displacement in lateral or y-direction: (a) isotropic view of model; (b) surface in contact with welder; (c) surface on side of UAM stack, which is visible by laser vibrometer.

The model and experiment comparison in Figure 5.20 demonstrate good correlation. Because the laser is manually positioned near the top of the stack, it is not feasible to measure the maximum displacement, especially since another weld foil is welded onto the stack. Hence, it would be expected that the measurement would be less than the maximum displacement. The close correlation of model and experiment also support LTI modeling efforts. In particular, the close results support the accuracy of the shear force estimate from the LTI model.

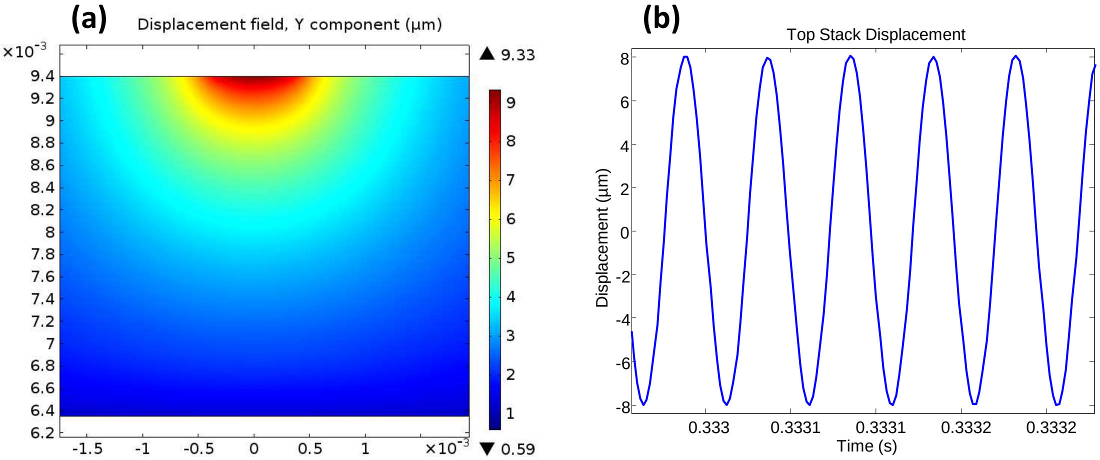

Figure 5.20: UAM stack motion comparison: (a) contour plot of y-displacement of side of UAM stack; (b) experimental displacement for top of UAM stack. Due to the laser measuring near the top of the stack, the peak displacement cannot be feasibly measured and will be less. As a result, the model and experiment show good correlation.

Because the model and experiment demonstrate good correlation, the expression (5.6) relating power draw with system stiffness can be quantitatively evaluated. The variables which are constant (C) can be lumped together to estimate the expected slope value,

$$P_{e,avg} = C \cdot K_{system}, \text{ where } C = \frac{1}{\eta}\frac{1}{2}x_{system}x_{welder}\omega. \tag{5.7}$$

It was shown and described previously that the system motion is a fraction of the total welder motion, i.e., near 29%. Using the estimated shear force values of 1420 and 2800 N in Figure 5.8 and the stiffness estimates of 450 and 813 MN/m in Figure 5.16 for aluminum and steel baseplates, respectively, one can estimate the average stack deformation to be 3.16 and 3.44 μm. Because sonotrode motion is near 10 μm (1.26 m/s) in Figure 5.8 instead of the prescribed 11 μm, the percentage of stack motion to sonotrode motion is closer to 33% instead of 29%. This increase in percentage occurs due to the motion of the sontrode decreasing during welding. Consequently, the expression can be simplified using this motion relation,

$$C = \frac{1}{\eta}\frac{1}{2}\frac{1}{3}x_{welder}^2\omega. \tag{5.8}$$

Using this relation, a value of 2.63 W-m/MN is calculated, which is near the experimental slopes of 2.70 and 2.78 W-m/MN in Figure 5.17. This close correlation implies that power draw can be estimated if the welder amplitude and system stiffness are known. Further, because power magnitude is correlated with consolidation quality and bond quality, this expression can be used to select a welder amplitude for adequate bonding. This correlation allows the UAM user to minimize weld trials and extrapolate welding procedures to different UAM systems or constraint fixtures. Constraint fixtures influence the welding process, and the next section explains how to estimate the constraint impedance or dynamic stiffness.

5.4 Chuck Impedance and Baseplate Slip

Modal testing was carried out on the baseplate/vacuum chuck anvil structure to estimate the mechanical impedance or dynamic stiffness of the structure near 20 kHz. A high frequency impact hammer (PCB 086C80) was used to impart a force (F) onto the structure while two high frequency accelerometers (352A60) were used to measure motion ($\ddot{X}$), see Figure 5.21. Similar to hammer testing in Chapter 3, ten exponentially windowed averages were used to calculate FRFs using the QUATTRO signal analyzer. Accelerometers were used here as opposed to the non-contact laser vibrometer due to the size of the anvil structure being very large. Additionally, concurrent measurements of the baseplate and vacuum chuck structure were desired. To emulate representative operating conditions, a 12.7 mm (0.5 in) thick aluminum baseplate was used and constrained with vacuum.

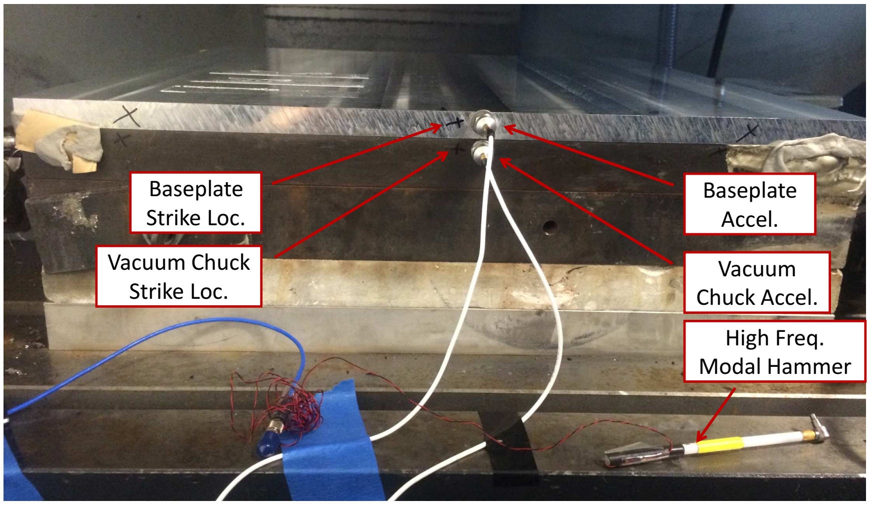

Figure 5.21: Modal hammer testing of baseplate and vacuum chuck anvil structure. This test is used to measure the mechanical impedance of the structure.

Mechanical compliance function (c) results are shown in Figure 5.22 for the driving point measurement of the vacuum chuck, the driving point measurement of the baseplate, and the cross measurements of baseplate to vacuum chuck. The mechanical compliance function is in units of m/N and was calculated by dividing the measured acceleration response by the square of the frequency,

$$c = \frac{\ddot{X}}{F}\frac{1}{\omega^2}. \tag{5.9}$$

Ordinary coherence is shown with the measurement, and it is near 1 for the frequencies of concern, i.e., measurement is consistent. To calculate the impedance or dynamic stiffness (N/m), the mechanical compliance function was inverted, see Figure 5.23.

Both compliance and stiffness magnitudes for the measurement locations are similar near 20 kHz except the baseplate driving point measurement. This difference in magnitude may originate from the strike point being aluminum as opposed to steel, its flexibility being larger due to added height, and because of the flexible coupling between the chuck and baseplate. For modeling purposes in the previous section, a stiffness of 2 GN/m was utilized and shown to produce excellent results. This value was calculated by averaging the cross measurement impedance magnitude between 19 and 21 kHz.

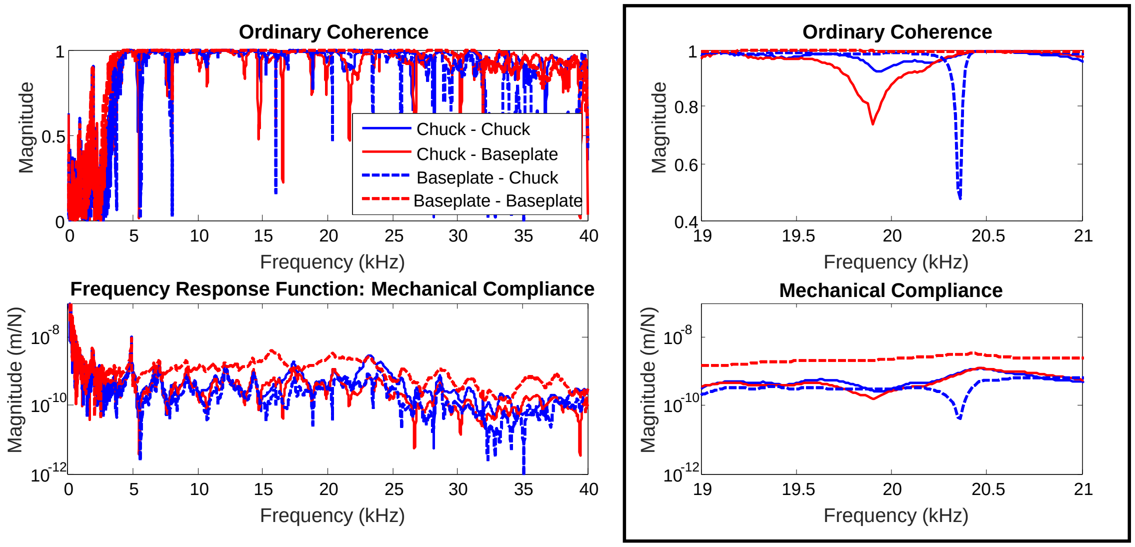

Figure 5.22: Frequency response function analysis of the mechanical admittance with corresponding coherence. All of the curves are similar near 20 kHz except the baseplate driving point measurement.

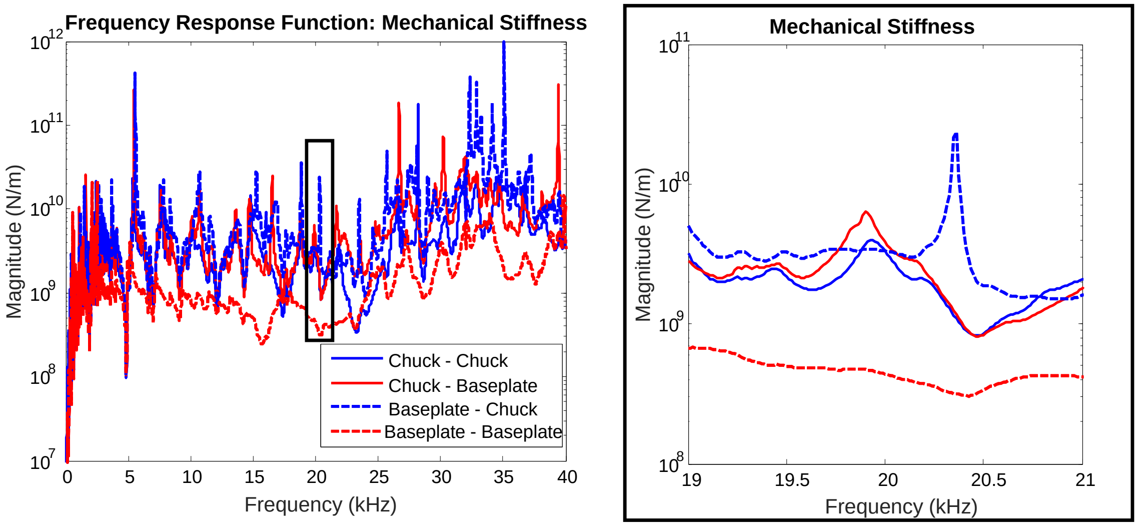

Figure 5.23: Mechanical impedance of baseplate/vacuum chuck anvil. The impedance is about 2 GN/m near 20 kHz.

Slip of a 25.4 mm (0.5 in) thick Al 6061-T6 baseplate with the vacuum chuck and sonotrode was evaluated to understand magnitude and phase differences between the components. Phase and magnitude behavior is important because the proposed equivalent circuit of the system does not incorporate slip dynamics, see Figure 5.12. Relative magnitude and phase between the components was measured using a Polytec laser vibrometer (PSV-400) and two shock accelerometers (PCB 350B02) for the sonotrode, baseplate, and vacuum chuck, respectively. The test design is shown in Figure 5.24. The high frequency data acquisition on the laser vibrometer was used to record the signals concurrently at 512 kHz sampling frequency.

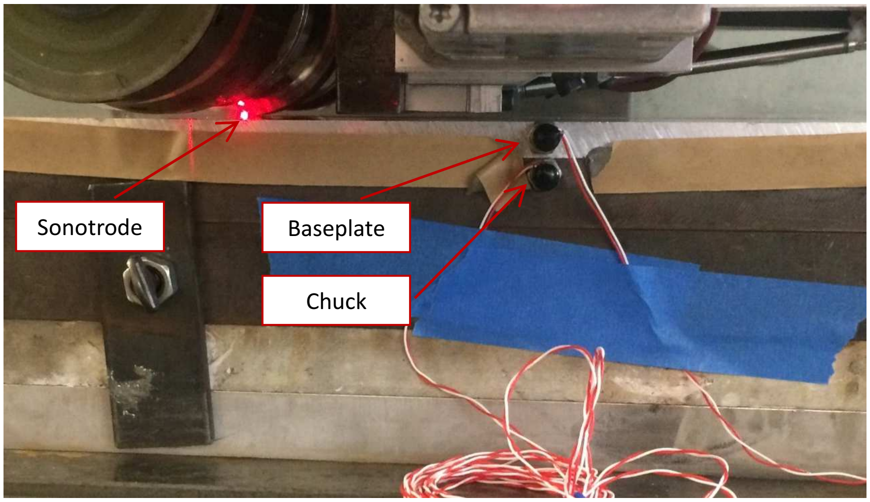

Figure 5.24: Slip evaluation of baseplate on vacuum chuck. Sonotrode motion was also measured to evaluate phase relationships between the baseplate and chuck.

Welding parameters for the test were chosen to be representative for aluminum foil welding, i.e., 32 μm p-p, 5 m/s (200 in/min), 5000 N, and room temperature (no pre-heat). Results of the synchronized waveforms are shown in Figure 5.25(a). To compare motion, component acceleration was used. Sonotrode acceleration was calculated by numerically differentiating velocity as done in the previous section. It is shown in the plot that the acceleration of the sonotrode is steady near 25 kG while that of the baseplate/chuck is near

1 kG, or near 4% of the prescribed motion. The baseplate and chuck also have different magnitudes and these magnitudes differ at separate points in time.

The relative phase angles of the signals were analyzed to evaluate conditions of slip and stick between the components, see Figure 5.25(b)-(c). This analysis was completed by using the FFT algorithm within Matlab to calculate the sliding average phase angle between the two signals for a windowed processing block size of 4096 points. The time traces were originally sampled at 512 kHz, so each processing block contained near 160 cycles. As shown in the plots, intermittent stick and slip occur throughout the weld.

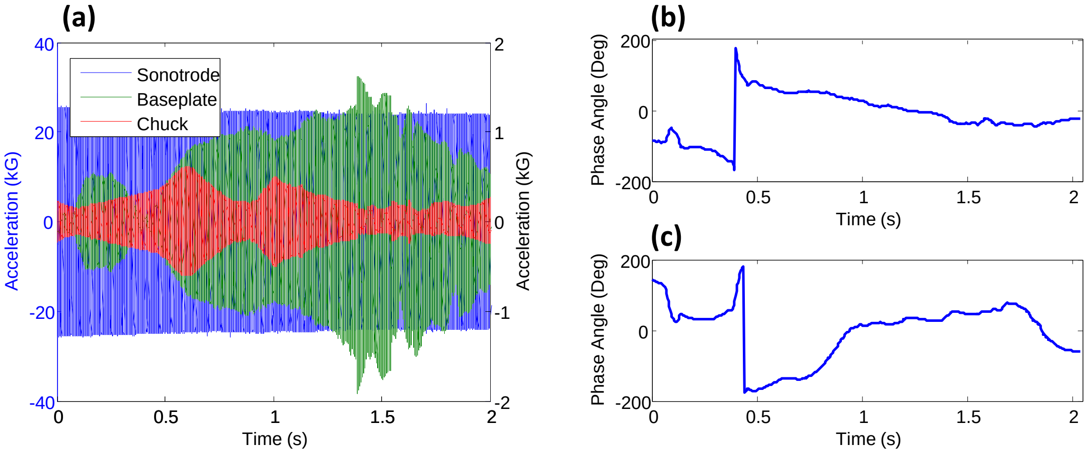

Figure 5.25: Test design for evaluating baseplate slip between sonotrode and vacuum chuck.

This intermittent slip and stick influence the effort required by the welder to reach the prescribed displacement limit of 32 μm p-p. To illustrate the influence of slip/stick on welder effort, the following cosine function multiplication (γ) can be defined,

$$\gamma = cos(\theta) \cdot cos(\phi). \tag{5.10}$$

The angles here are the relative angles between the baseplate and vacuum chuck (θ) and baseplate and sonotrode (ϕ). A value of 1 implies that all of the components are in phase while a value of 0 implies that at least one of the components are out of phase. This relative phase angle expression (γ) is shown with average electric power draw in Figure 5.26.

It is shown in the figure that the fluctuations in average power during the UAM are somewhat correlated with γ. When γ increases toward one, the power also increases shortly thereafter. When γ approaches zero, power decreases shortly thereafter. This correlation between the two quantities exist because relative component motion influences the welder effort. Hence, it is believed that the slip/stick fluctuation creates the noise in the power fluctuation during welding. However, the net motion of the baseplate/vacuum chuck is less than 4% of the total motion of the sonotrode. Hence, the remaining 96% of motion is imparted into the weld foil, UAM stack, and subsurface baseplate. In other words, baseplate slip is not strongly influencing the process aside from introducing variability.

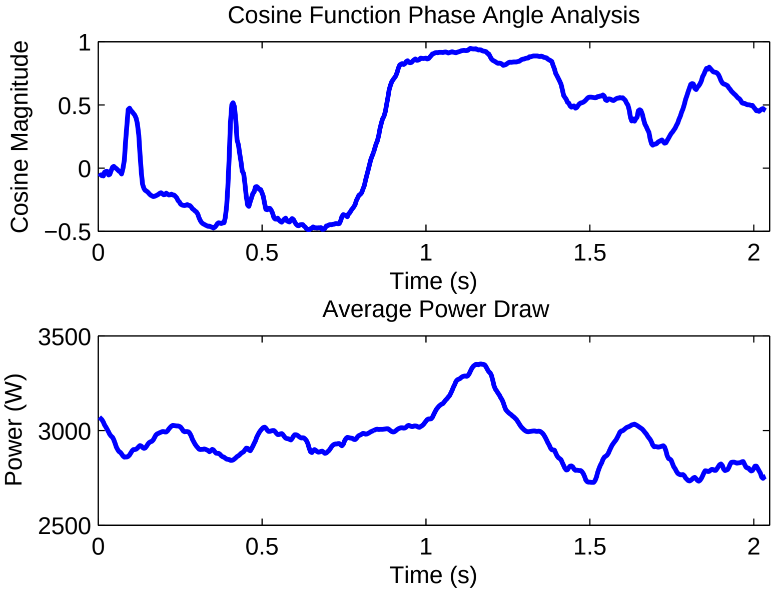

Figure 5.26: Correlation between phase angle and average electric power.

Because some slip does occur between the baseplate and vacuum chuck here, constant mass baseplates were used when comparing the welding of aluminum foil onto aluminum and steel baseplates. This constant mass condition creates similar interia loading on the welder when slip occurs, which, in turn allow stiffness effects to be isolated.

5.5 Summary

The influence of dissimilar weld foil and baseplate metals on the UAM process was studied in this chapter. Before this study, it was believed that the weld foil strength influenced the effort of the welder or average electric power draw. It has been shown herein that weld foil strength does not substantially influence the electric power. Instead, the elastic system compliance influences welder effort.

Finite element modeling was carried out to qualitatively and quantitatively confirm observed experimental average power profile trends. Vacuum chuck impedance and baseplate slip were also investigated to inform and improve on modeling efforts. Stiffness and power correlations were found to be in close agreement. As a result, this work can be used to predict required welder amplitudes for new material systems and new weld fixture designs instead of performing costly weld pilot studies. Predictive relations in UAM have not been successfully developed prior to this study. To predict the required welder amplitude, the system stiffness and minimum electric power are needed. For example, if one knows that a good quality aluminum bond consumes near 3000 W of average electric power, this power value can be used with a linear elastic model of the system to estimate the required welder amplitude to achieve a similar quality aluminum bond.

Chapter 6
NI-AL INTERFACE STRENGTH AND BONDING MECHANISMS

6.1 Introduction

The purpose of this Chapter is to understand and improve the interfacial shear strength of metal matrix composites fabricated via ultrasonic additive manufacturing (UAM). NiTi-Al composites fabricated using UAM have shown a dramatic decrease in thermal expansion compared to Al, yet thermal blocking stresses developed during thermal cycling have been found to degrade and eventually cause interface failure. It has also been confirmed from previous work that the UAM process does not break up the as-built oxide layer on the NiTi fiber and that the bond mechanism is largely a mechanical interlock or a friction fit [33].

To improve understanding of the interface and guide the development of stronger NiTi-Al composites, the interface strength was investigated through the use of single fiber pullout tests. Different commercially available surface finishes and fiber geometries were also evaluated to see if bonding character improved. It was found that the matrix yielded prior to the interface breaking for all the fiber surface finishes and not the ribbon geometry. In other words, fiber surface finish did not influence the bond strength for the fiber geometry. Instead, it was found that a circular fiber geometry exhibited improved adhesion with the matrix over the ribbon due to the consolidation characteristics. It was determined that the failure mode was matrix failure because adhered aluminum was consistently observed on all of the fiber pullout samples. The ribbon geometry did not have adhered aluminum, and delamination was present in the sample. The measured pullout loads from the fiber geometry were then utilized as an input to a finite element model for stress and shear lag analysis, which, in turn showed that the Al matrix experienced a peak shear stress near 230 MPa. This stress is above the ultimate shear strength of the aluminum matrix (150-200 MPa), thus this large stress corroborates with matrix failure observed during testing.

The influence of various fiber surface finish on consolidation characteristics and bond mechanisms was also studied with scanning electron microscopy, energy dispersive X-ray spectroscopy, optical microscopy, and focused ion beam microscopy. It was found that large plastic flow of the matrix around the fiber during the UAM process crimps the tape interface and provides a kinetic path for dynamic recrystallization of the Al, i.e. grain refinement of the Al around the fiber. This crimping does not occur for the ribbon geometry because the square like geometry limits fiber rotation and plastic flow during welding. The newly formed micron and submicron equiaxed grains are similar in size to the surface asperities of the consolidated fibers. As a result, small grains could become entrapped within these asperities and significantly enhance the mechanical interlocking and pullout resistance for all surface finishes. It was also found that a more rough fiber enhanced this plastic flow and consolidation quality around the fiber. Aspects of this chapter were submitted and accepted to *Composites Part B* [37].

6.2 Sample Manufacture

In this study, Al 6061-H18[3] was utilized as the metal matrix for the NiTi-Al UAM composite. The NiTi fiber diameter utilized, for all surface finish types, was 0.28 mm (0.011”), as supplied by Nitinol Devices and Components, Inc. NiTi ribbon similar in size to the fiber with an oxide surface finsh was also evaluated. The material was shape-set to be straight and was super-elastic prior to embedding (Austenite finish temperature above room temperature). Super-elastic fibers were selected compared to shape memory due to available material supply. Welding was performed with a 7 micron Ra surface roughness sonotrode on 101.6 mm by 76.2 mm (4" by 3") Al 6061-T6 baseplates near 4.76 mm (0.1875") in thickness. The baseplates were constrained with a custom metal matrix composite fabrication fixture and vacuum chuck. Foils with a width of 23.81 mm (15/16") and a thickness of 0.152 mm (0.006") were utilized. The welding parameters used in this study are presented in Table 6.1. These parameters were chosen from a recent design of experiment for optimal weld parameters for UAM of Al 6061-H18 [92].

---

[3] 6061-H18 foil as supplied by the vendor was fabricated by cold rolling 6061-O stock material to a H18 temper.

Table 6.1: Ultrasonic welding parameters used in study.

Parameter	**Value**
Temperature	22°C (70°F)
Force	6000 N
Amplitude	32.76 μm (70%)
Speed	84.6 mm/sec (200 in/min)

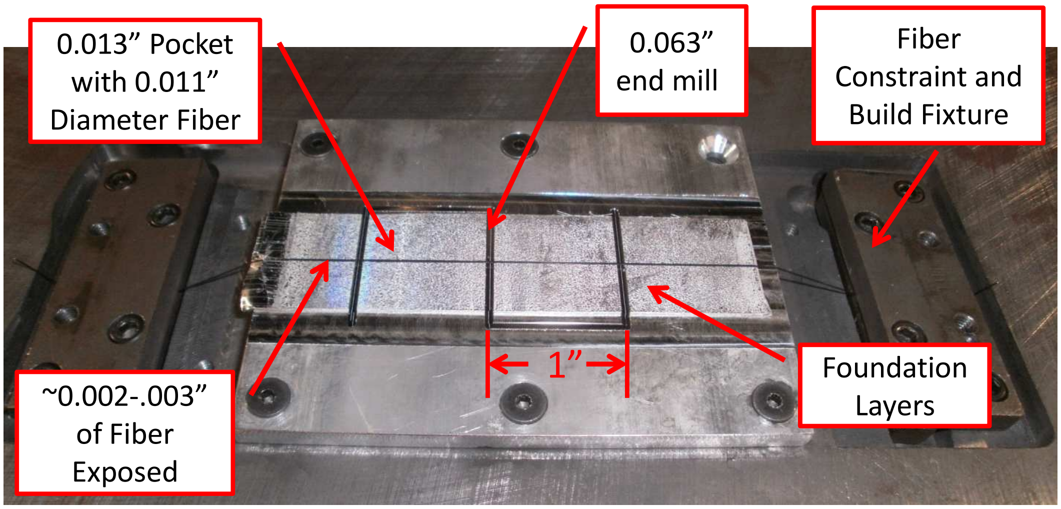
0.013" Pocket with 0.011" Diameter Fiber
0.063" end mill
Fiber Constraint and Build Fixture
~0.002-.003" of Fiber Exposed
1"
Foundation Layers

Figure 6.1: Sample manufacture with details.

To embed a fiber, a ball end mill was utilized to cut a slightly oversized pocket to aid in fiber placement and encapsulation. For the ribbon, a square end mill was used. The depth of the pocket was slightly less than the diameter of the fiber to enhance frictional scrubbing, help promote consolidation, and minimize loads on the fiber. A similar no-load fiber embedding method has been presented [55]. It is shown in Figure 6.1 how the fiber is constrained prior to embedding.

Laser machining was not utilized in this study to (i) minimize aluminum oxide formation in the fiber pocket prior to embedding and (ii) to improve the geometry accuracy of the pocket. It has been found that obtaining adequate pocket geometries for fibers in aluminum is difficult when compared to milling. To isolate the fiber, additional machining operations were run intermittent of welding and fiber encapsulation to ensure the embedded fiber was within a representative weld zone of the UAM process. After machining and welding, samples were removed with electrical discharge machining to minimize cutting stresses on the sample and to achieve small sample dimensions. Appendix D details this manufacturing process. Final samples were near 3.175 mm (0.125") in thickness and 22.86 mm (0.9") in width with the NiTi fiber embedded close to center, Figure 6.2. The fiber length to pull out from the matrix was chosen to be 1 mm (0.04") or near 3 diameter lengths because fiber strain is transferred to the matrix near the edge of the composite due to shear lag [14, 63]. This length was also chosen for feasible manufacturing and handling during testing.

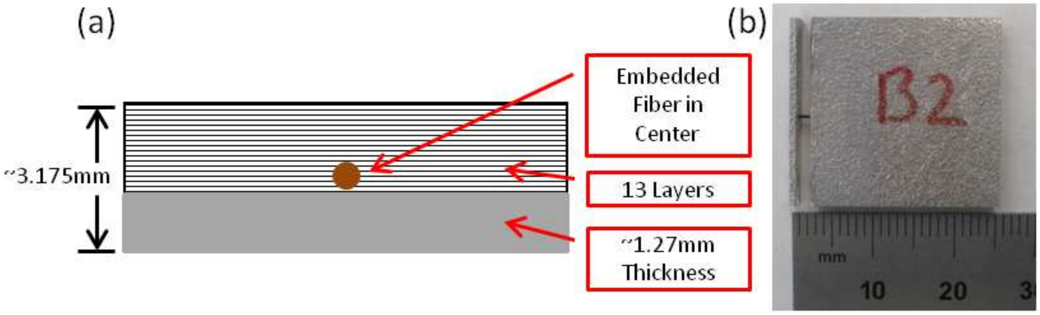

Figure 6.2: Sample details: (a) schematic of sample cross section with key fabrication details; (b) physical sample ready to test post manufacture.

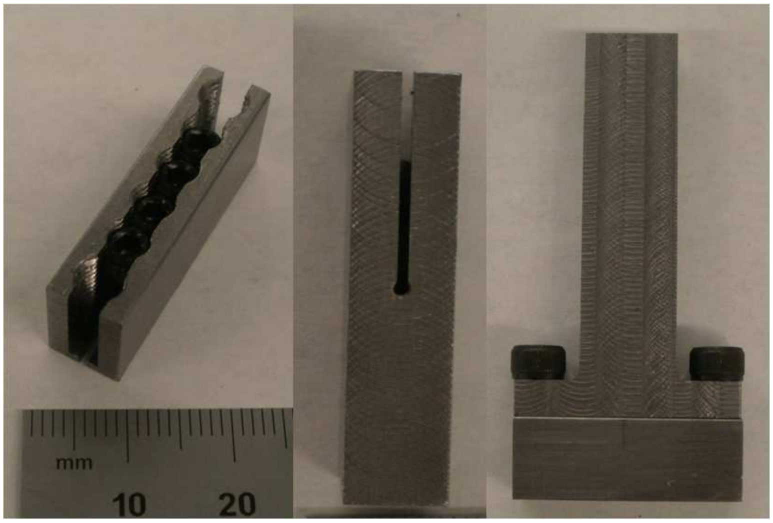

Figure 6.3: Custom fiber pullout test fixture used in study.

6.3 Fiber Pullout Testing

Although fiber pullout tests have been detailed in the literature [14, 65, 52], no standard has been developed for this type of test. Consequently, a custom fixture was developed and built to fit into square tensile test grips, Figure 6.3. This test fixture design was inspired and improved from previous interface strength testing of UAM composites [53, 62]. Key features and improvements of this test fixture design are: (i) the ability to load samples by sliding them to center, (ii) a close fit to the samples thickness and the use of closely spaced set screws to minimize sample misalignment, rotation, and bending, and (iii) an oversized hole drilled at center to minimize fiber misalignment in the testing process. This fixture is made with AISI 1018 Cold Worked Steel to avoid failure and minimize test fixture deformation.

Testing was performed on a TestResources 131R1000-6 load frame with MTS Advantage mechanical wedge type grips and an optional environmental chamber. The load frame is equipped with a 2.2 kN load cell with a maximum resolution of 1.3 N if all sensor errors are considered. The displacement sensor has a resolution of 0.002 μm. A detailed test setup is shown in Figure 6.4. A load rate of 1.27 mm/min (0.05 in/min) was applied to

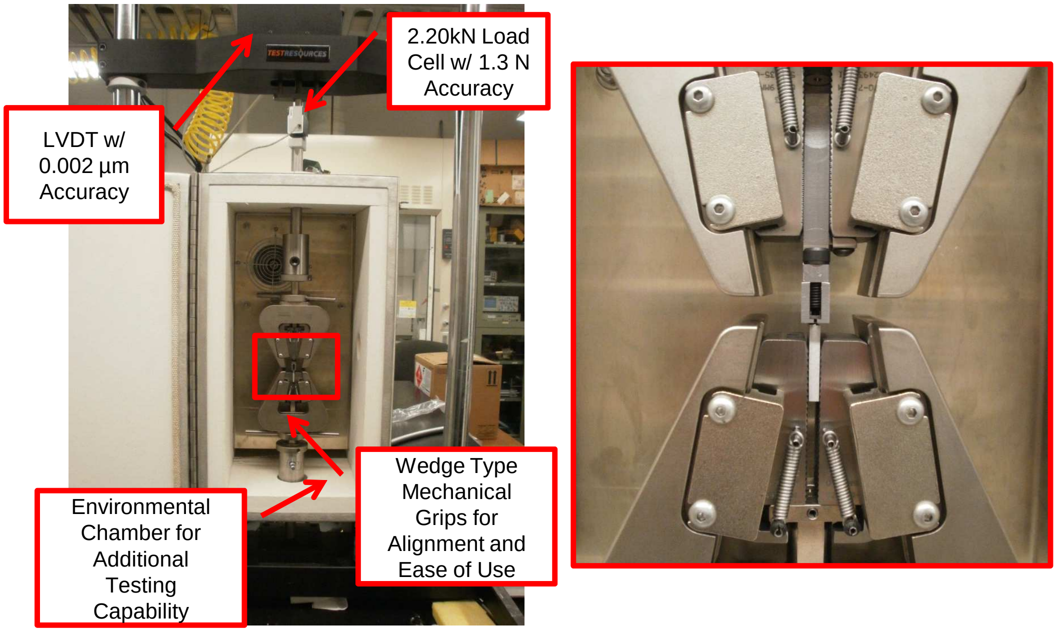
2.20kN Load Cell w/ 1.3 N Accuracy
LVDT w/ 0.002 µm Accuracy
Environmental Chamber for Additional Testing Capability
Wedge Type Mechanical Grips for Alignment and Ease of Use

Figure 6.4: TestResources load frame used for testing with key specifications listed. The area boxed in red illustrates how the test fixture and sample are loaded into the machine.

the load frame controller once the sample was secured and aligned within the grips. Due to the somewhat fast load rate and sample failure, a data sampling rate of 250 samples/s was utilized to acquire enough data points. The total travel distance was selected to be 2.54 mm (0.1”) to ensure that the fiber had completely pulled out of the test fixture before the test was stopped. Measured data included time traces of force and distance. More details of the testing procedure and the pullout fixture are given in Appendix D.

A representative fiber pullout force-displacement curve and tested oxide surface finish sample are shown in Figure 6.5. Key details have been highlighted on the curve to explain test conditions, material behavior, and failure progression. It is emphasized that aluminum remains on the surface of the fiber post failure, which implies matrix rather than interface failure.

Table 6.2 summarizes fiber pullout test results for the study. All of the samples failed at a similar load level, though differences in the average shear strength can be observed. The average shear strength was calculated by dividing the peak pullout load by sample

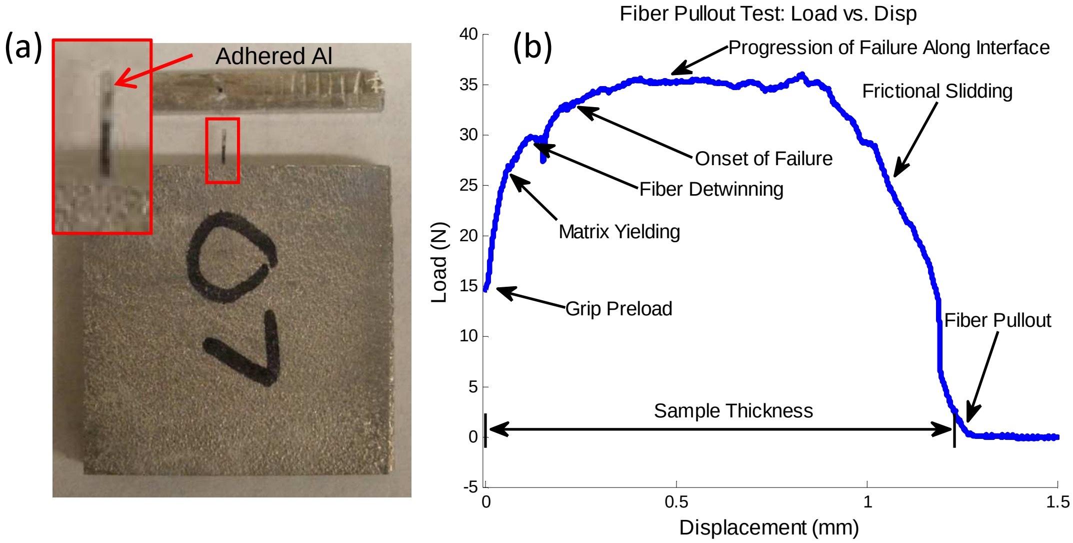

Figure 6.5: Representative pullout test result for oxide sample 7: (a) photo of sample after failure illustrating adhered aluminum to surface of fiber; (b) detailed force-displacement pullout test curve.

thickness. Several samples were tested for each surface finish, exhibiting consistent results.

Figure 6.6 qualitatively compares the ribbon and fiber geometries for the oxide surface finish. Matrix failure via plastic deformation did not occur for the ribbon geometry as it did for the fiber geometry. Quantitative results for the ribbon also showed less plastic deformation during the pullout. However, testing for the ribbon geometry exhibited errors during testing and cannot be confidently used to draw conclusions.

6.4 Fiber Pullout Modeling

In conjunction with fiber pullout testing, a finite element model (FEM) was developed within COMSOL to simulate fiber pullout test conditions. The purpose of this model is to estimate sample loading behavior prior to failure, i.e., quantify interfacial stresses, bending loads, deformation behavior, etc, and not the exact failure mechanics. This model does not incorporate the nonlinear transformation behavior of the NiTi, matrix plasticity, or any residual stresses from the manufacturing process due to the model being used to analyze

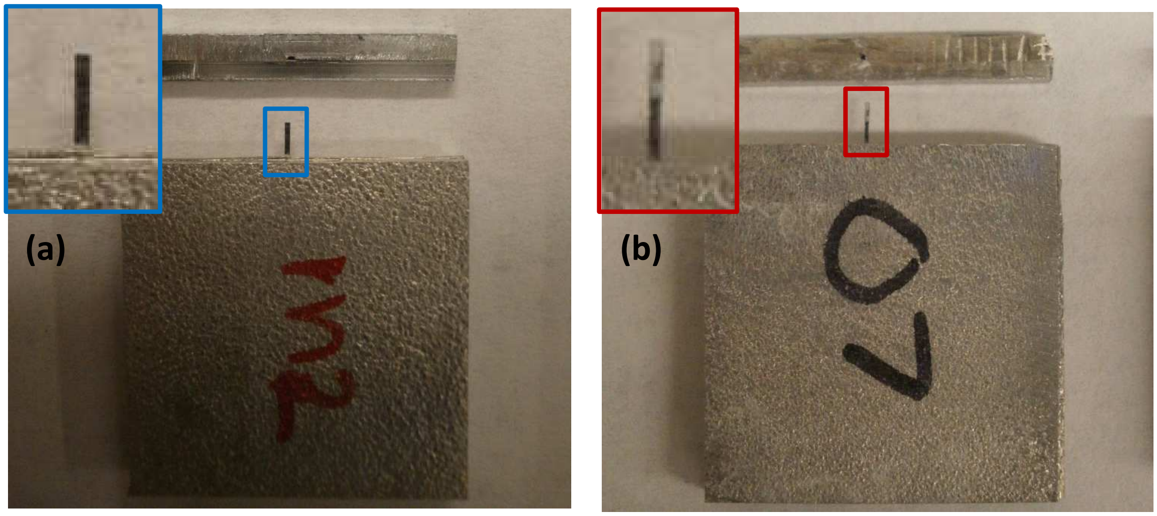

Figure 6.6: Influence of NiTi geometry: (a) ribbon; (b) fiber. The ribbon geometry does not exhibit matrix failure via plastic deformation.

Table 6.2: Fiber pullout summary for all surface finishes.

	Oxide	**Roughened**	**Etched**	**Polished**
Number of Samples	8	7	3	9
Avg. Peak Force (N)	37.7	40.5	36.3	37.9
Stdev Peak Force (N)	5.8	10.7	12.5	9.0
Avg. Sample Length (mm)	1.22	1.02	1.35	1.45
Stdev Sample Length (mm)	0.11	0.20	0.15	0.07
Avg. Shear Stress (MPa)	35.8	45.3	31.1	29.9
Stdev Shear Stress (MPa)	6.7	8.2	12.4	7.5

the interfacial stress behavior up to the point of failure initiation and not during the failure. It is a safe assumption to not incorporate the transformation behavior of the super-elastic wire during pullout testing here because (i) material utilized in experimentation has a high detwinning stress and will begin to transform when the matrix plastically deforms (see Figure 6.7), and (ii) the material cannot physically undergo enough strain to transform into Martensite [74]. Consequently, NiTi is modeled in the Austenitic state within the FEM. Material properties are listed in Table 6.3 [4] while key details and assumptions of the FEM construct are shown in Figure 6.9. Lastly, to describe the deformation behavior efficiently, a graded mesh made with tetrahedral elements was utilized within the fiber and matrix, Figure 6.8. For the fiber, approximately 10 elements make up the fiber diameter (perpendicular to the fiber axis) while 40 are used for the axis. The mesh utilized in the FEM was obtained by refinement until the averaged peak stress (see Result section) differed less than 2% in magnitude from the previous magnitude over the first 0.12 mm in fiber length.

Table 6.3: FEM material properties.

Property	**Al**	**NiTi**
Modulus (GPa)	69	57.5
Poisson's ratio	0.33	0.3
Density (kg/m^3)	2700	6450

The FEM calculations show that deformation is highly localized around the fiber, as desired, to minimize unwanted bending loads. Displacement around the fiber is large due to the high stress experienced during testing. Localized bending around the fiber does occur, yet the displacements from bending alone are near an order of magnitude smaller than those from fiber loading. Consequently, bending influences can be assumed non-influential on test

---

[4] Material properties obtained from www.matweb.com and from tensile testing

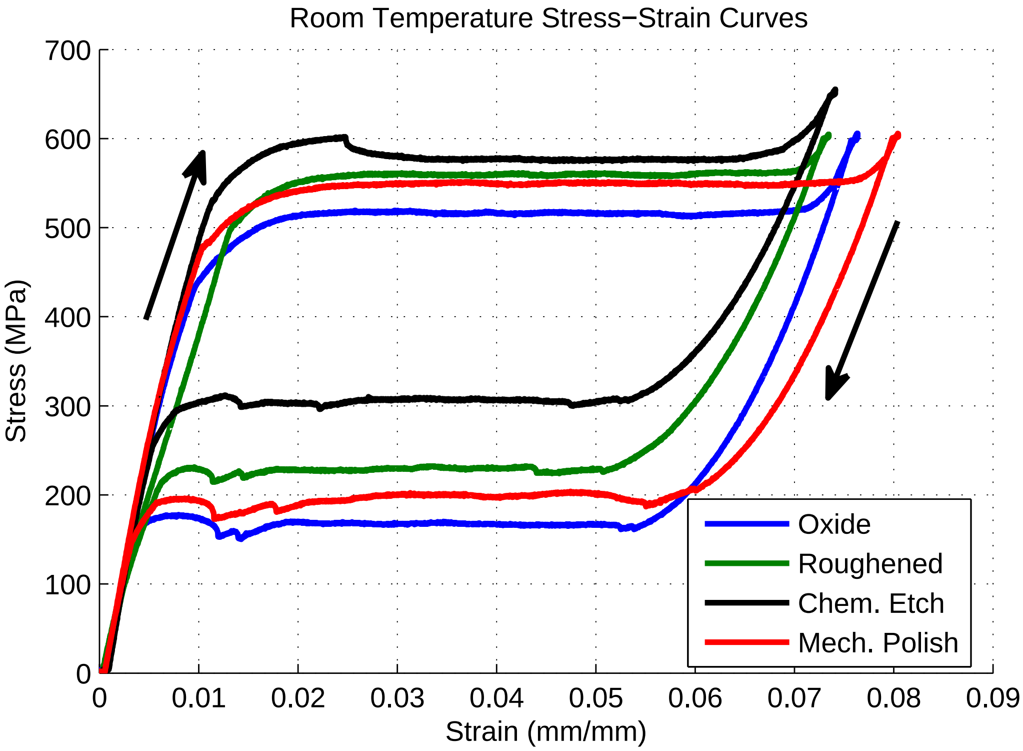

Figure 6.7: Room temperature stress-strain curves of fibers utilized in this study. Data was taken using ASTM F2516 - 07e2, Standard Test Method for Tension Testing of Nickel-Titanium Superelastic Materials. Data shows a high detwinning stress and large elongation to form Martensite.

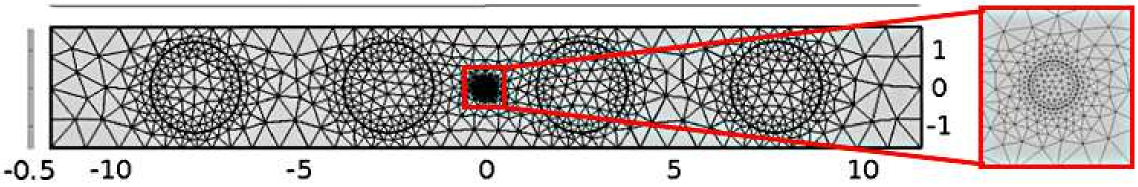

Figure 6.8: Graded mesh of FEM with zoomed in region on fiber.

results.

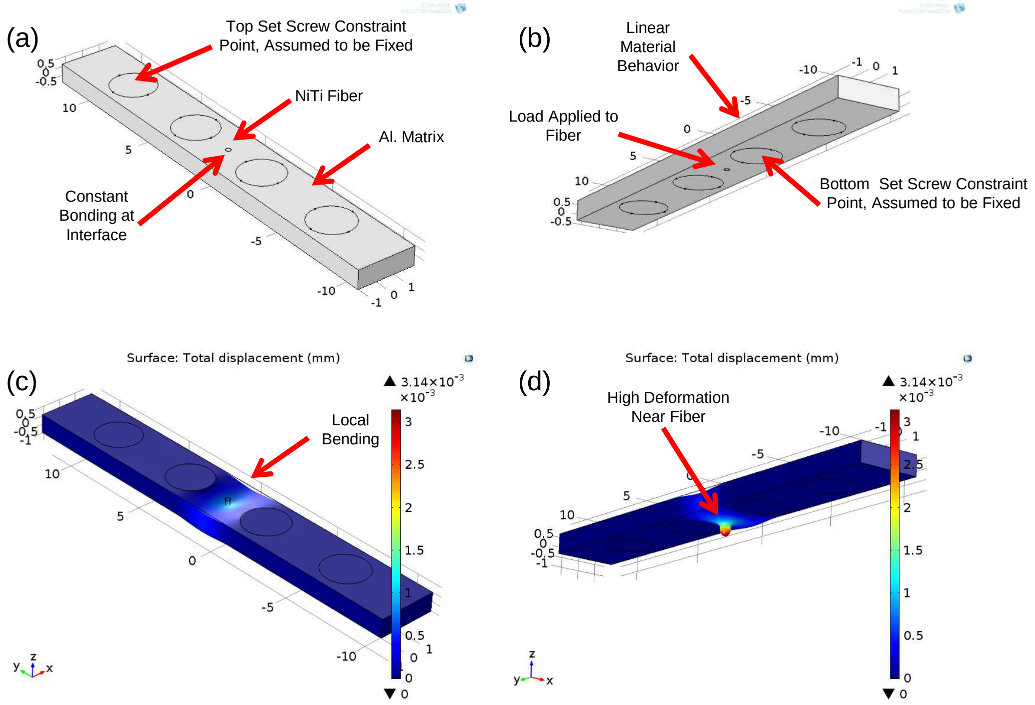
(a)
Top Set Screw Constraint Point, Assumed to be Fixed
NiTi Fiber
Al. Matrix
Constant Bonding at Interface
(b)
Linear Material Behavior
Load Applied to Fiber
Bottom Set Screw Constraint Point, Assumed to be Fixed
Surface: Total displacement (mm)
(c)
Local Bending
▲ 3.14×10⁻³
×10⁻³
3
2.5
2
1.5
1
0.5
0
▼ 0
Surface: Total displacement (mm)
(d)
High Deformation Near Fiber
▲ 3.14×10⁻³
×10⁻³
3
2.5
2
1.5
1
0.5
0
▼ 0

Figure 6.9: FEM of fiber pullout test showing key assumptions and details: (a) top view of sample; (b) bottom view of sample; (c) displacement view from top of sample; (d) displacement view from bottom of sample.

Calculated interfacial shear stresses for the fiber geometries are shown in Figure 6.10. A load of 40 N was applied to the fiber since the experiments show that this load consistently produces failure. Three sample thicknesses were considered: 1.0, 1.2, and 1.4 mm. Shear stresses are concentrated near the edge of the sample but they drop off quickly away from the edge, due to shear lag between the fiber and matrix. Other FEM analysis of NiTi composites have shown similar stress profile behavior [90]. As a consequence of this short distance where the load is transferred from the fiber to the matrix, called the critical fiber length [14], very large localized stresses will be observed, which, in turn, cause failure in a progressive fashion down the fiber. As a result of these large localized stresses and progressive failure behavior, failure is expected to occur at the weakest composite element.

Table 6.4: Fiber pullout comparison between FEM and empirical results. Average peak shear stress was computed by averaging first 5 data points near fiber edge while average shear stress averaged all data points over fiber length.

Thk. (mm)	**Avg. Peak τ (MPa)**	**Avg. FEM τ (MPa)**	**Avg. Exp. τ (MPa)**
1.0	177.6	46.5	45.3 (Roughened)
1.2	174.2	38.6	35.8 (Oxide)
1.4	168.4	32.6	29.9 (Polished)

Due to the ultimate shear strength of NiTi (500 MPa) being much larger than the strength of the aluminum tape (150-200 MPa), failure is expected to initiate at the matrix or the interface rather than the fiber.

Table 6.4 lists the calculated average peak stress and average stress for each sample thickness. The average peak shear stress was calculated by averaging the 5 closest elements to the fiber edge, i.e., the first 0.12 mm of the sample, while the average stress utilized all of the data points. The peak stress was averaged due to the exact peak value being difficult to confidently estimate due to the edge introducing a mathematical singularity in the FEM calculation.

Correlation with the experimental data was done by calculating the average shear stress from the ratio of the measured peak pullout force and the total shear area of the fiber. Because of machining variability, each sample had a different thickness: the sample with roughened fiber had a thickness of 1 mm, the oxide sample had a thickness of 1.2 mm, and the mechanically polished sample had a thickness of 1.4 mm. The resulting stresses are shown in the last column of Table 6.4. The average peak shear stress is largely independent of sample thickness, which, in turn, correlates well with consistently observed failure loads for all samples and smearing of the average shear stress for longer sample thicknesses. Additionally, it is noted that the average peak shear stress is near or above the ultimate shear strength of the aluminum tapes utilized in the UAM process.

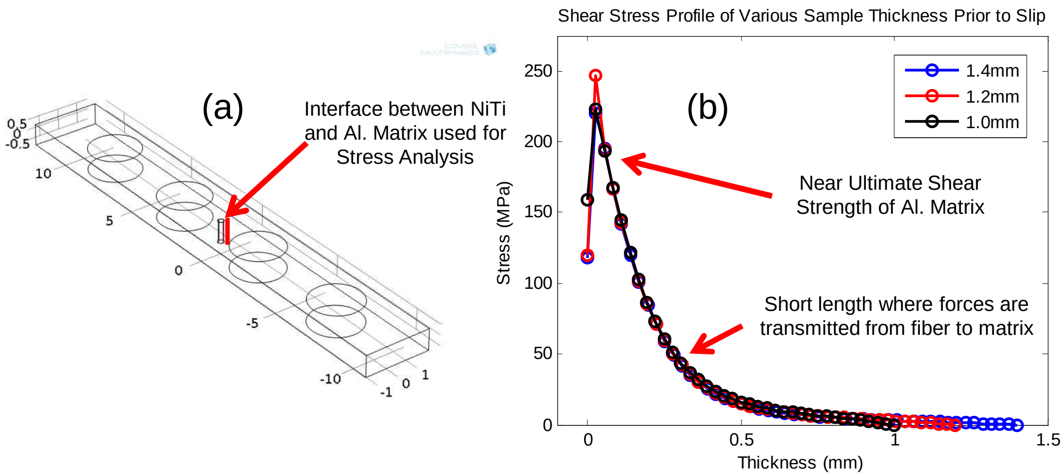

Figure 6.10: Shear stress analysis of fiber-matrix interface for 40 N load: (a) stresses were calculated on the line shown; (b) shear stress calculation along the thickness of the aluminum sample, for the three different sample thicknesses considered. Peak stresses are observed to occur at the same depth in the aluminum sample.

6.5 Microscopy and Microstructure Characterization

In addition to mechanical testing and modeling, various microscopy analyses were performed to qualitatively and quantitatively study the NiTi-Al interface. Electron and focused ion beam microscopy were performed using a FEI Quanta 200 SEM with EDS capability and FEI Helios NanoLab^{TM} 600 DualBeam FIB/SEM, respectively[5]. Optical images were acquired with an Olympus GX71 microscope. SEM imaging was done to evaluate consolidation quality and examine the NiTi-Al interface while simultaneous EDS line scans were performed across various interface regions to quantify diffusion and oxide concentration. Optical and focused ion-beam imaging were performed to analyze grain refinement and failure behavior near a previously embedded mechanically roughened fiber, i.e., the fiber had been pulled out prior to imaging.

SEM Imaging and EDS were done with an electron acceleration voltage of 15-20 keV, a spot size of 4-5 nm, and a working distance of ≈12 mm. EDS scan distance was near 15 μm for all samples while sample spacing was near 1 μm. However, the resolution of the EDS is near 4 μm. Consequently, some data smearing occurs near the interface. Finally, each EDS sample point was measured for 20 seconds to fully measure energy states of the atoms of concern.

---

[5] Microscopy was done at OSU's Center for Electron Microscopy and Analysis (CEMAS) using a FEI Helios NanoLab 600 DualBeam FIB/SEM. The dual beam feature of this microscope allows the user to toggle back and forth seamlessly between the ion and electron beam columns.

Initially, optical imaging was utilized after etching the aluminum surface with an electrolytic Barker's solution, i.e., near 1% fluoroboric acid, to expose grains [1]. After etching, differential interference contrast (DIC) was utilized to observe the grain structure around the fiber. In order to enhance imaging of small grains formed near the fiber during the UAM process, focused ion beam imaging was utilized to expose grain boundaries by etching away a few nanometers of material at an oblique angle with an accelerating voltage of 30keV. Ion beam etching works in a similar manner to chemical etchants by exposing grain to grain contrast via grain orientation, yet material removal is more controlled. Once the material is etched away with the ion beam, small grains are more easily imaged with the SEM.

6.5.1 Consolidation Quality and Interface Composition

SEM images of sample cross sections for each surface finish are presented in Figure 6.11. These samples were not used in mechanical testing, but were made separately with the same welding conditions as the pullout samples. Tape interfaces cannot be identified easily, which illustrates the consolidation effectiveness of UAM. The Al 6061-T6 baseplate material can be identified as the area with the slight contrast difference directly below the fiber.

It can be seen that all the fibers were encapsulated well with some void character in the fibers with a lower surface roughness. Unexpectedly, some of these voids occur near the bottom of the fiber in the oxide and chemically etched surface finishes compared to the top of the fiber, like the mechanically polished finish. It is believed that this void character is related to the surface roughness of the fiber. In particular, the oxide, chemically etched, and mechanically polished fibers do not demonstrate adequate surface roughness for full encapsulation. On the other hand, the roughened fiber shows no void presence due it the fiber demonstrating sufficient surface roughness. More discussion and evidence on fiber surface roughness will be given in Chapter 7.

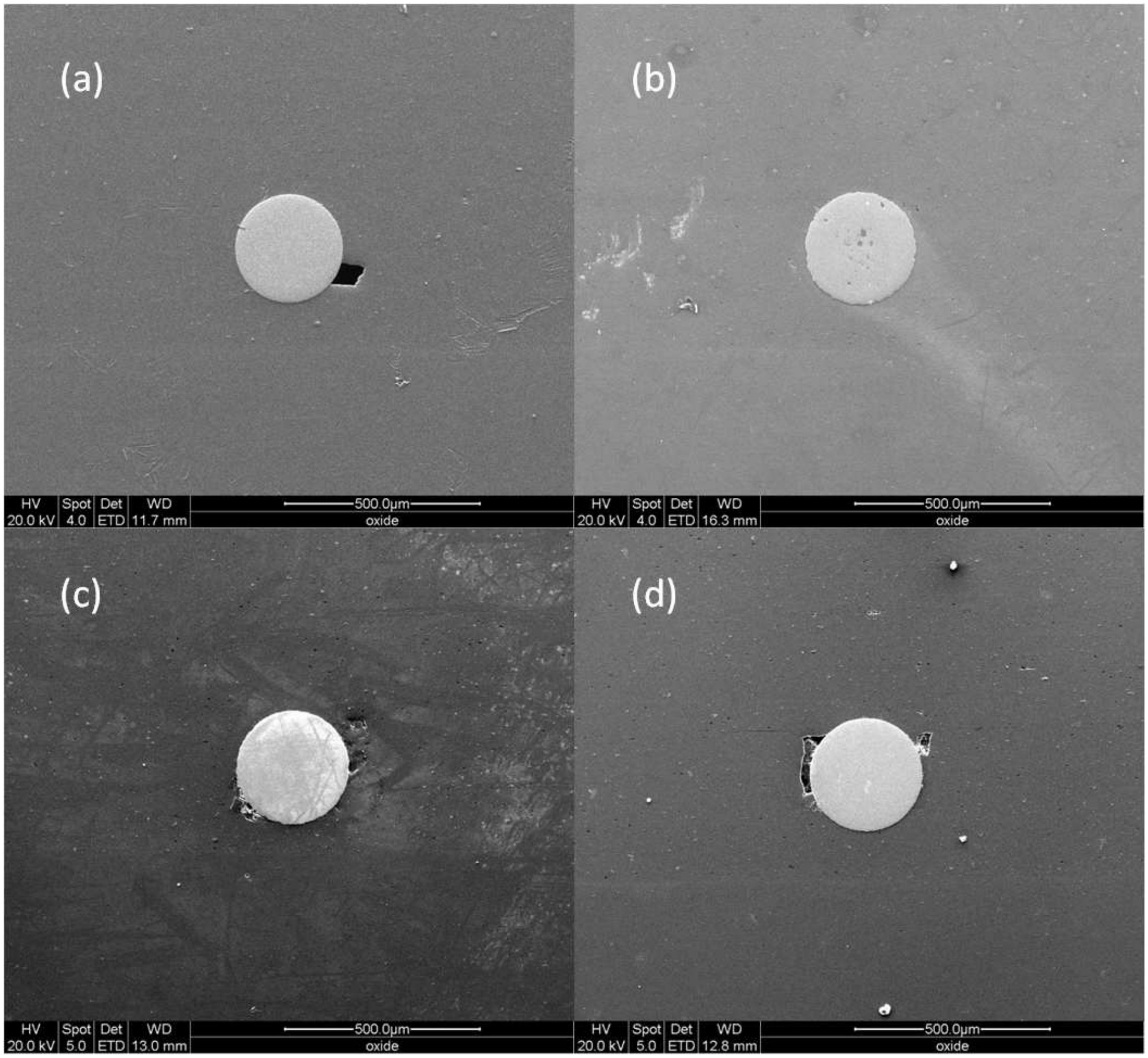
(a)
(b)
(c)
(d)
HV 20.0 kV Spot 4.0 Det ETD WD 11.7 mm 500.0μm oxide
HV 20.0 kV Spot 4.0 Det ETD WD 16.3 mm 500.0μm oxide
HV 20.0 kV Spot 5.0 Det ETD WD 13.0 mm 500.0μm oxide
HV 20.0 kV Spot 5.0 Det ETD WD 12.8 mm 500.0μm oxide

Figure 6.11: SEM images of embedded NiTi fibers utilized in study: (a) oxide surface finish; (b) mechanically roughened surface finish; (c) chemically etched surface finish; (d) mechanically polished surface finish.

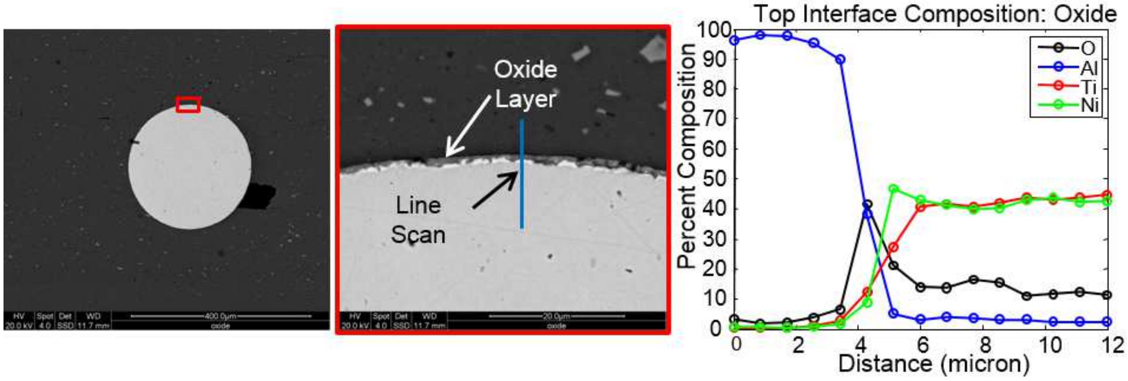

Figure 6.12: SEM image of top of oxide surface finish fiber with corresponding EDS line scan.

EDS line scans with corresponding SEM images for the surface finishes are shown Figures 6.12-6.15, respectively. It is shown in Figure 6.12 that a uniform oxide layer near 2 micron in thickness can be observed in the micrograph and in the EDS line scan. This oxide layer prohibits metallic bonding and limits the bonding to mechanical interlocking. On the other hand, no obvious oxide layer can be observed visually or with EDS for the other surface finishes. As a result, metallic bonding may occur when the as-built oxide layer is removed. It cannot be confidently said what the exact bond constituents are for the mechanically roughened, chemically etched, or mechanically polished surface finishes. However, some oxides do appear to become trapped in the surface roughness of the roughened fiber, as seen in Figure 6.13. For all the surface finishes under investigation, oxygen is observed within the fiber. This oxide is believed to be titanium dioxide which formed post sample polishing.

6.5.2 Microstructure Characterization for Pulled-Out Samples

To better understand matrix failure and consolidation character around the fiber, the microstructure was analyzed around a pulled-out mechanically roughened fiber. Optical images of an etched surface using DIC optical microscopy are shown in Figure 6.16. The tape interface is observed to crimp around the previously embedded fiber exhibiting large

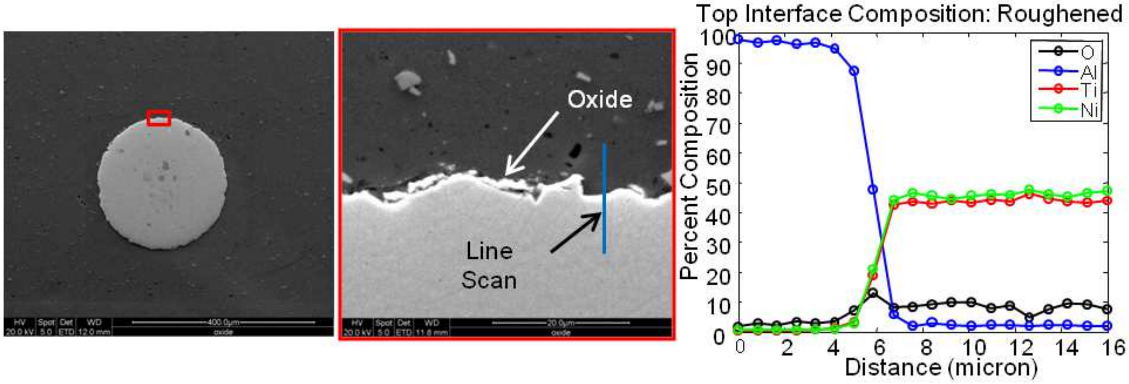

Figure 6.13: SEM image of top of mechanically roughened surface finish fiber with corresponding EDS line scan.

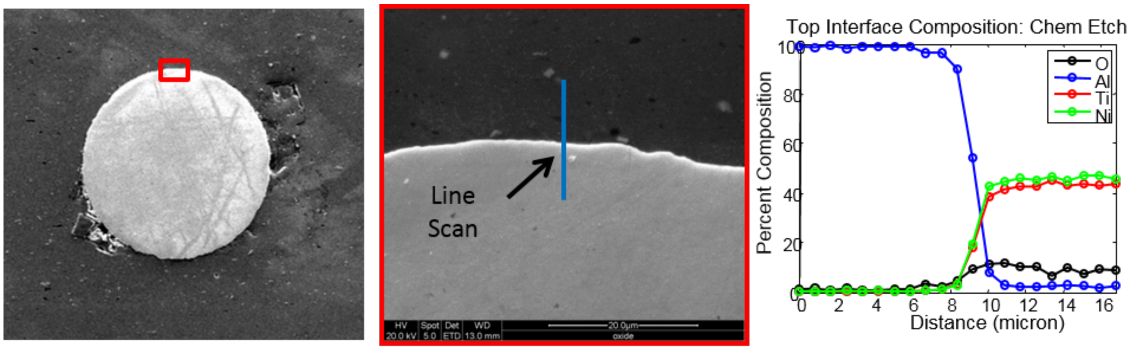

Figure 6.14: SEM image of top of chemically etched surface finish fiber with corresponding EDS line scan.

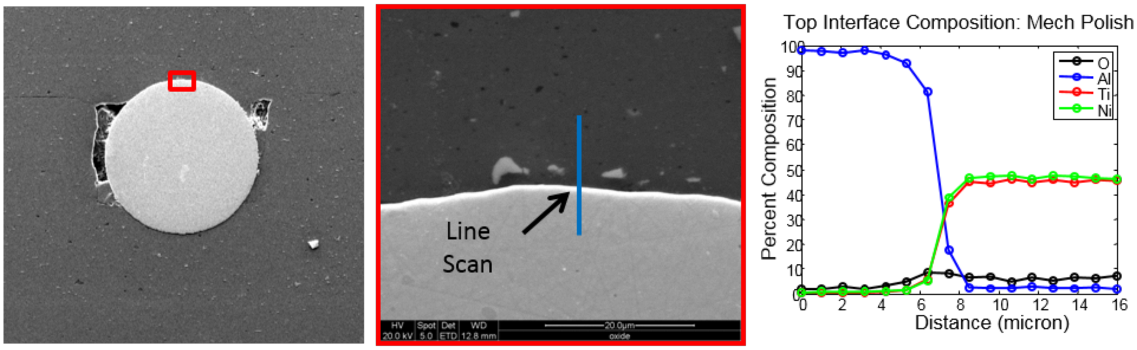

Figure 6.15: SEM image of top of mechanically polished surface finish fiber with corresponding EDS line scan.

plastic flow. The original tape grain structure consists of long flat grains which result from cold rolling fabrication. These grains appear to flow in and around the fiber due to the circular geometries of the fiber and machined out pocket. Lastly, the tape interfaces can be identified only due to the chemical etchant attacking small grains of similar orientation [24].

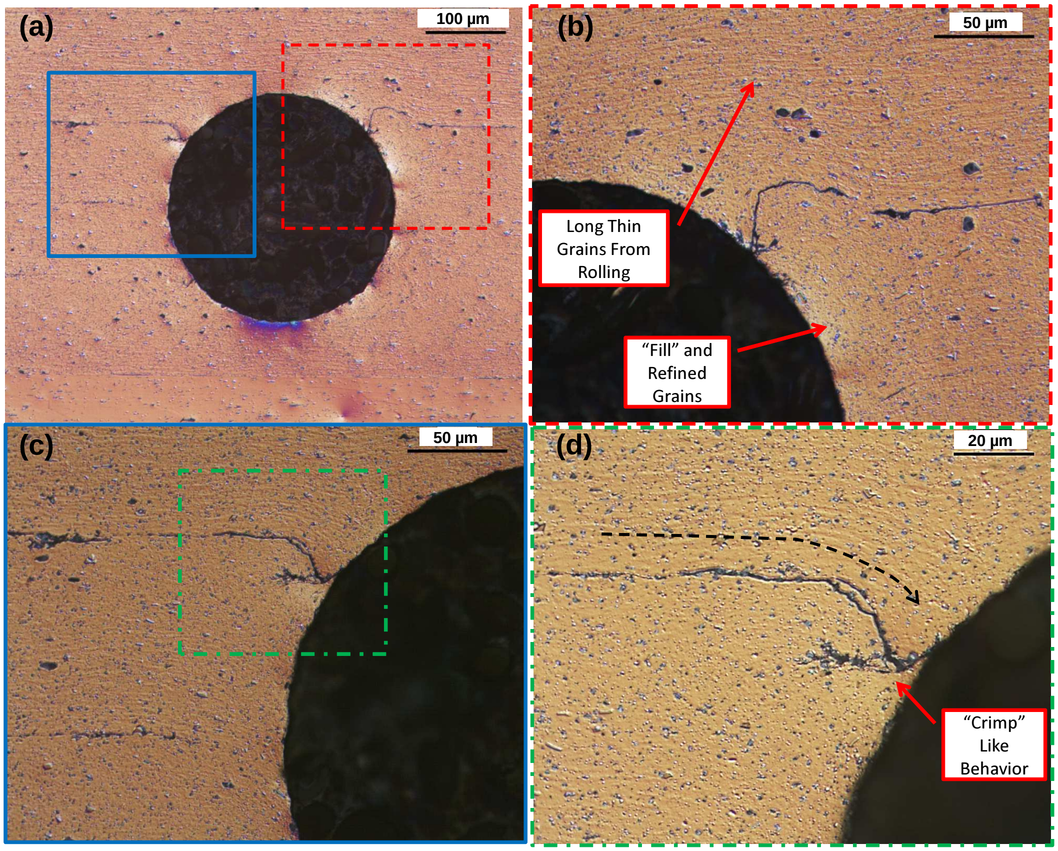

Figure 6.16: Optical images of etched sample at various magnifications using DIC to show grain structure around pulled out fiber: (a) overall view; (b) right top and side; (c) left top and side; (d) zoomed-in left side.

The optical images in Figure 6.16 give insight into the consolidation microstructure, but the fine grain recrystallization observed at tape [49, 20, 24] and fiber interfaces [61, 22] in the UAM process cannot be clearly distinguished. As a result, FIB imaging was utilized to better characterize and observe this fine grain microstructure. In Figure 6.17(a), the microstructure transitions from long flat grains to fine equiaxed grains near the previously consolidated fiber. The flow of aluminum around the fiber and into the pocket can be more clearly seen, as highlighted with arrows in Figure 6.17(b). A crack is observed along the tape crimp, which likely formed during mechanical testing and was intensified once a chemical etchant was utilized. No obvious cracks were observed with the pristine NiTi-Al composite, see Figure 6.18.

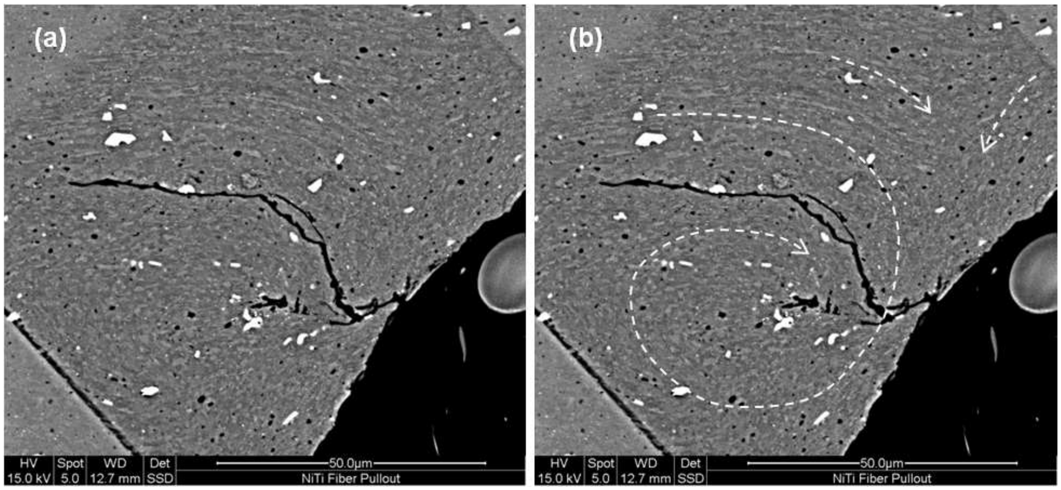
(a)
HV 15.0 kV
Spot 5.0
WD 12.7 mm
Det SSD
50.0μm
NiTi Fiber Pullout
(b)
HV 15.0 kV
Spot 5.0
WD 12.7 mm
Det SSD
50.0μm
NiTi Fiber Pullout

Figure 6.17: Focused ion beam etched surface: (a) grain structure without flow detail; (b) grain structure with flow detail.

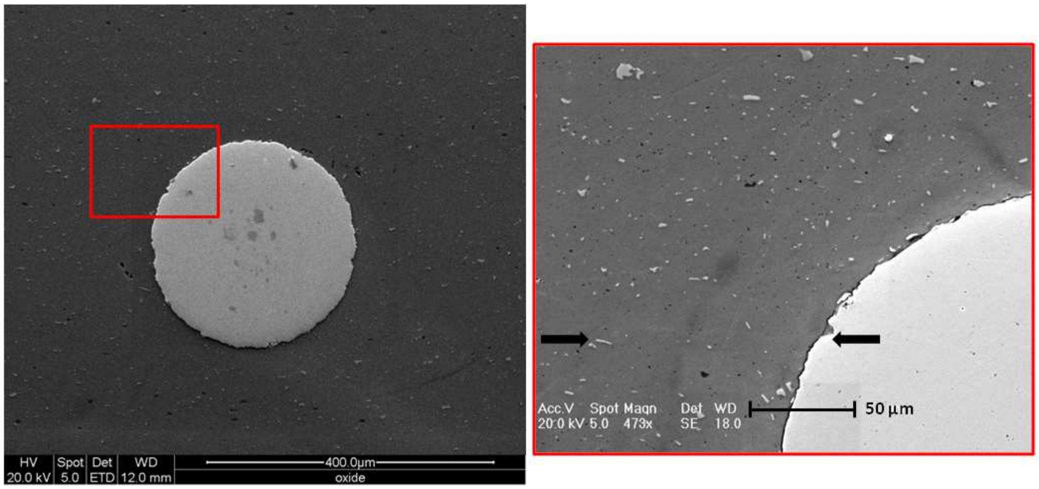

Figure 6.18: Analysis of pristine roughened NiTi fiber prior to pullout. Arrows identify the approximate tape interface.

Due to the tape crimping and exhibiting large plastic flow around the fiber, a robust bond is formed which entails micron and submicron sized grains. Because micron and submicron grains are formed around the fiber during construction, it is likely that grains near in size compared to fiber surface asperities were able to form. As a result, the matrix would fail via shear because submicron grains would become trapped within the asperities of the fiber, which, in turn would lead to robust mechanical interlocking and high resistance to shear at the NiTi-Al interface. Similar to the EDS line scans, it cannot be confidently said that all of the surface finishes failed via subgrain entrapment, but this idea does corroborate well with the oxide surface finish due to the limited possibility of metallic bonding.

Lastly, a pulled-out ribbon and fiber geometry are compared, see Figure 6.19. It is shown that the ribbon geometry has interface delamination due to interface crimping not occurring during consolidation like the circular fiber geometry. Ribbon geometries have been used by previous researchers [34, 75]. However, composites built with multiple ribbons have demonstrated significant delamination and composite failure [75]. Chapter 7 aims to remedy interface delamination with the use of circular fibers.

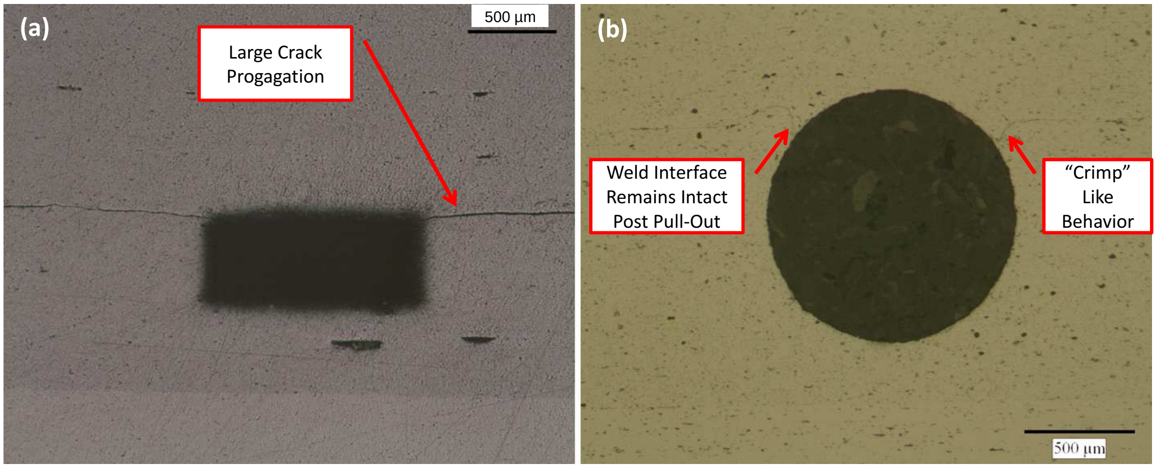

Figure 6.19: Influence of NiTi geometry: (a) ribbon; (b) fiber. The ribbon geometry exhibits delamination while the fiber geometry remains intact due to the interface crimping near the fiber.

6.6 Summary

In summary, interfacial shear stress and bond mechanisms were studied as a function of NiTi fiber surface finish for NiTi-Al UAM composites with the use of fiber pullout testing and microscopy. This study was carried out to improve and understand the NiTi-Al interface for improved design and modeling of NiTi-Al composites due to previous work showing proof of interface failure and frictional bonding between the matrix and fiber. With this study, strong evidence is presented that the matrix is in fact the weakest link in the composite for all surface finishes due to consistent observation of remaining aluminum on pulled out fibers and simulated peak shear stress being near or above the shear stress of the welded aluminum tape. Consequently, bond mechanisms for all fiber surface finishes supersede the strength of the aluminum matrix and show that there is no clear optimal surface finish. However, with the use of stronger aluminum matrices or characterization of the interface at elevated temperatures, surface finish may play a larger role in failure.

It has also been confirmed from previous work that the UAM process does not break up the oxide layer on the oxide surface finish fiber and that the bond mechanism is largely a mechanical interlock or a friction fit. On the other hand, the other surface finishes have no observable oxide layer that would prohibit metallic bonding. Although the exact bond mechanisms cannot be determined for each fiber, the mechanically roughened fiber appears to be the best from a potential bond strength perspective because it offers both increased frictional coupling, the possibility of metallic bonding, and enhanced consolidation character. Understanding the relationship between surface roughness and bond quality is needed for future work.

Microstructure examination around a failed mechanically roughened fiber was carried out to investigate why matrix failure occurred. It was found that large plastic flow of the matrix during the UAM process crimps the tape interface and provides a kinetic path for dynamic recrystallization of the aluminum, i.e., favorable grain refinement of the aluminum around the fiber. Due to the matrix near the fiber recrystallizing, micron and submicron equiaxed grains are formed, which are similar in size to the surface asperities of the consolidated fibers. As a result, small grains could become entrapped within these asperities which significantly enhance the mechanical interlocking and pullout resistance for all surface finishes.

The work presented herein lays out a clear framework for (i) embedding fibers, (ii) measuring interface strength, (iii) and evaluating bonding mechanisms. This framework can be extrapolated to other fiber types, sizes, and materials. If possible, channels should be machined for the embedded fiber. It is also recommended to use circular fiber geometries to enhance consolidation behavior.

Chapter 7

SCALING-UP NITI-AL COMPOSITES

7.1 Introduction

The focus of this Chapter is two fold. The first aspect is to evaluate the feasibility of circular or round fiber geometries in NiTi-Al composites which have had the as-built oxide surface finish removed in the commercial fiber fabrication process. It was shown in Chapter 6 that round fibers demonstrated enhanced joint properties over ribbon type fiber geometries, which in turn could enable composite scale-up. It was also shown that metallurgical bonding may take place between the matrix and fiber once the oxide layer was removed. The second aspect of the paper is to develop an accurate model that describes composite behavior. This modeling effort was carried out via collaboration with X. Chen and P. Anderson of the Material Science and Engineering Depart at OSU.

Multi-layer NiTi-Al composites were fabricated and tested with Al 6061-H18 foil and mechanically polished NiTi fibers. It is shown that the thermal expansion of aluminum can be reduced by over 50% by incorporating a low volume fraction of NiTi fibers (13-20%). These composite continued to exhibit this reduced thermal expansion over multiple heating and cooling cycles. The corresponding simulations utilized a microstructural constitutive model of NiTi implemented in ABAQUS. Good correlation is achieved with the model and experimental data. Aspects of this chapter have been published in *Shape Memory and Superelasticity* [15].

7.2 Composite Manufacture and Testing

7.2.1 Material Stabilization (Training) and Characterization

Mechanically polished 0.381 mm (0.015) diameter NiTi fibers were obtained from Nitinol Devices & Components, Inc. for this study. The fibers had an austenite start temperature above room temperature and were shape-set to be straight. A stabilization process was applied to the fibers prior to composite construction [36] in order to minimize changes in flow stress and inelastic strain when the NiTi fibers were incorporated into the Al matrix, see Figure 7.1. The stabilization process involved cycling the material 10 times at 75°C to ensure that the material was in the super-elastic state, i.e., above the Austenite finish temperature. These cycles were performed using a TestResourses 131R1000-6 tensile frame with MTS Screw Action Grips with serrated faces and a thermal chamber.

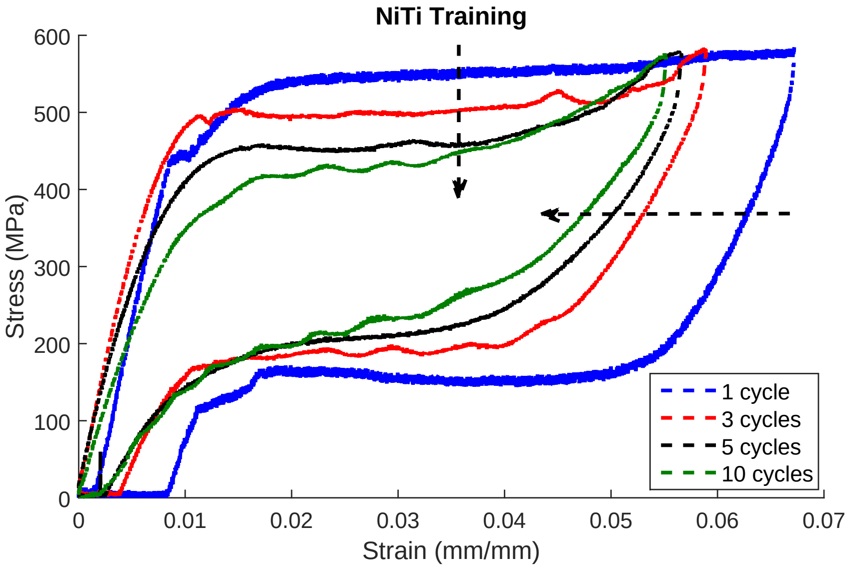

Figure 7.1: Stabilization or training of NiTi fibers prior to embedding.

The stabilized NiTi fibers were then characterized using isothermal tensile testing and differential scanning calorimetry (DSC). Isothermal tensile tests were performed on a 158.8

mm (6.25 in) long piece of NiTi fiber at 23°C (room temperature), 65°C, 75°C, and 85°C to quantify the stress as a function of temperature. The nominal strain rate was 0.8%/min to minimize internal heating during the test in accordance with ASTM F2516, Standard Test Method for Tension Testing of Nickel-Titanium Super-Elastic Materials. The nominal strain was determined by dividing measured displacement by the fiber length. The curves are shown in Figure 7.2.

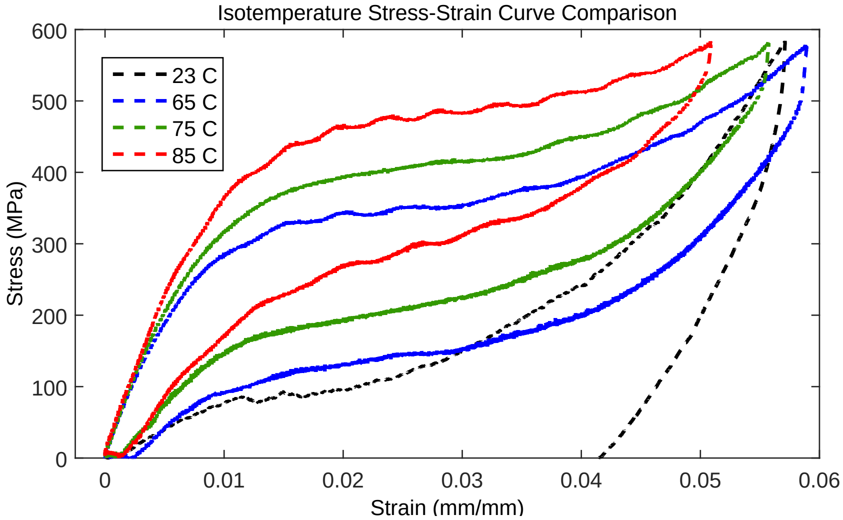

Figure 7.2: Isotemperature stress-strain curves of NiTi fiber at various temperatures.

The austenitic transformation temperatures were measured using a TA Instruments 2920 Differential Scanning Calorimeter. The sample was first cooled to near -10°C to ensure that the NiTi fiber was in the martensitic state or below the martensite finish (M_f) temperature. The sample was then heated to 100°C at 10°C/min while simultaneously measuring the reference heat flow. The transformation temperatures were determined by fitting lines to both sides of the transformation peak and finding the intersections between the plateaus as specified in ASTM F2004, Standard Test Method for Transformation Temperature of Nickel-Titanium Alloys by Thermal Analysis. This DSC system was not used to measure the martensitic transformation temperatures because reliable results for cooling could not always be achieved. DSC curves are shown in Figure 7.3 for the as-received and stabilized material.

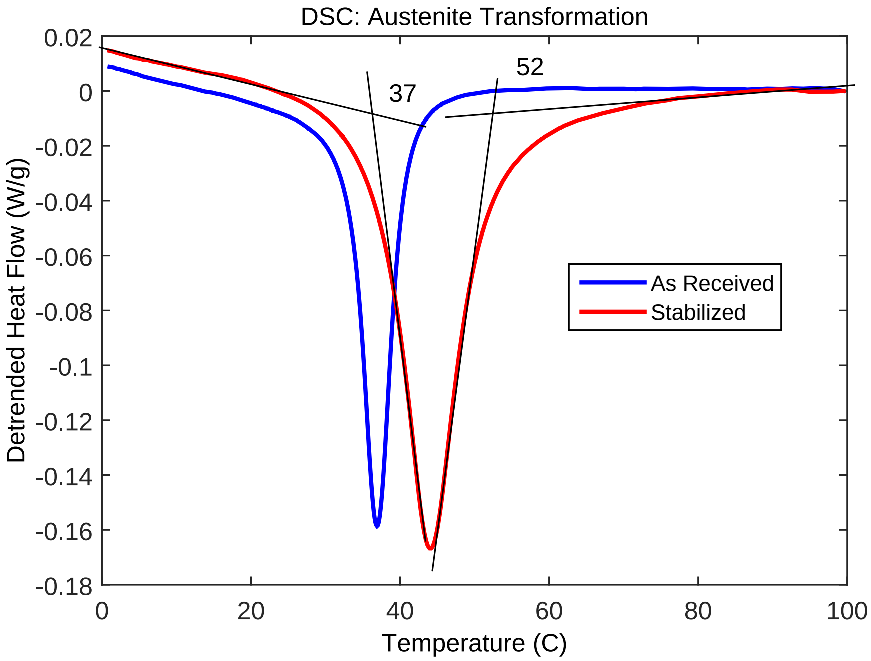

Figure 7.3: Differential scanning calorimeter measurements on as-received (not stabilized) and stabilized measurements.

Using the isotemperature stress-strain curves and the DSC data, a stress-temperature phase diagram can be produced [36]. This diagram yields insight into how the composite will behave. It can also be used for analysis purposes when evaluating the thermo-stress interaction of the NiTi with the aluminum matrix. In particular, it can be used to evaluate the progress of the transformation, likelihood of plastic deformation, and the impact of multiple heating cycles. The phenomenological properties of NiTi found via characterization and displayed in the phase diagram are listed in Table 7.1.

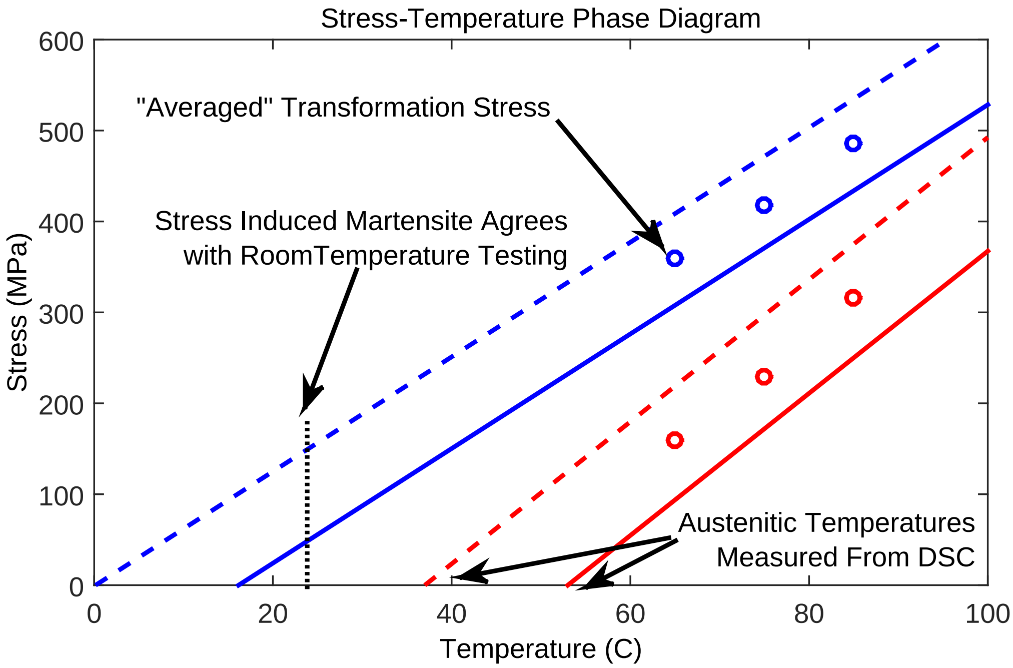

Figure 7.4: Stress-temperature phase diagram for stabilized NiTi. The diagram was assembled using isotemperature stress-strain and DSC measurements. This phase diagram can be used to shed insight into composite performance.

Table 7.1: Phenomenological properties of NDC 380 μm diamter NiTi found via characterization.

E_M(MPa)	E_A(MPa)	C_M(MPa/^oC)	C_A(MPa/^oC)	$A_s(^oC)$	$A_f(^oC)$	$M_f(^oC)$	$M_s(^oC)$	ϵ_0(%)
20	50	6.8	7.8	37	52	0	16	2.5

7.2.2 Composite Design, Fabrication, and Testing

The 9 kW UAM system was utilized for composite construction. The metal matrix used in this study was Al 6061-H18. Foils were 0.152 mm (0.006 in) in thickness and 25.4 mm (1 in) in width. Aluminum 6061 was chosen for its high strength to weight ratio and close compatibility with UAM.

The composite design for this study placed NiTi fibers away from shared interface boundaries to minimize delamination risk. The upper and lower portion of a fiber did not share the same common boundary with the upper and lower portions of a neighboring fiber, see Figure 7.5(a). A 0.397 mm (0.016 in) diameter ball-nose end mill was used to cut a 0.356 mm (0.014 in) deep channel in the Al matrix to assist in the encapsulation and placement of the NiTi fibers during consolidation. The channel dimension was 0.025 mm (0.001 in) less than the NiTi fiber diameter to enhance scrubbing and plastic flow of the Al around the fiber and into the pocket, Figure 7.5(b). Welding was conducted on 101.6 mm × 76.2 mm × 4.76 mm (4.0 in × 3.0 in × 0.188 in) Al 6061-T6 build plates that were constrained in place using a custom baseplate, fabrication fixture, and vacuum chuck, see Figure 7.6. Similar procedures were done in Chapter 6 when fabricating the fiber pull-out samples. Table 7.2 lists the parameters that were used to weld the aluminum tapes. These parameters were obtained from a recent design of experiments for optimal welding parameters of Al 6061-H18 [92]and they have been shown to be sufficient in pilot NiTi-Al welds.

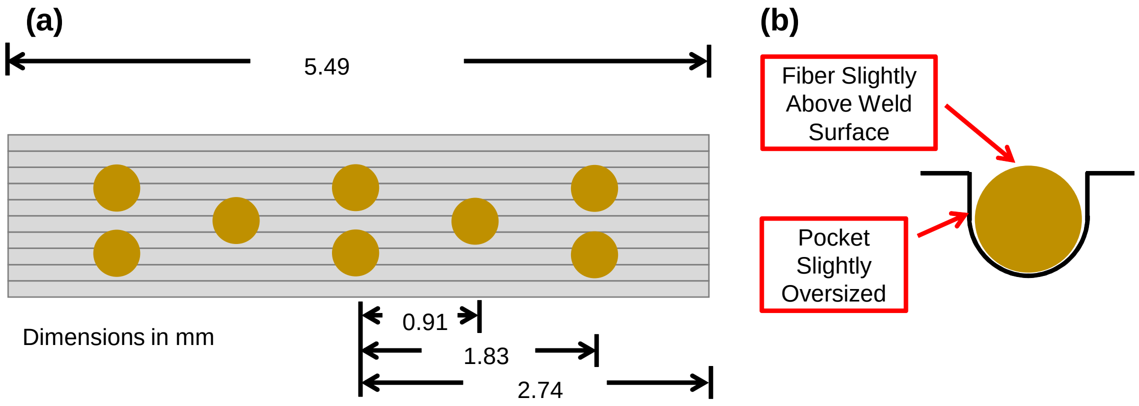

Figure 7.5: Composite design: (a) fibers were strategically placed to eliminate shared interface boundaries and minimize possible delamination; (b) pocket design for fiber placement.

Table 7.2: Ultrasonic welding parameters used in study.

Parameter	**Value**
Temperature	22°C (70°F)
Force	6000 N
Amplitude	32.6 μm
Speed	84.6 mm/sec (200 in/min)

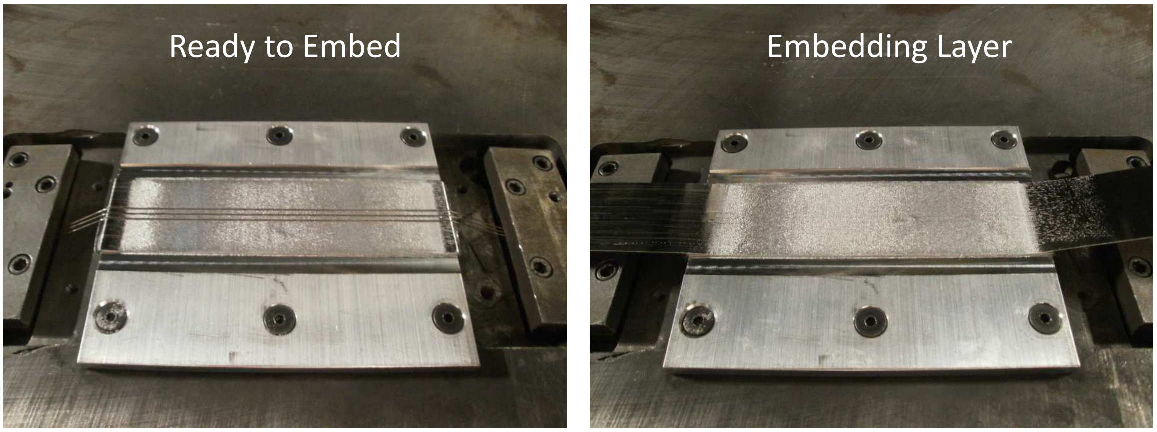

Figure 7.6: Manufacture of composite. The fibers are manually placed in the milled channels and constrained via the fabrication fixture. An ideal consolidation layer shows no shinny spots, i.e., voids around fibers or unwelded areas.

Removal of the completed composite from the surface of the build plate was done in multiple steps: (i) CNC milling to reduce the composite geometry to the desired dimensions, (ii) manual milling to remove the build plate from under the composite, and (iii) a slow speed cutting with a high volume coolant flow to remove the end of the composite attached to the remaining build plate without significant heat generation. Two composites were fabricated. Each measured approximately 5.49 mm × 74.00 mm × 1.27 mm (0.22 × 2.91 ×

0.05). The NiTi volume fractions for the two composites were 13% and 13.8% respectively. Slight manufacturing variations in the removal process caused the volume fraction to be slightly different. One of these composites are shown in Figure 7.7 with attached strain gauges for thermal testing. Appendix E lists the steps of this fabrication process.

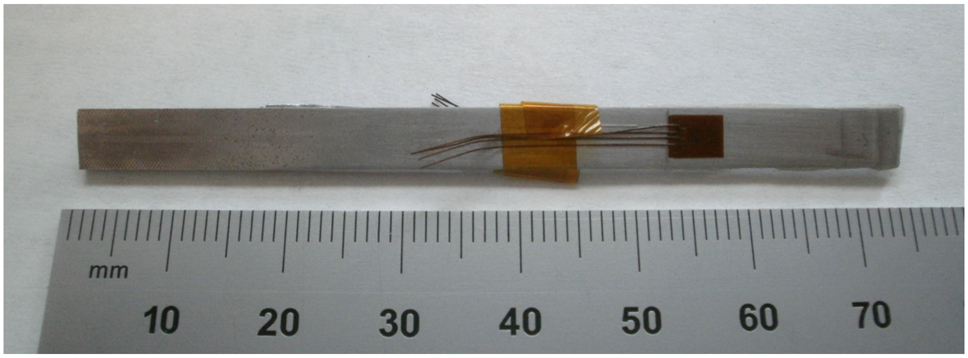

Figure 7.7: Composite removed from baseplate and ready for thermal expansion testing.

Thermal testing was performed on the composites using a custom 15.24 cm × 15.24 cm (6.0 × 6.0) thermal chamber with foil-faced fiberglass insulation, Figure 7.8. The top of the chamber was equipped with a circular viewing window. A Milwaukee Variable Temperature Heat Gun supplied heated air to the chamber, and this air was deflected upon entering the chamber with an aluminum baffle to produce even heating of the samples. Composite CTE measurements were made by mounting strain gauges on a reference piece of UAM Al 6061 and composite so that the relative strain difference between the two materials could be determined [89]. The composite and the reference sample were mounted within the chamber in a free-stress, cantilevered condition. Micro Measurement WK 13031CF350 strain gauges were mounted to the top and bottom sides of both samples, approximately 3.8 cm (1.5) from the fixed end. The temperatures of each sample were measured using type-J thermocouples with Omegatherm 201 thermal conductivity paste at the composite thermocouple interface to ensure accurate measurements. The outputs of the strain gauges and thermocouples were connected to a National Instruments data acquisition system, which interfaced with a LabVIEW VI for recording data. Before each sample was tested, the strains were zeroed using the calibration features within LabVIEW. Each test was performed by heating the sample from room temperature to approximately 100°C using the slowest speed setting on the heat gun (near 45 min. to reach 100°C). Samples were then cooled back to room temperature by setting the heat gun to 30°C and allowing the chamber to equilibrate with the room once the heat gun could no longer provide cooling (near 1 hr). A detailed test procedure with the LabVIEW VI are given in Appendix E.

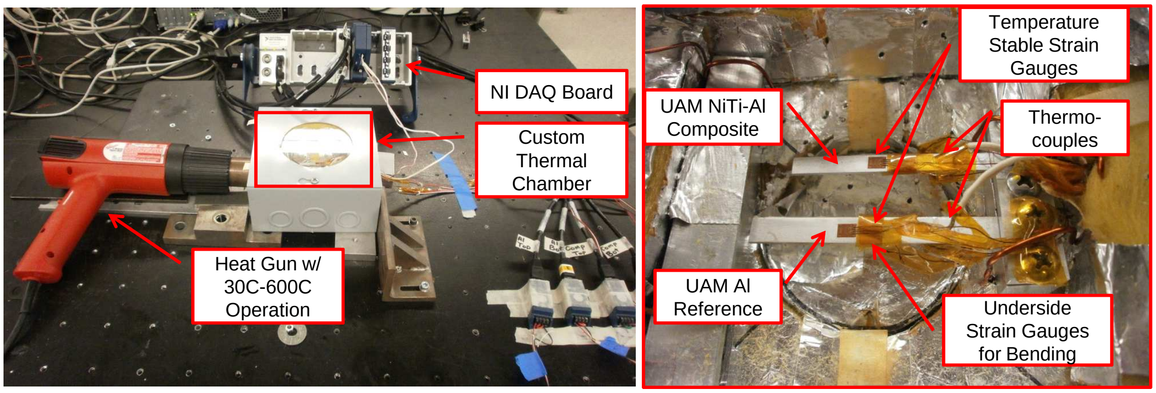
NI DAQ Board
Custom Thermal Chamber
Heat Gun w/ 30C-600C Operation
UAM NiTi-Al Composite
Temperature Stable Strain Gauges
Thermo-couples
UAM Al Reference
Underside Strain Gauges for Bending

Figure 7.8: Thermal test utilized to measure composite CTE. Important test elements have been detailed.

The empirical strain-temperature results for both NiTi-Al composites and pure UAM Al-6061 are shown in Figure 7.9. The composites begin transforming near 40°C and exhibit compression from the NiTi. Transformation near 40°C is expected because of the A_s temperature. The compression of the composite from the NiTi is also expected because the NiTi remains in tension after the first cycle. The fibers are in tension due to the NiTi not fully transforming back to the initial fiber state. Further cycling shows coalescence. The stress-temperature path of the NiTi is schematically shown in Figure 7.10. The first cycle also demonstrates curvature during heating, which may be linked to the collapse of voids within the UAM build and plasticity of the matrix. The NiTi-Al composites exhibit CTEs less than 50% of Al-6061.

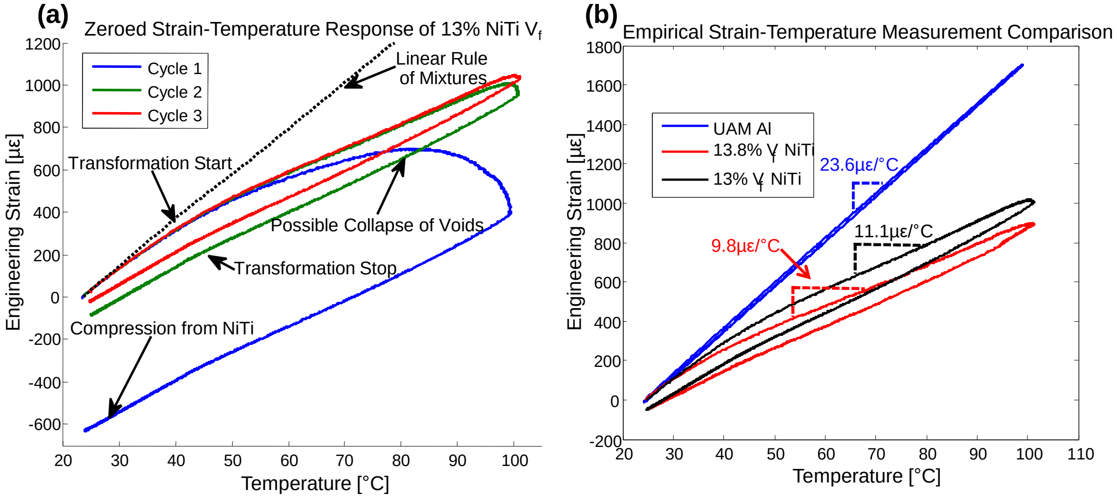

Figure 7.9: Empirical strain-temperature results: (a) 13% NiTi volume fraction composite for 3 cycles; (b) comparison of Al (no NiTi), composite with 13% volume fraction and composite with 13.8% volume fraction. Fit slopes from 40 to 100°C are given.

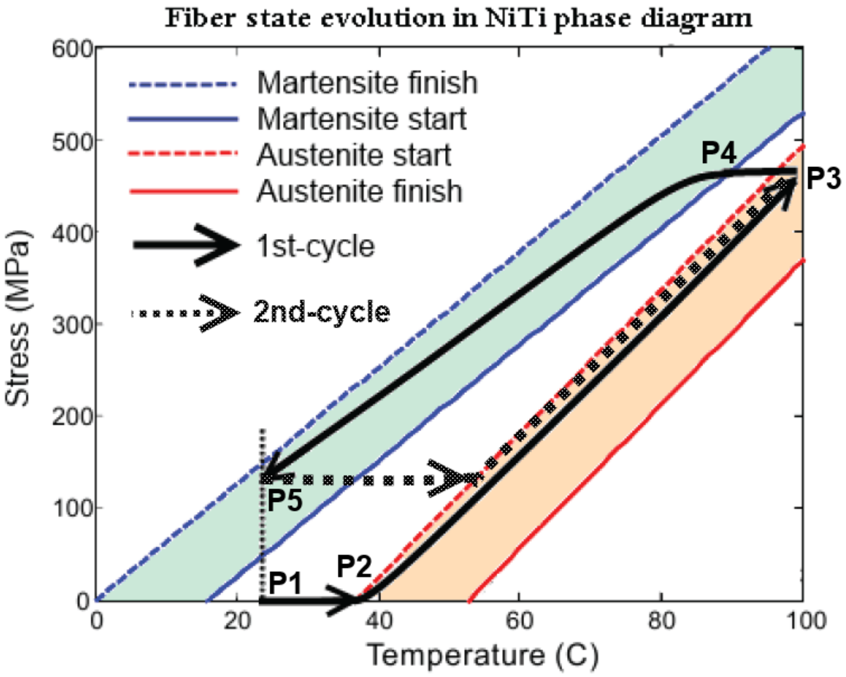

Figure 7.10: Schematic illustration of axial stress state of NiTi during temperature cycling, shown on the stress-temperature phase diagram. The first temperature cycle of the material creates a state of tension due to the material not fully transforming back to the initial Martensitic volume fraction. Subsequent cycles coalesce.

Optical images of the end of the composite before and after heating are shown in Figure 7.11. To avoid actuation during sample mounting, the samples were mounted in epoxy. Imaging was carried out to qualitatively evaluate the integrity of the fiber-matrix interface. The composite end was imaged to assess the shear transfer taking place between the NiTi fiber and Al matrix. Damage in the composite due to testing is likely to initiate at the composite end. The image is inverted since the image is not of the same sample but is of the same cross section, i.e., some material was removed between samples with a saw. As a result, key fibers have been boxed. Some voids are present in the composite prior to testing, yet no obvious cracking can be seen. After testing, the composite remains crack free and voids appear to collapse around the fibers.

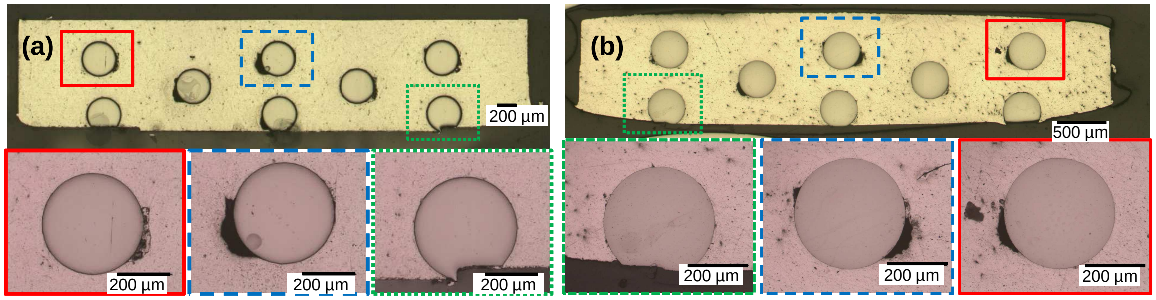

Figure 7.11: End cross section of 13.8% NiTi composite: (a) the composite before heating, some void presence can be seen with no obvious cracking; (b) the composite after 3 heating cycles, little to no cracking formed during thermal cycling.

Strain to failure and ASTM creep testing was carried out on a welded piece of Al 6061-H18 at 100°C to evaluate the plasticity behavior of the metal, see Figure 7.12. Both samples utilized a sub-sized ASTM dog-bone geometry for testing and used Micro Measurement WK 13031CF350 strain gauges. The metal demonstrates ductility shortly after the ultimate strength of the material. This ductility could enable the void collapse around the fibers. The aluminum also exhibits large amounts of creep. Creep in this alloy is somewhat expected due to it not being heat treated after rolling and because residual stress is likily present in the material after construction. This creep behavior is also an enabler for void collapse within the sample around the fibers. Creep also explains the excessive curvature on the first heating cycle of the composite.

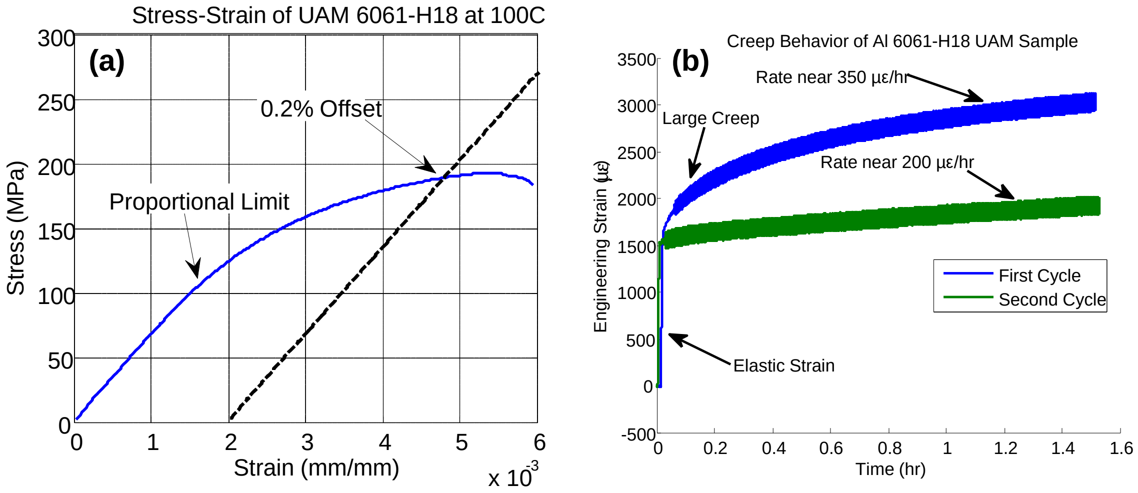

Figure 7.12: Al 6061-H18 plasticity at 100°C: (a) stress-strain showing ductility after 200 MPa; (b) creep test showing decreasing creep with cycling.

7.3 Composite Modeling

Numerical simulations of the composite were conducted by X. Chen to better understand the behavior of the fabricated Al-NiTi composite, especially the matrix-fiber interaction that determines its performance. The primary challenges in modeling are to accurately describe the response of isolated NiTi-fibers and the physics of stress redistribution within the fiber-matrix composite. A microstructural finite element constitutive model [64] was utilized to meet both challenges. This model is implemented as a User-defined MATerial (UMAT) subroutine in the commercial finite element package ABAQUS [3]. Due to the computation requirements of the model, the Ohio Supercomputer Center was utilized.

This microstructural model describes underlying NiTi physics, i.e., texture effects, martensite variant interaction, and crystal plasticity. Overall, it can simulate a variety of engineering materials and predict the stress redistribution and local thermo-elastic response within the composite. Previous models of NiTi-Al composites utilized a phenomenological approach implemented in MATLAB [34, 35]. Although they require little computational power, these models describe only the axial stress state of the NiTi fiber and did not predict the interface or shear stress. They also utilize empirical properties of the material, which limits simulation capability.

The NiTi fiber response was calibrated to the stress-strain response at three different temperatures and the critical transformation temperatures determined from Differential Scanning Calorimetry (DSC), see Figure 7.13. The difference between the model and experimental curves is near 10%. More details on this calibration process and model parameters can be found in Chen et al [15].

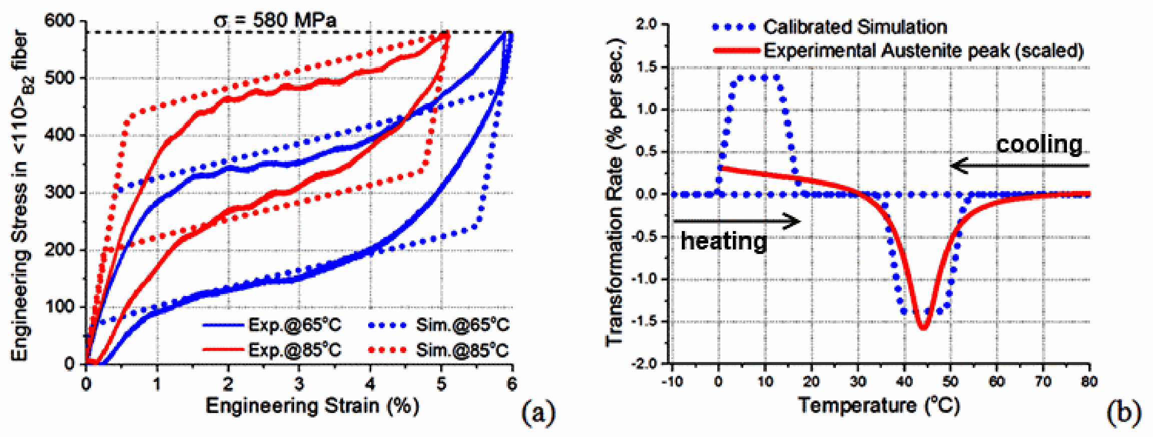

Figure 7.13: NiTi FE model calibration showing the fit to experimental data: (a) uniaxial tension at 65°C and 85°C for a <110>B2-oriented NiTi fiber; (b) DSC curves.

After calibration, the UAM fabrication process and thermal testing process was virtually simulated. First, the fiber is stretched to 400 MPa above A_f and then cooled below M_f to form stress induced or oriented Martensite. Then, the aluminum matrix is bonded to the fiber at room temperature. Four thermal cycles are then imposed upon the matrix. This simulation procedure is graphically detailed in Figure 7.14.

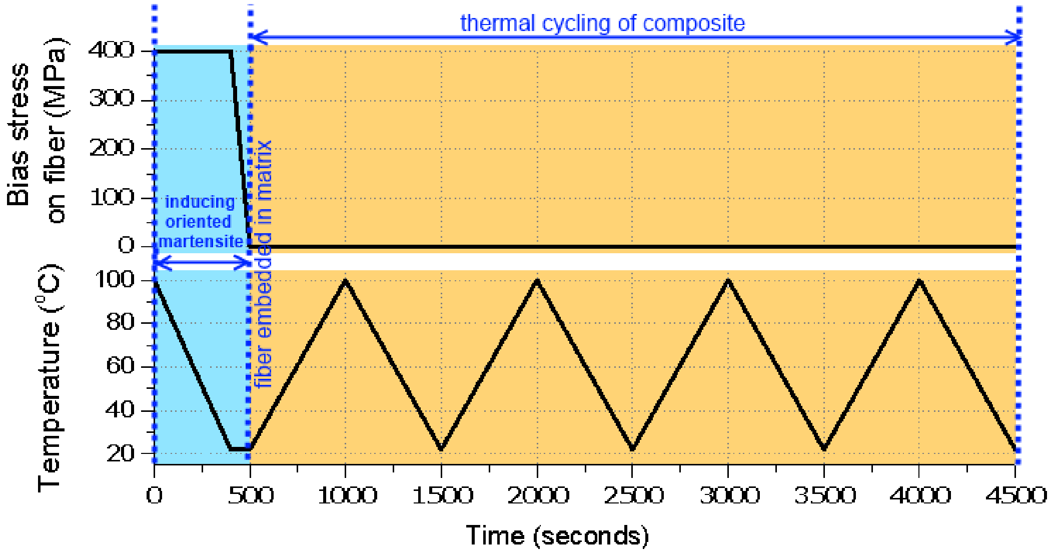

Figure 7.14: Simulated mechanical and thermal loadings: the NiTi fiber is first cooled under a tensile stress of $\sigma_{\text{bias}} = 400$ MPa in the absence of Al matrix to induce oriented martenite, and then unloaded at 22°C (blue regime). This is followed by embedding the fiber in matrix at $t = 500$s. The heating-cooling cycle of the composite from 22°C to 100°C is repeated 4 times (orange regime) to study the evolution of performance.

Modeling assumptions and model variables are thoroughly detailed in Chen et al [15]. Key similarities across the simulations are that no plasticity is assumed in the NiTi, one eighth of the composite is simulated with the use of symmetry, 13% volume fraction of the fiber is assumed, a fiber aspect ration of 20:1 is used, uniform heating and cooling is assumed within the composite, and no-slip occurs between the fiber and matrix. The FEM is shown in Figure 7.15.

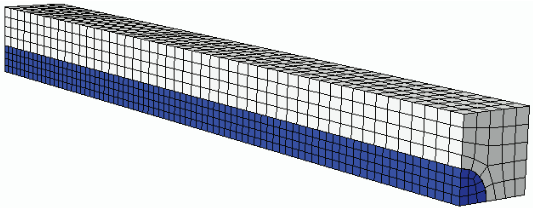

Figure 7.15: The finite element model of the composite. Three mirror-plane conditions are applied two of them through the center axis of the fiber (shown in blue), while the remainder is perpendicular to the fiber.

Results for an elastic aluminum matrix is shown in Figure 7.16. An elastic matrix describes the general qualitative trends of the composite well. Quantitative disagreements lie with respect to the shape of the first cycle and the amount of hysteresis present (ϵ_{hyst} in subsequent cycles. Results for an aluminum matrix with plasticity, void collapse, and a reduced driving force for the NiTi are shown in Figure 7.17. Very close qualitative and quantitative results were obtained. Void collapse and plasticity create the curvature found during the first temperature cycle. The reduced driving force causes the simulation to match the empirical hysteresis behavior. It is suspected that the ultrasonic welding process could cause dislocation motion and grain rotation within the NiTi, which, in turn would influence the hysteresis of the material. This hypothesis requires further investigation.

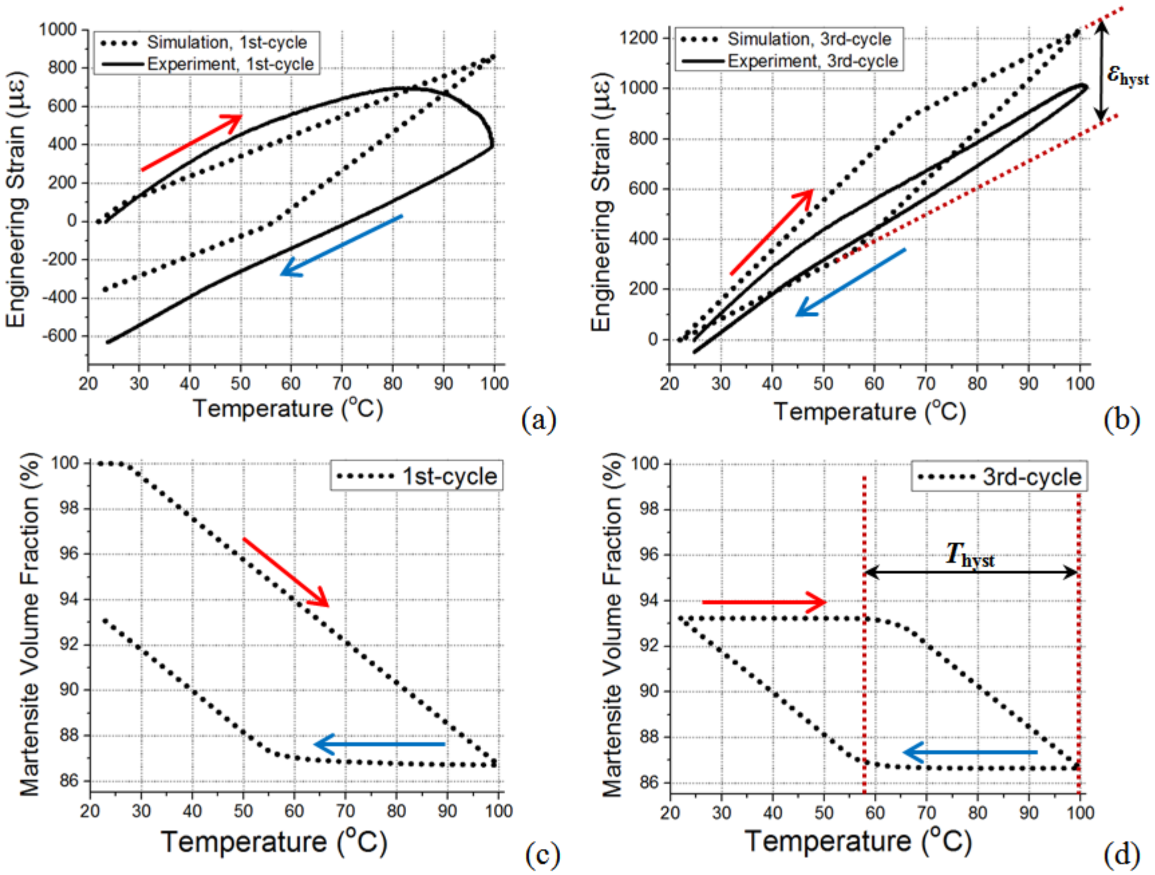

Figure 7.16: Simulation results for a Al-NiTi composite with a thermo-elastic (non-plastic) matrix: (a) first cycle; (b) subsequent cycles (which overlap); (c) and (d) corresponding evolution of martensite volume fraction in the NiTi fiber. The simulation describes general trends with modest quantitative agreement.

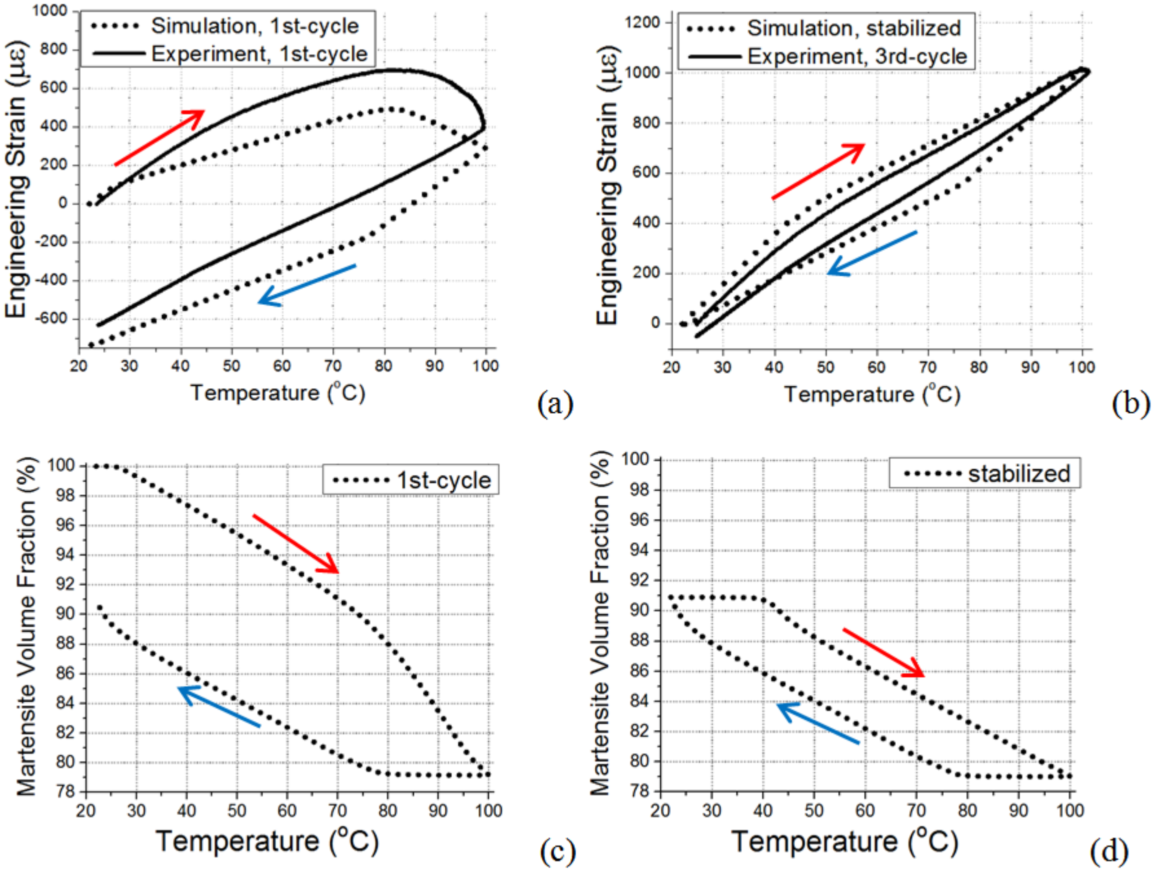

Figure 7.17: Simulation results for a Al-NiTi composite with plasticity, void collapse, and a modified driving force for the NiTi: (a) first cycle; (b) subsequent cycles (which overlap); (c) and (d) corresponding evolution of martensite volume fraction in the NiTi fiber. The simulation describes general trends with close quantitative agreement.

Modeling efforts have shown close agreement with empirical observations. The influence of grain texture and fiber aspect ratio on composite performance is also evaluated in Chen et al [15]. Optimal textures exist for enhanced thermal response efficiency. In other words, less NiTi can be used to create the same thermal response for specific textures. Albeit, some of these textures may not be possible to fabricate, the model provides insight into new ways to improve the composite. Fiber aspect ratio does not impact composite response once the aspect ratio is sufficently large (greater than 10 here). This behavior is consistent with fiber composite shear-lag theory [14].

7.4 State-of-the-Art

NiTi-Al composite construction can be expedited with the use of larger fibers. The engineering trade-off is that consolidation behavior often degrades with larger fibers. It was found that this degradation in consolidation behavior can be remedied with a rough surface finish on the fiber, see Chapter 6. Consequently, larger fiber geometries were embedded with various surface finishes to qualitatively compare consolidation behavior, see Figure 7.18. It is shown that a rougher surface finish enhances consolidation quality while a more smooth finish often leaves voids.

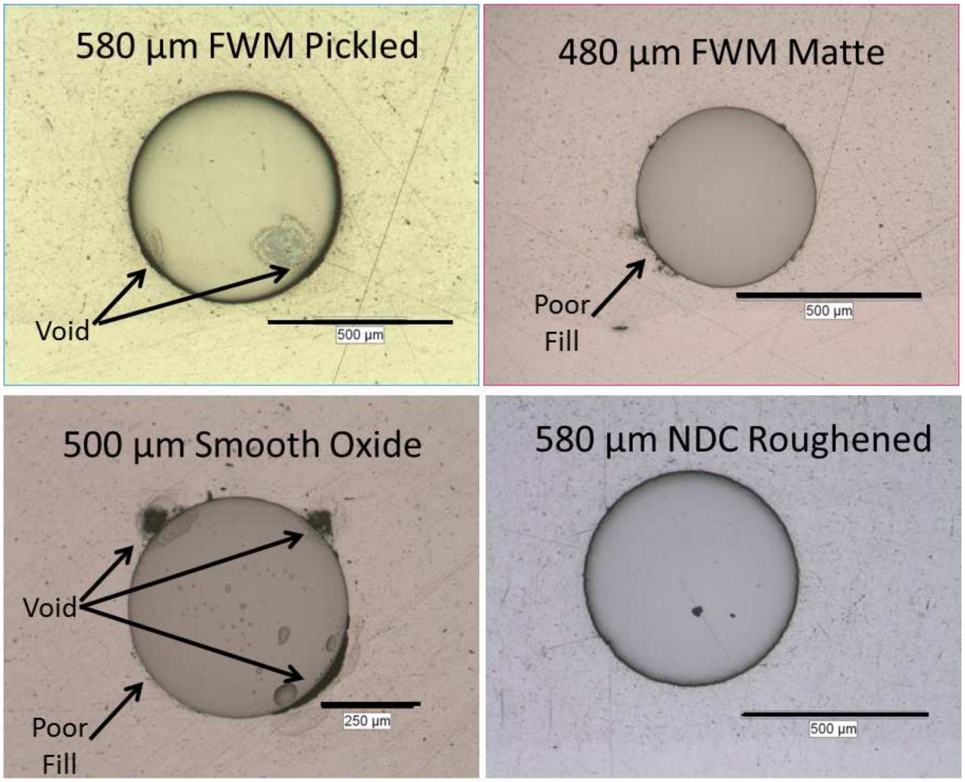
580 µm FWM Pickled
Void
500 µm
480 µm FWM Matte
Poor Fill
500 µm
500 µm Smooth Oxide
Void
Poor Fill
250 µm
580 µm NDC Roughened
500 µm

Figure 7.18: Consolidation evaluation of NiTi fibers near 500 μm in diameter. A more rough surface finish enables improved consolidation quality.

Pickled NiTi No. 6 material was ordered from Fort Wayne Metals (FWM) to continue

Table 7.3: Phenomenological properties of 580 μm diameter FWM NiTi No. 6 found via characterization.

E_M(MPa)	E_A(MPa)	C_M(MPa/^oC)	C_A(MPa/^oC)	A_s(^oC)	A_f(^oC)	M_f(^oC)	M_s(^oC)	ϵ_0(%)
20	40	6.3	7.5	48	62	7	23	2.5

NiTi-Al composite research. The diameter of the material is 580 μm, and the Austenite start temperature is designed to be near room temperature. The phenomenological properties are listed in Table 7.3. These properties were obtained following similar characterization procedures as those described in Section 7.2.1. Using these properties along with a rule-of-mixture NiTi-Al model, the thermal expansion performance of the composite can be estimated for a specific volume fraction. The desired response is 5 $\mu\epsilon/^oC$, and it was found that a volume fraction of 18% is required, see Figure 7.19. More details on this model are given in Chapter 8.

Empirical thermo-mechanical results for the composite are shown in Figure 7.20. Due to manufacturing tolerances, the final volume fraction of the composite is near 19.5%. It is shown that the average coefficient of thermal expansion (CTE) after the first temperature cycle is near 6.5 $\mu\epsilon/^oC$ for the heating and cooling curves. Separately, CTEs of 5.9 $\mu\epsilon/^oC$ and 7.2 $\mu\epsilon/^oC$ for the heating and cooling portions, respectively. These CTE differences lie in the stress influence coefficients for each respective transformation (see Table 7.3). The average composite CTE is near 28% of the CTE for homogeneous Al. In other words, a reduction of 72% was achieved for a multi-fiber composite after multiple cycles.

Metallurgical cross sectioning and polishing was carried out to evaluate consolidation quality before testing, see Figure 7.21. Cracks and voids are present in the composite. It is suspected that the cracks originated due to the fiber pockets not being deep enough, which, in turn limits consolidation effectiveness. Voids originate from the surface finish not having an adequate surface finish. Despite these consolidation limitations, the thermo-mechanical response of the composite is near estimates. If consolidation quality is improved, it is suspected that this performance will only improve.

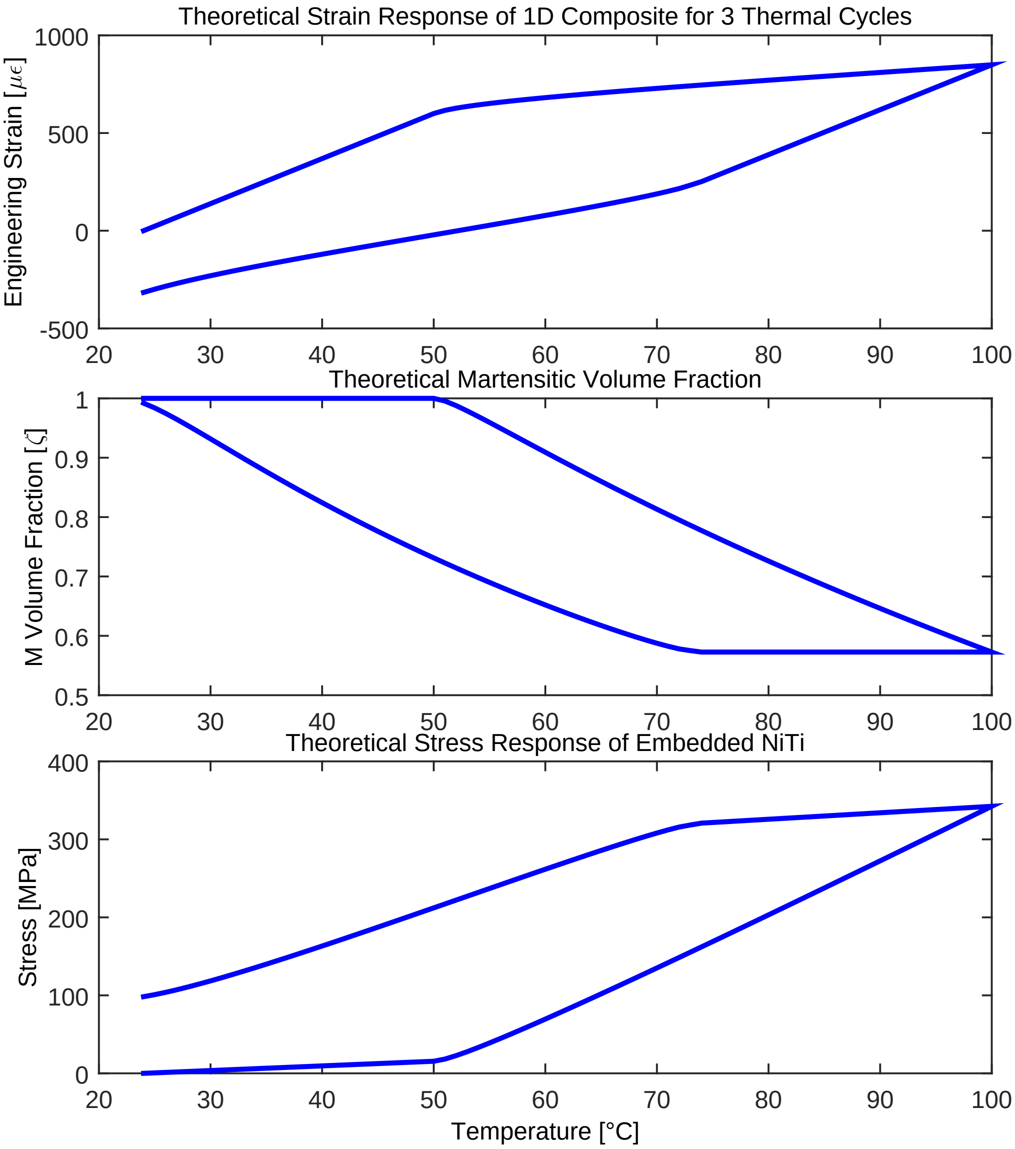

Figure 7.19: Estimated thermal expansion response using improved Hanlen NiTi-Al composite model. A thermal expansion of 5 $\mu\epsilon/^{\circ}C$ was obtained using a volume fraction of 18%.

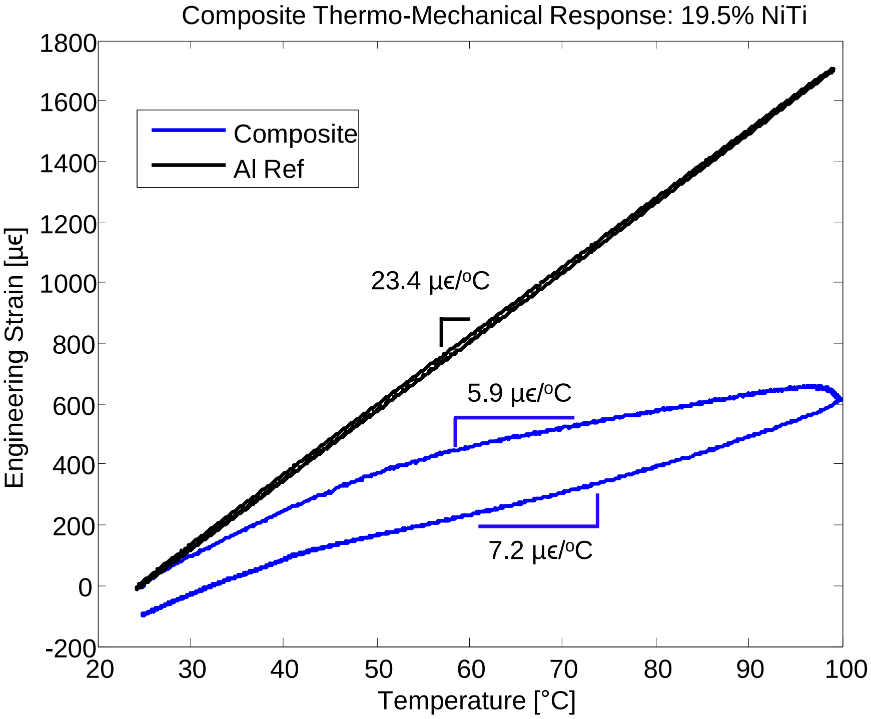

Figure 7.20: Thermal expansion response of state-of-the-art NiTi-Al composite. A thermal expansion reduction of 72% was obtained when compared to homogeneous Al.

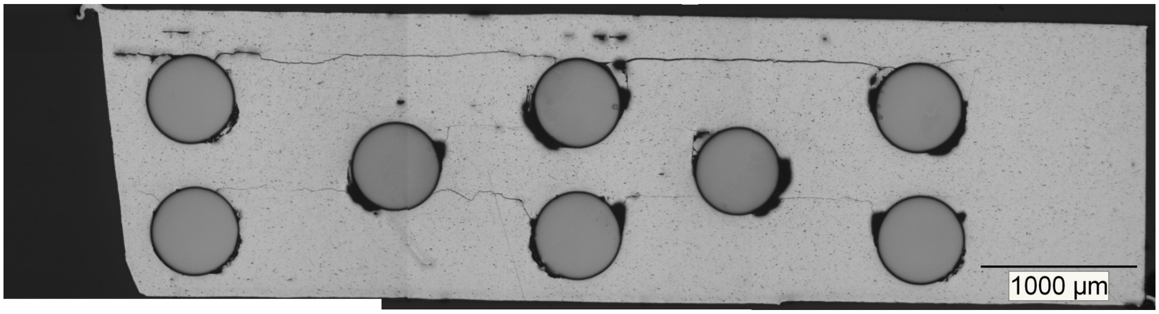

Figure 7.21: State-of-the-art NiTi-Al composite cross section. Cracks and voids are present within the build due to inadequate channel depth. Despite non-ideal consolidation characteristics, the composite performs near expectations.

7.5 Summary

This chapter evaluates procedures for scaling up NiTi-Al composites in UAM. The chapter starts with selecting, preparing, and understanding the shape memory NiTi material. The requirement to train or stabilize NiTi material once procured is discussed. The characterization techniques of isothermal stress-strain testing and differential scanning calorimetry are then discussed. These characterization tests can be used to find the stress-temperature phase diagram of the material.

Composite fabrication and testing techniques are then given. More details about composite fabrication and CTE testing are given in Appendix E. Reproducible low thermal expansion values are given for the first time. The behavior of the composite is also described using the stress-temperature phase diagram. Further behavior is described through high temperature stress-strain and creep testing of the aluminum matrix. This mechanical testing is used to inform collaborative modeling efforts with the Anderson group at Ohio State. This modeling effort qualitatively and quantitatively described the composite performance.

Lastly, state-of-the-art composite design and testing results are reported. This composite used unprecedented fiber sizes to achieve the largest functional NiTi-Al composite to date. This composite also exhibited the lowest thermal expansion, despite having cracks and voids. These selection, fabrication, and testing procedures can be used to construct a large NiTi-Al composite for engineering applications.

Chapter 8

IMPROVEMENTS TO THE HAHNLEN MODEL

8.1 Introduction

This chapter discusses improvements to the phenomenological Hahnlen NiTi composite model. This model was originally formulated by R. Hahnlen [34], and the model utilizes the Brinson phenomenological model for NiTi [11] combined with elastic solid mechanics to estimate composite response [40]. Because the model utilizes lumped parameters to estimate response, low computational power resources can be used to run the model when compared to the more detailed microstructural NiTi FEM presented in Chapter 7, which was run at the Ohio Supercomputer Center. Albeit computationally more efficient, the model over-estimates composite response due to incorporating only the axial stress state.

The chapter starts off by explaining the assumptions of the Hahnlen NiTi-Al composite model and its limitations. Improvements to the model are then presented and described. Both models are then compared against empirical data to better illustrate improvements. Lastly, empirical axial (x direction) and lateral (y direction) strains are compared against the improved model and found to demonstrate good qualitative and quantitative agreement.

8.2 Hahnlen Model Summary and Limitations

The Hahnlen model [34] utilizes the Brinson phenomenological model [11] combined with solid mechanics [40] to estimate composite response for a given fiber volume fraction (v_f). The model begins by formulating the Brinson model in terms of strain and not stress,

$$\epsilon_f = \frac{1}{E_f}\sigma_f + \alpha_f \Delta T + \epsilon_0(\zeta_s - \zeta_{so}), \tag{8.1}$$

where ϵ_f is the fiber or axial strain, E_f the modulus of the material as a function of the Martensite volume fraction (ζ), σ_f is the axial stress, α_f is the coefficient of thermal expansion, ΔT is the temperature rise in the material, ϵ_0 is the amount of recoverable strain in the shape memory alloy or NiTi fiber, ζ_s is the instantaneous stress induced Martensite volume fraction, and ζ_{so} is the initial stress induced Martensite volume fraction. For the NiTi used in this thesis, temperature induced Martensite does not occur due to the Martensite start temperature being near or lower than room temperature. Hence, the initial stress induced Martensite volume fraction is equal to the total Martensite volume fraction.

If one assumes that no slip occurs between the NiTi and aluminum matrix within the composite, the strains along the axial direction (x) can be equated. If one only includes the axial strain, the following expression for axial fiber stress can be found,

$$\sigma_f = \frac{E_m(\alpha_m - \alpha_f)\Delta T}{\frac{E_m}{E_f} + V_x} - \frac{E_m \epsilon_0(\zeta_s - \zeta_{so})}{\frac{E_m}{E_f} + V_x}. \tag{8.2}$$

The m subscript here represents the matrix while f represents the fiber. V_x is a commonly occurring expression composed of the fiber volume fraction (v_f) along the axial direction of the fiber (x direction),

$$V_x = \frac{v_{x,f}}{v_{x,f} - 1}, \tag{8.3}$$

where $v_{x,f}$ is the ratio of axial fiber area over the total cross sectional area of the composite. V_x linearly relates the axial matrix stress to the axial fiber stress,

$$\sigma_{x,m} = V_x \sigma_{x,f}. \tag{8.4}$$

This model is implemented in Matlab by iteratively solving the stress relationship (8.2) within the expected transformation bounds determined by the stress influence coefficients on the stress-temperature phase diagram. Outside of these transformation bounds, the composite is assumed to exhibit linear material behavior, i.e. no NiTi transformation term in the expression (8.2). The calculated stress as a function of temperature is then utilized to estimate composite strain. Because both the fiber and matrix strains are equal to the composite strain, either can be used to estimate the total composite strain. For simplicity, the matrix strain is used. Matrix strain is calculated by first relating the fiber stress to the matrix stress via V_x. Then, strain is calculated using linear elastic mechanics in the axial direction only.

The Hahnlen model enables fast and easy NiTi composite simulation. However, the model has been found to over-estimate response by Hahnlen [34] and by the author. To identify why the model over-estimates response, the limitations of the model are given below with proposed solutions/explanations:

- Lack of incorporation of Poisson ratio effects, i.e., other normal stress states.
  - These other normal stress states can be incorporated using additional constraints and assumptions of the fiber and matrix. This is the most substantial improvement to the Hahnlen model.
- No incorporation of NiTi anisotropy.
  - NiTi anisotropy is difficult to incorporate because measuring the full compliance matrix and thermal expansion matrix of NiTi wire is nontrivial. It is assumed in this work that NiTi is a homogenous material and can be modeled soley with the modulus of elasticity and the Possion ratio.
- No incorporation of fiber shear-lag.
  - In large aspect ratio fiber composites, the influence of shear lag on bulk response is negligible since shear lag is localized to the end of a composite within a few fiber

  diameters. Because all tested composites have large aspect ratios, neglecting end effects is adequate.

- Stress-state influence on Martensitic variants is not included.
  - Incorporating the influence of multiple stress states on the Martensitic variants is not easy. However, if the material is trained in one direction, it can be assumed that the variants are influenced primarily by that stress state only.

8.3 Improvements to the Model

A comprehensive force balance between internal forces within the composite in the x, y, and z directions is shown in Figure 8.1. These free-body-diagrams are drawn to articulate the incorporation of the other normal stress states. Assuming that the NiTi behaves as a homogeneous material, the Brinson expression (8.1) can be modified to include the y and z components,

$$\epsilon_{x,f} = \frac{1}{E_f}\big[\sigma_{x,f} - \mu_f(\sigma_{y,f} + \sigma_{z,f})\big] + \alpha_{x,f}\Delta T + \epsilon_0(\zeta_s - \zeta_{so}). \tag{8.5}$$

The strain in the y is also written assuming that the recoverable strain in the y direction can be estimated via the Poisson ratio,

$$\epsilon_{y,f} = \frac{1}{E_f}\big[\sigma_{y,f} - \mu_f(\sigma_{x,f} + \sigma_{z,f})\big] + \alpha_{y,f}\Delta T - \mu_f\epsilon_0(\zeta_s - \zeta_{so}). \tag{8.6}$$

A similar expression (8.6) exists for the z direction. Likewise for the strain in the matrix,

$$\epsilon_{x,m} = \frac{1}{E_m}\big[\sigma_{x,m} - \mu_m(\sigma_{y,m} + \sigma_{z,m})\big] + \alpha_{x,m}\Delta T. \tag{8.7}$$

Similar expressions (8.7) exist in the Y and Z directions too.

From the list of assumptions in Section 8.1 and from the free body diagrams in Figure 8.1, the following assumptions can be made:

- Equivalent strain in the axial or x direction for the fiber and matrix. This is true considering that the fiber and matrix are assumed to move together if no interface

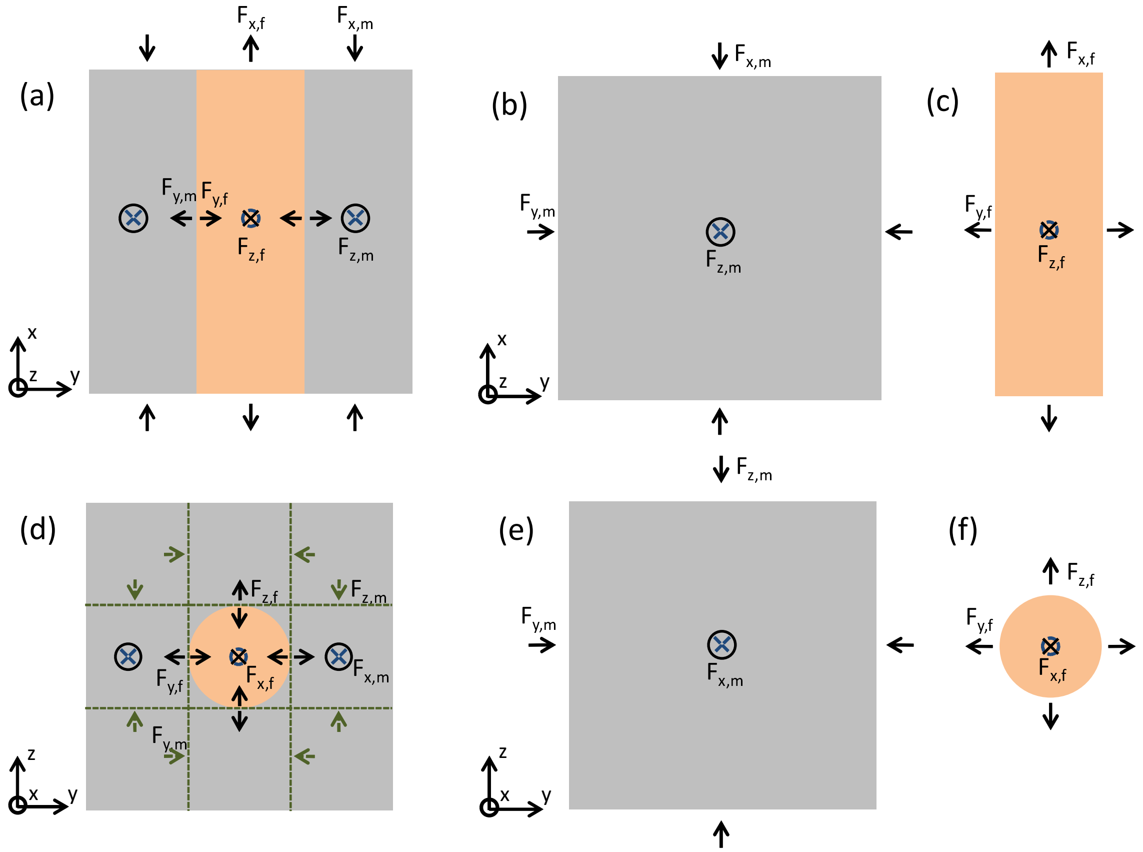
(a)
$F_{x,f}$
$F_{x,m}$
$F_{y,m}$
$F_{y,f}$
$F_{z,f}$
$F_{z,m}$
x
z
y
(b)
$F_{x,m}$
$F_{y,m}$
$F_{z,m}$
x
z
y
(c)
$F_{x,f}$
$F_{y,f}$
$F_{z,f}$
(d)
$F_{z,f}$
$F_{z,m}$
$F_{y,f}$
$F_{x,f}$
$F_{x,m}$
$F_{y,m}$
z
x
y
(e)
$F_{z,m}$
$F_{y,m}$
$F_{x,m}$
z
x
y
(f)
$F_{z,f}$
$F_{y,f}$
$F_{x,f}$

Figure 8.1: NiTi-Al composite force analysis: (a) xy plane of representative composite area element; (b) projected forces from (a) onto the matrix; (b) projected forces from (a) onto the fiber; (d) zy plane of representative composite area element; (e) projected forces from (d) onto the matrix; (f) projected forces from (d) onto the fiber. In general, the interface is in tension, which, in turn puts the matrix in compression in the z and y directions and the fiber in tension in the z and y directions.

slip occurs. This is an original assumption utilized in the Hahnlen model.

$$\epsilon_{x,f} = \epsilon_{x,m} \tag{8.8}$$

- Equivalent strain in the y and z directions for the fiber and matrix. This assumption is true only for areas of the composite which are stressed from the constraint. Thus, a follow-up assumption will be given shortly to homogenize the composite and allow these strain constraints to be applied to the entire composite.

$$\epsilon_{y,f} = \epsilon_{y,m} \text{ and } \epsilon_{z,f} = \epsilon_{z,m} \tag{8.9}$$

- Strain in y and z directions are equal in both the fiber and matrix. This assumption is true if the stress distribution is symmetric in both the y and z directions.

$$\epsilon_{y,f} = \epsilon_{z,f} \text{ and } \epsilon_{y,m} = \epsilon_{z,m} \tag{8.10}$$

- Force balance between fiber and matrix in actuation or axial direction (x). This is another original assumption in the Hahnlen model. The fiber volume fraction in the x direction, $v_{x,f}$, is often expressed as a reoccurring ratio, V_x (see 8.4). The fiber volume fraction is expressed as the ratio of cross sectional area of fiber against the composite. The expression for $v_{x,f}$ and V_x is shown again for completeness,

$$\sigma_{x,m} = (\frac{v_{x,f}}{v_{x,f} - 1})\sigma_{x,f} = V_x \sigma_{x,f}, \text{ where } v_{x,f} = \frac{n\pi D^2}{4W^2}, \tag{8.11}$$

here n is the number of fibers in the composite, D is the fiber diameter, and W is the width and height of the composite (assuming a square geometry). These dimensions are detailed in Figure 8.2(a).

- Force balance between fiber and matrix in passive directions of fiber (y and z). The force balance takes place between the acting perpendicular fiber area, DL, and the acting matrix area constrained by the fiber, $(W - D)L$,

$$\sigma_{y,m} = (\frac{v_{y,f}}{v_{y,f} - 1})\sigma_{y,f}, \text{ where } v_{y,f} = \frac{DL}{WL} \text{ or } 2\sqrt{\frac{v_{x,f}}{\pi}} \text{ for circle geometry,} \tag{8.12}$$

where L is the length of the fiber. This force balance only takes place in the cross hashed region in Figure 8.2(a), which has been verified via COMSOL simulation, see Figure 8.2(b). Consequently, the actual volume of matrix influenced is smaller than the total volume. In other words, the entire matrix does not participate in the force balance. To homogenize the stress across the entire volume, the ratio (H_R) of actual volume (V_A) of matrix influenced over the total volume (V_T) of matrix needs to be found,

$$H_R = \frac{V_A}{V_T} = \frac{\big((W-D)D + D^2 - \frac{\pi D^2}{4}\big)L}{\big(W^2 - \frac{\pi D^2}{4}\big)L} = \frac{v_{y,f} - v_{x,f}}{1 - v_{x,f}}. \tag{8.13}$$

To incorporate H_R, the force balance can be multiplied to distribute the stress over the entire volume (V_y),

$$\sigma_{y,m} = \big(\frac{v_{y,f}}{v_{y,f} - 1}\big)\big(\frac{v_{y,f} - v_{x,f}}{1 - v_{x,f}}\big)\sigma_{y,f} = V_y \sigma_{y,f}. \tag{8.14}$$

- Because the strains in the fiber and matrix are equal in the y and z directions and materials are assumed to be homogeneous, the respective stresses are also equal,

$$\sigma_{z,f} = \sigma_{y,f} \text{ and } \sigma_{z,m} = \sigma_{y,m}. \tag{8.15}$$

- Assume that the Poisson ratio is equal in the matrix and fiber for simplicity,

$$\mu_f = \mu_m. \tag{8.16}$$

Using these assumptions and expressions 8.5 and 8.7, the fiber stress in the axial direction can be found by equating axial strains (see expression 8.8),

$$\sigma_{x,f} = \frac{\mu(\frac{E_m}{E_f} + V_y)\sigma_{y,f}}{\frac{E_m}{E_f} + V_x} + \frac{E_m(\alpha_m - \alpha_f)\Delta T}{\frac{E_m}{E_f} + V_x} - \frac{E_m \epsilon_0 (\zeta_s - \zeta_{so})}{\frac{E_m}{E_f} + V_x}. \tag{8.17}$$

Note that expression (8.17) for the axial stress (x direction) is identical to the Hahnlen model expression (8.2) for the axial stress, yet an additional term arises from the Poisson ratio. Likewise, the stress in y can be found,

$$\sigma_{y,f} = \frac{\mu(\frac{E_m}{E_f} + V_x)\sigma_{x,f}}{(1-\mu)(\frac{E_m}{E_f} + V_y)} + \frac{E_m(\alpha_m - \alpha_f)\Delta T}{(1-\mu)(\frac{E_m}{E_f} + V_y)} - \frac{E_m \mu \epsilon_0 (\zeta_s - \zeta_{so})}{(1-\mu)(\frac{E_m}{E_f} + V_y)}. \tag{8.18}$$

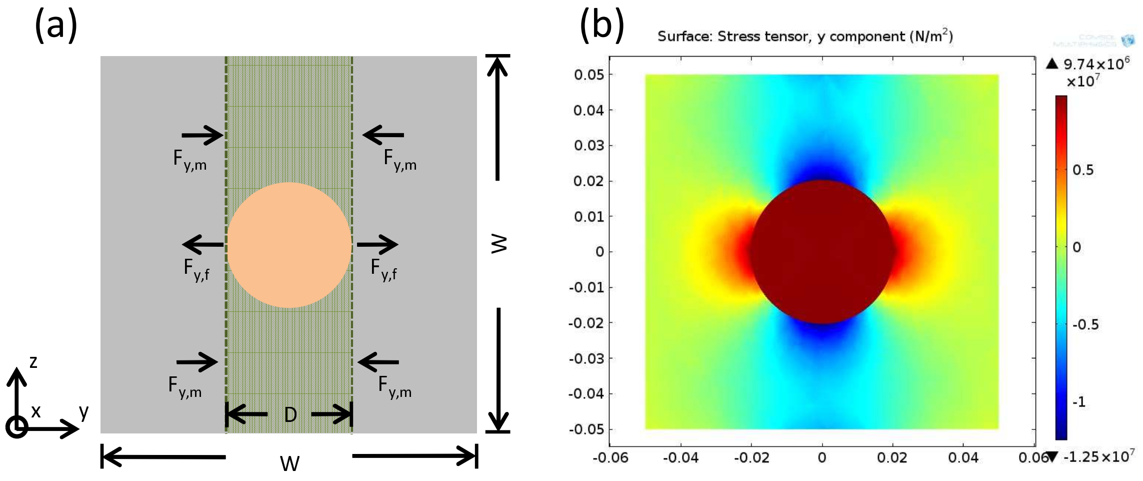

Figure 8.2: Volume fraction analysis for y stress: (a) a representative composite element illustrating how the stress will be localized to the area bound by the fiber; (b) COMSOL simulation of 13% NiTi and Al illustrating validity of assumption due to the entire fiber being in tension while only areas bound by the fiber in the matrix are in compression.

Similar to expression (8.17), there is a Poisson ratio term, a temperature term, and a transformation term. If (8.18) is substituted into (8.17), the following expression can be found for the axial stress,

$$\sigma_{x,f} = C_H \frac{E_m(\alpha_m - \alpha_f)\Delta T}{\frac{E_m}{E_f} + V_x} - \frac{E_m \epsilon_0 (\zeta_s - \zeta_{so})}{\frac{E_m}{E_f} + V_x}, \tag{8.19}$$

where,

$$C_H = \frac{1+\mu}{1-\mu-2\mu^2}. \tag{8.20}$$

Similarly for the y stress,

$$\sigma_{y,f} = C_H \frac{E_m(\alpha_m - \alpha_f)\Delta T}{\frac{E_m}{E_f} + V_y}. \tag{8.21}$$

The temperature stress term in expressions (8.19) and (8.21) is the only term which is influenced by multiple stress components. The transformation term only occurs in the actuation direction (8.19), and it is the same form as originally modeled by Hahnlen (8.2).

8.4 Empirical Validation

The original and improved Hahnlen model are compared in Figure 8.3(a) against the first cycle of a 13% v_f composite. It is shown in the plot that the original (1D) model overestimates the response of the composite while the improved model (3D) exhibits improved correlation up to the yield point of the composite. This model error becomes more significant with larger volume fractions, see Figure 8.3(b).

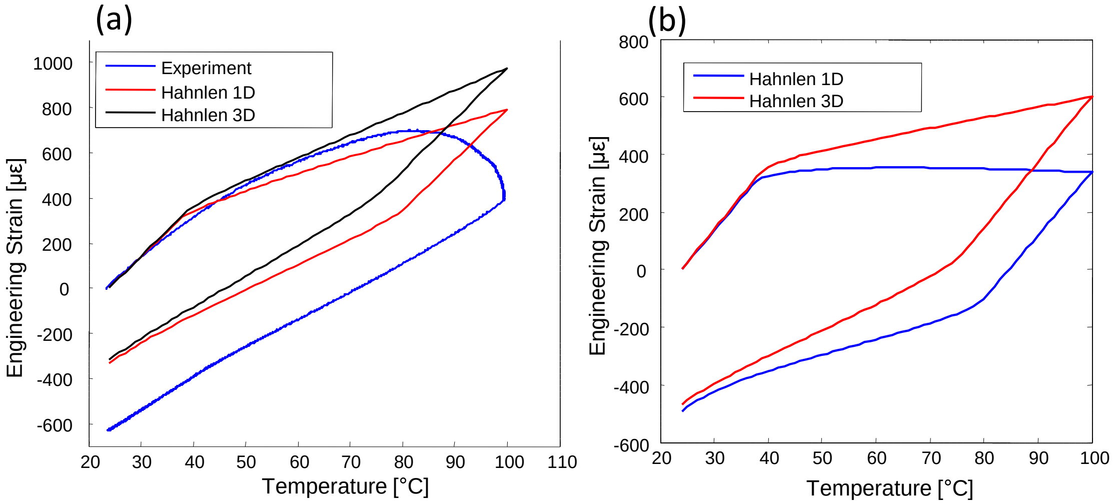

Figure 8.3: Comparison of original (1D) and improved Hahnlen model (3D): (a) models shown against experiment for 13% v_f; (b) models with 18% v_f. The 1D model overestimates response, and this error becomes larger at higher volume fractions.

Chapter 7 discusses state-of-the-art results for a 19.5% v_f composite. The size of this composite allowed mounting of strain gauges in the axial (x) and lateral (y) directions. First cycle response of this composite is compared against the improved model and homogenous aluminum in Figure 8.4. In general, the model (i) describes the hysteretic behavior of the composite and (ii) estimates the similar magnitude response in both strain directions. The hysteretic behavior in the laterial (y) direction is small due to the material not actuating in that direction. Instead, hysteresis originates in the changing modulus of elasticity of the

NiTi. Yielding and void collapse of the composite is not described with this model.

The response of Figure 8.4(a) is expected from previous composite testing (see Chapter 7). On the other hand, the response of Figure 8.4(b) is not intuitive at first due to the composite strain being larger than homogenous aluminum. This large strain response occurs due to the large compressive stress in the axial direction of the composite. As a result, an outward bulging occurs and dramatically increases the lateral strain response.

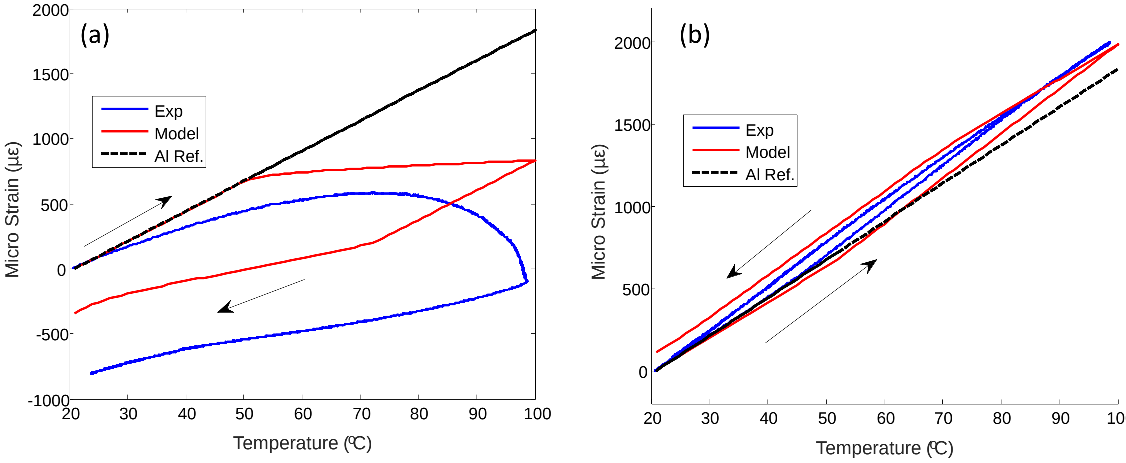

Figure 8.4: Validation of model against 19.5% v_f: (a) first cycle of axial (x) strain; (b) first cycle of lateral (y) strain. Arrows are shown to illustrate heating and cooling response directions of the composite. General trends and magnitudes are described with the model.

8.5 Summary

This chapter describes improving state-of-the-art phenomenological modeling of NiTi-Al composites originally devised by R. Hahnlen. Improvement is required to improve model accuracy and to obtain composite strain results in the radial direction of the fiber. The key improvement to the model is the incorporatation of the radial stresses. Many assumptions are given to homogenize the stresses in the composite and to describe the behavior of the NiTi. Despite the many assumptions, the improved model describes composite performance more accurately in the axial direction and closely describes the strain behavior in the radial direction. A big picture flow diagram of the algorithm used herein is shown in Appendix F.

This improved model is useful for designing composites with tailorable thermal expansion in multiple directions. The model uses the assumption of a fiber embeddment currently, but can be easily modified to incorporate sheet materials. This model is also much faster and more easy to implement than the microstructural NiTi FEM discussed in Chapter 6. The tradeoff is that it does not capture the full stress tension and is not as adaptable to other kinds of analysis, i.e., thermal, electrical, etc.

Chapter 9

CONCLUSION

9.1 Summary of Findings

The thesis begins by discussing how increased mechanical energy input into welds was found to enhance bond strength and quality during a statistical parametric study. This relationship between welder energy and bond strength was investigated further, and it was found that enhanced average electric weld power led to increased recrystallized grain volume at the weld interface. More recrystallized grain volume is observed with higher welder amplitudes due to enhanced strain energy input into the interface combined with recrystallization being a strong function of strain. Improved bonding occurs when more recrystallized grains are present because the grain boundaries act as barriers to crack and dislocation propagation within the microstructure, i.e., Hall-Petch relationship. Because grain boundaries each have their own associated energy, a higher concentration of grains implies more energy storage in the microstructure. A Conservation of Energy expression has been proposed to explain and relate mechanical strain input energy with resultant recrystallized grain volume energy. Additionally, compliance of the UAM part was found to influence the power draw or effort of the welder. As the UAM part became more compliant with increasing layers, the average electric power draw decreased. This decrease in power was remedied by increasing the welder amplitude since welder amplitude influences mechanical power input. The impact of this relationship is that welder amplitude can be used to control the average electric weld power input, and ultimately, resultant component quality.

Because electrical energy input into the structure impacts bond quality, it is of interest to understand the energy conversion within the welder itself. In other words, it is important to understand the energy conversion from electrical to mechanical domains within the welder because mechanical energy input into the weld is what influences bond quality. A linear time invariant (LTI) model is proposed to describe this energy conversion. The system inputs of welder current and welder shear force are used with the system outputs of welder velocity and voltage to describe the energy transfer characteristics of the system. The model utilizes classic electroacoustics theory for piezoelectric devices to develop an equivalent circuit of the system. Experimental frequency response functions (FRFs) of the welding assembly are then compared to the developed equivalent circuit to ensure the model describes the welder adequately. Close agreement was found between theory and experiment. In-situ measurements of the welder operating under no load were then taken to evaluate welder performance as a function of amplitude level. These in-situ measurements were then used to calibrate the model.

The LTI system level model is used to back calculate the magnitude of the shear force when welder velocity and average electric power draw are measured during welding. Welder efficiency during UAM can also be calculated using calculated shear force, measured welder velocity, and measured average electric power draw. Welder shear force and efficiency in UAM has not been measured or estimated prior to this work. The shear force magnitude was found to be near 2000 N while welder efficiency was near 80% for standard Al 6061-H18 foil welding procedures. The influence of changing processing conditions, i.e., welder amplitude, weld speed, and normal force, on shear force magnitude and efficiency was also studied. Welder velocity was found to strongly influence the shear force magnitude and efficiency while normal force and weld speed showed little to no influence. The LTI model was also used to explain and study high frequency harmonic content in the welder velocity signal. This harmonic content is largest at the odd harmonics and changes with build stiffness. This information was used to hypothesize the shear force profile during welding.

Different weld foils with significantly different strengths were welded on a common baseplate to understand the weld foil material impact on welder effort, i.e., electric power consumption and welder amplitude. These foils were annealed 4130 steel, Al 6061-T6, and annealed 110 Cu. Originally, it was thought that the weld foil strength dictated welder effort. Instead, it was found that the system elastic stiffness influenced welder effort or power consumption. The system stiffness is composed of the weld foil, UAM build, baseplate and vacuum chuck. An equivalent circuit is proposed to describe the connection between these components and how they can be treated as mechanical springs in series. To estimate component stiffness, finite element modeling in COMSOL and hammer testing was utilized. Stiffness estimates were then used to qualitatively and quantitatively relate system power consumption with system elastic stiffness. This correlation allows the UAM user to predict the required welder amplitude if the system stiffness and target welder power are known. This prediction capability aids in reducing time and effort of weld pilot studies for new materials and UAM part mounting configurations. The correlation also explains why empirically found welding conditions work for specific baseplates and weld foils.

In addition to improving UAM property-process state-of-the-art, research was done for scaling up NiTi-Al composites. This research began by evaluating the coupling between the NiTi and Al through interface strength testing, subsequent modeling, and microscopy analysis. Interface strength was investigated using single fiber pullout tests. Different commercially available surface finishes and fiber geometries were also evaluated to see if bonding character improved. This study was done because previous NiTi-Al research used ribbon geometry with an as-built oxide surface finish, which, in turn limited bonding to a frictional fit. Instead of surface finish playing a role in interface strength, it was found that the matrix yielded prior to the interface breaking for all the fiber surface finishes and not the ribbon geometry. It was determined that the failure mode was matrix failure because adhered aluminum was consistently observed on all of the fiber pullout samples. The ribbon geometry did not have adhered aluminum, and delamination was present in the sample. The measured pullout loads from the fiber geometry were then utilized as an input to a finite element model for stress and shear lag analysis, which, in turn showed that the Al matrix experienced a peak shear stress near 230 MPa. This stress is above the aluminum matrix shear strength of 150-200 MPa, thus this large stress corroborates with matrix failure observed during testing. Although fiber surface finish did not play a strong role in bond strength here, it is still recommended to construct composites with the oxide surface finish removed and with a small amount of roughness. These two attributes enable metallic bonding and enhance plastic deformation around the fiber, respectively. Hence, improved joint integrity and strength can be achieved.

Using lessons learned in the interface study, multi-layer NiTi-Al composites were fabricated and tested. For the first time, a consistent and repeatable thermal expansion reduction was achieved in NiTi-Al composites. Ultimately, thermal expansion was reduced to 25% of aluminum while simultaneously creating the largest functional composite to date. Thermal expansion of these composites are tailorable and their response can be predicted with improved models. The first modeling effort utilized a microstructural finite element model of NiTi implemented in ABAQUS. Due to the computational intensity of this model, it was run at the Ohio Supercomputer Center. Modeling was carried out by X. Chen of the P. Anderson group at Ohio State. Good correlation was achieved between the model and experimental data. This modeling framework allows for full stress tensor analysis along with other multi-physics simulations, i.e., thermal analysis, electrical analysis, etc. This framework also allows incorporation of texture or grain orientation of the NiTi.

The second model utilized phenomenological properties of NiTi and was implemented in Matlab. This modeling technique was proposed by R. Hahnlen initially and was improved upon in this thesis. Because the model utilizes phenomenological parameters to estimate response, low computational power resources can be used to run the model when compared to the more detailed microstructural NiTi FEM. The model was improved by incorporating the y and z normal stress states. With the incorporation of these stress states, the model more closely matches the axial (x direction) of the composite and allows the user to estimate the lateral (y direction) strain. These modeling approaches and scale-up efforts of NiTi-Al composites provide impressive thermal expansion results and understanding. This work enables future design and use of NiTi-Al composites in engineering applications.

9.2 Contribution and Significance

The contribution and significance of this research toward the state-of-the-art is summarized below:

- Qualitative correlation of weld energy input with bond quality via energy storage in new recrystallized interface grains
  - The mechanical and metallurgical domains on the topic of bond quality in UAM have been somewhat disjoint in existing literature. Literature which has incorporated both domains is limited, and these studies have not shown strong empirical evidence to support claims. The energy balance presented herein unifies the domains for the first time and provides strong qualitative empirical evidence to support the energy balance.
  - The presented energy balance concept builds a foundation for future quantitative microstructure modeling efforts.
  - This energy balance explains why plastic deformation imparted from UAM processing parameters and part compliance influence the formation of new recrystallized grains at the weld interface. The connection with the recrystallized grains and weld strength is then explained using Hall-Petch.
- Development of weld power as an in-situ process variable instead of amplitude
  - This control scheme provides consistent weld properties, structural compliance independence, and uses existing equipment. Consequently, this control approach allows the feasible construction of large UAM components with consistent properties, which, in turn will allow UAM to expand out of small niche areas and become more accepted.
  - Welder amplitude does not give any indication of the required activation energy to create a good bond. Welder power and speed, on the other hand, indicate the required energy for bonding directly. Hence, welder power and speed monitoring may prove to be useful for weld evolution modeling in UAM.

- Development of linear time invariant system level model of welder and innovative in-situ monitoring techniques
  - This model enables study of energy conversion within the welder, i.e., electrical to mechanical energy. Understanding this energy conversion is of utmost importance due to the mechanical power output of the welder being qualitatively correlated to bond quality. As a result, welder efficiency has been studied as a function of processing conditions for the first time and found to be near 80% for all combinations. This constant efficiency allows the UAM user to easily estimate welder shear force using a power balance between electrical and mechanical domains,

    $$P_{e,avg} = \frac{1}{\eta} P_{m,avg} = \frac{1}{\eta}\frac{1}{2}\delta\omega F_s. \qquad (9.1)$$
  - The model also enables direct estimation of the imparted shear force on the UAM part for the first time using calibrated transfer functions. Shear force estimation is useful for other modeling efforts in UAM, i.e., sonotrode design feedback, UAM part FEM, weld evolution modeling, etc. For example, Wolcott [94] utilized shear force estimates for Al 6061-H18 when evaluating residual stress in UAM components. Shear force loads were also used to inform FEM in this thesis, see Chapter 3 and Chapter 5.
  - It has been shown that high frequency harmonic content exists in the welder velocity spectrum. This high frequency content has been linked to changing build compliance of the system, and potentially, plastic deformation for the first time. Further evaluation of this harmonic content could yield insight into the full shear force waveform profile, i.e., plastic deformation behavior of the weld foil during welding.
- Evaluation of dissimilar material effects on UAM system performance
  - UAM can be used to create novel and unique dissimilar metal composites, yet the impact of dissimilar metal properties on welder performance is not well under-

  stood. It was found that system stiffness primarily influences welder effort–not weld foil strength. It has been shown that modeled system stiffness is qualitatively and quantitatively related to measured welder power draw.

  - This correlation of system compliance with power draw lays the groundwork for predicting UAM welder amplitude for new metal combinations and new weld piece mounting configurations instead of undertaking laborious time intensive pilot weld studies. Required model inputs are the system stiffness and a target weld power. The correlation was drawn using Al 6061-H18 weld foil, yet it is suspected other materials would behave in a similar manner,

$$P_{e,avg} = C \cdot K_{system}, \text{ where } C = \frac{1}{\eta}\frac{1}{6}x_{welder}^2\omega. \tag{9.2}$$

- Identification of optimal NiTi surface finish, pocket design, fiber geometry, fiber interface strength testing, and NiTi stabilization procedures
  - Without refined fiber-matrix interface design, large robust and functional UAM fiber composite structures are not possible.
  - Fiber embedding and testing procedures can be and have been extrapolated to other fiber types in UAM.
- Creating reliable, consistent, and functional multi-layer composites
  - Large functional NiTi-Al composites are required to convince designers that NiTi-Al composites are a viable option for tailorable light-weight CTE applications. For the first time, several composites have been built which demonstrate significant, consistent, and expected (modeled) thermal expansion reduction. These composites were also built with multiple fibers and multiple UAM layers, hence they were the largest functional composites built to date.
  - NiTi material selection and procedures have been detailed to explain the thought process behind selecting material for the given application.

  - Cost effective and accepted testing procedures have been given. Procedures for evaluating composite integrity/performance have also been detailed.

- Development and validation of more accurate NiTi-Al composite models
  - Accurate NiTi-Al models will allow designers to seamlessly implement NiTi-Al composites in application and provide improved understanding of thermo-mechanical interaction.
  - These models will minimize required testing for the designer and will aid in the implementation of more complicated designs, e.g., curves, bends, etc.
  - Two modeling frameworks have been pursued, each yielding their own respective advantages and disadvantages. Due to commercial NiTi solvers being available in Abaqus, it may be possible to implement the same FEM procedures with the built-in solver [86] over the customized computationally intensive solver used here. This built-in Abaqus solver uses phenomenological properties of NiTi and is widely used in the NiTi stent industry.

9.3 Future Work

Future work related to this thesis and UAM, in general, is outlined and briefly discussed in this section. This section serves as an assessment of current UAM state-of-the-art. The list here is not meant to be complete. Instead, the list items are key areas which the author feels are relevant to UAM in this point in time.

9.3.1 Future Research within Scope of Thesis

- *Mechanical testing of power compensated sample using out-of-plane ASTM tensile testing:* This work is needed to more rigorously evaluate the influence of power compensation discussed in Chapter 2 on UAM bond strength. Enhanced microstructure studies are also needed to complement the strength study. Key aspects of the microscopy would be quantifying the amount of new recrystallized grains, the grain size and grain texture, and residual stress around and within the recrystallized region. Performing this study initially with Al 6061-H18 is suggested due to the proven weldability of the alloy. Other alloys are also suggested to improve scalability of concepts and to understand differences.

- *Further investigation of system compliance relations with additional weld foil and baseplate metals:* As it stands, the proposed system stiffness relations are valid only with Al 6061-H18. Some supporting data from annealed 110 Cu, annealed 4130 steel, and Al 6061-T6 is also given to support trends, yet information is limited. It is suggested to evaluate other metals of interest in UAM which include but are not limited to titanium, stainless steels, copper, NiTi, etc. This evaluation will provide valuable information to support or identify differences in the proposed power and stiffness correlation.

- *Quantitative energy transfer analysis and modeling between sonotrode, weld foil, and UAM part:* Fundamental work in this area has been carried out by D. Foster [21], see Figure 9.1. The plot compares in-situ laser vibrometer measurements of the sonotrode, weld foil, and baseplate during the transition from tape slip to stick. This information is useful for identifying the time required for bonding and the transition characteristics from slip to stick. What is missing is quantitative modeling which connects bonding behavior to processing conditions and bond quality. This work was also carried out using a laser vibrometer system with a large spot size and within close proximity to the welder. Consequently, the weld foil in this study was larger than typical foils for the UAM process.

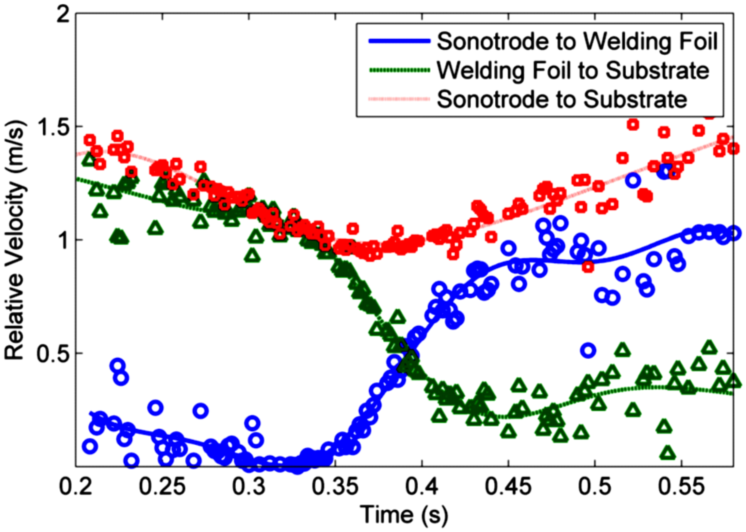

Figure 9.1: In-situ laser vibrometer measurements on sonotrode, weld foil, and baseplate from D. Foster [21].

- *Quantify the minimum mechanical energy input for bonding and improve energy balance between mechanical and metallurgical domains:* This work is required to understand energy thresholds for creating bonds in UAM and how this energy is transferred to the microstructure. Energy thresholds are required to extrapolate welding procedures and conditions to new weld fixtures and part designs. It is also required to inform microstructural evolution modeling, i.e., provide minimum activation energy information for bonding. The proposed energy balance in Chapter 2 qualitatively describes energy conversion to the interface microstructure for Al 6061-H18, yet additional work is needed to (i) understand differences between alloys, (ii) incorporate bulk deformation effects, (iii) and quantify the energy terms within the balance. The key energy component to understand better in terms of modeling and modeling variables is the recrystallization energy. Particular focus should be on differences between similar and dissimilar metal joints, and developing improved understanding of the recrystallization activation energy.

- *Deconvolve the shear force input during welding:* This work is required to more fully understand foil deformation behavior and sonotrode slip. Such a deconvolution can be carried out if welder velocity, electric current, and electric voltage are measured combined with having an adequate model to describe the respective transfer functions. This effort can be used to inform and improve understanding of the energy transfer between the sonotrode and weld foil. It can also be used to inform weld evolution modeling efforts.

- *Moving toward feasible implementation of Al 6061-T6 weld foil:* Al 6061 is a commonly utilized aluminum alloy in the aerospace and automotive sectors. Al 6061-H18, on the other hand, is not widely used and is somewhat unique to UAM. Al 6061-H18 is also not incredibly strong, is very brittle, and does not demonstrate good fatigue performance. With this being said, recent efforts have been made to make Al 6061-T6 material from 6061-H18 foil stock through heat treatment, see Chapter 5. The weld foil has been successfully produced and found to demonstrate enhanced strength and ductility over the as-received foil, see Figure 9.2. However, the elevated oven temperatures of the heat treatment process combined with the water quench create a thick oxide layer on the foil. As it stands, this oxide layer requires removal to create sufficient bonds. However, oxide removal is costly in time and effort. As a result, future efforts are required to improve the heat treating process to reduce the oxide formation. Further efforts are also required to efficiently remove the oxide layer.

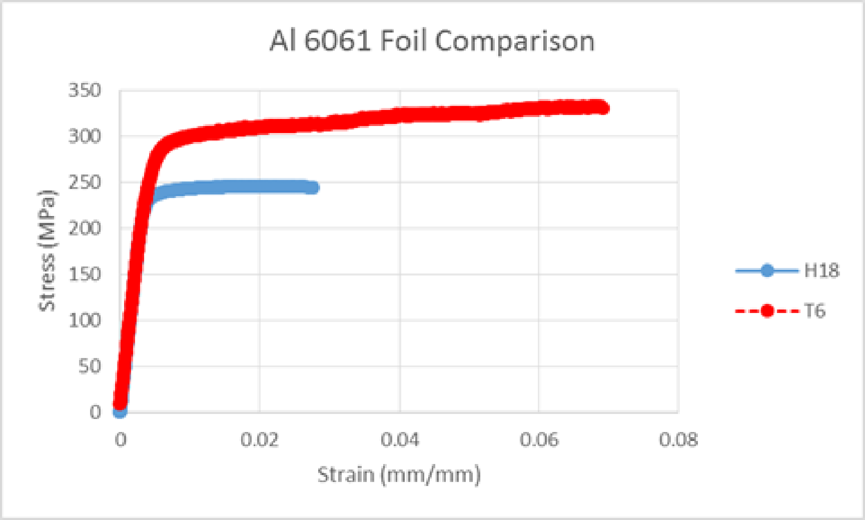

Figure 9.2: Stress-strain comparison of 6061 weld foils. T6 heat treatment increases the strength and ductility of the weld foil.

- *Transitioning to using NiTi sheet in NiTi-Al composites:* NiTi sheet is a commonly created and utilized NiTi form. Sheet is also a commonly used stock in UAM. Hence, moving toward NiTi sheet is a logical step in NiTi composite construction due to the elimination of pocket machining, increased throughput, and enhanced NiTi volume fractions. Preliminary work has been carried out to evaluate NiTi sheet welding with strong promise, see Figure 9.3-9.4.

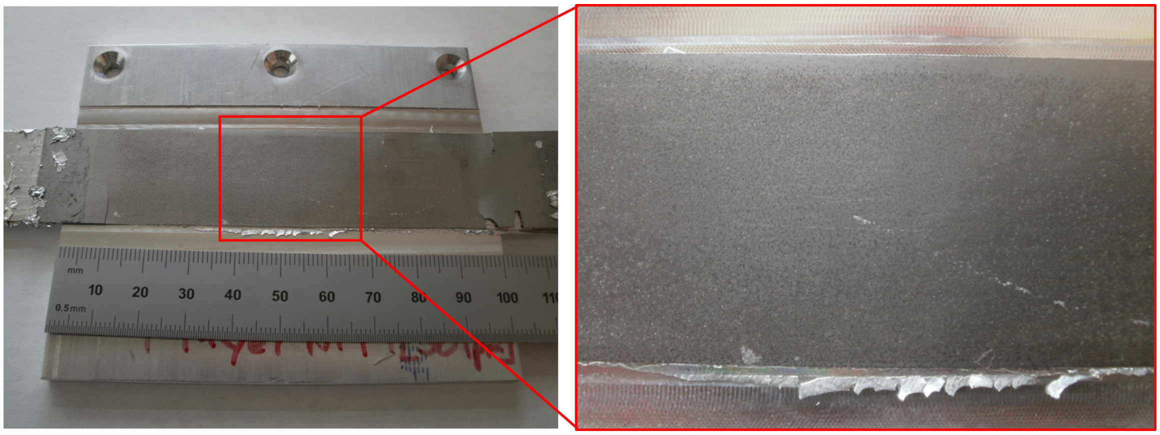

Figure 9.3: Preliminary results for joining NiTi to Al. The weld was achieved by using a slow travel speed, i.e. imparting large amounts of strain energy into the weld interface. It can be seen that the horn left a texture on the NiTi.

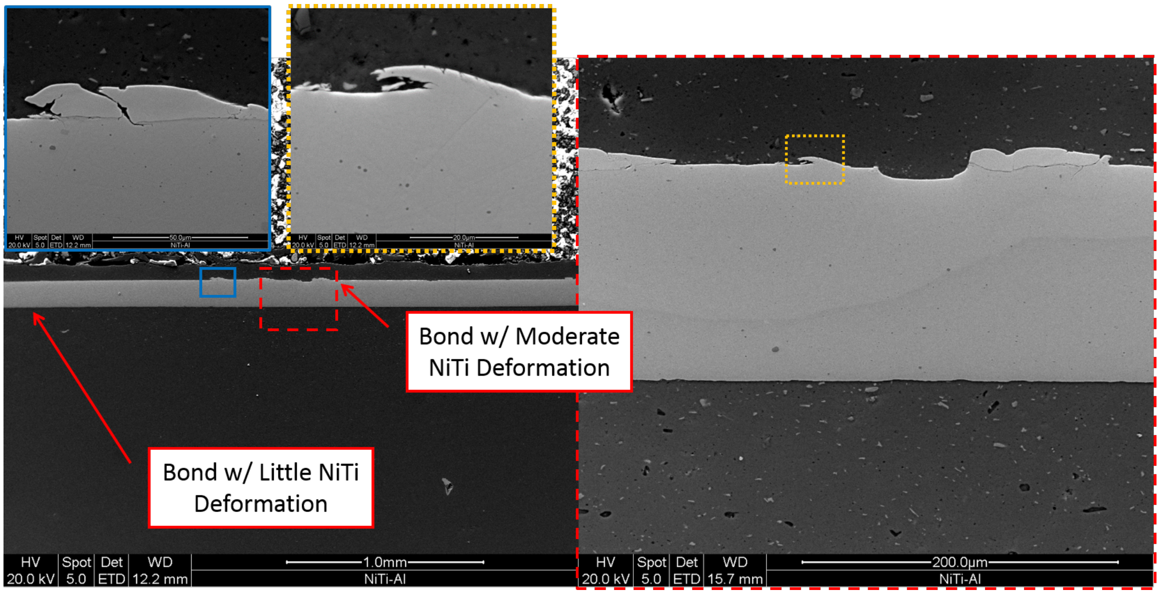
Bond w/ Moderate NiTi Deformation
Bond w/ Little NiTi Deformation
HV 20.0 kV Spot 5.0 Det ETD WD 12.2 mm 1.0mm NiTi-Al
HV 20.0 kV Spot 5.0 Det ETD WD 15.7 mm 200.0μm NiTi-Al

Figure 9.4: SEM images of Al-NiTi weld quality. It can be seen that the Al firmly sticks to the NiTi when welded due to high shear deformation while the welded NiTi onto the Al does not demonstrate much interface mixing due to the flat interface character.

- *Evaluating common weld defects with average electric power monitoring:* Average electric weld power can be utilized to identify stiffness changes related to defects in UAM, see Figure 9.5. Some of these defects may be tape veer, baseplate cracking, weld cracking, tape tear, etc. Understanding how these defects influence the welder is valuable because autonomous damage detection algorithms can then be developed. These algorithms can be used to stop the welder so the operator can intervene, can be used to correct for the flaw real-time, and can be used to quality components.

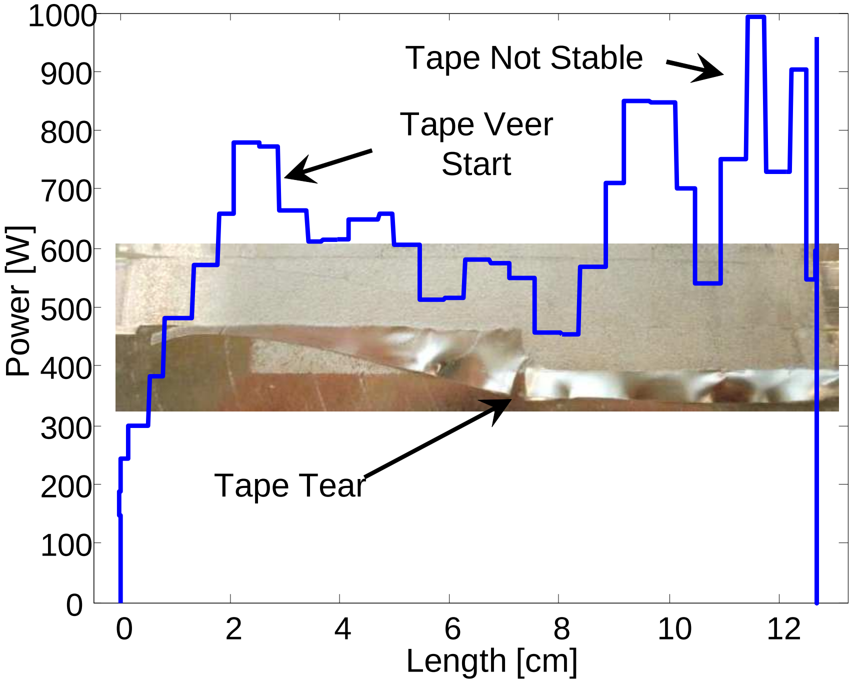

Figure 9.5: Tape veer identification using average electric weld power. The gradual change in contact stiffness can be observed in the power trace.

9.3.2 Required Research Outside of Thesis Scope

- *Quantitatively understand the impact of surface roughness and distribution on bond quality:* Surface roughness has proven to be an influential parameter in UAM [60, 93] with rougher surfaces leading to improved bonding, Figure 9.6. However, the quantitative understanding of this surface roughness interaction is not well understood, and it is believed that the strengthening mechanism is enhanced asperity deformation [93]. The current qualitative understanding is that a rougher surface may lead to a higher density of voids if sufficient scrubbing energy is not available [60], so selecting the optimal roughness is often done by reducing the amount of voids in the sample. With 9 kW UAM, gap-less structures can be obtained with rougher surfaces, see Figure 9.7, so the threshold of roughness magnitude has recently been increased when compared to 1 kW UAM. However, quantitaive understanding remains to be limited. To improve understanding of the impact of surface roughness on bond quality, a rigorous study of surface profile characterization, interface microstructure, mechanical testing, and modeling is needed.

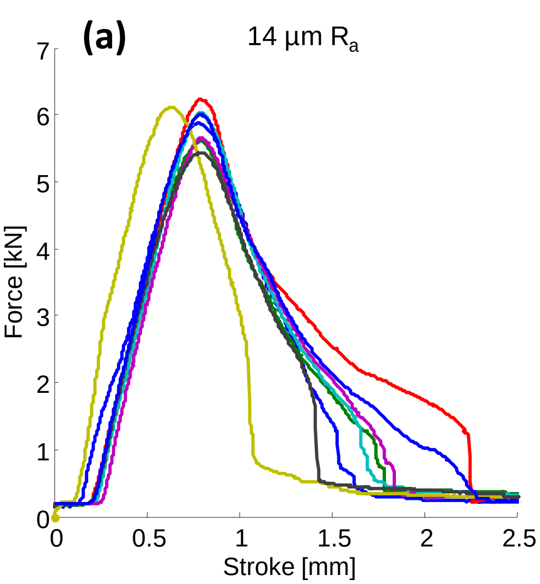

Figure 9.6: Push-pin results: (a) 14 μm Ra; (b) 7 μm Ra. 14 μm Ra shows consistently higher peak force and energy under the force-displacement curve [93].

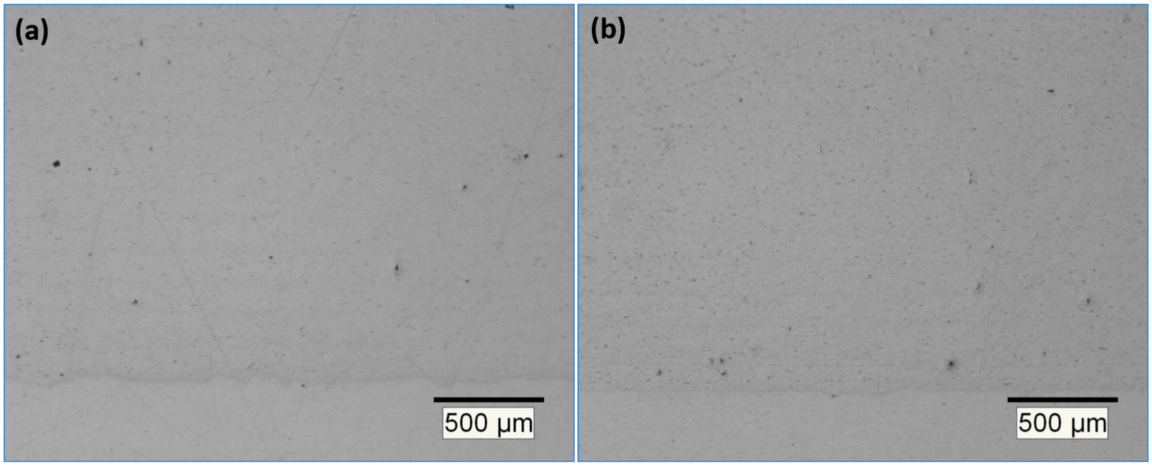

Figure 9.7: Cross section of UAM builds: (a) 14 μm Ra; (b) 7 μm Ra [93].

- *Reliable large structure construction:* UAM is a powerful additive manufacturing technology because its build envelope is very large when compared to competing metal printing methods. However, large structure construction is currently not bug free. Instead, occasional part failure can occur during construction, Figure 9.8. It is suspected that failure mechanisms include but are not limited to residual stress in the part [94], structural resonance, stress concentrators from edge effects, fatigue, and loading from the welder itself. Methods to achieve large builds reliably are currently being developed by Fabrisonic LLC with success, yet no published data is available. Solutions may be smart block design, block constraint, low temperature partial annealing, etc.

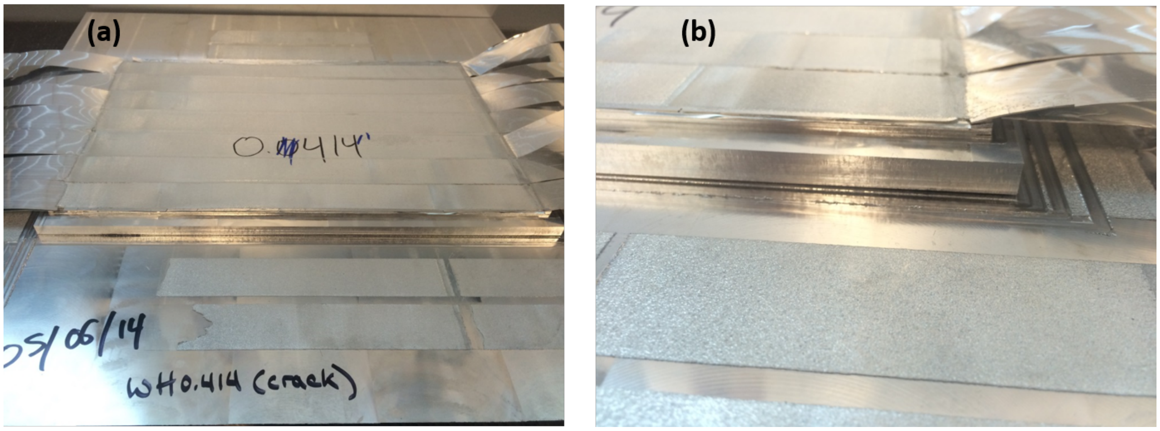

Figure 9.8: Baseplate cracking observed in large UAM build construction.

- *Understanding heat treatment mechanisms in similar metal welds:* Foundational work in this area has been carried out by Wolcott [93] and Sojiphan [82] looking at resultant heat treatment strength improvements and microstructure, respectively. Wolcott has shown that heat treating can lead to creating strengths near homogeneous material. Sojiphan has shown that heat treating causes recrystallization in the bulk structure but not the weld interface. As it stands, the strengthening mechanism is not well understood since the welded microstructure does not recrystallize. Further study is needed to (i) understand what happens to fractured oxygen around the weld interface and (ii) to understand interface microstructure change more thoroughly, i.e., texture, size, residual stress, transition to bulk microstucture, etc.

- *Develop weld envelopes for UAM:* Many other solid-state welding technologies utilize weld envelopes to describe obtaining ideal weld properties for a combination of processing parameters, e.g., impact welding. The author believes similar weld envelopes can be created for the UAM parameters of welder amplitude (or power) and weld speed since these two parameters make up the mechanical energy input. These weld envelopes should be constructed at constant force and temperature. These envelopes are needed to help UAM users achieve similar strengths in parts without sticking to the sonotrode.
- *Develop stick resistant sonotrode for UAM:* This sonotrode technology is required to reliably weld steel, titanium, and strong aluminum alloys. Fabrisonic LLC has been developing methods and techniques the past several years, yet none have proven to be successful to date. Examples include surface treatment and hybrid sonotrode material designs (ceramic and steel).
- *Understand microstructure evolution during UAM:* Because interfacial microstructure of welded materials influence bond strength and quality, it is useful to more clearly understand the evolution of the microstructure during the weld. Currently, the activation energy path and the recrystallization behavior of the microstructure is not well understood. Instead, competing arguments exist, i.e., the new refined grains may originate from subgrain refinement and enhanced dislocation density instead of dynamic recrystallization. Further, the impact of ultrasonic strain rates on this microstructure has not been rigorously studied or considered. One way of helping to understand this microstructure evolution is to stop the welder mid-weld. This experiment will provide a single snapshot illustrating initial tape slip to final bond.

Appendix A

Push-Pin Sample Manufacture, Testing, and Analysis

This appendix provides additional information on fabricating and testing push-pin samples which is not reported in literature or in this thesis.

Push-pin sample manufacture:

1. Weld 20 layer UAM stack to a particular length onto a particular baseplate material. Most baseplates are 12.7 mm (0.5 in) thick.

2. Use integrated CNC table to cut notches into sample with 3.175 mm (0.125 in) square end mill and, if applicable, begin to separate the samples. Notches are cut till penetrating near 17-18 layers of material. Hence, near 2-3 layers of material will remain on the sample. Initial push-pin sample manufacture utilized EDM cutting for separation in order to minimize cutting stress. More recently, the CNC stage has been used to separate the samples by milling about 6.35 mm (0.25 in) into the baseplate material, see Figure 2.4. Push-pin samples which have been cut with the CNC stage are shown in Figure A.1.

3. If the CNC stage is not used to completely separate the push-pin samples, use band saw to separate remainder. Band saw cutting is much faster than the CNC stage.

4. Use manual 3 axis mill to put in slightly oversized blind hole. Mount sample upside down into vice and use slightly oversized end mill for 10 mm pin. Parallels will need

to be used to keep the sample square. A collet with a set screw is recommended to avoid end mill slippage. Plunge the end mill till it goes 5-6 layers deep into the sample. In other words, the plunge depth is 2-3 layers deeper than the notch depth. It is recommended to utilize a stop which references off of the stack edge. This stop will allow faster sample manufacture and holes which are center to the sample.

5. If applicable, trim up sample edges for aesthetics. At this point, the sample edge does not influence the test.

6. Use shop air to clean out blind hole of any chips. The finalized part is shown in Figure A.2. Note that edges do not need to be completely machined if test procedure permits.

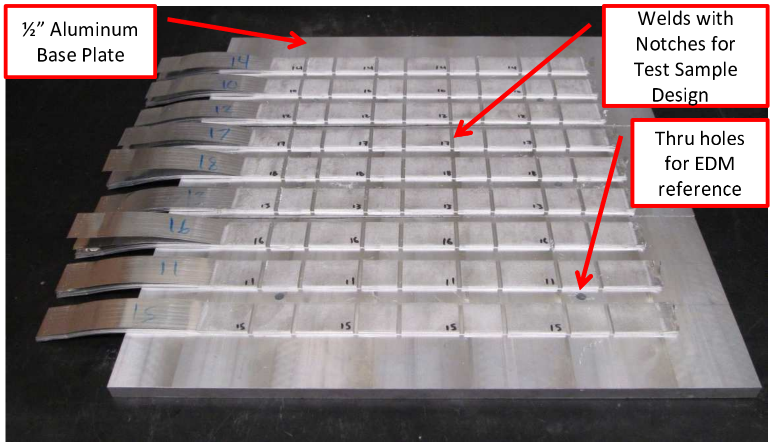
½" Aluminum Base Plate
Welds with Notches for Test Sample Design
Thru holes for EDM reference

Figure A.1: Push-pin samples ready for EDM or band saw.

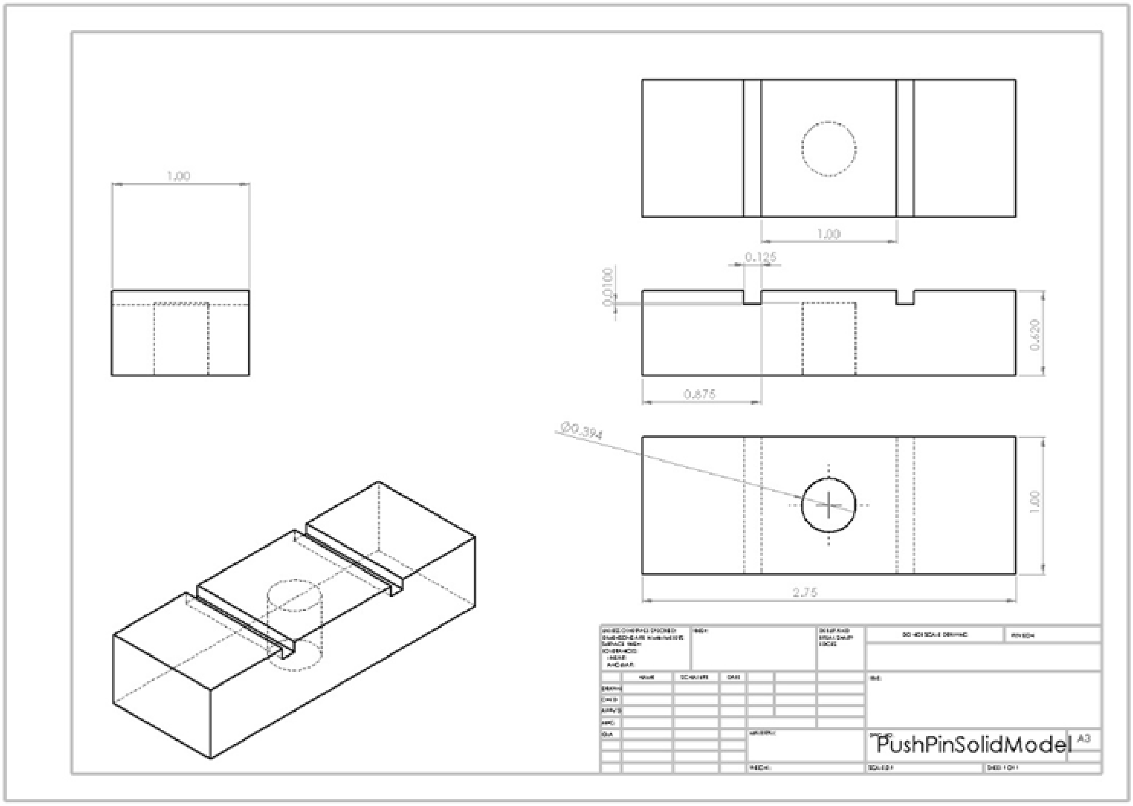

Figure A.2: Finalized push-pin sample drawing.

Push-pin Sample Testing:

1. Obtain access to Gleeble thermo-mechanical tester and ensure high force jaws are installed. A three-point bend fixture on a tensile frame may also work for this test. If a Gleeble is to be used, it is advised to consult with a person who is savvy with the system. A pin diameter of 10 mm and length near 80 mm is recommended for the test. The Gleeble is shown in Figure A.3.
2. Setup the software. Prescribe a pin stroke length or displacement which will fully penetrate the sample (10 mm is recommended). Use displacement rate recommended by Wolcott [92]. Plan to record displacement, load, and time.
3. Load the sample onto the pin. Use air actuation to move the sample near the jaws in the Gleeble. For a load frame, manual positioning may be used.

4. Start the test from the software. On the Gleeble, the mechanical button must be engaged to allow software interaction.
5. Remove sample and save data as text file for later data processing.
6. Repeat steps 3-5 until testing is completed.

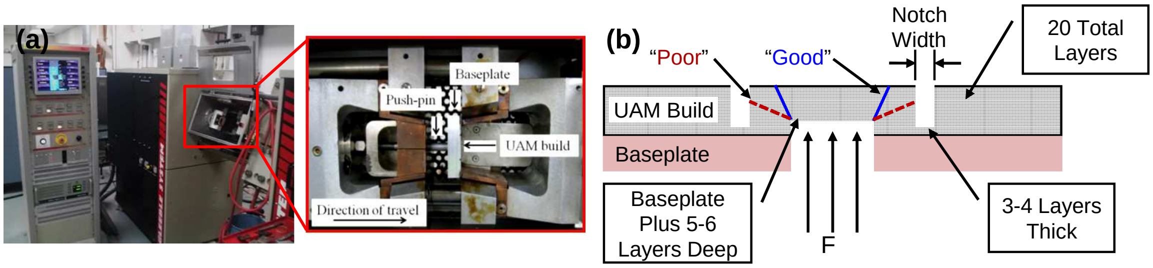
(a)
Baseplate
Push-pin
UAM build
Direction of travel
(b)
"Poor"
"Good"
Notch Width
20 Total Layers
UAM Build
Baseplate
Baseplate Plus 5-6 Layers Deep
F
3-4 Layers Thick

Figure A.3: Push-Pin testing: (a) Gleeble thermal-mechanical tester utilized for push-pin testing with key test details shown in the inset; (b) push-pin sample details with key sample details shown for testing and failure.

Push-Pin Data Analysis:

1. It is recommended to analyze the collected data with computer code, either that be MATLAB or in MS Excel with a macro.
2. Load text file (ASCII) data.
3. Align force-displacment data with logical expressions in code for presentation purposes.
4. Implement numerical integration over force-displacement region.
5. Report force-displacment graphs, peak force values, and integral results.
6. It is also useful to evaluate the failure profile of the sample to draw correlations or conclusions from the force-displacement graph, see Figure A.4.

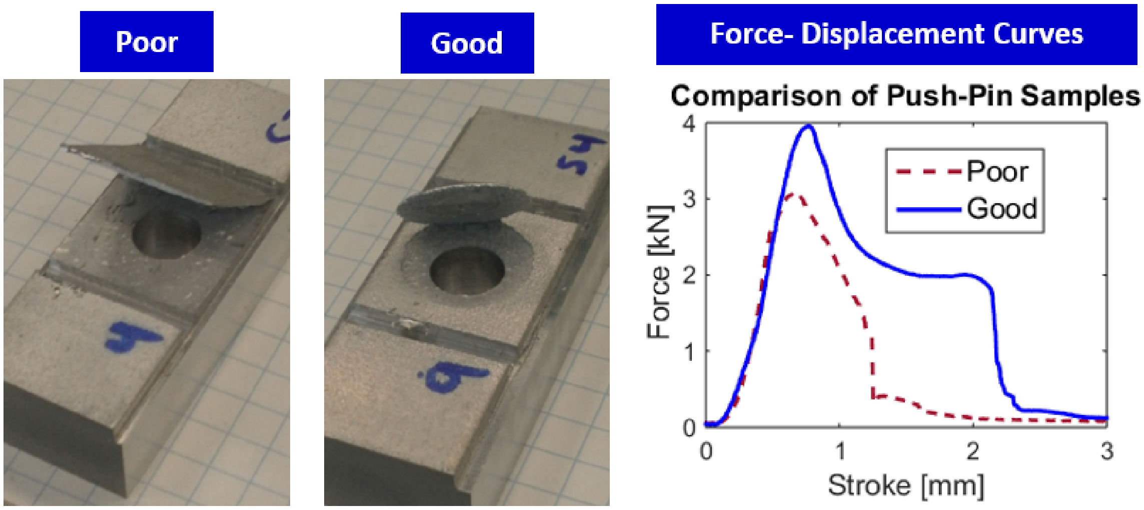

Figure A.4: Push-Pin test result summary. Examples of good and bad welds with their corresponding force-displacement curves.

Appendix B

IDENTIFYING LTI MODEL PARAMETERS

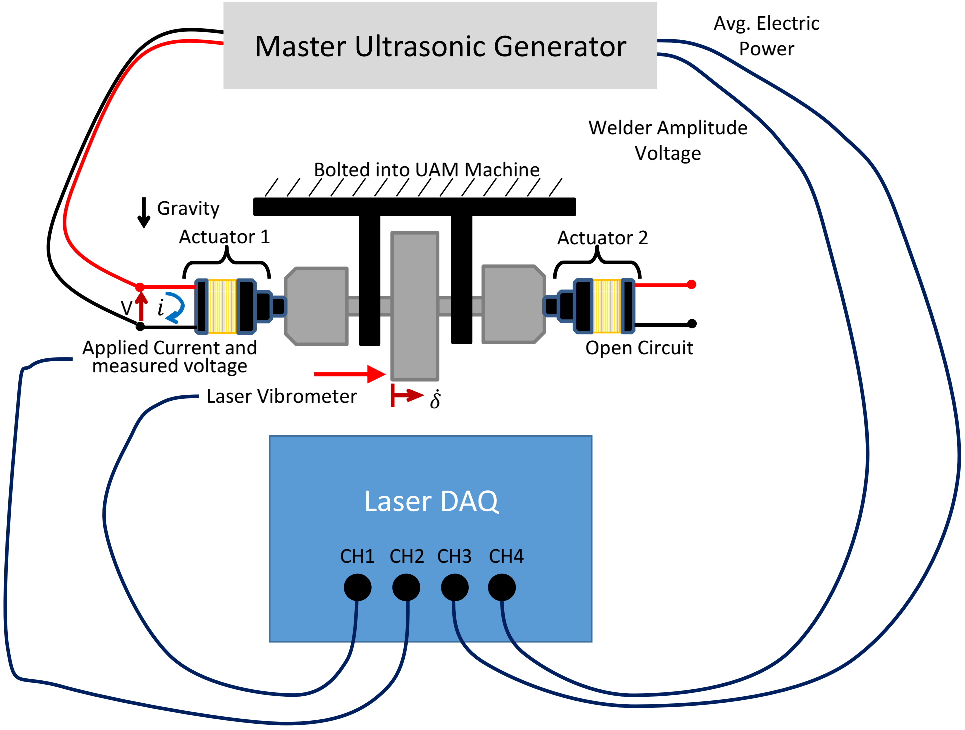
Master Ultrasonic Generator
Avg. Electric Power
Welder Amplitude Voltage
Bolted into UAM Machine
Gravity
Actuator 1
Actuator 2
V
i
Applied Current and measured voltage
Open Circuit
Laser Vibrometer
$\dot{\delta}$
Laser DAQ
CH1
CH2
CH3
CH4

Figure B.1: Wire schematic for finding mechanical mobility circuit model parameters for welder.

The purpose of this appendix is to describe the process of identifying the mechanical mobility circuit representation model parameters of the welder. Required measurement channels are welder velocity, welder power, welder amplitude voltage channel, and welder electric voltage. Each are measured by a laser vibrometer, analog output channel from ultrasonic generator, analog output channel from ultrasonic generator, and high frequency high voltage probe, respectively. If one has a high frequency current probe available, that measurement channel may also be measured. This procedure is done with the machine door open.

1. Disconnect the slave transducer. This will ensure all actuation is done by the master transducer. For 1 kW systems, this step is not required.
2. Connect voltage probe to transducer, focus laser vibrometer onto sonotrode, and connect the measurement channels to a high speed data acquisition device, see Figure B.1. A sampling frequency of 512 kHz is recommended for capturing the 20 kHz signal in the time domain. Sample time can be short (less than 1 second). Ensure the voltage probe connections are (i) out of the laser vibrometer's visual and (ii) that sufficient isolation is achieved to avoid electrical arching. It should be noted that the electrical ground of the transducer is connected to the machine table ground.
3. Actuate the welder under no load at various amplitude levels, e.g., 30, 40, 50, 60, 70, 80, 90%, etc., and record the respective signals. It is suggested to evaluate at least six different levels and evaluate the welder level of interest, i.e., the level which welding will occur.
4. Calculate peak values of welder velocity and welder voltage by identifying the peak value in the time domain for each signal. This needs to be done for each evaluated amplitude level. The Matlab function FINDPEAKS is useful in accomplishing this goal. Low pass filtering may be done on the signals to remove any higher order content above the 20 kHz driving frequency if needed. The Matlab funciton FILTFILT is suggested for filtering.
5. Fit a line between the various measured peak values for velocity and voltage to identify the coupling coefficient or the electro-mechanical transformer coefficient for the mobility circuit.

6. If current probe is used, go to step 7. Otherwise, estimate peak current from LTI model using the peak welder velocity, the coupling coefficient, and an estimate for H_m^*,

$$i = \frac{\dot{\delta}}{\Phi H_m^*}. \tag{B.1}$$

   Using estimated peak current, calculate average electric power along with measured peak voltage,

$$P_{e,avg} = \frac{1}{2} iV \tag{B.2}$$

   Compare this estimate of average electric power with the measurement of average electric power. Iteratively change the value for H_m^* until close agreement is achieved between the power quantities. The welder has now been calibrated to the LTI model. An example of the calibrated model is shown in Figure 3.14 [6]

7. If a current probe and voltage probe are not available, go to the final step. Otherwise, calculate average electric power using the definition and measured quantities. Compare with the measurement and ensure agreement prior to proceeding. Using the LTI model for welder velocity and voltage, estimate H_m directly using welder velocity,

$$H_m^* = \frac{\dot{\delta}}{\Phi i}, \tag{B.3}$$

   and using welder voltage,

$$H_m^* = \frac{V}{\Phi^2 i}. \tag{B.4}$$

   The two estimates should be close. An average between the two estimates may be used. The LTI model is now calibrated [7].

8. Fit a line between peak welder voltage and welder amplitude voltage for each evaluated amplitude level. This can be used to identify the amplitude setting (voltage level) on the welder during in-situ welding measurements if desired.

---

[6] It is also possible to directly calculate H_m^* using the combined definitions for welder velocity and power. By estimating H_m^* at each amplitude level, an average of H_m^* can be found.

[7] This step has not been validated by the author due to the access of a voltage and current probe not always being available

Appendix C

IN-SITU MEASUREMENT WELDING PROCEDURE

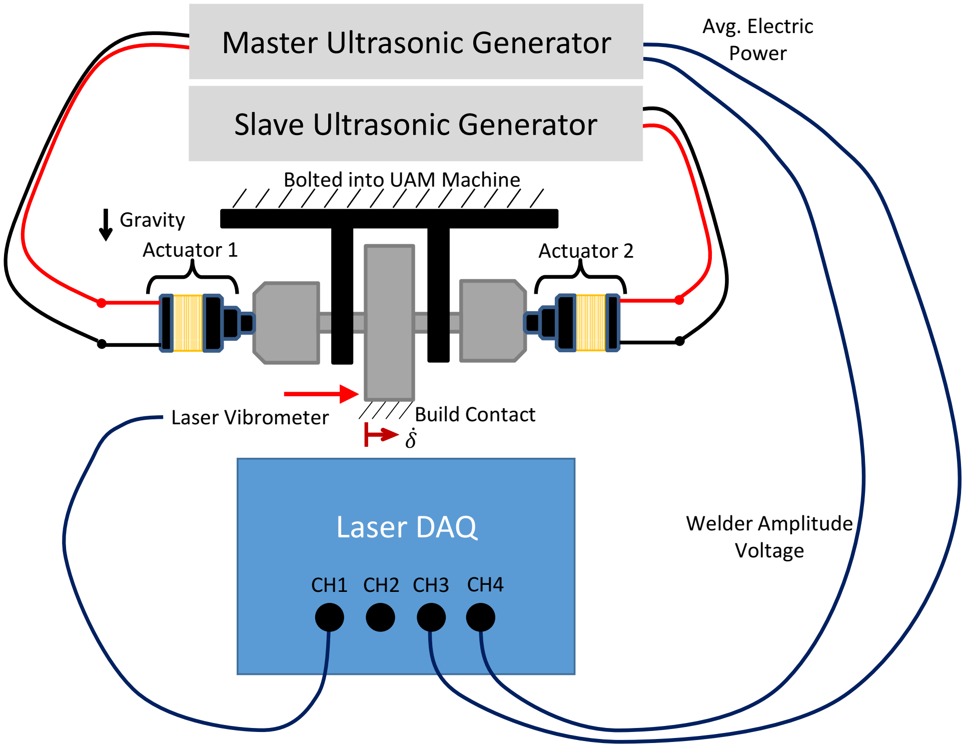

Master Ultrasonic Generator
Avg. Electric Power
Slave Ultrasonic Generator
Bolted into UAM Machine
Gravity
Actuator 1
Actuator 2
Laser Vibrometer
Build Contact
$\dot{\delta}$
Laser DAQ
CH1
CH2
CH3
CH4
Welder Amplitude Voltage

Figure C.1: Wire schematic for finding mechanical mobility circuit model parameters for welder.

The purpose of this appendix is to describe the methods for measurements during welding. Required measurement channels are welder velocity, welder power from the master, and welder amplitude voltage channel. Each are measured by a laser vibrometer, analog output channel from ultrasonic generator, and an analog output channel from ultrasonic generator. If one would like to measure weld power from the slave, that measurement channel may also be measured. The slave channel is not required because the master channel is nearly equal. This procedure is done with the machine door open.

1. Ensure all transducers are connected to their respective power supplies. For 1 kW systems, this step is not required.
2. Connect measurement channels to high speed laser data acquisition (DAQ), see Figure C.1.
3. Setup welder for welding near edge of baseplate, i.e., find baseplate, mill surface flat (recover), pre-texture, and weld a layer of foil about 10 cm (4 in) from the edge of the baseplate. This location helps for laser vibrometer measurements due to improved visibility of the sonotrode.
4. This step happens quickly and can be done with a reduced feed rate if needed. Start welder for a weld. When close to the baseplate, slow travel speed down to 1 or 5%. With the normal load display on the machine screen, identify when the sonotrode makes contact with the baseplate or UAM build. Stop the program once contact is made (500 N from load cell).
5. Align and focus laser on sonotrode.
6. Do this step with the normal load display on the machine screen. Press restart button to terminate the program (not emergency stop). With the travel speed still set to a slow value (1 or 5%), manually job the welder up off of the baseplate (Z+). Use the visual readout of the load value to verify the correct jog direction (load should decrease).

7. Run the welder program again. Once the welder makes contact with the baseplate surface and is audibly heard (welding begins), start sampling data. Save the data. Repeat this step for multiple welds on the baseplate or UAM build.

8. Once all data is collected, use the calibrated LTI model (see Appendix B) to estimate shear force as presented in Chapter 4. It is suggested to low pass filter the data before processing due to measurement noise. High frequency measurement noise originates in surface variation of the sonotrode as it rolls. Evaluating the shear force when the welder is under no load is also recommended. The value should be near zero.

Appendix D

FIBER PULLOUT MANUFACTURE AND TESTING

The purpose of this appendix is to provide supplemental information for manufacturing and testing fiber pullout samples. Manufacturing utilized EDM machining as a step to minimize cutting stresses on samples with this particular sample design, see Chapter 6. However, EDM adds a step of complexity, time, cost, and may introduce reference errors. It is recommended to utilize the manufacturing procedure as a guideline to fabricate samples in the future. It is also recommended to eliminate the use of EDM if possible and perform all machining with the integrated CNC stage.

Sample Manufacture:

1. Use small plate manufacturing fixture which has embedded fiber constraint feature, see Figure D.1. This fixture uses screws to constrain the plate, and these screws have been known to come loose during welding. It is recommended to periodically check screw tightness during the welding step.

2. This step is only required if EDM machining is to be done. Center plate with spindle using edge finder (this requires manual operation of CNC).

3. Find plate, recover middle, pre-texture, and weld 3 layers. The goal here is to achieve a total build height near 0.406 mm (0.016 in). This build height allows for the fiber to be near the center of the sample after manufacture, see Figure D.6(a).

4. Cut perpendicular grove into weld for sample separation using a 1.5875 mm (1/16 in)

square end mill. The grove depth is recommended to be 0.254 mm (0.01 in) into the baseplate.

5. Cut a grove down the center of the weld for fiber encapsulation using a ball end mill. The grove depth is slightly undersized the fiber diameter. The mill size is slightly oversized the fiber diameter.
6. Lay fiber into grove under constraint from fixture and prepare for encapsulation, see Figure 6.1. Weld over fiber. No significant shinny spots near the embedded fiber should be observed. If shinny spots are observed, the channel depth is too deep and should be remedied for future welds. If tape tearing occurs, the channel depth is likely not deep enough. Continue welding until final sample height is achieved (13 layers here).
7. Remove welded material at grove using the same program in step 4. The end mill should be run such that it is slightly above the layer 3 surface.
8. Using a razor blade, score and remove remaining foil material over the perpendicular groves in the sample. A pick is recommended for helping remove the scored material. The encapsulated wire should be exposed, see Figure D.2. Use caution when working with softer materials other than NiTi.
9. Using a manual 3-axis mill, locally remove the material on the backside of the pullout samples until the baseplate is 1.27 mm (0.05 in) thick. Material removal was done with a 12.7 mm (0.5) square end mill. Remaining material was left to maintain stiffness of sample in the vice, hence why baseplate material was used in the sample design.
10. Using a 1.5875 mm (1/16 in) square end mill, align and cut backside perpendicular notches by referencing off of baseplate edge. The perpendicular notch should go all the way through the plate and fibers should be visible. Take caution to not cut too deep and destroy the fiber. Figure D.3 details the 3-axis milling operations.
11. Using wire EDM, cut samples out such that cutting path minimizes stress of samples.

A recommended cutting pattern is shown in Figure D.4. Actual cutting of samples is shown in Figure D.5. The exact cutting path may depend on EDM operator preference and experience with previous samples. It was not uncommon to damage samples in this step of the process.

12. Using a fine file, clean up sample edges for loading into test fixture. A representative finalized sample is shown in Figure D.6(b).

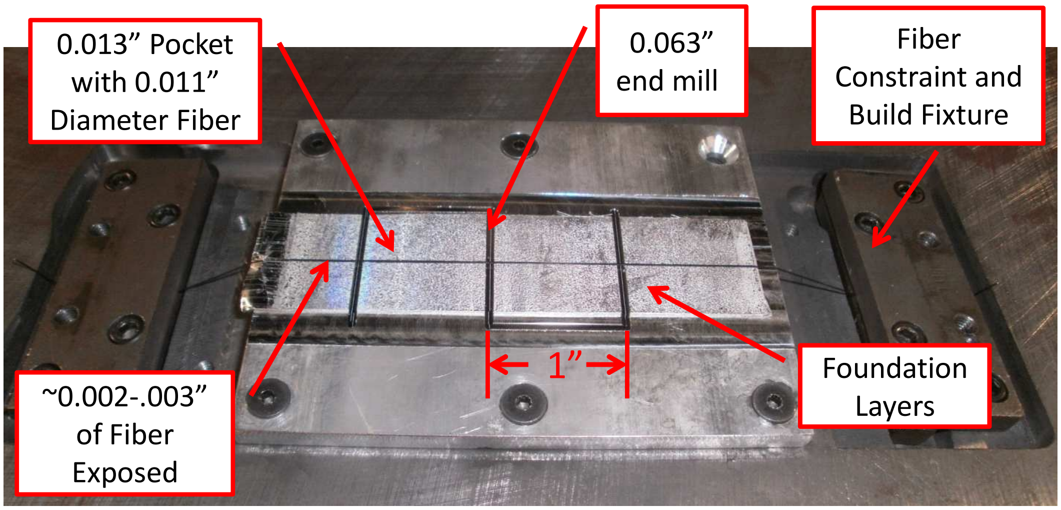
0.013" Pocket with 0.011" Diameter Fiber
0.063" end mill
Fiber Constraint and Build Fixture
~0.002-.003" of Fiber Exposed
1"
Foundation Layers

Figure D.1: Pullout sample manufacture with details.

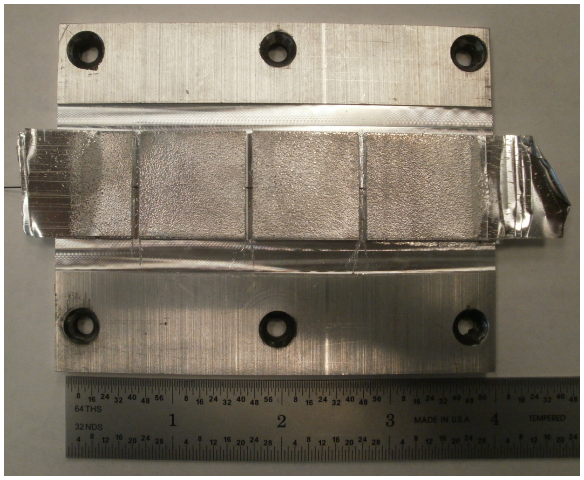

Figure D.2: Photo of removed foil after razor blade scoring, step 8. The NiTi wires are visible.

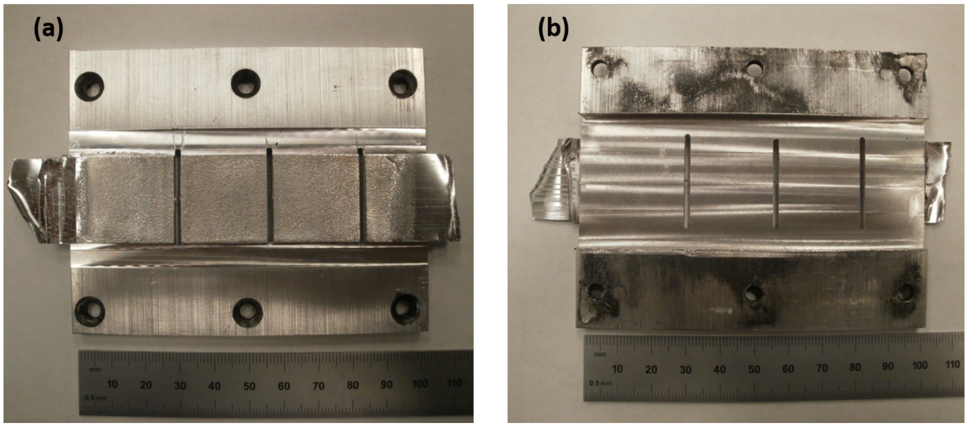

Figure D.3: 3-axis milling: (a) weld side with perpendicular notch penetrating through the entire sample; (b) backside of sample with removed baseplate material and cut notches.

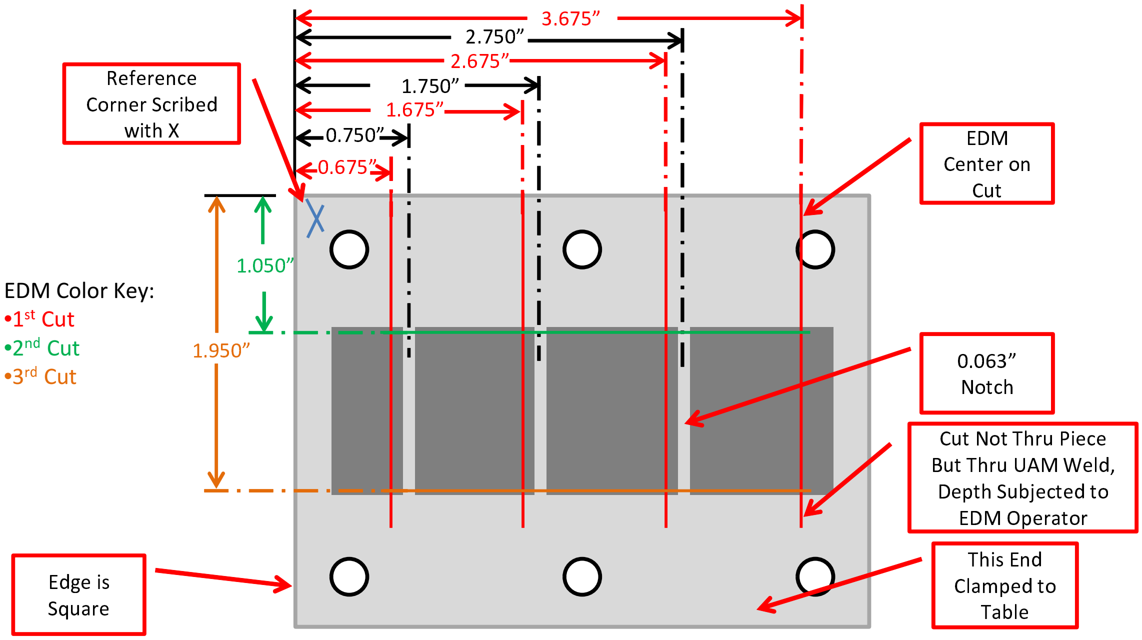
3.675”
2.750”
2.675”
1.750”
1.675”
0.750”
0.675”
Reference Corner Scribed with X
X
EDM Center on Cut
1.050”
1.950”
EDM Color Key:
•1st Cut
•2nd Cut
•3rd Cut
0.063” Notch
Cut Not Thru Piece But Thru UAM Weld, Depth Subjected to EDM Operator
Edge is Square
This End Clamped to Table

Figure D.4: Drawing of wire EDM cutting passes and dimensions. These cutting passes were selected to minimize stress on samples. This cutting path may not be optimal for reducing stress or for reducing EDM cutting time.

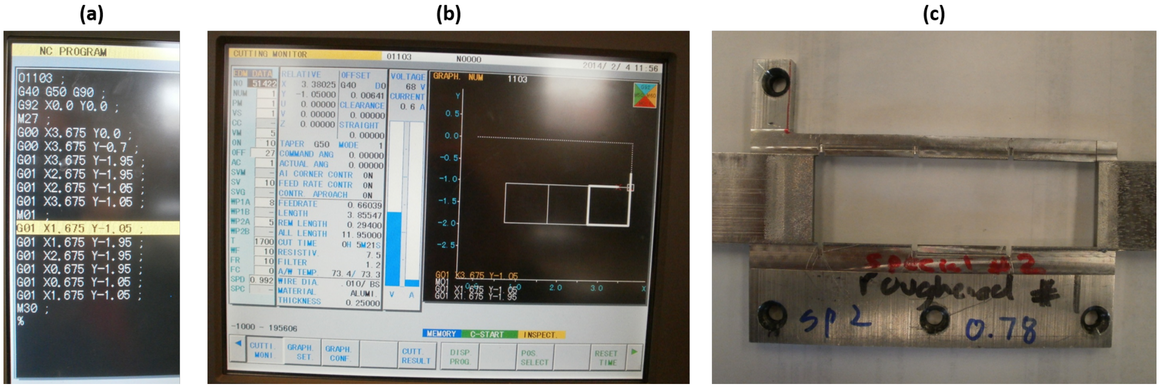
(a)
(b)
(c)
NC PROGRAM
CUTTING MONITOR
MEMORY
C-START
INSPECT.
SP 2
roughened #
0.78

```
01103 ;
G40 G50 G90 ;
G92 X0.0 Y0.0 ;
M27 ;
G00 X3.675 Y0.0 ;
G00 X3.675 Y-0.7 ;
G01 X3.675 Y-1.95 ;
G01 X2.675 Y-1.95 ;
G01 X2.675 Y-1.05 ;
G01 X3.675 Y-1.05 ;
M01 ;
G01 X1.675 Y-1.05 ;
G01 X1.675 Y-1.95 ;
G01 X2.675 Y-1.95 ;
G01 X0.675 Y-1.95 ;
G01 X0.675 Y-1.05 ;
G01 X1.675 Y-1.05 ;
M30 ;
%
```

Figure D.5: Wire EDM cutting: (a) G-code for sample removal; (b) machine path for sample removal; (c) removed samples showing location where wire came into baseplate.

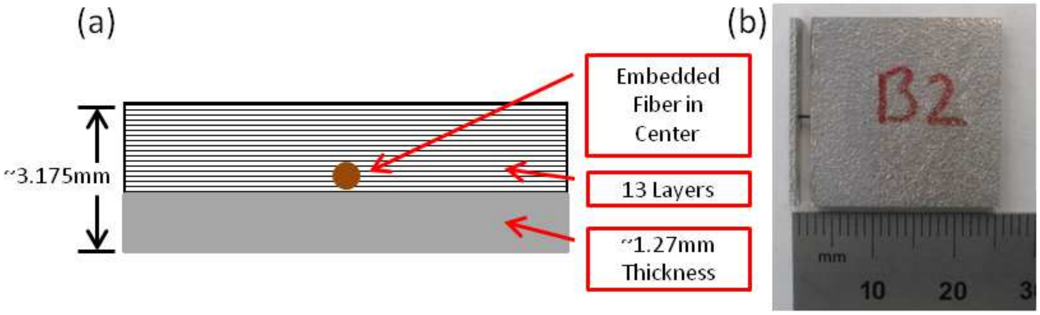

Figure D.6: Pullout sample details: (a) schematic of sample cross section with key fabrication details; (b) physical sample ready to test post manufacture.

Sample Testing:

1. Obtain pullout test fixture. Drawings of these components are shown in Figure D.7 while a photo of the fixture is shown in Figure D.8.
2. Ensure load frame is aligned.
3. Design a program to move the grips apart at a fixed rate, 1.27 mm/min (0.05 in/min) was used in this study. Total travel distance was 2.54 mm (0.1 in) It is suggested to test the study before sample testing.
4. Load pullout sample into fixture by sliding it in. Tighten setscrews to constrain sample. Then, attach grip adapter for testing.
5. Load grip adapter into top grip while bottom grip is oversized.
6. Jog grips into place, and slowly tighten botttom grip onto pullout sample. A pre-load will be applied near 15 N (2-3 lbf). For more fragile samples, it is suggested to use less of a pre-load if possible. The loaded fixture into load frame grips is shown in Figure D.9.
7. Start the load frame program to pull the sample apart.
8. Save force and displacement signals from test for analysis.

9. Remove sample from grips and repeat procedure until all tests are done. A representative failed sample with the force-displacment profile is shown in Figure D.10.

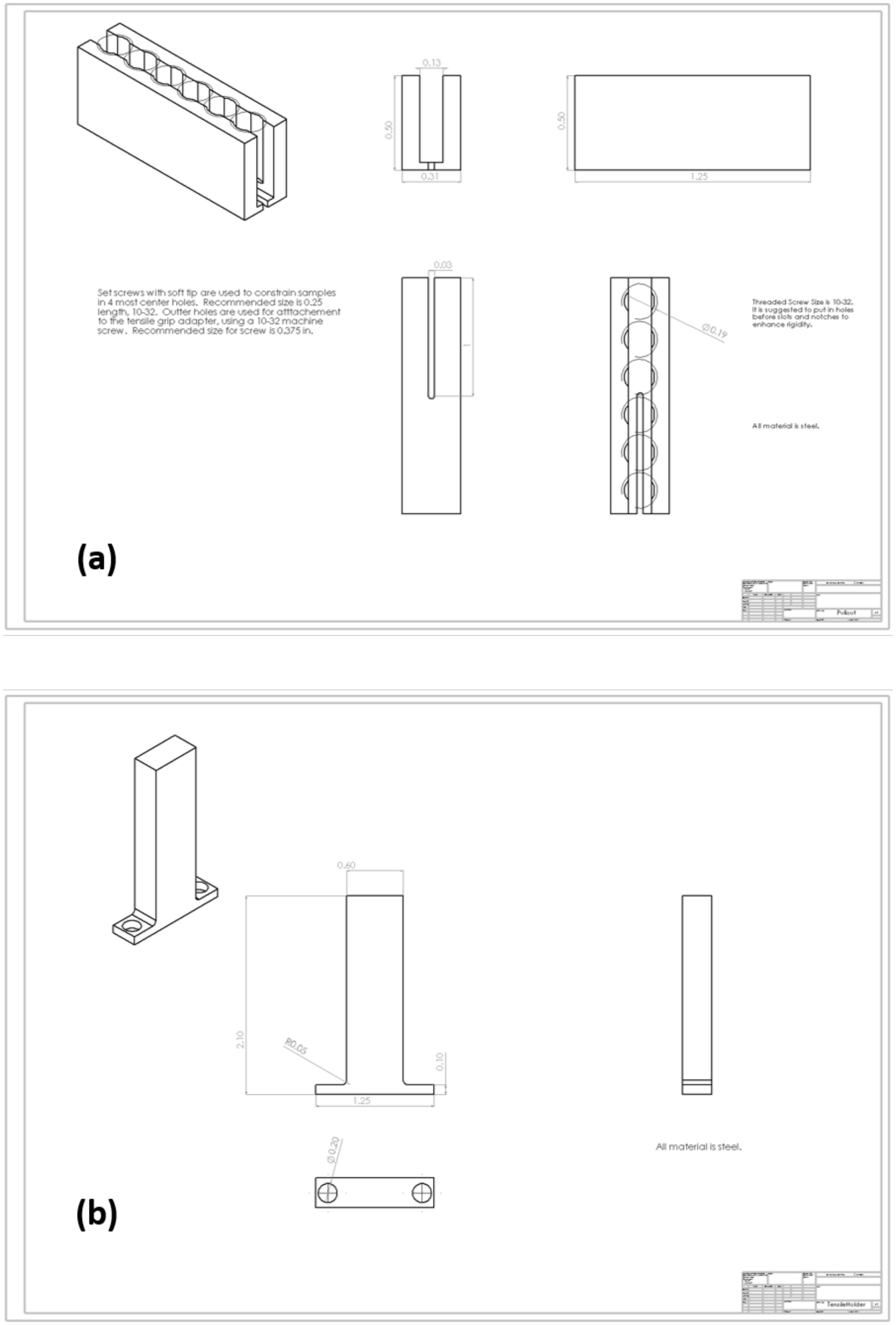
0.13
0.50
0.31
0.50
1.25
0.03
1
Ø0.19
(a)
Pullout
0.60
2.10
R0.05
0.10
1.25
Ø0.20
(b)
TensileHolder

Set screws with soft tip are used to constrain samples in 4 most center holes. Recommended size is 0.25 length, 10-32. Outter holes are used for atttachement to the tensile grip adapter, using a 10-32 machine screw. Recommended size for screw is 0.375 in.

Threaded Screw Size is 10-32. It is suggested to put in holes before slots and notches to enhance rigidity.

All material is steel.

All material is steel.

Figure D.7: Pullout testing fixture drawings: (a) pullout fixture; (b) grip adapter.

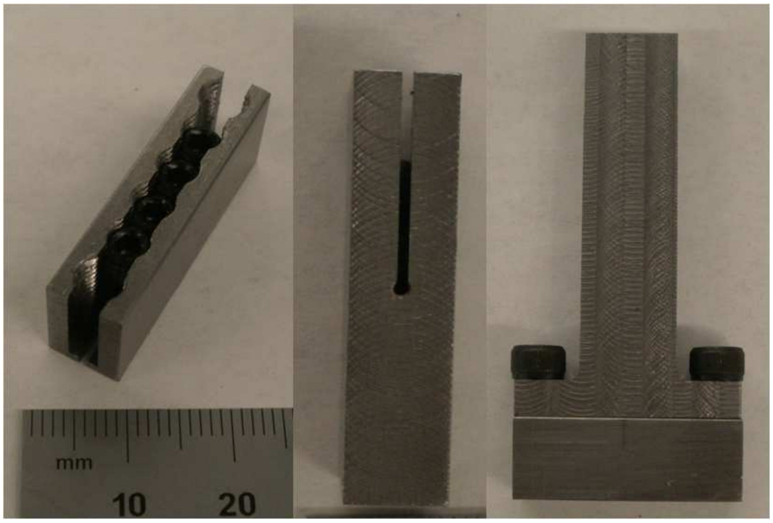

Figure D.8: Custom fiber pullout test fixture used in study.

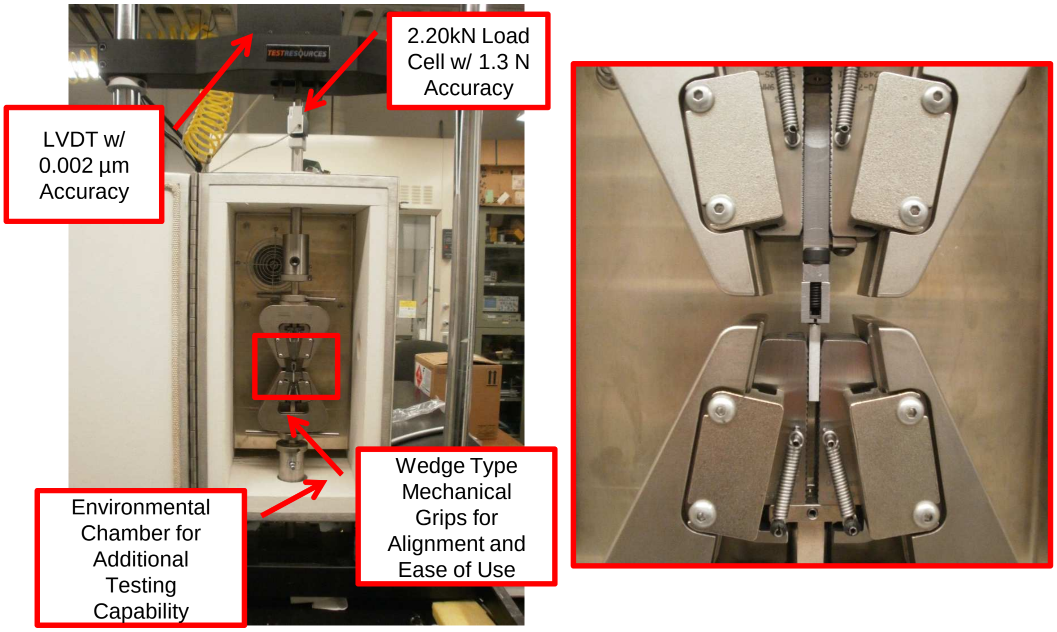
2.20kN Load Cell w/ 1.3 N Accuracy
LVDT w/ 0.002 µm Accuracy
Environmental Chamber for Additional Testing Capability
Wedge Type Mechanical Grips for Alignment and Ease of Use

Figure D.9: TestResources load frame used for testing with key specifications listed. The area boxed in red illustrates how the test fixture and sample are loaded into the machine.

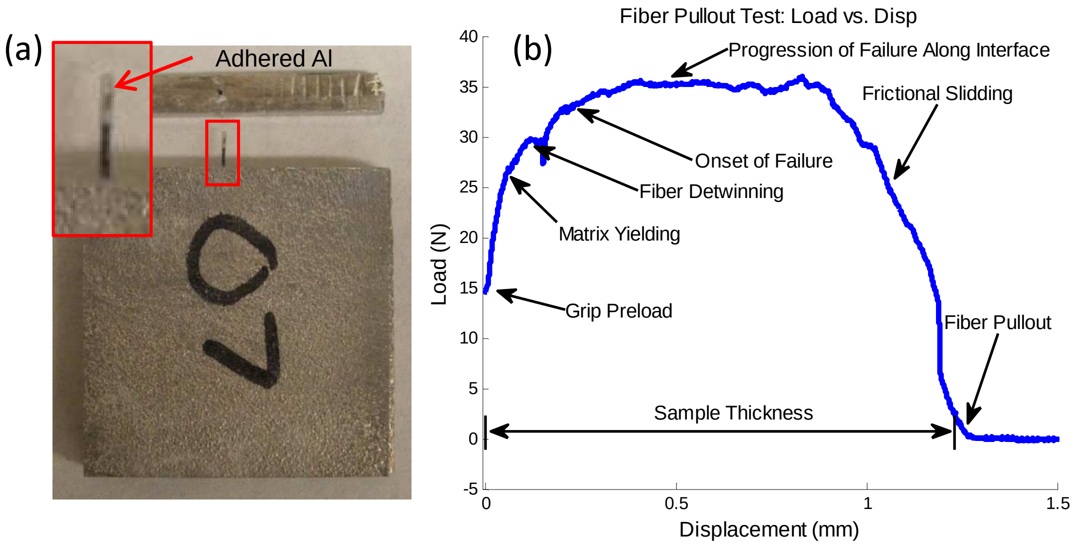

Figure D.10: Representative pullout test result for oxide sample 7: (a) photo of sample after failure illustrating adhered aluminum to surface of fiber; (b) detailed force-displacement pullout test curve.

Appendix E

NiTi-Al Composite Manufacture and CTE Testing

This appendix provides additional information for fabricating and testing NiTi-Al composites.

Composite Manufacture:

1. Obtain desired NiTi form, surface finish, and performance specifications. Fort Wayne Metals is a mid-west supplier which produces material to order within a timely fashion. Characterize the obtained material to evaluate properties, see Chapter 7. This characterization provides insight into volume fraction requirements and transformation temperatures.
2. Train the material in a load frame above the A_f transformation temperature to eliminate plasticity before embedding, see Figure 7.1. Multiple fibers may be trained at one time.
3. Create a scaled size version schematic of the composite for reference, see Figure E.1.
4. Create three programs. Two of the programs are for cutting groves in the composite at particular layers. The other is for defining the composite edge after embedding is finished.
5. Iteratively weld, cut groves, lay fibers, weld...until composite is finished. Photos and details are given in Chapter 7.

6. Define the composite edge with the third program and machine the top of the composite flat (an offset recover program is suggested).

7. Remove from fiber fabrication fixture. Cut away material locally under composite sample on back-side, i.e., leave ends of composite/baseplate intact to avoid collapse in machine vice. This machining can be done with integrated CNC or with manual 3-axis mill.

8. Use a band saw to remove excess baseplate material. Do not cut through the sample.

9. Use a slow speed saw with coolant flow to cut through ends of composite to avoid heating sample. Many microscopy labs have slow speed saws. Composite fabrication is complete, see Figure E.2.

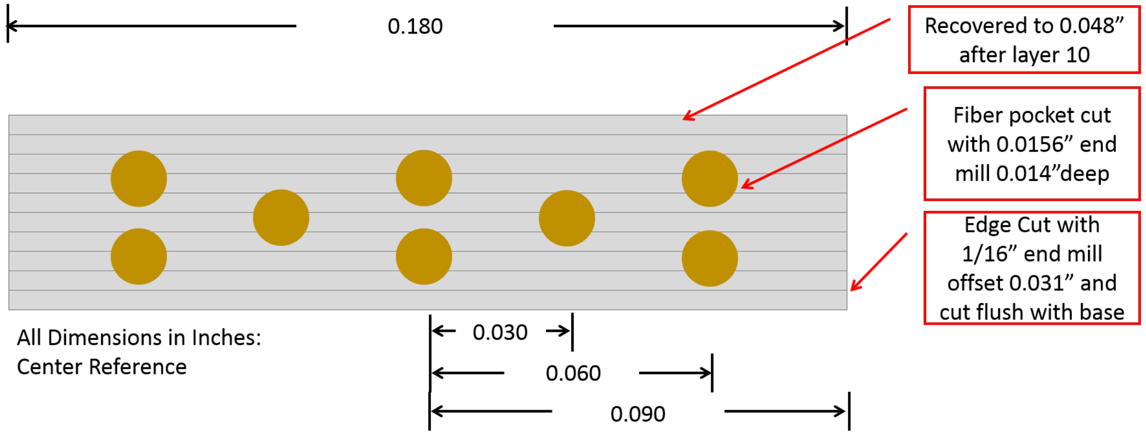
0.180
Recovered to 0.048” after layer 10
Fiber pocket cut with 0.0156” end mill 0.014”deep
Edge Cut with 1/16” end mill offset 0.031” and cut flush with base
All Dimensions in Inches:
Center Reference
0.030
0.060
0.090

Figure E.1: Example scaled composite schematic to aid in composite manufacture.

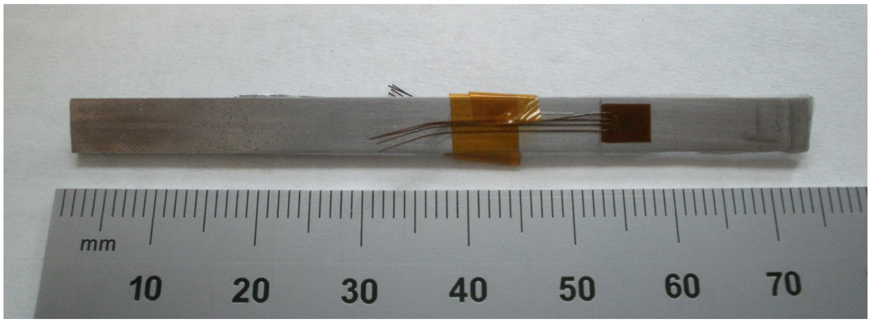

Figure E.2: Composite removed from baseplate and ready for thermal expansion testing.

Composite CTE Testing:

1. Obtain a thermal chamber with a controllable heat source. For example, recent CTE testing has been carried out in a load frame thermal chamber with a temperature controller over the heat chamber used in this thesis due to enhanced temperature control. The thermal chamber used in this thesis is shown in Figure E.3.
2. If using an aluminum matrix, obtain strain gauges for aluminum from Vishay MicroMeasurements. Otherwise, obtain strain gauges for the matrix material. Mount these strain gauges to both sides of the composite for uneven bending strain reasons. It is suggested to use a room temperature cure strain gauge glue from Vishay.
3. Obtain a homogenous reference piece of material. A welded piece of material was used in this study to ensure the reference was made with the same matrix material. Mount a strain gauge to this material.
4. Put sample and reference into thermal chamber and mount in a stress free configuration, i.e., clamped at one end.
5. Mount thermocouples to samples. It is suggested to use a compound to enhance thermal coupling, such as Omegatherm from Omega. It is also suggested to use a thermocouple type which is useful for the temperature range of interest (type-J used here).

6. Ensure strain gauges are connected and balanced.

7. Heat and cool samples while measuring strain and temperature of samples. Strain and temperature were measured using a VI built in LabVIEW, see Figure E.4. It is suggested to use a heating and cooling rate which the thermal chamber can accurately control, such as 0.5 C/min.

8. Heat and cool samples further until steady-state behavior is achieved (typically 3 full thermal cycles).

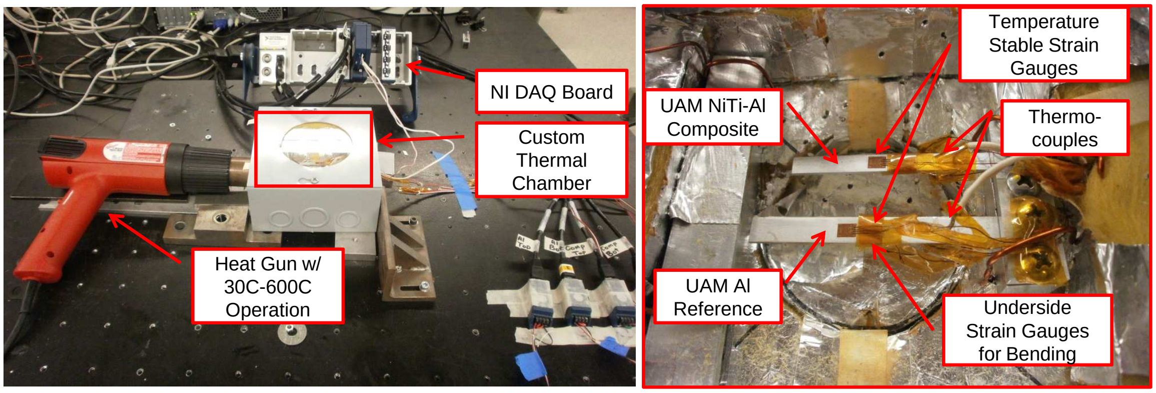
NI DAQ Board
Custom Thermal Chamber
Heat Gun w/ 30C-600C Operation
Temperature Stable Strain Gauges
UAM NiTi-Al Composite
Thermo-couples
UAM Al Reference
Underside Strain Gauges for Bending

Figure E.3: Thermal test utilized to measure composite CTE. Important test elements have been detailed.

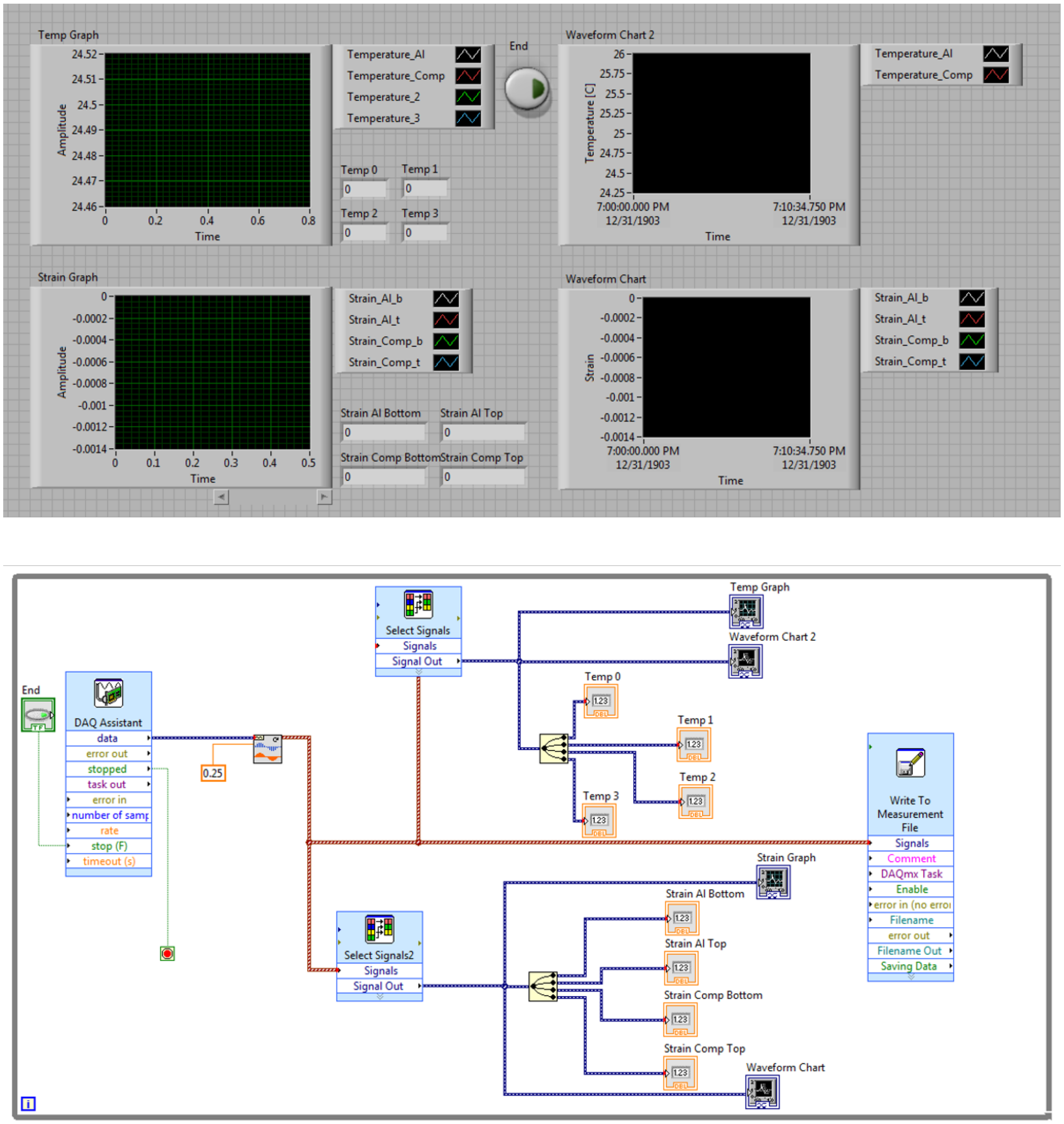
Temp Graph
Amplitude
24.52
24.51
24.5
24.49
24.48
24.47
24.46
0
0.2
0.4
0.6
0.8
Time
Temperature_AI
Temperature_Comp
Temperature_2
Temperature_3
End
Temp 0
Temp 1
Temp 2
Temp 3
Waveform Chart 2
Temperature [C]
26
25.75
25.5
25.25
25
24.75
24.5
24.25
7:00:00.000 PM 12/31/1903
7:10:34.750 PM 12/31/1903
Time
Temperature_AI
Temperature_Comp
Strain Graph
Amplitude
0
-0.0002
-0.0004
-0.0006
-0.0008
-0.001
-0.0012
-0.0014
0
0.1
0.2
0.3
0.4
0.5
Time
Strain_AI_b
Strain_AI_t
Strain_Comp_b
Strain_Comp_t
Strain AI Bottom
Strain AI Top
Strain Comp Bottom
Strain Comp Top
Waveform Chart
Strain
0
-0.0002
-0.0004
-0.0006
-0.0008
-0.001
-0.0012
-0.0014
7:00:00.000 PM 12/31/1903
7:10:34.750 PM 12/31/1903
Time
Strain_AI_b
Strain_AI_t
Strain_Comp_b
Strain_Comp_t
End
DAQ Assistant
data
error out
stopped
task out
error in
number of samp
rate
stop (F)
timeout (s)
0.25
Select Signals
Signals
Signal Out
Temp Graph
Waveform Chart 2
Temp 0
Temp 1
Temp 2
Temp 3
Write To Measurement File
Signals
Comment
DAQmx Task
Enable
error in (no erro
Filename
error out
Filename Out
Saving Data
Strain Graph
Strain AI Bottom
Strain AI Top
Strain Comp Bottom
Strain Comp Top
Waveform Chart
Select Signals2
Signals
Signal Out

Temp 0: 0
Temp 1: 0
Temp 2: 0
Temp 3: 0
Strain AI Bottom: 0
Strain AI Top: 0
Strain Comp Bottom: 0
Strain Comp Top: 0

Figure E.4: LabVIEW VI used to measure strain and temperature of samples during thermal cycling.

Appendix F

Improved Hahnlen Model Algorithm Flowchart

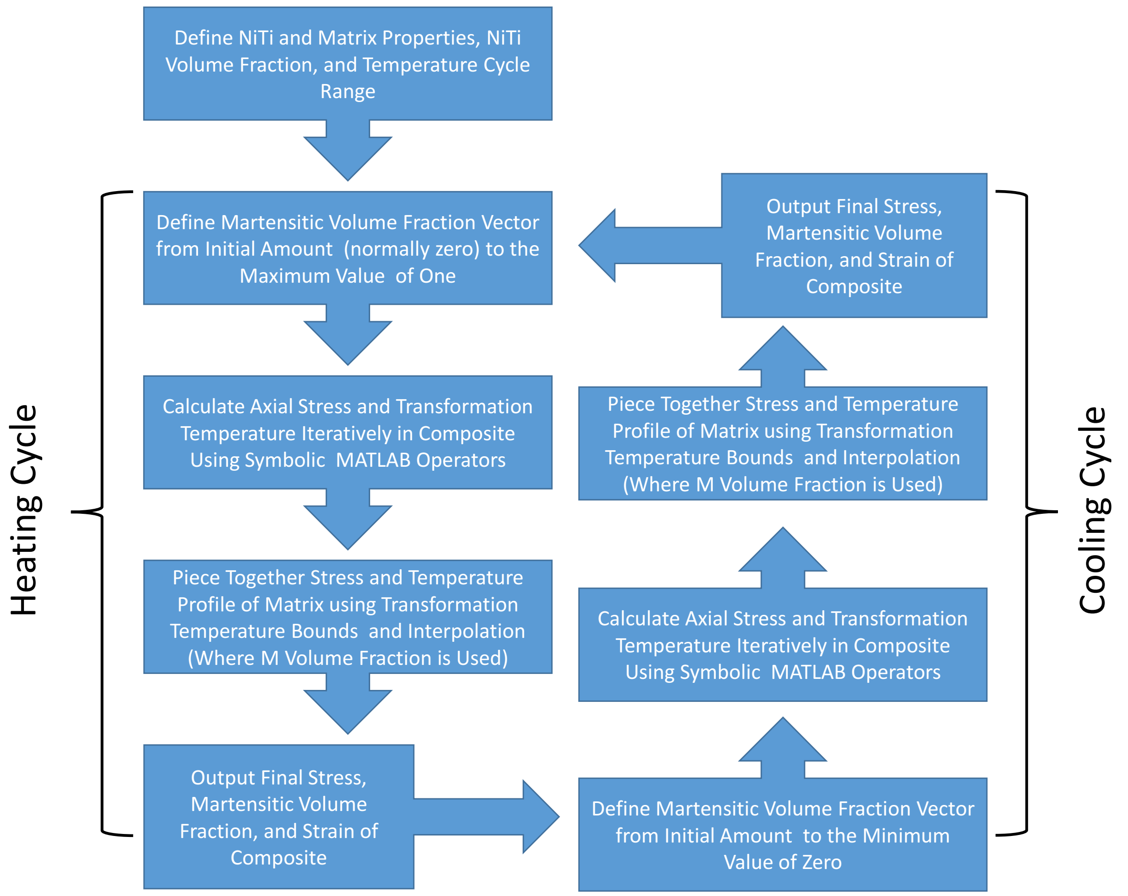
Define NiTi and Matrix Properties, NiTi Volume Fraction, and Temperature Cycle Range
Define Martensitic Volume Fraction Vector from Initial Amount (normally zero) to the Maximum Value of One
Calculate Axial Stress and Transformation Temperature Iteratively in Composite Using Symbolic MATLAB Operators
Piece Together Stress and Temperature Profile of Matrix using Transformation Temperature Bounds and Interpolation (Where M Volume Fraction is Used)
Output Final Stress, Martensitic Volume Fraction, and Strain of Composite
Heating Cycle
Define Martensitic Volume Fraction Vector from Initial Amount to the Minimum Value of Zero
Calculate Axial Stress and Transformation Temperature Iteratively in Composite Using Symbolic MATLAB Operators
Piece Together Stress and Temperature Profile of Matrix using Transformation Temperature Bounds and Interpolation (Where M Volume Fraction is Used)
Output Final Stress, Martensitic Volume Fraction, and Strain of Composite
Cooling Cycle

Figure F.1: Big picture algorithm flow diagram of improved Hahnlen model. Other more detailed flow diagrams of the model are given in Hahnlen's thesis [34].

Bibliography

[1] *ASM Handbook: Volume 9 Metallography and Microstructures.* American Society for Materials International, 1985.

[2] *Heat Treating of Aluminum Alloys, Heat Treating, Vol 4,.* American Society for Materials International, 1991.

[3] *ABAQUS 6.11 Documentation.* Dassault Systèmes Simulia Corporation, 2011.

[4] Dukane Communication. private communication, 2015.

[5] Manufacturing.gov, October 2015.

[6] Reza Abbaschian, Lara Abbaschian, and Robert E. Reed-Hill. *Physical Metallurgy Principles.* Cengage Learning, 2010.

[7] AE Techron. Technical Manual: LVC5050 Power Supply Amplifier, 2002.

[8] Randall J Allemang. *Vibrations: Experimental Modal Analysis.* University of Cincinnati Structural Dynamics Research Laboratory, 2007.

[9] Wohlers Associates. Wohlers Report 2014. Technical report, 2014.

[10] B. Bhushan. *Introduction to Tribology, Ch3: Contact Between Solid Surfaces.* John Wiley and Sons Ltd, 2013.

[11] L.C. Brinson. One-dimensional constitutive behavior of shape memory alloys: Thermomechanical derivation with non-constant material functions and redefined martensite internal variable. *Journal of Intelligent Material Systems and Structures*, 4:229–242, 1993.

[12] Sponsored by the National Institute of Standards and Technology. Measurement Science Roadmap for Metal-Based Additive Manufacturing. Technical report, 05 2013.

[13] T. K. Caughey. Sinusoidal Excitation of a System With Bilinear Hysteresis. *Journal of Applied Mechanics*, 27(4), 1960.

[14] K.K. Chawla. *Composite Materials: Science and Engineering.* Springer, 1998.

[15] Xiang Chen, Adam Hehr, Marcelo J. Dapino, and Peter M. Anderson. Deformation Mechanisms in NiTi-Al Composites Fabricated by Ultrasonic Additive Manufacturing. *Shape Memory and Superelasticity*, 1(3):294–309, 2015.

[16] Xudong Cheng, Arindom Datta, Hongseok Choi, Xugang Zhang, and Xiaochun Li. Study on Embedding and Integration of Microsensors Into Metal Structures for Manufacturing Applications. *Journal of Manufacturing Science and Engineering*, 129:416–424, 2007.

[17] H.P.C. Daniels. Ultrasonic welding of metals. *Ultrasonics*, 3(4), 1965.

[18] Clarence de Silva. *Vibration: Fundamentals and Practice.* CRC Press LLC, 2000.

[19] E. De Vries. *Mechanics and Mechanisms of Ultrasonic Metal Welding.* PhD thesis, The Ohio State University, Columbus, OH, 2004.

[20] R.R. Dehoff and S.S. Babu. Characterization of interfacial microstructures in 3003 aluminum alloy blocks fabricated by ultrasonic additive manufacturing. *Acta Materialia*, pages 1–12, March 2010.

[21] D. R. Foster, G. A. Taber, S. S. Babu, and G. S. Daehn. In situ velocity measurements of very high power ultrasonic additive manufacturing using a photonic Doppler velocimeter. *Science and Technology of Welding and Joining*, 19(2):157–163, 2014.

[22] R. J. Friel and R. A. Harris. A nanometre-scale fibre-to-matrix interface characterization of an ultrasonically consolidated metal matrix composite. *Proceedings of the Institution of Mechanical Engineers, Part L: Journal of Materials: Design and Applications*, 224(1):31–40, 2010.

[23] R.J. Friel. *Power Ultrasonics: Ch13: Power ultrasonics for additive manufacturing and consolidation of materials.* Elsevier, 2015.

[24] H.T. Fujii, M.R. Sriraman, and S.S. Babu. Quantitative evaluation of bulk and interface microstructures in Al-3003 alloy builds made by very high power ultrasonic additive manufacturing. *Metallurgical and Materials Transactions A: Physical Metallurgy and Materials Science*, 42(13):4045–4055, December 2011.

[25] James M. Gibert. *Dynamics of Ultrasonic Consolidation.* PhD thesis, Clemson University, Clemson, SC, USA, 2009.

[26] James M. Gibert, Eric M. Austin, and Georges Fadel. Effect of height to width ratio on the dynamics of ultrasonic consolidation. *Rapid Prototyping Journal*, 16(4).

[27] James M. Gibert, Georges Fadel, and Mohammed E. Daqaq. On the stick-slip dynamics in ultrasonic additive manufacturing. *Journal of Sound and Vibration*, 332:4680–4695, 2013.

[28] K. Graff. *Ultrasonic Additive Manufacturing*, volume 6A, Welding Fundamentals and Processes. American Society for Metals International, 2011.

[29] K. Graff, J. Devince, J. Keltos, and N. Zhou. *Ultrasonic Welding of Metals*, volume 9.3. American Welding Society, 2000.

[30] K.F. Graff. *Power Ultrasonics, Ch14, Ultrasonic metal forming: materials*. Elsevier, 2015.

[31] K.F. Graff. *Power Ultrasonics: Ch6: Power ultrasonic transducers: principles and design*. Elsevier, 2015.

[32] K.F. Graff, M. Short, and M. Norfolk. Very High Power Ultrasonic Additive Manufacturing (VHP UAM). In *International Solid Freeform Fabrication Symposium*, Austin, TX, 2011.

[33] R. Hahnlen and M.J. Dapino. NiTi-Al Interface Strength in Ultrasonic Additive Manufacturing Composites. *Composites Part B: Engineering*, 59:101–108, 2014.

[34] R.M. Hahnlen. *Characterization and Modeling of Active Metal-Matrix Composites with Embedded Shape Memory Alloys*. PhD thesis, The Ohio State University, Columbus, OH, 2012.

[35] Ryan Hahnlen and Marcelo J. Dapino. Stress-Induced Tuning of Ultrasonic Additive Manufacturing. In *Proceedings of SPIE Vol 8342*, San Diego, CA, 2012.

[36] D. J. Hartl and D. Lagoudas. *Shape Memory Alloys: Modeling and Engineering Applications, CH2*. Springer, 2008.

[37] A. Hehr and M.J. Dapino. Interfacial shear strength estimates of NiTiAl matrix composites fabricated via ultrasonic additive manufacturing. *Composites Part B: Engineering*, 77:199–208, 2015.

[38] A Hehr and M.J. Dapino. Dynamics of Ultrasonic Additive Manufacturing. *Ultrasonics*, In Review.

[39] A Hehr, P.W. Wolcott, and M.J. Dapino. Effect of Weld Power and Build Compliance on Ultrasonic Consolidation. *Rapid Prototyping Journal*, 22(2), 2016.

[40] R.C. Hibbeler. *Mechanics of Materials*. Pearson Prentice Hall, Upper Saddle River, NJ, 6th edition, 2005.

[41] C.D. Hopkins, S.A. Fernandez, and M.J. Dapino. Statistical Characterization of Ultrasonic Additive Manufacturing Ti/Al Composites. *Journal of Engineering Materials and Technology*, 132, 2010.

[42] C.D. Hopkins, P.J. Wolcott, M.J. Dapino, A.G. Truog, S.S. Babu, and S.A. Fernandez. Optimizing Ultrasonic Additive Manufactured Al 3003 Properties With Statistical Modeling. *Journal of Engineering Materials and Technology*, 134, 2012.

[43] F. Humphreys and M. Hatherly. *Recrystallization and Related Annealing Phenomena*. Elsevier, 2004.

[44] F.V. Hunt. *Electroacoustics: The Analysis of Transduction and Its Historical Backaground*. Cambridge: Harvard University Press, 1954.

[45] IEEEl. IEEE Std 176-1987: Standard on Piezoelectricity, 1988.

[46] W.D. Iwan. A Distributed-Element Model for Hysteresis and Its Steady-State Dynamic Response. *Journal of Applied Mechanics*, 33(4), 1966.

[47] G.D. Janaki Ram, C. Robinson, Y. Yang, and B.E. Stucker. Use of ultrasonic consolidation for fabrication of multi-material structures. *Rapid Prototyping Journal*, 13(4):226–235, 2007.

[48] G.D. Janaki Ram, Y. Yang, and B.E. Stucker. Effect of Process Parameters on Bond Formation During Ultrasonic Consolidation of Aluminum Alloy 3003. *Journal of Manufacturing Systems*, 25(3):221, 2006.

[49] K. Johnson. *Interlaminar Subgrain Refinement in Ultrasonic Consolidation.* PhD thesis, Loughborough University, Loughborough, UK, 2008.

[50] Gregory S. Kelly, Suresh G. Advani, John W. Gillespie Jr., and Travis A. Bogetti. A model to characterize acoustic softening during ultrasonic consolidation. *Journal of Materials Processing Technology*, 213(11):1835–1845, 2013.

[51] Gregory S. Kelly, M. Scott Just Jr, Suresh G. Advani, and John W. Gillespie Jr. Energy and bond strength development during ultrasonic consolidation. *Journal of Materials Processing Technology*, 214(8):1665–1672, 2014.

[52] R.J. Kerans and T.A. Parthasarathy. Theoretical Analysis of the Fiber Pullout and Pushout Test. *Journal of the American Ceramic Society*, 74(7), 1991.

[53] C. Kong, R. Soar, and P. Dickens. Ultrasonic consolidation for embedding SMA fibres within aluminium matrices. *Composite Structures*, 66:421–427, 2004.

[54] C.Y. Kong, R.C. , and P.M. Dickens. Optimum process parameters for ultrasonic consolidation of 3003 aluminum. *J. of Materials Processing Tech.*, 146(2):181–187, 2004.

[55] C.Y. Kong and R.C. Soar. Fabrication of metal–matrix composites and adaptive composites using ultrasonic consolidation process. *Materials Science & Engineering A*, 412(1–2):12–18, 2005.

[56] C.Y. Kong and R.C. Soar. Method for embedding optical fibers in an aluminum matrix by ultrasonic consolidation. *Applied Optics*, 44(30):6325–6333, 2005.

[57] C.Y. Kong, R.C. Soar, and P.M. Dickens. Characterisation of aluminum alloy 6061 for the ultrasonic consolidation process. *Materials Science & Engineering A*, 363(1-2):99–106, 2003.

[58] C.Y. Kong, R.C. Soar, and P.M. Dickens. A model for weld strength in ultrasonically consolidated components. *Journal of Mechanical Engineering Science, Part C*, 219:83–91, 2004.

[59] P. Kumar and D. Lagoudas. *Shape Memory Alloys: Modeling and Engineering Applications, CH1.* Springer, 2008.

[60] Dezhi Li and Rupert Soar. Influence of sonotrode texture on the performance of an ultrasonic consolidation machine and the interfacial bond strength. *Journal of Materials Processing Technology*, 209:1627–1634, 2009.

[61] Dezhi Li and Rupert C. Soar. Plastic flow and work hardening of Al alloy matrices during ultrasonic consolidation fibre embedding process. *Materials Science and Engineering A*, 498(1–2):421–429, 2008.

[62] Dezhi Li and Rupert C. Soar. Characterization of Process for Embedding SiC Fibers in Al 6061 O Matrix Through Ultrasonic Consolidation. *Journal of Engineering Materials and Technology*, 131, 2009.

[63] Zong-Fu Li and D. T. Grubb. Single-fibre polymer composites: Part I Interfacial shear strength and stress distribution in the pull-out test. *Journal of Material Science*, 29, 1994.

[64] S Manchiraju and PM Anderson. Coupling between martensitic phase transformations and plasticity: A microstructure-based finite element model. *International Journal of Plasticity*, 26(10):1508–1526, 2010.

[65] D.B. Marshall, M.C. Shaw, and W.L. Morris. Measurement of Interfacial Debonding and Sliding Resistance in Fiber Reinforced Intermetallics. *Acta Metallurgica et Materialia*, 40(3), 1992.

[66] Warren P. Mason. *Electromechanical Transducers and Wave Filters*. D. Van Nostrand Company, Inc., 1942.

[67] E. A. Neppiras. Motional feed-back systems for ultrasonic transducers. In *Ultrasonics*, London, UK, 1971.

[68] E.A. Neppiras. Ultrasonic welding of metals. *Ultrasonics*, 3(3), 1965.

[69] E.A. Neppiras. New Magnetostrictive Materials and Transducers: Part I. *Journal of Sound and Vibration*, 8(3), 1968.

[70] J.O. Obielodan, A. Ceylan, L.E. Murr, and B.E. Stucker. Multi-material bonding in ultrasonic consolidation. *Rapid Prototyping Journal*, 13(3):180–188, 2010.

[71] Office of Transportation and Air Quality. EPA and NHTSA Set Sandards to REduce Greenhouse Gases and Improve Fuel Economy for Model Years 2017-2025 Cars and Light Trucks. Technical report, United States Environmental Protection Agency, 2012. EPA-420-F-12-051.

[72] United States Government Accountability Office. 3D Printing: Opportunities, Challenges, and Policy Implications of Additive Manufacturing. Technical report, 06 2015.

[73] D. Paul and B. Stucker. A study of subgrain formation in Al 3003 H-18 foils undergoing ultrasonic additive manufacturing using a dislocation density based crystal plasticity finite element framework. *Journal of Applied Physics*, 113, 2013.

[74] Yousef Payandeh, Fodil Meraghni, Etienne Patoor, and Andre Eberhardt. Effect of martensitic transformation on the debonding propagation in Ni-Ti shape memory wire composite. *Material Science and Engineering A*, 518:35–40, 2009.

[75] Joshua D Pritchard. Design, Fabrication, and Analysis of a Multi-Layer, Low-Density, Thermally-Invariant Smart Composite via Ultrasonic Additive Manufacturing. Master's thesis, The Ohio State University, Columbus, OH, USA, 2014.

[76] Bjorn Richter, Jens Twiefel, and Jorg Wallaschek. *Energy Harvesting Technologies: Ch4: Piezolectric Equivalent Circuit Models*. Springer, 2009.

[77] C. Robinson, C. Zhang, G.D. Janaki-Ram, E. Siggard, B.E. Stucker, and L. Li. Maximum height to width ratio of free-standing structures built by ultrasonic consolidation. In *Proceedings of the 17th Solid Freeform Fabrication Symposium*, Austin, TX, August 2006.

[78] D.E. Schick, R.M. Hahnlen, R. Dehoff, P. Collins, S.S. Babu, M.J. Dapino, and J.C. Lippold. Microstructural Characterization of Bonding Interfaces in Aluminum 3003 Blocks Fabricated by Ultrasonic Additive Manufacturing. *Welding Journal*, 89:105s–115s, May 2010.

[79] A. Siddiq and E. Ghassemieh. Theoretical and FE Analysis of Ultrasonic Welding of Aluminum Alloy 3003. *Journal of Manufacturing Science and Engineeringl*, 131, 2009.

[80] Jennifer Mueller Sietins. *Exploring Diffusion of Ultrasonically Consolidated Aluminum and Copper Films Through Scanning and Transmission Electron Microscopy*. PhD thesis, University of Delaware, Newark, DE, USA, 2014.

[81] E. Siggard. Investigative research into the structural embedding of electrical and mechanical systems using ultrasonic consolidation. Master's thesis, Utah State University, Logan, UT, 2007.

[82] K. Sojiphan, M.R. Sriraman, and S.S. Babui. Stability of Microstructure in Al3003 Builds made by Very High Power Ultrasonic Additive Manufacturing. In *Proceedings of the 17th Solid Freeform Fabrication Symposium*, Austin, TX, August 2010.

[83] Niyanth Sridharana, Paul Wolcott, Marcelo Dapino, and S.S. Babu. Microstructure and texture evolution in aluminum and commercially pure titanium dissimilar welds fabricated using ultrasonic additive manufacturing. *Scripta Materialia*, 117:1–5, 2016.

[84] M.R. Sriraman, S.S. Babu, and M. Short. Bonding characteristics during very high power ultrasonic additive manufacturing copper. *Scripta Materialia*, 62:560–563, January 2010.

[85] M.R. Sriraman, M. Gonser, H.T. Fujii, S.S. Babu, and M. Bloss. Thermal transients during processing of materials by very high power ultrasonic additive manufacturing. *Journal of Materials Processing Technology*, 211:1650–1657, 2011.

[86] Dassault Systems. Abaqus Technology Brief: Simulation of Implantable Nitinol Stents. Online Document:

http://www.3ds.com/fileadmin/PRODUCTS/SIMULIA/PDF/tech-briefs/LS-Simulation-of-Implantable-Nitinol-Stents-03, 2010.

[87] A.G. Truog. Bond Improvement of Al/Cu Joints Created by Very High Power Ultrasonic Additive Manufacturing. Master's thesis, The Ohio State University, Columbus,OH, 2012.

[88] C.M. van der Burgt and H.S.J. Pijls. Motional Positive Feedback Systems for Ultrasonic Power Generators. *IEEE Transactions on Ultrasonics Engineering*, 10(1), 1963.

[89] Vishay. Measurement of Thermal Expansion Coefficient Using Strain Gages. Technical report, Micro-Measurements, 2010. TN-513-1.

[90] Yulong Wang, Limin Zhou, Zhenqing Wang, Haitao Huang, and Lin Ye. Analysis of internal stresses induced by strain recovery in a single SMA fibermatrix composite. *Composites: Part B*, 42:1135–1143, 2011.

[91] D.R. White. Ultrasonic consolidation of aluminum tooling. *Advanced materials & processes*, 161(1):64–65, 2003.

[92] P. Wolcott, A. Hehr, and M.J. Dapino. Optimized welding parameters for Al 6061 ultrasonic additive manufactured structures. *Journal of Materials Research*, 29(17), 2014.

[93] P. Wolcott, A. Hehr, and M.J. Dapino. Process Improvements and Characterization of Ultrasonic Additive Manufactured Structures. *Journal of Materials Processing Technology*, 233, 2016.

[94] Paul.J. Wolcott. *Ultrasonic Additive Manufacturing: Weld Optimization for Aluminum 6061, Development of Scarf Joints for Aluminum Sheet Metal, and Joining of High Strength Metals*. PhD thesis, The Ohio State University, Columbus, OH, 2015.

[95] Shailendra Yadav and Charalabos Doumanidis. Thermomechanical Analysis of an Ultrasonic Rapid Manufacturing (URM) System. *Journal of Manufacturing Processes*, 7(2):153–161, 2005.

[96] Y. Yang, G.D. Janaki Ram, and B.E. Stucker. An analytical energy model for metal foildeposition in ultrasonic consolidation. *Rapid Prototyping Journal*, 16(1):20–28, 2010.

[97] C. Zhang and L. Li. A Friction-Based Finite Element Analysis of Ultrasonic Consolidation. *Welding Journal*, 87:187–194, 2008.

[98] Chunbo Zhang, Andrew Deceuster, and Leijun Li. A method for bond strength evaluation for laminated structures with application to ultrasonic consolidation. *Journal of Materials Engineering and Performance*, 18(8), November 2009.